Imperial College London

2012

Department of Chemistry
Imperial College London

NOVEL TECHNOLOGIES FOR HIGH SENSITIVITY ANALYTE DETECTION

Submitted for the Degree of Doctor of Philosophy by Miki Yamazaki

Except where specific reference is made, the material contained in this thesis is the result of my own work. This thesis has not been submitted in whole or in part for the reward of a degree at this or any other university, and does not exceed 100,000 words in length.

Mikihide Yamazaki

May 2012

Abstract

Microfluidic devices are attracting interest for point-of-care diagnostics due to their low unit cost, low reagent and sample usage, fast analysis times and portability. Fluorescence is the most widely used detection method in microfluidics due to its high sensitivity, excellent dynamic range, ease of implementation and non-invasive nature. Fluorescence detection has accordingly been widely used for the interrogation of microfluidic devices, with the majority of reports to date having used non-integrated laser excitation sources coupled with off-chip optics and photodetectors. For point-of-care applications, there is a growing need for self-contained systems which incorporate the microfluidic chip and all associated optical components into a compact, low-cost package. Highly compact systems of this kind would eliminate the need for expensive dedicated bench-top instrumentation. As such they would find multiple uses in the home, ambulance and GP's surgery, where their ability to provide immediate and/or frequent testing would enable faster, more responsive and ultimately more successful treatment.

Work undertaken in this thesis focuses on developing highly sensitive analyte detection systems that would enable the use of cheap optical and electronic components. To accomplish this, two separate methods, based on optical filters and time-gated detection of phosphorescent polymer beads, were investigated. We describe a simple technique for fabricating non-emissive colour filters based on the sensitisation of a highly porous nanostructured metal-oxide film with a monolayer of dye molecules. The resultant filters exhibit much less autofluorescence than conventional colour filters, and are a viable low cost alternative to interference filters.

In separate work $Ru(dpp)_3$-doped polystyrene/bisphenol A diglycidyl ether polymer phosphorescent beads developed by Dr. Edwards (Imperial College London) were used to demonstrate the feasibility of highly sensitive of low-cost time-gated detection. This method was applied to a simple biotin assay to show their bio-assay applicability.

Acknowledgements

My journey through this PhD course has been a tough one and I would not have been able to complete this thesis without the help and encouragement from the amazing people around me.

Firstly I would like to thank my supervisors, Prof Andrew deMello and Prof. John deMello for giving me the opportunity to undertake this PhD. This thesis would not have been possible without their help, guidance, and patience for which my mere gratitude will not suffice.

An enormous thank you must go to Dr. Siva Krishnadasan for his technical contribution to this work. Without Siva, it would have probably taken me an extra year to complete my PhD! Your good advice and support has been invaluable, for which I am extremely grateful. Thank you Dr. Angharad Edwards for your research into phosphorescent polymer beads. Chapter four is an extension of her research and I dedicate this chapter to you entirely. Thank you also to Dr. Adrian Nightingale, Korn Boonkoom, Christina Pang and my other colleagues in the AdM and JdM group for your friendship and help. I am also very grateful to the members of Prof. James Durrant and Dr. Saif Haque's groups for their technical contributions to this thesis. Further thanks must go to Dr. Oliver Hofmann, Dr. Gihan Ryu, Dr. Miguel Ramon and Jasmine Sze of Molecular Vision Ltd for sharing their expertise in optics and filter fabrication. Molecular Vision has helped me countless times by allowing me to use their facilities. A special thank you to my crazy Russian friend Alex, who kept me entertained in the office. I shall never forget your awesome house parties (especially the 'communist night')!

I would also like to express my sincere gratitude to my friends from my undergraduate course: Henry, Tim, and Yau for their continuous friendship. Outside of Imperial College, I must also thank my friends from school - James, Rupert, Jamie, and Ed to name but a few. Thank you Kie, Yuri, Kiki, and all my Japanese friends for your support! Without you all, my life in the UK would have been very different.

Last but certainly not least, I must thank my family. お父さん、お母さん、かおちゃん、ゴロー＆タローWords cannot express how grateful I am for your support. I could not have done anything without you all.

「挑戦した後の失敗より、何もしない事を恐れろ」

“Fear not failure, but the failure to try at all”

本田宗一郎

Souichirou Honda (CEO, Honda Motor Company)

Table of Content

Abstract 1
Acknowledgements 2
Table of Content 6
List of Figures 10
List of Abbreviations 16
1 Introduction 19
1.1 Diagnostics 19
1.2 Point of care diagnostics 20
1.3 Towards portable point of care diagnostics devices 22
1.3.1 Microfluidic technology 22
1.3.2 Fluorescence detection 23
1.3 Excitation source and detectors 25
1.4 Optical Filters 28
1.5 Titania 32
1.5.1 Crystal Structure of TiO_2 33
1.5.2 Optical and Electronic properties of TiO_2 34
1.5.3 Dye sensitization of TiO_2 34
1.5.4 Synthesis of TiO_2 nanoparticles 35
1.5.4.1 Effect of pH on colloidal size 37
1.5.5 Nanoporous TiO_2 thin films 38
1.5.5.1 Effect of the sintering temperature 39
1.6 Summary 40
2 Nanoporous TiO_2 Optical Filters 42
2.1 Optical filters based on TiO_2 42
2.2 Experimental 43
2.2.1 Preparation of the Filter 44
2.2.1.1 Titanium Oxide Thin Films 44
2.2.1.2 Zirconium Oxide Thin Films 45
2.3 Oxide Film - Characterization Methods 46
2.3.1 Scanning Electron Microscopy 46

2.3.2 Nitrogen Porosimetry 47
2.4 Oxide Film – Results 50
2.4.1 Scanning Electron Microscopy (SEM) 50
2.4.2 Profilometer and Nitrogen Porosimetry 53
2.5 Dye Sensitization of TiO_2 – Results 55
2.6 Integrating sphere quantum yield measurements 60
2.6.1. Principles 60
2.6.1. Results 65
2.7 Autofluorescence Measurements 66
2.7.1 FDS doped Polydimethyl Siloxane (PDMS) 66
2.7.2 Absorption Measurements 66
2.7.3 Autofluorescence measurements 68
2.8 Using the Filters 71
2.8.1 Detection of Rhodamine 6G 71
2.9 Photo-degradation of Titania based filters 73
2.10 Summary 75
3 Short Pass TiO_2 Filters 77
3.1 Introduction 77
3.2 Short Pass Filters 77
3.2.1 Sensitising Titania in the Red 77
3.2.2 Fabricating Short pass filters 80
3.3 Plastic Filters 82
3.3.1 Introduction 82
3.3.2 Fabricating filters on Plastic Substrates 84
3.3.2.1 Types of Plastics available 84
3.3.2.2 Using Conventional Paste 84
3.3.2.3 Using Surfactant Free (SF) Paste 87
3.3.2.4 Using Acetate tape as a Sealant 89
3.3.2.5 New Screen Printing Format 90
3.3.2.6 Summary 91
3.3.3 Autofluorescence measurement of the Plastic Filters 91
3.3.3.1 Autofluorescence measurement 91

3.4 Transfluosphere Detection 93
3.4.1 Testing the Plastic Short Pass filter with Transfluosphere 93
3.4.2 Machined Testing Rig 97
3.4.3 Machined Testing Rig with Constant Current LED Driver 100
3.4.3.1 Pulsed Constant Current LED Driver and Lock-in Amplifier 102
3.4.4 Suppression of LED tail light in the NIR to improve Detection Limits 104
3.4.4.1 NIR Absorbing Dye Based Plastic Filter 105
3.4.4.2 NIR Blocking filter based on Cobalt Complex 107
3.4.4.3 $(TOMA)_2CoBr_4$ doped Polyvinylpyrrolidone (PVP) filter 107
3.4.4.4 Photodetector with a narrower Spectral Response 110
3.5 Summary 111
4 Phosphorescence Detection 115
4.1 Introduction 115
4.1.1 Time-gated detection 117
4.2 Phosphorescent dye doped polymer beads 118
4.2.1 Dye selection and their optical properties 118
4.2.2 Polymer Selection 121
4.2.3 $Ru(dpp)_3$ PS-co-MA/BPA nano-beads 122
4.2.3.1 Precipitation Polymerization 122
4.2.3.2 Experimental 124
4.2.3.3 Determining the ideal Synthesis Conditions 125
4.2.3.4 Stirring rate influence 125
4.2.3.5 Surface carboxyl group quantification 127
4.2.3.6 Reality Check 129
4.2.4 Time-Gated Photoluminescence Detection of the beads 131
4.3 Biotin Detection using $Ru(dpp)_3$-doped PS-co-MA/BPA beads 137
4.3.1 Bio-functionalized Polymer beads 137
4.3.1.1 Introduction to Biotinylation 137
4.3.1.2 Biotinylating the Phosphorescent Nano Beads 138
4.3.2 Magnetic Beads 142
4.3.2.1 Using magnetic beads 142
4.3.2.2 Experimental 143

4.3.2.3 Effect of conjugation 145
4.3.2.4 Biotin detection 146
4.3.2.5 Photostability of the Beads 148
4.4 Summary 149
5 Conclusion & Future work 152
5.1 Conclusion 152
5.1.1 Dye-sensitised titania based filters 152
5.1.2 Time-gated phosphorescence detection 153
5.2 Future work 154
6 References 157
7 Appendix 169
7.1 Constant current LED driver 169
7.2 Constant current pulsed LED driver 169
7.3 Time-gated detection 170
7.4 PLQE measurements of the beads 171
7.5 TC-SPC 171
7.6 List of Publications 171

List of Figures

Fig. 1-1 – Picture taken from ref. [9] to illustrate A) the clinical demand for diagnostic solutions that enable fast and accurate patient triage –e.g. in a heart attack, B) where a portable POC devices can be used to assist physicians to make time-critical decisions C) The device operation is automatic and simple, only requiring 'a drop' of sample for analysis. D) Patient is diagnosed in a matter of minutes and swiftly treated. 21
Fig. 1-2 (Left) Picture of a microfluidic "chemostat" designed to study the growth of a microbial population. taken from ref. [13] (Right) Comparison with a standard laboratory chemostat array for growing and processing yeast samples. Both have similar functions yet microfluidic technology has enabled miniaturisation and automation of such experiments. (Picture taken from Yeast Resource center ref. [14]) .. 22
Fig. 1-3 A Jablonski energy diagram. 24
Fig. 1-4 (Left) Schematic diagram to show the structure of an organic light emitting diode which is comprised of a transparent anode or cathode sandwiching conductive polymer layers where electron/hole recombination occurs. (Right) Schematic shows the basic working principle of an OLED. (Bottom) Picture to show the compact and flexible nature of OLEDs. 26
Fig. 1-5A Schematic diagram showing the two detection component geometries. An orthogonal geometry is typically used in conventional bench top fluorometers, and it prevents significant excitation light from reaching the detector. The face-on geometry allows convenient integration of microfluidic devices and the detector components; however, this configuration can flood the detector with light from the excitation source – masking the typically weak emission signal. 28
Fig. 1-5B Schematic diagram showing a face-on geometry with short and long-pass filters in place. Broad emission from the LED is sharpened by passing it through a short –pass filter to prevent spectral overlap with the analyte emission. The sample is excited by this sharpened LED light. A long-pass filter prevents any unabsorbed LED light to reach the detector. 29
Fig. 1-6 Photo showing the highly autofluorescent nature of a commercial Schott glass filter (OG550, Schott AG, Germany) when illuminated with a 110 mW, 442 nm HeCd laser (IK5751I-G, Kimmon, Japan). 30
Fig. 1-7 Photo showing the Sudan II doped PDMS substrate fabricated by Bliss et. al., which incorporated optical waveguides to maximise signal to noise ratio by increasing the optical path-length. The microfluidic device was designed to perform DNA fragment analysis [33]. This method for filtering excitation light is limited by the range of non-autofluorescent dyes available [15]. 30
Fig. 1-8 (Left) a picture to show how interference filter selectively transmit specific wavelength bands through constructive and destructive interference [52] and (Right) their typical transmission spectrum taken from [53]. 31
Fig. 1-9 Photo and a schematic to show the hybrid filter fabricated by Richards et. al., [54]. 32
Fig. 1-10 Schematic of the crystalline structures of the three main TiO_2 forms: **Left**) Anatase, **Centre**) Rutile, and **Right**) Brookite. 33
Fig. 1-11 Schematic showing the four main dye adsorption mechanism on titania surface. 35
Fig. 1-12 Schematic summarising the common routes for the production of titania nano-colloids using titanium tetrachloride and alkoxy-titanates as precursors. Different polymorphs of titania are produced depending on pH, temperature, additives, and ageing time. The diagram is adapted from [71]. 36
Fig. 1-13 pH dependence of TiO2 particle size in sol (taken from ref. [62]) 38
Fig. 1-14 Schematic showing the function of surfactant/polymer additives in 1) preventing aggregation of the titania colloids in sol-gel and 2) providing a template to form nanoporous structures upon sintering. 39
Fig 2-1 **Energy diagram for a dye coupled to anatase titania (Left) A)** Ultrafast electron injection (<100 fs, depending on the dye) into the conduction band of TiO_2. **B)** Relaxation of the excited electron in the conduction band and the trap states (Internal conversion). **C)** Non radiative charge recombination with the dye cation. **D)** Internal conversion with in the S_1 state followed by subsequent fluorescence emission. 43

Energy diagram for a dye coupled to ZrO_2 A) Ultrafast electron injection into the ZrO_2 trap state (<100 fs) **B)** Electron relaxes down the 'trap' energy levels, and **C)** back transfer into the lower vibrational level of the dye excited state energy level (450 fs) before relaxing down to the ground state via fluorescence (160 ps) **E&F)** Alternatively the electron relaxes down via trap states and recombine at the ground state Alizarin, with no emission (recombination time frame of 2.4 ps) (Adapted from [86]). 43
Figure 2-2 Titanium Oxide / Zirconium Oxide thin films, doped with corresponding dyes (Alizarin and Fluorescein) exposed under UV lamp (365 nm). Films prepared with Zirconium Oxide shows significant emission in comparison to the films prepared with titania. The zirconia films were highly scattering and so appear white and opaque in both visible and UV light..... 44
Fig. 2-3 Screen Printing Ti/Zr oxide paste onto a glass substrate. **A)** A Glass substrate is taped onto a flat surface with a standard 3M scotch tape and 100 ml of the oxide paste is deposited on the substrate. A glass rod is used to spread the oxide paste on to the exposed region of the glass substrate **B & C)** The oxide paste is left to dry for approximately 10 minutes causing the film to become clear. **D)** Dried oxide layer is now ready to be sintered in air..... 45
Fig. 2-4 Diagram illustrating inelastic and elastic scattering of electron. 46
Fig 2-5 Diagram of a model BET plot showing the amount of gas adsorbed (in mol/g) vs relative pressure, P/P_0. 49
Fig 2-6 All images were taken at x200000 magnification and at 1.5 $x10^{-9}$ T pressure. Images are in order of sintering temperature, starting from 750 °C down to 150 °C (750, 650, 450, 250, and 150). The last picture just shows the film cracking at high temperature sintering (in this case 750 °C.)..... 50
Fig 2-7 Size distributions of the surface features seen on the titania substrate sintered at 750 °C, 650 °C, and 450 °C. Size distributions of 100 random surface features were obtained through ImageJ analysis software. 51
Fig. 2-8 Results from the profilometer, displaying average results of three films taken at three different points (9 measurements in total for each sintering temperature). The graph on the right shows a diagram of a typical result from a Profilometer 53
Fig. 2-9 & Table 2-1 Results from the BET surface analyser for non-dye doped titania films. All films were prepared as described in section 2.2.1. ITO glass of equal area is used as a reference to a lamellar type surface. Effective surface area of the TiO_2 film was calculated from the BET surface area and the amount of titania used to fabricate each film (34 mg for all samples). 54
Table 2-2 Table to show the chemical structure and the optical properties of the dyes employed in fabricating long pass filters. 56
Fig. 2-10A Normalised absorption spectrum of the dye in solution and the titania long-pass filter. 57
Fig. 2-10B Transmission spectrum of Titania long-pass filters prepared in different solvents..... 58
Fig. 2-11 Transmission spectrum of Titania long-pass filters prepared in solvents with the highest solubility of the corresponding dyes. Concentration ranged from 0.01 M to $1x10^{-6}$ M. 59
Table 2-3 Table showing solvents for various filters..... 60
Fig. 2-12 Schematic of the integrating sphere setup. 61
Fig. 2-13 – Diagram to show the three separate experiments for obtaining the photoluminescence quantum efficiency values for thin film samples..... 62
Fig. 2-14 – Example spectra for measurement of thin film MEH-PPV taken from ref. [108] 63
Table. 2-4 Overall results from the integration sphere measurements. PLQE of three titania samples and three zirconia samples (prepared at 450 ^{o}C) were measured. Results displayed here are the relative intensities in counts. 65
Fig. 2-15 - Dye doped PDMS filter in petri dish after 48h of room temperature curing..... 66
Fig. 2-16 **(Above)** Absorption spectra of single-layer titania films sensitised with various anthraquinone- and fluorescein-derived dyes. **(Below)** Absorption spectra of three commercially sourced Schott glass colour filters, and an FDS-doped PDMS filter; also shown for comparison are calculated absorption spectra for four-layer FDS- and Alizarin-sensitised titania stacks determined from the single-layer absorption spectra. 67
Fig. 2-17 - Schematic of configuration used for autofluorescence measurements. A 1.1 mW laser beam from a 442 nm HeCd laser is directed onto the front side of the filter and a fibre-optic coupled to a CCD

spectrometer is placed against the rear-side of the filter immediately behind the laser spot, leading to collection of directly transmitted laser light and filter autofluorescence. 68
Fig.2-18A Autofluorescence spectra for the three Schott Glass colour filters, the FDS-doped PDMS and the FDS-sensitised titania filter. All samples were excited at 442 nm with an integration time of 15 min. 69
Fig.2-18B Autofluorescence spectra for the six dye-sensitised titania films under identical conditions. Note, the spectra are shown on a magnified scale relative to 2-18 (A). 70
Fig.2-19 Photograph taken during the autofluorescence measurements using the conditions described in Fig. 2-17. Titania based filters sensitised (right) with FDS only shows a reflected laser spot, while commercial (left) and FDS-doped PDMS (center) shows significant autofluorescence. 70
Fig.2-20 Schematic of configuration used for concentration measurements. The 1.1 mW laser spot from a 440 nm HeCd laser and a silicon photodiode were positioned opposite one another on the front and back surfaces of a cuvette, with the long-pass filter tightly inserted between the rear of the cuvette and the photodiode, leading to collection of transmitted laser light, analyte fluorescence and filter autofluorescence. 71
Fig. 2-21A Signal versus concentration of Rhodamine 6G in ethanol. Three types of filters were used: 1) a four-layer FDS-sensitised titania stack, 2) a four-layer Alizarin stack, and 3) a commercial Schott glass colour filter OG530. The experiment used 1.1mW HeCd Laser (KIMMON, Japan) as the light source, and the signal was detected using a Si photodiode (S1226-8BQ, Hamamatsu, Japan) coupled to a Keithley 6517 electrometer. 72
Fig. 2-21B Schematic to show the concept of LOD shown on a 'model' signal versus concentration plot (not to scale). Standard deviations (σ) obtained from repeated measurements are used to calculate the LOD. 72
Fig. 2-22 Normalised absorbance of filters sensitised with A) Ti-FDS and B) Ti-Alizarin over period of 24h under continuous illumination by 442 nm of monochromatic light (0.04 mW/cm^2). A 50-80 % reduction in absorption is observed due to photodegradation. 74
Fig. 2-23 Normalised absorbance of encapsulated filters based on A) Ti-FDS and B) Ti-Alizarin over period of 24 h under the same illumination conditions as Fig. 2-22 74
Fig. 3-1 Absorption Spectra of the blue dyes dispersed in ethanol. 78
Fig. 3-2 Cationic and anionic dyes adhere to negatively and positively charged titania, respectively. 80
Fig. 3-3 (A) Titania film 'sensitised' with xylene cyanol dye without any surface charge altering treatment. The titania film shows of transparent patches where dye adhesion did not occur even after 24 h of immersion in the dye solution. (B) Titania film sensitised using surface charge treatment showed greatly improved dye adhesion 81
Fig. 3-4 (A) Absorption spectra of four-layer stacked titania films sensitised with Methyl Blue (B) Remazol Brilliant Blue. (C) 1,1'-Diethyl -4,4' Carbocyanine Iodide and (D) Xylene Cyanol. 82
Fig. 3-5 Proposed low temperature fabrication steps for using conventional paste. 85
Fig. 3-6 Filters fabricated using conventional paste on **A**) glass with 450 °C annealing, **B**) plastic substrate (PC) with 120 °C followed by UV/O_3 treatment, (**C**) PC with UV/O_3 treatment first followed by 120 °C sintering, and D) PC with 120 °C sintering only. In all cases precursor from Nanopac, which contained surfactants was used. 86
Fig. 3-7 Ti-Short pass filter fabricated by 120 °C sintering followed by UV/O_3 treatment. The filter showed poor mechanical stability with the titania layer cracking and flaking off upon flexing the filter 87
Fig. 3-8 Filters fabricated using conventional surfactant-containing pastes + 450 °C annealing on glass substrate, surfactant free paste with 120 °C annealing on plastic (PC), and surfactant free paste with no annealing on PC. 88
Fig. 3-9 Schematic to show the new filter fabrication steps on plastic substrates [137]. Additional titania surface charge moderation step may be necessary depending on the sensitizer 88
Fig. 3-10 Normalised Absorbance of A) acetate tape encapsulated Ti-FDS filters and B) Ti-Xylene Cyanol filters over a period of 3h under continuous illumination by 500 nm monochromatic light. 89

Fig. 3-11 Schematic to show the new doctor blading format used to fabricate uniformly sensitised titania plastic filters. The new format allows the titania to dry with uniform thickness. Inset shows a plastic Xylene Cyanol sensitized short pass filter fabricated using both the old and the new doctor blading formats.....90
Fig. 3-12 (**A**) Autofluorescence spectra for an unsintered Ti-FDS long-pass filter on PET under 1 mW 442 nm HeCd excitation. Also shown for reference is a commercial Schott glass filter obtained under identical conditions. (**B**) Autofluorescence spectra for an unsintered Ti-XC short-pass filter on PET under 0.5 mW 633 nm HeNe excitation. All other acquisition conditions were the same. Spectra for the titania-based filters have been enlarged by a factor of 1000 for clarity. 92
Fig. 3-13 Excitation and Emission spectra of the T-8861 Transfluospheres 93
Fig. 3-14 Absorption spectra of FDS-sensitised titania long-pass filter and Xylene Cyanol- sensitised titania short-pass filter.....94
Fig. 3-15A Simple schematic diagram of the sheet plastic constructed test device.....94
Fig. 3-15B Pictures of the test device used to measure the transfluosphere signal.....95
Fig. 3-16 (**Top**) Optical characteristic of the cyan LED (505nm) measured with a fibre-optic coupled CCD spectrometer. Inset picture and the spectra also show the LED with a single Xylene Cyanol sensitized glass Ti-short pass filter (**Bottom**) – Spectrum shows effective blocking of the cyan LED light up to 670 nm by using both the short and long pass filters. Inset picture shows no apparent light leakage.....96
Fig. 3-17 Signal versus transfluosphere bead concentration using titania short and long pass filters. The measurement set up is shown in Fig. 15A. 97
Fig. 3-18 Left (**A**) -505 nm LED (20 mA) connected to a 9 V battery supply. (**B**) - Plastic Short pass filter inserted in a filter holder. The short pass filter is placed directly in front of the LED light source. (**C**) - Quartz cuvettes containing the transfluosphere solutions are placed in the cuvette holder. The holder is machined so that cuvettes are held tightly. (**D**) - Plastic Long pass filter inserted in a filter holder. The Long pass filter is placed directly in front of the detector. (**E**) – silicon photodiode connected to Keithley electrometer. Right – photograph of the machined rig.....98
Fig. 3-19 Signal versus transfluosphere bead concentration in distilled water using the machined rig and titania short- and long-pass filters.....98
Fig. 3-20 Signal versus concentration of transfluosphere in distilled water. (Left) using the original plastic rig and (Right) Using the machined rid. The graph is plotted on a linear scale and focuses on the low concentration region. 99
Fig. 3-21 (**A**) Variation in LED intensity with time under battery operation and constant current operation (**B**) Signal intensity for $1x10^9$ beads μl^{-1} using LED driven with a power supply at constant voltage and current over 300 s time period.....100
Fig. 3-22 Signal versus transfluosphere bead concentration in distilled water using the machined rig and titania short and long pass filters. The LED is driven with a homemade 20mA constant current driver. The graph is plotted on a log-log scale. 101
Fig. 3-23 Signal versus concentration of transfluosphere in distilled water using the machined rig and titania short- long pass filter. The LED is driven with an in-house 20 mA constant current driver. 101
Fig. 3-24 Diagram to show the output response of a phase sensitive detection with cosine reference waveform and a square-wave signal waveform. More details in equation 3A-3F. 102
Fig. 3-25 Signal versus transfluosphere bead concentration in distilled water using the machined rig and titania short and long pass filter. The LED was driven with an in-house 20 mA pulsed constant current driver. The signal was measured with a Si-photodetector coupled to a lock-in amplifier.....104
Fig. 3-26 The transmission spectra of the Kentek prototype NIR blocking filter shows between 5-30% transmission in the desired stop band (700 – 800 nm) and relatively good transmission at the transfluosphere emission (70 %). Inset shows the actual NIR blocking filter. Inset shows a picture of the prototype plastic IR filter.....106
Table 3-2 A table to show the summary of the background signal under different conditions. 106
Fig. 3-27 Signal versus transfluosphere bead concentration using the machined rig and titania short- long pass filter. The LED is driven with an in-house 20 mA pulsed constant current driver. The signal was measured with

a Si-photodetector was coupled lock-in amplifier. An additional NIR blocking filter was added at the front of the photodetector to cut the LED tail light leakage in the NIR region 106
Fig. 3-28 Structure of $(TOMA)_2CoBr_4$. $(TOMA)^+$ and Br^- ions have weak electric fields and cause low energy gap in d-orbital splitting which corresponds to their absorption in the Red region of the spectrum. 108
Fig. 3-29 (Above) Transmission spectrum of single spin coated and drop casted $(TOMA)_2CoBr_4$ doped PVP on glass. Inset picture shows the drop casted $(TOMA)_2CoBr_4$ doped PVP on glass. 108
Fig. 3-30 A schematic to show the NIR absorption in radicals. This schematic has been adapted from [150]. 109
Fig. 3-31 Signal versus transfluosphere bead concentration in distilled water using the machined rig and titania short- long pass filter. The LED was driven with an in-house 20mA pulsed constant current driver. The signal was measured with a Hamamatsu S7686 narrow spectral response Si-photodetector coupled to a lock-in amplifier (Stanford Research Systems, SR830). 110
Table 3-3 A table to show the summary of the transfluosphere detection experiments. 111
Fig. 4-1 Schematic to show mechanism of a commonly found immunoassay using an antibody functionalised luminescent polymer beads 116
Fig. 4-2 Schematic to show how time-gated detection works. Adapted from [165]. 117
Fig. 4-3A Chemical structures of **A**) $Ru(dpp)_3$ and **B**) $Ru(bpy)_3$. 119
Fig. 4-3B (**Left**) Normalised absorption and emission spectra of $Ru(dpp)_3$ in DMF. (λ_{ex} = 470 nm) (**Right**) Metal-to-Ligand Charge Transfer (MLCT) that occurs in $Ru(dpp)_3$ upon absorption. 119
Fig. 4-4 A Jablonski diagram to illustrate the decay paths of $Ru(dpp)_3^{2+}$. k_F is the rate of fluorescence, k_{NR} rate of non-radiative decay, k_{ISC} rate of inter system crossing, and k_P rate of phosphorescence. 120
Fig. 4-5 Selection of Ruthenium dye, polymer, and cross-linking agents for producing phosphorescent polymer micro-beads described in this chapter. 122
Fig. 4-6 A schematic to show the formation of $Ru(dpp)_3$-doped polymer nano-beads by precipitation 123
Fig. 4-7 Schematic of synthesis procedure for $Ru(dpp)_3$ doped PS-co-MA/BPA polymer nano-beads 124
Fig. 4-8 SEM images of the $Ru(dpp)_3$ doped PS-co-MA/BPA beads synthesised at different stirring rates. Beads synthesised at 600 rpm was the conditions used by Edwards. 126
Fig. 4-9 Size distribution of the spherical $Ru(dpp)_3$ doped polymer beads. Non-spherical beads were omitted from the count. 126
Fig. 4-10 – Schematic to show the titration procedure of $Ru(dpp)_3$ doped PS-co-MA/BPA bead. Phase 1) Beads are suspended in 1 mM NaCl solution to promote ion exchange and to further liberate protons. Phase 2) slow addition of 0.05 M NaOH solution neutralises the liberated protons, decreasing the solution conductivity due to decreased ion mobility. Phase 3) further addition of NaOH increases the overall ion content of the titrates, increasing the conductivity. 128
Fig. 4-11 Titration curve of $Ru(dpp)_3$ doped PS-co-MA/BPA bead. Equivalence point was reached with 76.8 µl of 0.05 M NaOH solution, which equates to 35.5 µmole/g of surface acidic group content. 128
Fig. 4-12 Schematic to show the sequence of events in time-gated detection. One cycle is approximately 50 µs. 131
Fig. 4-13A Dose response curve for $Ru(dpp)_3$ doped PS-co-MA/BPA in aqueous solution, obtained using the time-gated detection system. Inorganic LED (E1L31-3B0A2, Toyoda Gosei, Japan) was used as an excitation source and silicon photodetector (S5972, Hamamatsu, Japan) as the detector. 132
Fig. 4-13B (**Left**) Dose response curve for $Ru(dpp)_3$ doped PS-co-MA/BPA in aqueous solution, obtained using the time-gated detection system. Measurements shown on fig 4-13A were repeated with a fresh batch of beads. 100 µL of 0.01 M aqueous FDS solution were added to the FDS-less bead solution during the measurements. (**Right**) Picture taken during the experiment conducted in Fig. 4-13B. (**A**) $Ru(dpp)_3$ doped PS-co-MA/BPA in aqueous suspension and (**B**) the same $Ru(dpp)_3$ doped PS-co-MA/BPA aqueous suspension with 100 µL of 0.01 M aqueous FDS solution. 133
Fig. 4-14A Picture shows the prototype time-gated detection system under development by deMello et. al. The setup is connected to a voltmeter as a temporary read-out display for easier presentation. Picture below shows the internal electronics - needless to say that this device can be further miniaturised. 134

Fig. 4-14B Picture shows the time-gated setup under operation with FDS doped PVP film. Read out from the Lock-in amplifier indicates no-signal in both dark and ambient light conditions for FDS PVP films, since time-gated detection rejects signals that are not in its detection window. 135
Fig 4-15 Chemical structure of Biotin and its variant, amine-PEG-Biotin. Valeric acid component of Biotin can be modified to accommodate side groups such as amine-polyethylene glycol (PEG) spacer arms. Solubility of the biotin can be modified through use of such side groups, and spacer arm lengths are typically modified to reduce steric hindrance (to improve detection sensitivity). 138
Fig 4-16 Scheme showing how the biotinylation of the synthesised beads was carried out. Addition of EDC and Sulpho-NHS to the beads forms semi-stable amine reactive NHS ester. This prevents any carboxyl groups from being regenerated and ensures that all available carboxyl have reacted. Addition of amine-PEG_8-biotin forms a stable amide bond between the carboxyl groups on the beads and the amine moiety of biotin. The reaction is carried out in a 0.1 M MES solution at pH 6.0. Finally the reaction is 'quenched' by washing the biotinylated beads with 0.1 M pH 7.2 PBS. Beads were purified multiple times using a centrifuge to remove any free biotin and reactants. 139
Fig 4-17 ATR-FTIR spectrum of biotinylated $Ru(dpp)_3$-doped PS-co-MA/BPA beads. Also shown are the control spectrum of non-biotinylated $Ru(dpp)_3$-doped PS-co-MA/BPA beads and biotin for comparison. Biotinylated beads were extensively washed with 0.1 M PBS to eliminate any un-bound biotin. 140
Fig 4-18 Emission and excitation spectra of the biotinylated beads. Also for comparison are the spectra for non-biotinylated beads. 141
Fig 4-19 Phosphorescence lifetime obtained through TC-SPC. Lifetime of both beads show negligible differences. 141
Fig 4-20 PLQE data obtained through integration sphere measurements of **A**) non-biotinylated beads and **B**) biotinylated beads due to the scattering nature of the beads. Equipment used for this experiment is identical to that of chapter two, section 2.6. Measurements were carried out with 8 ms and 30 ms integration times – see chapter 2 section 2.6. Units for all the experimental parameters are in $mW.m^{-2}$. 142
Fig 4-21 Schematic to show the biotinylated bead filtration using the streptavidin coated magnetic beads (Dynabeads®MyOne™ Streptavidin C1, Life Technology, UK). The magnetic beads are large in size (1 µm) compared to the phosphorescent beads (approximately 300nm). The long spacer arm of the amine-PEG_8-biotin (Sigma Aldrich, UK) allows multiple beads to be anchored to the magnetic beads via the streptavidin-biotin link. 143
Fig. 4-23 A) Emission/excitation spectra of the magnetic bead conjugate compared to biotinylated beads. B) Phosphorescence lifetime of the magnetic bead conjugate. Also shown are results for the bead in their biotinylated and biotinylated forms. C) PLQE spectra of the magnetic bead conjugate. All measurements were acquired with the same procedure and equipment as section 4.3.1.2. 145
Fig. 4-24 Phosphorescence signal intensity response to biotin concentration. Also plotted are the signal intensity of the supernatant and the sum of both phosphorescence signals. 146
Fig 4-24 Plot shows the phosphorescence signal intensity response to biotin concentration. Also plotted are the signal intensity of the supernatant and the sum of both phosphorescence signals. Concentration of the magnetic beads used here was halved and the supernatant solutions were not 'washed' 147
Fig 4-25 Plot shows the phosphorescence signal intensity of the beads over a span of 1200 min 148
Fig 4-26 Picture to show the sedimentation of phosphorescent beads after 48 h. 149
Fig. 5-1 diagram showing the structure of the proposed multi-layered titania filter 154
Fig. 7-1 Circuit diagram of the constant current LED driver used in section 3.4.3. Uses a LM344 current source and a single resistor to maintain the current at 20 mA. Taken from ref. [218] 169
Fig. 7-2 Circuit diagram of the pulsed constant current LED driver used in section 3.4.3.1. Uses a HP 8011A pulse generator for the pulse input. Circuit was designed and built by Mr Steve Atkins of Imperial College London 169
Fig. 7-3 Schematic of the equipment used in Chapter 4, section 4.2.4. Time-gated detection was performed using a PIC board (MikroElektronika, PIC-Ready) driven 480 nm LED at 8.8 kHz. Gated integrator used the IVC102 IC precision integrating amplifier which can integrate low-level input current for a user-defined period.

Input current charges a small feedback capacitors and the voltage across the capacitors are measured before being reset. Analogue Lock-in circuit used were taken from ref [197] and constructed by Mr Steve Atkins of Imperial College London. 170

List of Abbreviations

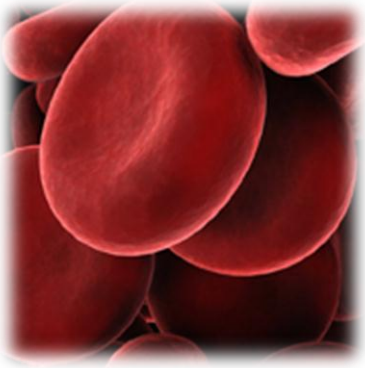
A = molecular weight of the adsorbed gas.
A.I. = Artificial Intelligence
ATR-FTIR= Fourier Transform Infrared
BET = Brunauer, Emmett, and Teller
BPA = Bisphenol A glycidyl ether
c = BET constant described in Equation 2F
CADs = Computer Aided Diagnostics
CCD = Charge coupled device
CW = Continuous wave
DMF = Dimethylformamide
DMSO = Dimethyl Sulfoxide
DSSC = Dye sensitised solar cells
E_{Ads} = Heat of adsorption for the first layer
E_L = Heat of condensation
E_v = Band gap
eV = electron volts
FAB = Fragment Antibody Binding
FC = Fragment Crystallisable
FDS = Fluorescein Disodium Salt
He-Cd = Helium-Cadmium
HOMO = Highest occupied molecular orbital
hv = energy of a photon given by planks constant and frequency
IgG = Immunoglobulin G
ITO = Indium tin oxide
LED = Light emitting diode
LIA = Lock-in amplifier
LMCT = Ligand to metal charge transfer
LOD / Λ = Limit of detection
LP = Long pass
LUMO = Lowest occupied molecular orbital
MLCT = Metal to ligand charge transfer
N_A = Avagadro's Number
n = Refractive index
NIR = Near Infrared
OLEDs = Organic light emitting diodes
OPD = Organic photodetector
P = Equilibrium Pressure
P_0 = Saturation Pressure
PBS = Phosphate buffer saline
PC = Polycarbonate

PDMS = polydimethylsiloxane
PEG = Polyethylene glycol
PET = Polyethylene terephthalate
POC = Point of care
PS-co-MA = polystyrene-co-maleic acid
R = Gas Constant ($8.314 JK^{-1}mol^{-1}$)
rpm = Rotations per minute
$Ru(bpy)_3$ = Tris(bipyridine)ruthenium
$Ru(dpp)_3$ = Tris(4,7-diphenyl-1,10-phenanthroline)-ruthenium
S = adsorption cross section
S_0 = Electronic ground state
S_1= excited state
SEM = Scanning electron microscopy
SF = Surfactant free
Si = Silicon
SP = Short pass
T = Temperature in Kelvin (K)
TC-SPC = Time Correlated Single Photon Counting
TOMA = Methyltrioctyl-ammonium
UV = Ultra Violet
v = Adsorbed Gas in unit volume
V_m = Molecular volume of the gas itself
v_m = Monolayer Adsorbed volume
η = Quantum Yield
N = Total number of photons emitted per second
N_Ω= Photons are received per second over a solid angle Ω (Equation 2J)

CHAPTER 1

1

Introduction



1 Introduction

1.1 Diagnostics

From tasting urine to molecular analysis, diagnostic techniques have come a long way since the dawn of man, and new methods continue to be developed. Very early medical diagnosis was purely observation based, and visual inspection of urine for pus and blood (uroscopy) was routinely performed [1]. More advanced tools and methods for diagnostics such as microscopy, thermometers, and stethoscopes were not widely used until the end of the 19th century. It was not until the early 20th century that the first quantitative lab tests were introduced to diagnose cholera, typhoid, and tuberculosis [1, 2]. By the mid-20th century, clinical labs were commonly found in hospitals, and the use of precise measurements in diagnostics became standard. Many of the 'standard tests' such as eye tests, and IQ tests developed during this period were part of a movement to identify the 'norm' in human physiology [1]. Furthermore, chemical and bacteriological tests to identify diseases also evolved very rapidly during this period, allowing physicians to systematically link microbiology to bodily symptoms.

Vast improvements were made in medical diagnostics with the introduction of computers in the mid-to-late 20th century. Algorithms were developed to analyse large medical data sets [3] and Artificial Intelligence (AI) and Computer Aided Diagnostics, were widely used to help physicians to detect medical anomalies from body scan images such as mammograms [4]. However, despite the significant advances in medical diagnostic techniques over the past few decades, the majority of diagnostic tests are still performed in centralised laboratories where tests are often expensive and time-consuming.

One such example is urine testing (urinalysis), which requires urine samples from the patients to be collected over a 24 h period and typically another 24 hours for the results [5]. The whole process can take up to 96 hours due to the need for the collected urine to be logistically transferred to a centralised laboratory for testing [6]. Centralised laboratories have arisen because the instruments used for urinalysis (and other tests) are expensive, and require specialised training for operation. Some on-the-spot tests are available but these are currently used mainly for initial screening due to their qualitative nature [6]. There are many conditions where time is critical to the survival of patients, hence fast and quantitative diagnostic tests at the point of care are urgently needed.

1.2 Point of care diagnostics

The current global Pont-of-Care (POC) diagnostics market is dominated by simple in-vitro diagnostic tests that are self-administered (such as colorimetric tests for glucose in blood which). POC diagnostics is a fast growing market that was worth $40 billion in 2008 [7]. With an increasing demand for high quality healthcare in developed nations, the size of the diagnostic market is projected to reach $60 billion by 2014 [8]. The challenge for researchers involved in this growing field is to develop low-cost and accurate (yet rapid) diagnostic techniques that can bring the traditional lab test to the point of care, and so enable swift and effective treatment of patients.

In developing countries the consequences of quantitative point-of-care technology would be far reaching, enabling governments to avoid the cost of establishing national networks of diagnostic laboratories (as currently exist in developed countries) and to instead move directly to a distributed healthcare model based entirely around point of care testing. In the developed world, POC technology would find multiple uses in hospitals, ambulances and GPs' surgeries, where its ability to provide immediate and accurate testing would enable faster, more responsive and ultimately more successful treatment. POC technology can facilitate patient-monitoring at home and so alleviate the pressures that are currently placed on the already overloaded medical services. Furthermore, the application of POC technology could be expanded to drug screening or forensic analysis. Fig. 1-1 shows how such portable diagnostic equipment could be used in hospitals to perform quantitative tests to diagnose patients with time-critical conditions (such as heart attack suffers) quickly and efficiently.

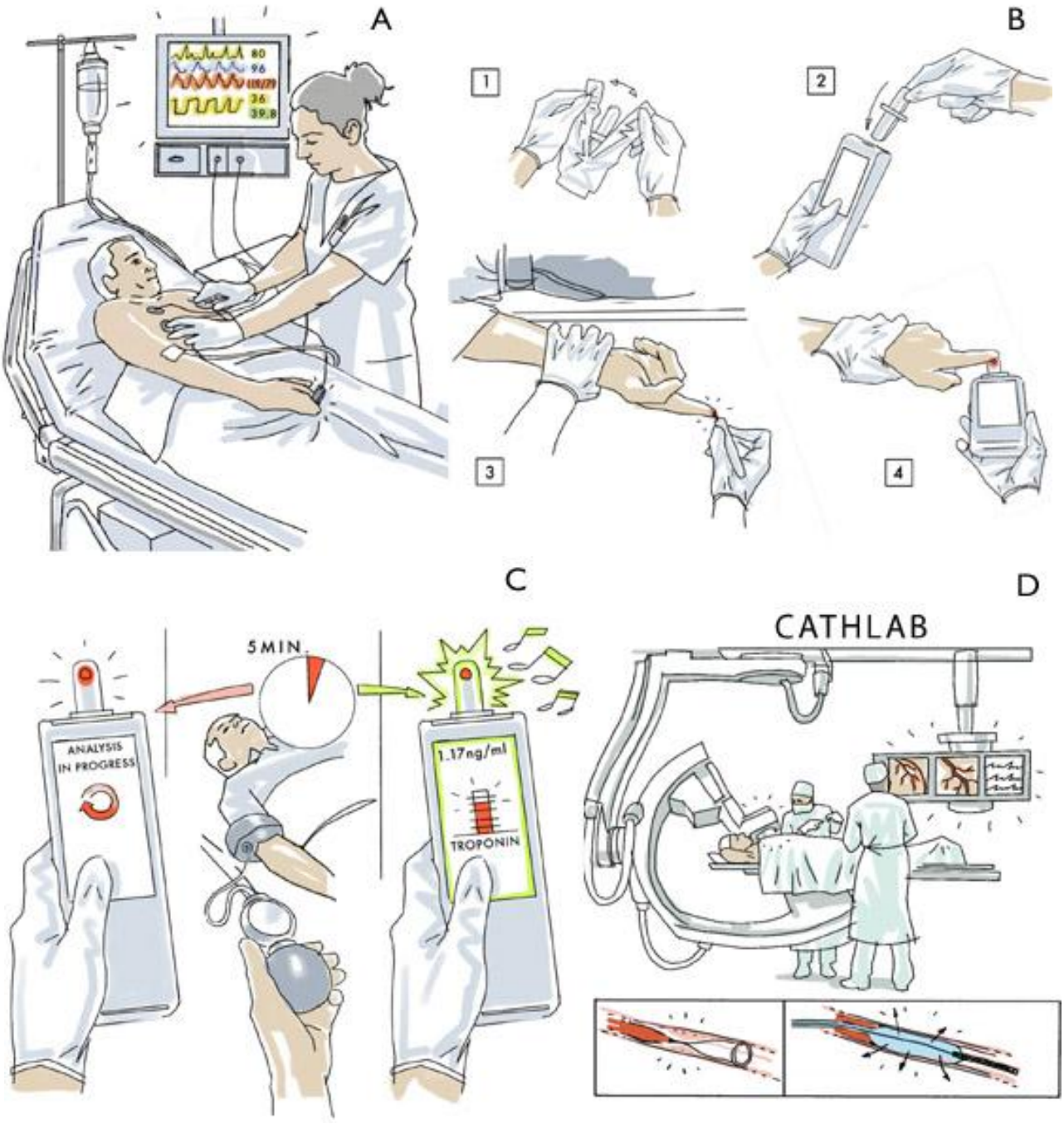


Fig. 1-1 – Picture taken from ref. [9] to illustrate A) the clinical demand for diagnostic solutions that enable fast and accurate patient triage –e.g. in a heart attack, B) where a portable POC devices can be used to assist physicians to make time-critical decisions C) The device operation is automatic and simple, only requiring 'a drop' of sample for analysis. D) Patient is diagnosed in a matter of minutes and swiftly treated.

1.3 Towards portable point of care diagnostics devices

1.3.1 Microfluidic technology

Some of the most exciting research in the last few decades has been in the field of nanotechnology and miniaturisation of analytical equipment. The core technology for the realisation of low cost portable POC devices is microfluidics, which is a technology that allows manipulation of fluids in sub-millimetre channels [10]. Microfluidics is attracting interest in the field of point of care diagnostics due to its low unit cost, low usage of sample and reagents, fast analysis times, portability, and ability to manipulate small amounts of fluid [11] (Fig.1-2). This technology is essentially the miniaturisation and integration of chemical and analytical processes into a single substrate, hence the commonly used term "Lab-on-a-chip" technology [10]. A key objective for microfluidic technology, is to provide a low-cost, and portable analyte detection device capable of POC application [12].

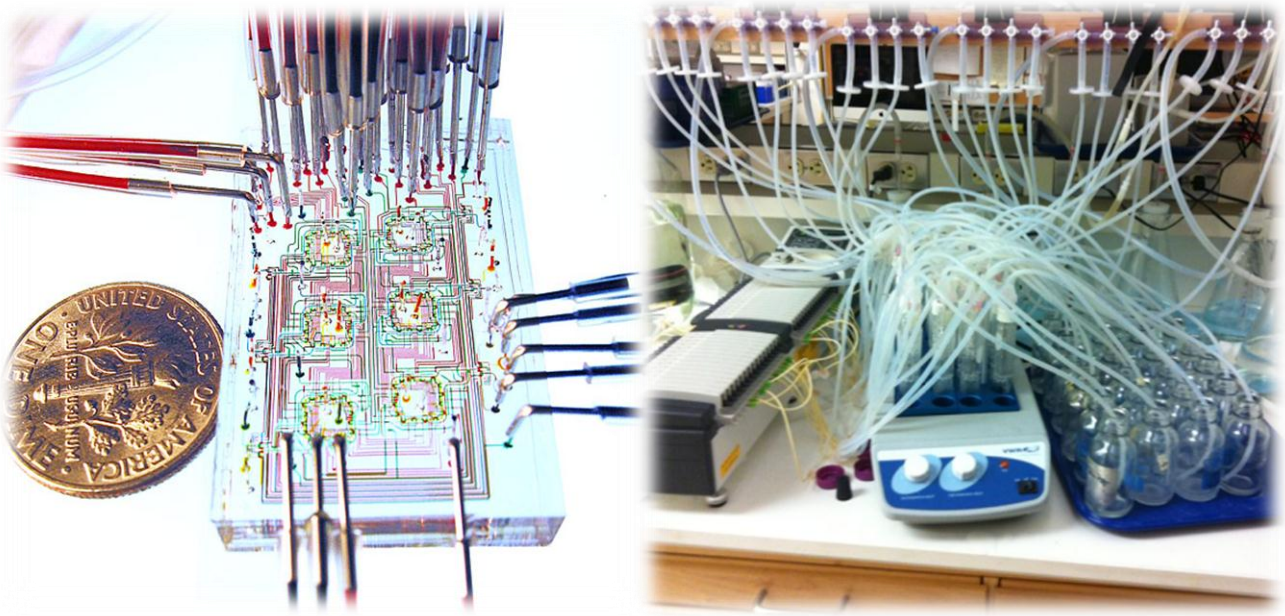


Fig. 1-2 (Left) Picture of a microfluidic "chemostat" designed to study the growth of a microbial population. taken from ref. [13] (Right) Comparison with a standard laboratory chemostat array for growing and processing yeast samples. Both have similar functions yet microfluidic technology has enabled miniaturisation and automation of such experiments. (Picture taken from Yeast Resource center ref. [14])

Portable POC devices will only find widespread usage when they can provide a comparable level of quantification and reliability to current lab-based analytical methods. Typical stages in a diagnostic process include analyte sampling, sample pre-treatment, chemical reaction, analyte separation, and

analyte detection. The last of these steps is often the most challenging due to the small quantities of analyte present, particularly in microfluidics devices where the absolute number of detectable analyte molecule is limited due to the small channel width and the detection window area. Consequently, highly sensitive detection systems are needed where typically "nano-molar" sensitivity (or better) is required for most diagnostic applications [11, 15]. In practice, optical methods – most notably fluorescence detection – are often the only ones that can provide adequate sensitivity. The reason fluorescence detection provides such high sensitivity is that unlike other optical detection methods such as absorption spectroscopy, fluorescence is measured against a dark background. Furthermore, very sensitive photodetectors with high quantum efficiencies and low noise levels are available which makes fluorescence the ideal detection method for a microfluidic device.

Considerable efforts have therefore been devoted to developing high performance optical components for use with microfluidic devices, including both active components such as light-sources [16-20] and photodetectors [16, 18, 19, 21-24], and passive components such as prisms, [22] micro-lenses, [25] filters, [26, 27] mirrors, [28] gratings, [29] waveguides, [30, 31] and polarisers. It is often the performance of the passive components rather than the active ones that determines the final sensitivity of the system. [26, 32, 33]

1.3.2 Fluorescence detection

Fluorescence occurs when an absorbed photon triggers the emission of another photon of lower energy. When molecules absorb photons, they are excited from their S_0 ground state to their S1 excited state, i.e. $S_0 + hv \longrightarrow S_1$ (where $h\,v'$ = the energy of a photon). In the case of a fluorescent molecule, emission of light is observed when the molecule relaxes from this excited state back to its ground state (i.e. $S_1 \longrightarrow S_0 + hv''$). The phenomenon is best described by the use of a Jablonski diagram. (Fig. 1-3)

As seen from Fig.1-3, the ground and excited states contain multiple vibrational energy states. The molecule is excited to different vibrational states depending on the energy (wavelength) of the incoming photon. Since the molecule is unstable in a high vibrational state configuration, it readily relaxes to the lowest excited state configuration – a process known as internal conversion, with its excess energy being lost as heat. This effect results in a Stoke's shift of the emission, with the emitted photon being red-shifted relative to the absorbed photon.

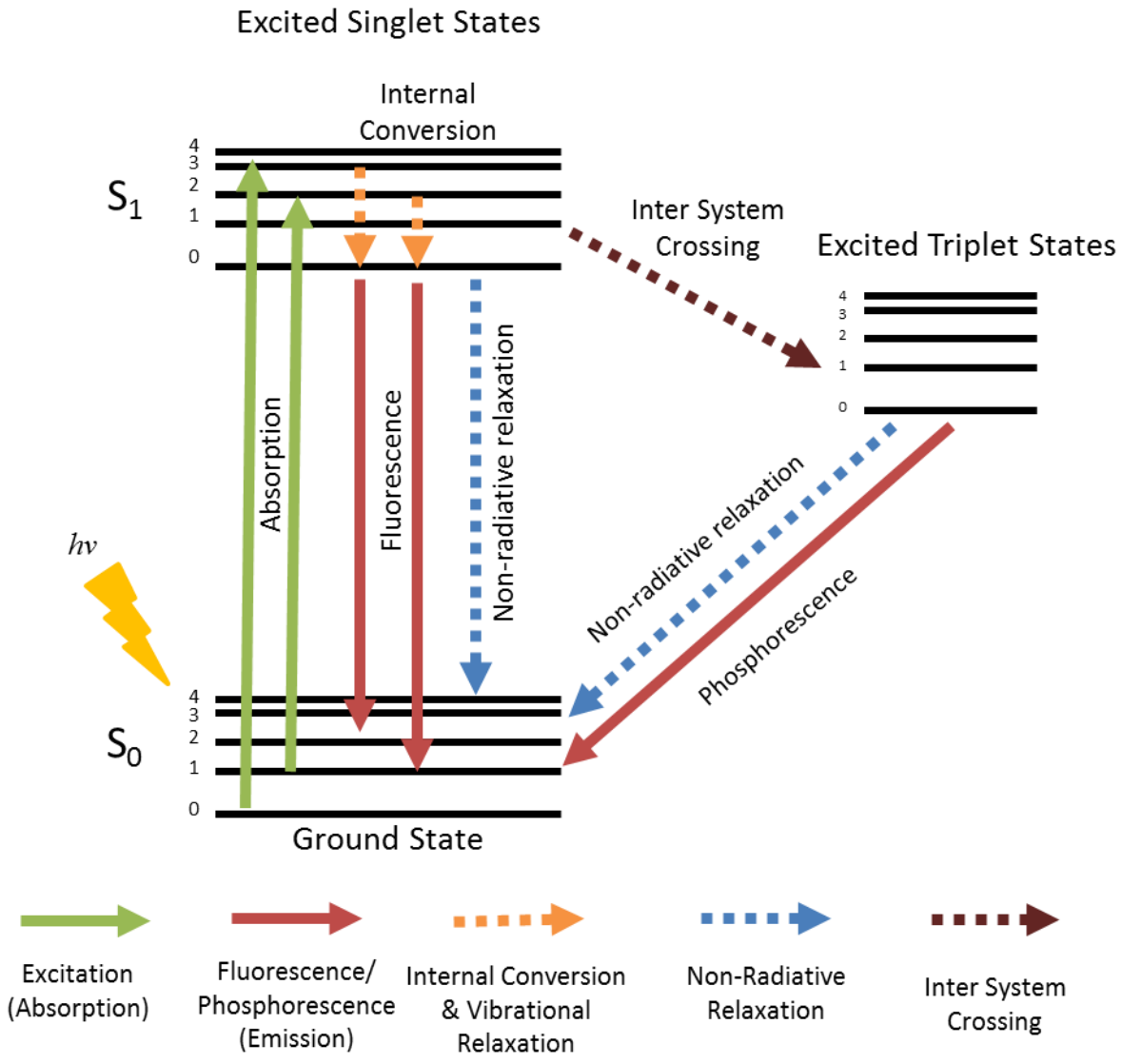


Fig. 1-3 A Jablonski energy diagram.

In phosphorescence the excited molecule undergoes an intersystem crossing into a lower-lying energy state of higher spin multiplicity, typically a triplet state as shown in Fig. 1. Such transitions are most common when 1) vibrational levels of the excited states overlap and 2) heavy-atoms are present in the molecule since there is substantial spin-orbit coupling. Once the molecule is "trapped" in its triplet state, it can only relax down to its singlet ground state by 'spin-forbidden' transition - radiatively or non-radiatively. Although it is termed 'forbidden' it still occurs however, at a significantly slower rate compared to $S_1 \rightarrow S_0$ transitions. Radiative relaxation from the triplet state to the singlet ground state is called phosphorescence and this type of emission forms the basis of time-gated luminescence detection (discussed further in Chapter 4).

For fluorescence, it is desirable for the excitation light to have a low divergence and a narrow emission spectra. Hence most researchers use lasers, and early reports on laser-induced fluorescence in microfluidic devices used gas-phase lasers. Such lasers are expensive and bulky, which makes them ill-suited for field applications [34-37]. Several examples of low-cost and compact laser diodes being used in conjunction with microfluidic devices have been reported however, they still rely on bulky and expensive optics (such as confocal microscopes) for detection that are ill-suited for miniaturisation [30, 38]. A more recent trend has been the development of microfluidic devices with integrated optical components that uses relatively compact and low-cost laser diodes, waveguides and photodetectors [33, 39-41]. For example, Zhixiong *et.al.,* has shown that a micro-arrayed waveguide grating integrated microfluidic platform excited by a laser diode is capable of fluorescence spectroscopic analysis [42]. However detection systems that utilise laser diodes still suffer from narrow spectral coverage and high power consumption [43]. State-of-the-art microfluidic devices overcome this problem by switching to inorganic/organic light emitting diodes (LEDs and OLEDs) which offers low cost, low power consumption, and broader spectral coverage, albeit with much broader line widths [16, 18, 26, 44, 45].

1.3 Excitation source and detectors

LEDs are a semiconductor based light source and they are constructed by placing p-type and n-type semiconductors in contact, thus creating a p-n junction. P-type materials are made by addition of a trivalent impurities (such as boron, aluminium, and gallium) to a quadvalent materials (silicon) creating electron deficiencies called 'holes' in the lattice which can act as a positive charge carrier. N-type materials are made by the addition of pentavalent impurities, which contribute free electrons to the lattice, greatly increasing the conductivity of an intrinsic semi-conductor. In a forward bias (switched on) electrons near the p-n junction diffuse across to combine with the holes, falling into a lower energy level and releasing energy in the form of photons. The wavelength of the light is determined by the bandgap energy of the materials forming the p-n junction – providing some tuneability of the emission properties. Inorganic photodiodes operates much like the LED in reverse where photons are absorbed to create a photocurrent. Numerous examples of LEDs and photodiodes used in conjunction with microfluidic devices have been reported and extensive review articles on this matter are available [45].

Another class of excitation source that has generated significant commercial interest is the OLED. Major electronic companies have started mass production of OLEDs for the next generation of ultra-flat screen displays and lightings. Typical OLEDs comprise two semiconducting polymers (electron and hole

transport layers), sandwiched between two electrodes (Fig.1-4), where one electrode is made from an optically transparent material such as ITO (Indium-Tin Oxide). When a voltage is applied across the electrodes, electrons and holes move according to the electric field. Charges drift through their respective transport layers and recombine at the interface (Fig. 1-4). This recombination results in the formation of an exciton (bound state of electrons and holes) and an emission of a photon with a frequency given by the energy gap between the highest occupied molecular orbital and the lowest unoccupied molecular orbital of the semiconducting polymers employed [46].

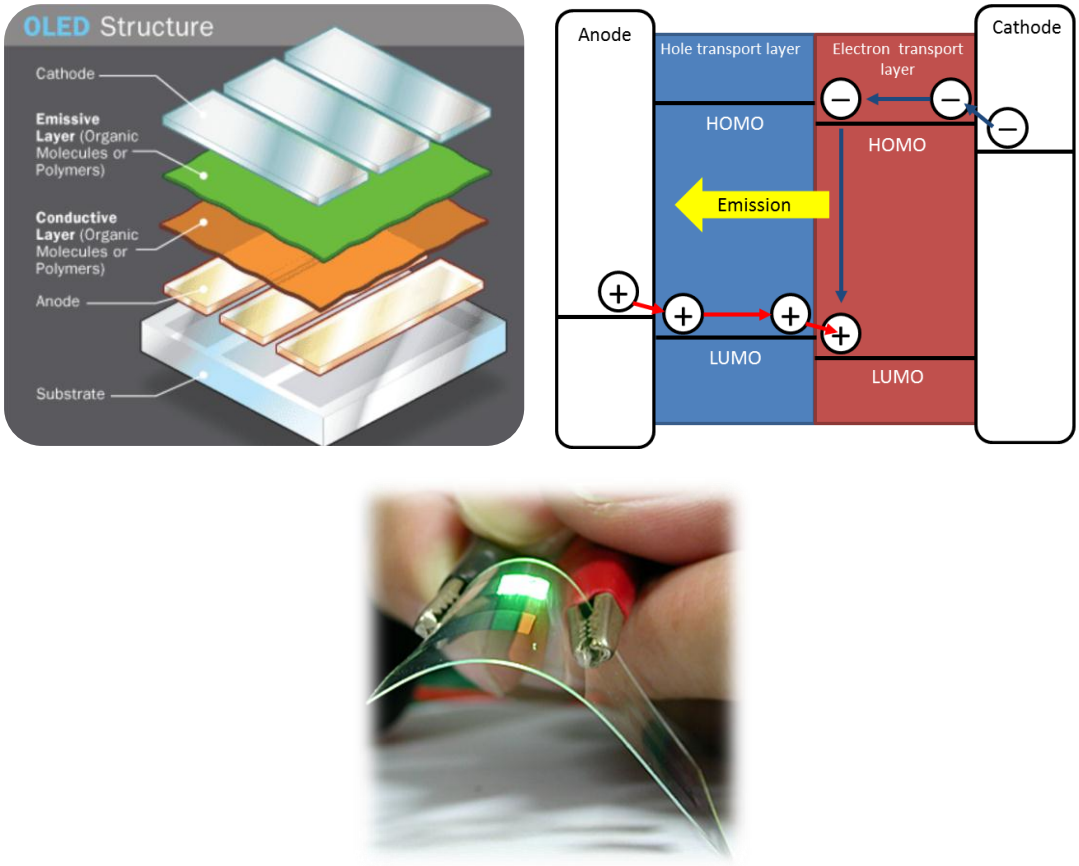


Fig. 1-4 (Left) Schematic diagram to show the structure of an organic light emitting diode which is comprised of a transparent anode or cathode sandwiching conductive polymer layers where electron/hole recombination occurs. (Right) Schematic shows the basic working principle of an OLED. (Bottom) Picture to show the compact and flexible nature of OLEDs.

The same configuration can be used in reverse as a photodetector where the fluorescence light from the analyte causes the excitons inside the active layer to dissociate into their constituent electrons and holes, creating a photocurrent (organic photodiode – OPD) [46]. The interest in using OLEDs and OPDs as the optoelectronic components arises from 1) the possibility to tune the emission wavelength and the photodetector response curve through selection of the active layer material and 2) their small size and

weight (overall device thickness is typically in the sub-millimetre range) which results in easier device integration. Importantly, multiple OLED's or OPD's can be closely packed on a single substrate allowing for multipoint detection. There are many examples of OLEDs used in conjunction with a microfluidic device. For example Edel et. al., demonstrated the use of polyfluorene-based OLEDs in a microfluidic environment to detect carboxyfluorescein, and achieved limits of detection as low as 1 µM [20]. Yao *et. al.,* applied a combination of an OLED and a photomultiplier-tube to detect fluorescent protein samples in a microfluidic device [17]. However they reported a limit of detection that is roughly six orders of magnitude poorer than the laser-induced capillary electrophoresis method due to the weakly luminescent properties of their fabricated OLEDs [17]. Pais *et.al.,* reported a microfluidic device that used both OLEDs and OPDs to detect fluorescence signal from rhodamine 6G and achieved a limit of detection of 100 nM [47].

Recent advances in this field have allowed the efficiencies of OLEDs and OPD's to become comparable to their inorganic counterparts. The quantum efficiency (ratio of photons emitted to electrons injected) of an OLED is as high as 29% [48] compared to 38.9% for an InGaN (Indium Gallium Nitride) [49] based inorganic LEDs. As for the detector's performance, both inorganic and organic photodetectors have shown incident-photon-to-conducted-electron peak efficiencies to be near 100% [50]. OLEDs still have problems, however, which include broad emission profile, long-term stability, and limited spectral range (450nm-650nm). Many fluorescence assays require UV excitation, which precludes the use of OLEDs. Stable and bright, low-cost inorganic LEDs are widely used in miniaturised detection devices, and their ability to pulse rapidly makes them well suited for time-resolved applications (more on this topic in Chapter 4). Silicon photodiodes are also used to complement the detection system – owing to their low-cost, compact and wide spectral response nature. For now inorganic diodes are the more mature and better performing technology, but this may well change in the near future.

1.4 Optical Filters

Optical long-pass filters play a particularly important role in microfluidic devices. In conventional fluorescence detection, the excitation source and detector are usually arranged orthogonally to one another to prevent direct illumination of the detector by the excitation source. This orthogonal geometry, however, is difficult to implement in a microfluidic environment since it requires the production of optical-grade side-surfaces onto which optical components must somehow be mounted [26]. The light source and detector are most conveniently placed on the upper and lower faces of the microfluidic chip in a face-on geometry, but this would ordinarily flood the detector with direct light from the excitation source thus masking the typically weak fluorescence signal from the analyte. (Fig. 1-5A)

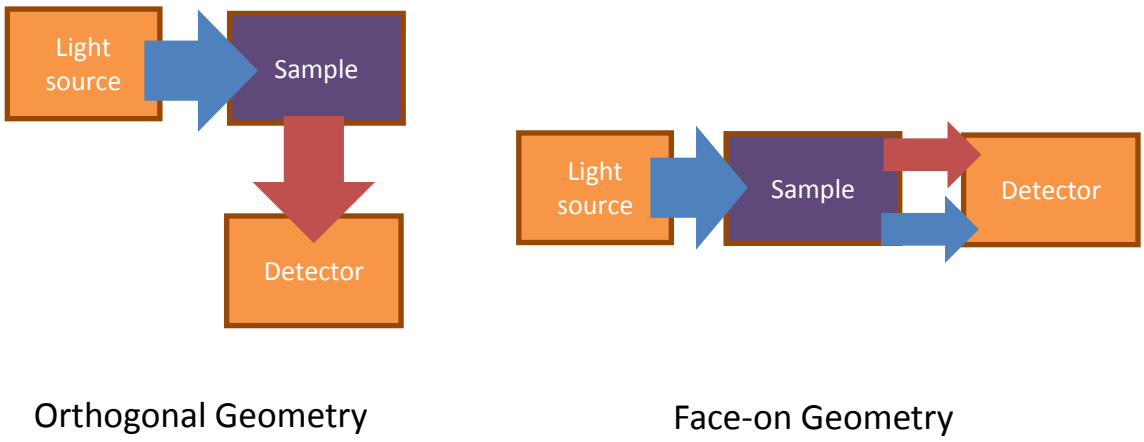


Fig. 1-5A Schematic diagram showing the two detection component geometries. An orthogonal geometry is typically used in conventional bench top fluorometers, and it prevents significant excitation light from reaching the detector. The face-on geometry allows convenient integration of microfluidic devices and the detector components; however, this configuration can flood the detector with light from the excitation source – masking the typically weak emission signal.

Furthermore, use of light sources with a broad emission profile such as OLEDs and inorganic LEDs (rather than a monochromatic light in conventional fluorometer or from a laser) can be problematic due to their long wavelength tail which often overlaps with the emission from the analyte. Key to differentiating the emission light from the excitation light in a face-on configuration is the use of a short-pass filter immediately after the light-source, together with a long-pass filter in front of the detector (Fig. 1-5B)

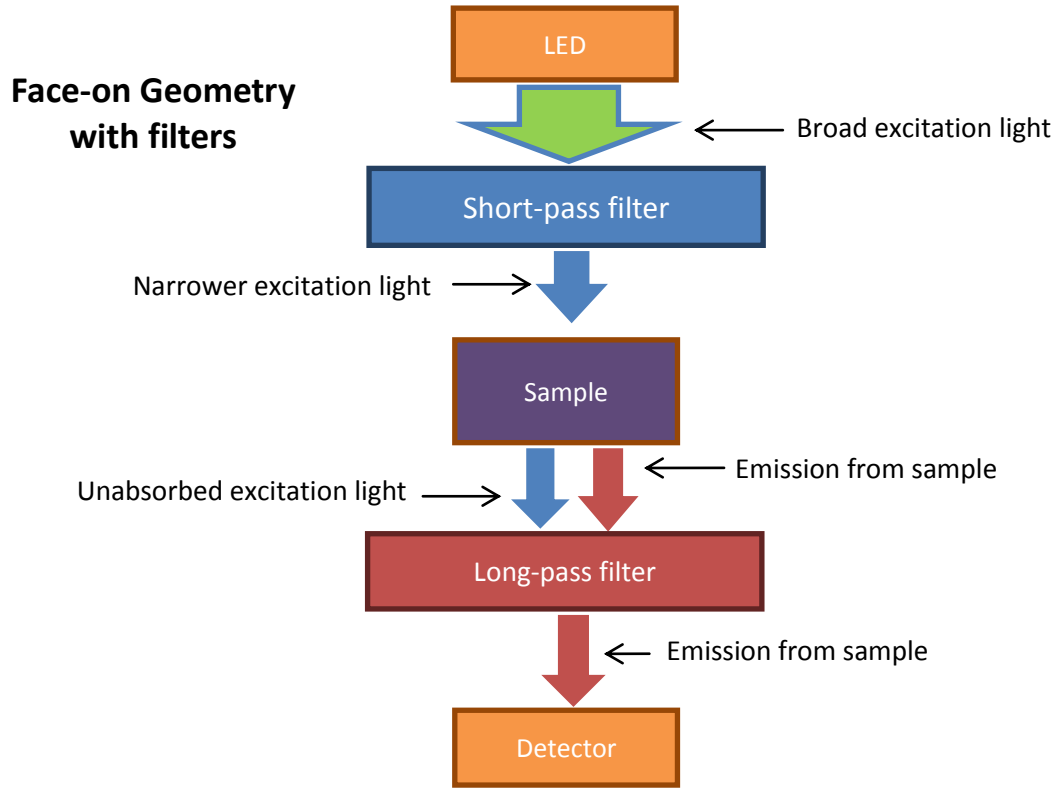


Fig. 1-5B Schematic diagram showing a face-on geometry with short and long-pass filters in place. Broad emission from the LED is sharpened by passing it through a short –pass filter to prevent spectral overlap with the analyte emission. The sample is excited by this sharpened LED light. A long-pass filter prevents any unabsorbed LED light to reach the detector.

The short-pass filter sharpens the emission spectrum of the light-source, removing any long-wavelength tail that would otherwise overlap the analyte signal (and so reduce sensitivity); while the long-pass filter blocks the sharpened excitation light, passing only the longer wavelength emission signal to the detector. For this approach to be successful the short- and long-pass filters must be chosen to display complementary transmission characteristics, i.e. the short-pass filter must block when the long-pass filter transmits, and vice-versa. The use of optical filters for this purpose is well established, but considerable difficulties are encountered when (as required for monolithic integration) the filter is placed in close proximity to the detector. In such circumstances any auto-fluorescence from the filter will add to the analyte-fluorescence, and so set a base-line beneath which it is difficult to measure a signal. Autofluorescence is a particular problem for colour filters formed by dispersing pigments or dye molecules in a glass or polymer host (Fig. 1-6). For the detection of low analyte concentrations, even very weak auto-fluorescence from the filter may obscure the desired signal, so it is essential to select dyes that not only have appropriate blocking and transmission characteristics but ones that are also completely non-emissive. Needless to say, the palette of usable materials is extremely limited.

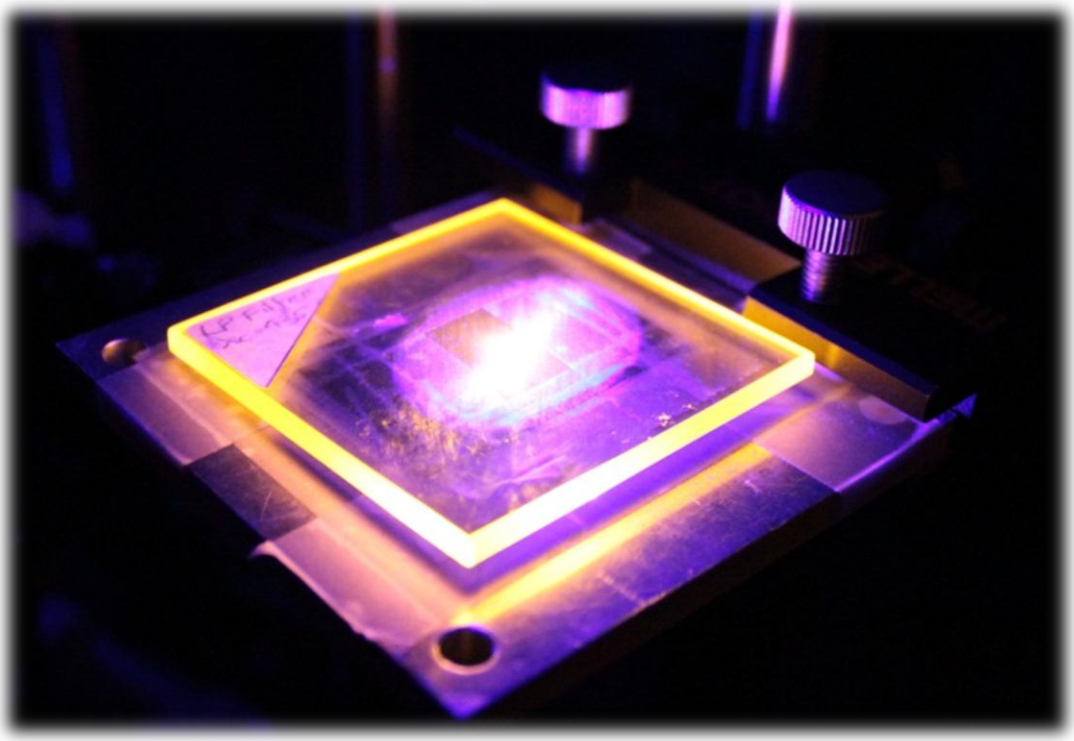


Fig. 1-6 Photo showing the highly autofluorescent nature of a commercial Schott glass filter (OG550, Schott AG, Germany) when illuminated with a 110 mW, 442 nm HeCd laser (IK5751I-G, Kimmon, Japan).

Hofmann *et al.,* used a dye-doped polydimethylsiloxane (PDMS) substrate as a long pass filter. (Fig. 1-7) This filter retained all the desirable characteristics of the PDMS substrate (for example flexibility and feature resolution), while exhibiting excellent transmission characteristics and low autofluorescence. In this case, the dispersion of Sudan II dye in PDMS effectively quenched any autofluorescence signal from the dye [26]. However, more recent work by Bliss *et al*. showed that the performance of such absorption filters (transmission characteristics and autofluorescence properties) are sensitive to the processing method and the dyes employed [33]. Furthermore, the doped substrate is in direct contact with the analyte fluid which can cause some of the dye to 'leach' into the fluid when in prolonged contact with the analyte sample.

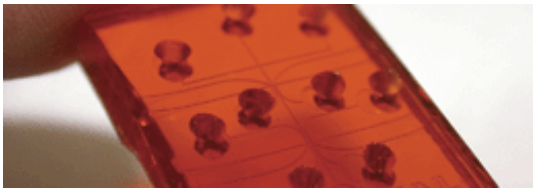


Fig. 1-7 Photo showing the Sudan II doped PDMS substrate fabricated by Bliss et. al., which incorporated optical waveguides to maximise signal to noise ratio by increasing the optical path-length. The microfluidic device was designed to perform DNA fragment analysis [33]. This method for filtering excitation light is limited by the range of non-autofluorescent dyes available [15].

Auto-fluorescence can be largely avoided by switching to interference filters that comprise of multilayer thin films of alternating refractive index. In for example a band pass filter that selected passes one wavelength λ, a dielectric spacer material (metal oxide) of thickness $\lambda/2$ is sandwiched between the two reflective surfaces. The reflective surface consists of $\lambda/4$-thickness alternating layers with high and low refractive indices, usually zinc sulphide (n = 2.19) and sodium hexafluoroaluminate (n = 1.34), respectively. When incident light passes through this reflective layer, a certain fraction of this light is reflected and transmitted to the next layer as shown in Fig. 1-8. This reflected light will constructively interfere if its 'wavelength half cycle' is the same as the thickness of the layer and any other wavelengths will destructively interfere. In an interference filter this constructively interfered light is reflected again back into the filter, where the process is repeated. The thickness and the refractive index of the material can be controlled to alter the reflective and transmission characteristics of the multi-layered structure, allowing for the fabrication of short- and long-pass filters as well as simple band-pass filters. The combination of such reflective layers and a single spacer layer is called a 'single cavity interference filter' [51].

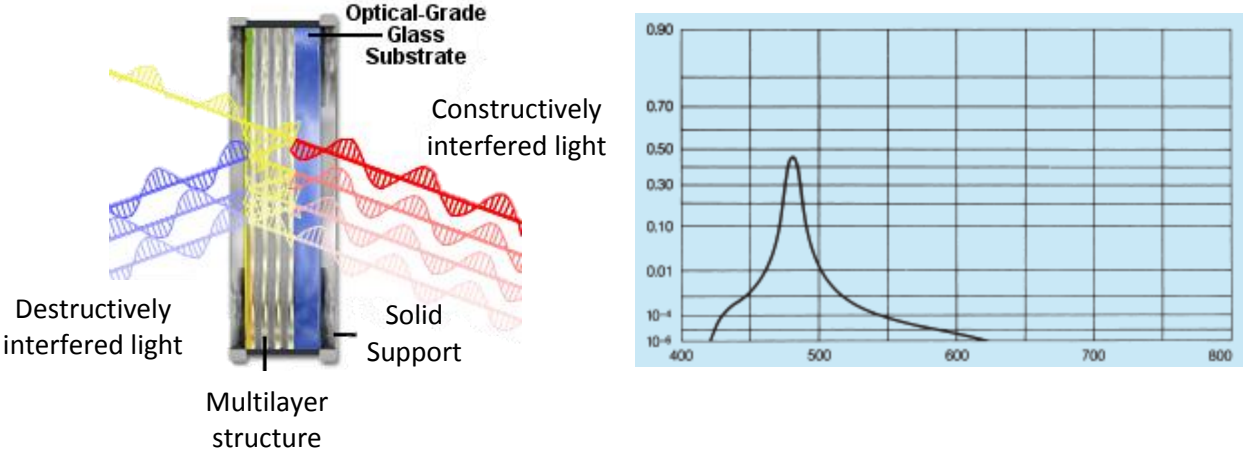


Fig. 1-8 (Left) a picture to show how interference filter selectively transmit specific wavelength bands through constructive and destructive interference [52] and (Right) their typical transmission spectrum taken from [53].

Interference filters typically have excellent characteristics in terms of strong blocking in the stop-band, high transmission in the pass-band, sharp roll-on (Fig. 1-8) and extremely low auto-fluorescence, but they are expensive to produce due to the complex multistep nature of their fabrication and hence they are ill-suited to low cost disposable applications. They also suffer from angular variability in their blocking/transmission characteristics, which can degrade their performance in actual use [33].

Recently Richards et. al., showed that, by combining interference filters with low-fluorescence colour filters, it is possible to produce high quality hybrid filters with low auto-fluorescence and minimal angular variation [54] (Fig. 1-9). They found that Orasol Red BL dye doped KMPR 1005 (epoxy-based photoresist) coated with a titania/silica interference filter produced the best results in terms of transmission and autofluorescence characteristics, although other combinations displayed appreciable autofluorescence.

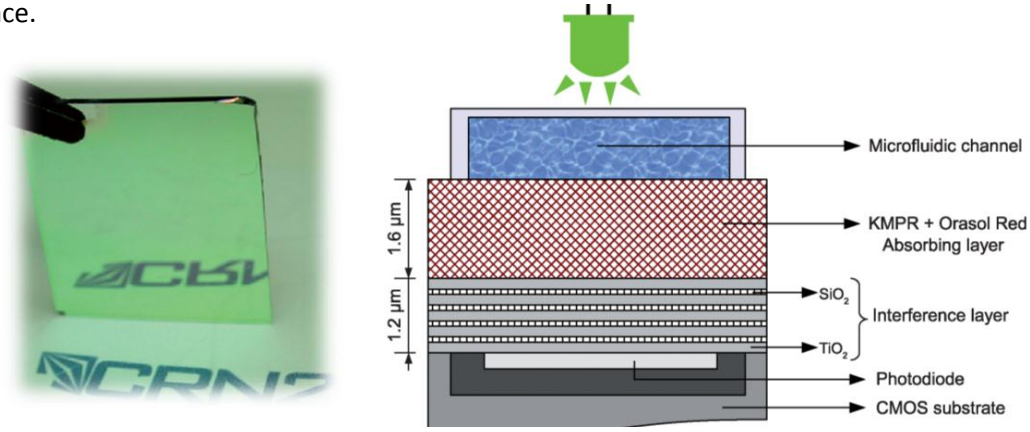


Fig. 1-9 Photo and a schematic to show the hybrid filter fabricated by Richards et. al., [54].

However, any solution based on interference filters, is likely to be restricted to high-end applications where cost is of secondary concern. Indeed, without a departure from the traditional fabrication methods of sputtering, evaporation and chemical vapour deposition, it is doubtful whether interference filters could ever form a part of an ultra-low cost disposable diagnostic technology. Attempts have been made by Chen et. al., to produce TiO_2/SiO_2 based interference filters via a sol-gel deposition technique but the resultant filters frequently delaminated (due to internal stress build up by cyclic annealing process). Furthermore, with this method it is very difficult to precisely control the oxide layer's thickness due to formation of porous structures [55]. In this thesis, we report a purely dye-based approach to fabricating high performance optical filters that avoids the expense and angular variability of interference filters, whilst overcoming the undesirable auto-fluorescence characteristics of conventional colour filters. In the next section (section 1.5), some basic properties of TiO_2 (titania) which play a major role in achieving this goal are presented.

1.5 Titania

In the late 1960's Fujishima and Honda [56] demonstrated successful photocatalytic splitting of water using sunlight and a electrochemical photocell with a titania anode and platinum cathode. Upon exposure of this electrochemical cell to sunlight, oxygen and hydrogen were generated at the anode and

cathode respectively. This pioneering work has sparked significant interest in the photoelectric properties of titanium and in particular its applications in heterogeneous catalysis and photovoltaics [57]. Titania exists in several crystalline forms, among which the most common are the *rutile*, *anatase, and brookite* polymorphs. In this chapter, we provide a brief outline of the optoelectronic characteristics of titania and the synthetic procedures used to produce nano-crystalline titania. In the next chapter, we describe a new application of nano-crystalline anatase titania, namely the fabrication of non-emissive optical filters for high sensitivity fluorescence detection.

1.5.1 Crystal Structure of TiO_2

The rutile and anatase phases of titania both crystallize in a tetragonal system, while the brookite structure is orthorhombic. In all polymorphs, a titanium ion (Ti^{4+}) is surrounded by six oxygen ions (O^{2-}) with a distorted octahedral configuration. [57-59] The crystal structures differ in the distortion of each octahedron, causing the assembly patterns of the crystals to differ significantly. In the rutile structure (Fig. 1-10), two edges (out of twelve) are shared forming a linear chain. This linear chain is joined by the sharing of corner oxygen atoms. In total, each octahedron is in contact with ten neighbouring octahedrons (two sharing edge oxygen pairs and eight sharing corner oxygen atoms).

With the anatase form (Fig. 1-10), four-edge oxygen pairs are shared and each octahedron is in contact with four neighbours. Brookite on the other hand crystallises in a orthorhombic crystal system, where three edges are shared per octahedron [60]. The basic unit cells of all polymorphs are shown in Fig. 1-10. These differences in lattice structure cause differences in densities and electronic band structures between the polymorphs as shown on Table 1-1. [59, 61]

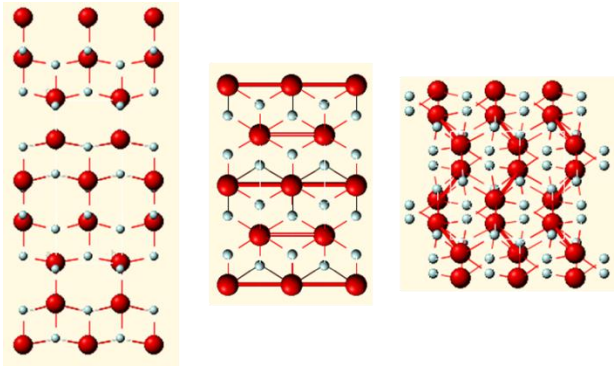


Fig. 1-10 Schematic of the crystalline structures of the three main TiO_2 forms: **Left**) Anatase, **Centre**) Rutile, and **Right**) Brookite.

Properties	Anatase	Rutile	Brookite
Crystal System	Tetragonal	Tetragonal	Orthorombic
Space groups	$I4_1/amd$	$P4_2/mnm$	mmm
Number of Titania /unit cell	4	2	8
Density (g/cm^3)	3.89	4.23	4.14
Band gap (eV)	3.30	3.00	3.18
Refractive Index (n)	2.488	2.908	2.704

Table 1-1 selected crystallographic data and physical properties of anatase, rutile, and brookite. Schematics and data extracted from ref [62].

1.5.2 Optical and Electronic properties of TiO_2

Due to the differences in the optoelectronic properties of different polymorphs of titania, they are used in distinct applications. Anatase titania is known for its high n-type mobility - which is due to it having a smaller electron effective mass than the other crystal phases, leading to a higher charge carrier mobility (4 cm^2Vs^{-1} compared to 0.1 cm^2Vs^{-1} for rutile titania at room-temperature) [63]. Hence anatase titania is frequently used in the field of photovoltaics [64]. Examples of brookite titania in practical applications are scarce for reasons that are not entirely clear, but Magne et. al., recently reported its application in dye sensitised solar cells (DSSCs), achieving a conversion efficiency of 5.97% (compared to approximately 11% for anatase based DSSCs) [65]. Rutile titania is used for pigment manufacturing due to its high refractive index (n = 2.90) (Fig. 1-10). Pigments that utilise rutile titania provide strong opacity due to strong optical scattering when compared to other metal oxides. In general the bulk crystals in all polymorphs exhibit wide band gaps ($E_{v\ Anatase}$ = 3.3 eV, $E_{v\ Rutile}$ = 3.1 eV, $E_{v\ Brookite}$ = 3.13 ev) which correspond to absorption in the UV range, leading to excited electrons in the unoccupied conduction band and positive holes in the valance band. Their charge carriers can interact with adsorbed molecules on the surface of the titania.

1.5.3 Dye sensitization of TiO_2

Titania can be sensitised in the visible region by attaching organic dyes onto its surface. These organic dyes can be linked to the titania surface by four different interactions: 1) covalent attachment by using linking groups, 2) electrostatic interactions, 3) hydrogen bonding, and 4) Van der Waals forces. The most stable and frequent reported method of attachment is covalent attachment, where groups

such as amides, carboxyls, and silanyls have been reported to form stable linkages with the surface hydroxyl groups on the titania [66]. The most common linkage between the surface titania and the dye is formed by dye molecules with carboxylic acid groups, which react with the titania surface hydroxyl groups to form esters (Fig. 1-11). Electronic interactions between titania and the excited state of the adsorbed dye is discussed in more detail in chapter two since this mechanism forms the basis for our non-emissive dye-sensitised optical filters. When the dye molecules are ionic in nature, the surface charge of the titania also plays an important role in assisting dye adsorption as discussed in chapter three. Hydrogen bonding can also occur between the titania surface hydroxyl groups and the carbonyl /NH_3 groups on the adsorbent [67] (Fig. 1-11). Strong Van der Waals interaction have been reported to serve as the driving force for the adsorption of large molecules such as lipid vesicles [68] but, this type of interaction is only dominant in the initial attraction of the molecule and does not form any permanent link.

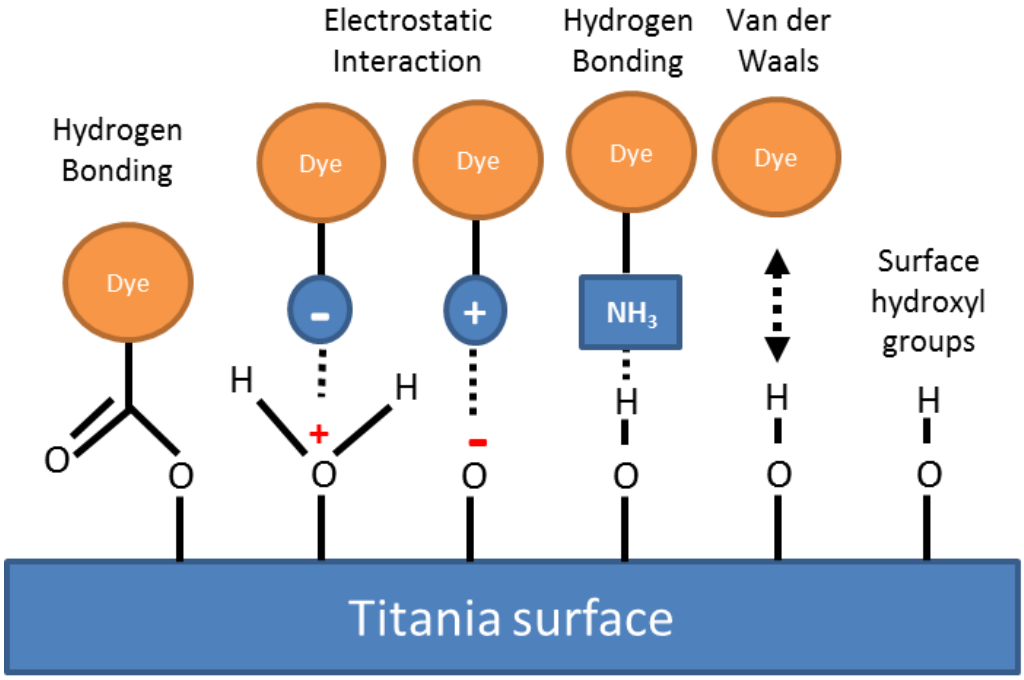


Fig. 1-11 Schematic showing the four main dye adsorption mechanism on titania surface.

1.5.4 Synthesis of TiO_2 nanoparticles

Titania nanoparticles are commonly synthesised by the 'low-temperature' hydrolysis of titania precursors (such as titanium alkoxides or titanium chloride) in a pH controlled environment. This process is outlined in the equation 1A.

$$TiX_4 + 2H_2O \rightarrow TiO_2 + 4HX \qquad \text{(Hydrolysis)} \qquad (1A)$$

where X = OR or Cl. Formula 1A shows that titania precursor spontaneously reacts with water (hydrolysis) to form titanium oxide. Titania nano-colloids are formed this way and depending on the synthetic conditions (pH of the environment, precursor employed and additives) and the post hydrolysis annealing temperatures used, the resulting polymorphs and the particle size can be controlled. These synthetic conditions are outlined in Fig. 1-12 [59, 69, 70].

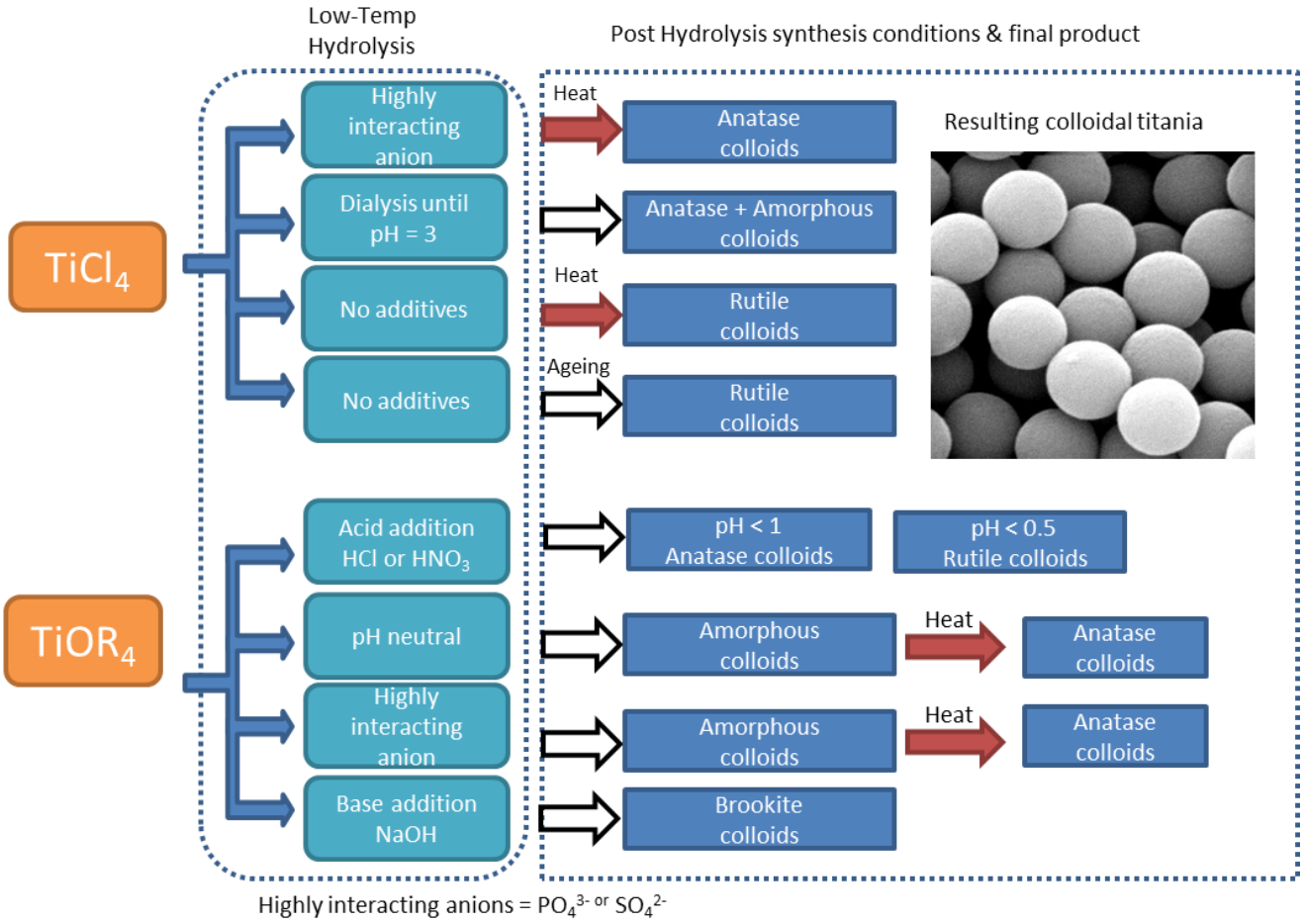


Fig. 1-12 Schematic summarising the common routes for the production of titania nano-colloids using titanium tetrachloride and alkoxy-titanates as precursors. Different polymorphs of titania are produced depending on pH, temperature, additives, and ageing time. The diagram is adapted from [71].

The formation of pure rutile at very low pH (<0.5) values from alkoxy-titanate is thought to be due to a dissolution-precipitation mechanism [70]. Cheng et. al., suggested that large amounts of Cl^- (or NO_3^-) would produce octahedral $[Ti(OH)_nCl_m]^{2-}$ complexes (m>n) that have a preference for corner oxygen sharing and thus form rutile titania [72]. Phase pure anatase synthesis typically occurs in solutions of pH > 1, where amorphous titania is insoluble and hence is unaffected by the dissolution-

precipitation mechanism. It has been suggested by Reyes-Coronado et. al., that anatase titania is formed upon heating amorphous titania due to its lower surface energy compared to other phases [70]. Furthermore, elevated temperatures (above 65 °C) were reported to favour edge oxygen pair sharing, thus favouring the formation of anatase titania [72]. Addition of anions such as PO_4^{3-} and SO_4^{2-} prevent the formation of ordered titania, causing amorphous phase titania to be formed [71]. Nagase et. al., reported that the addition of NaOH during the post hydrolysis treatment step results in phase pure brookite colloids [73] and a recent report by Jiao et. al., suggests that the sodium cations play a crucial role in forming brookite, by acting as a 'molecular scaffold' [74]. Hydrolysis of titanium tetrachloride generates hydrochloric acid and hence use of this precursor favours formation of rutile phase titania since titania colloid is formed in highly acidic conditions (see equation 1A) where it undergoes a dissolution precipitation mechanism.

Anatase is preferred in our case due to its lower refractive index which minimises optical scattering and its high band gap compared to other polymorphs of titania. Titania nano-colloids can be synthesised by a variety of other methods, including the hydrothermal method, chemical vapour deposition, electrovapour deposition, sonochemical, microwave and micelle methods [59].

1.5.4.1 Effect of pH on colloidal size

Titania colloids (made via hydrolysis) in aqueous suspension possess an electrical charge which is pH dependent [24]. Surface acidic/basic properties can be modified by the chemisorption of H^+ or OH^- from the solution such that [75]:

$$TiO_2 + H^+ \rightarrow TiO_2H^+ \text{ for pH } <3.5 \quad (1B)$$

$$TiO_2 + OH^- \rightarrow TiO_2(OH)^- \text{ for pH } > 3.5 \quad (1C)$$

It has been reported that the surface potential of titania in acidic (pH <3.5) or alkaline solutions (pH > 3.5) inhibits less aggregation, resulting in smaller colloids [24]. Fig. 1-11 shows the pH dependence of the titania crystal size. The trend shows that a high degree of aggregation occurs with titania pastes prepared at pH values between 3 and 8.

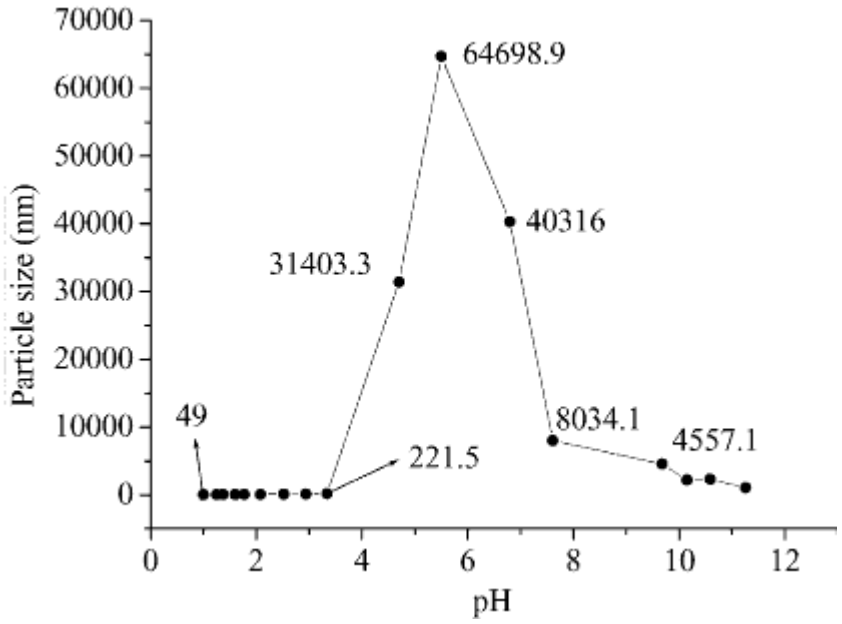


Fig. 1-13 pH dependence of TiO2 particle size in sol (taken from ref. [62])

1.5.5 Nanoporous TiO_2 thin films

New physical and chemical properties emerge as crystallite size is decreased down to the nano-scale, and an exponential growth of research activities in the field of nano-scale titania has occurred in the past few decades [59, 76-80]. In nano-metric materials, hole and electron transport are governed by the effect of quantum confinement [78]. For example, electron-hole pair recombination is reduced as particle size decreases and this has been attributed to an increase in surface imperfections that can act as electron/hole traps [81], and thereby improve the photocatalytic properties of titania by extending the lifetime of the radicals [82]. Furthermore, as particle size decreases, the surface–to-volume ratio (and hence specific surface area) increases, enhancing the amount of dye adsorption that can occur at the interface. Nanoporous titania thin films can offer the surface area enhanced properties of nano-colloidal titania solutions whilst offering interconnectivity between the titania providing a conductive 'scaffold' like structure. Such structures are required in fabricating devices such as DSSCs.

Surfactants and polymers such as ethylene glycol can be added to the synthesised colloidal suspensions (also referred to as sols) described above to prevent aggregation of the colloids (Fig. 1-14). Loss of the solvent leads to a transition from liquid-sol to sol-gel which can be spin-coated, dip-coated, or screen printed (details in Chapter 2) onto a glass substrate. The resultant film can be sintered at high

temperature to drive off any remaining solvents and induce coalescence between the titania colloids. Surfactants or polymers such as polyethylene glycol have been reported to prevent surface cracking during this sintering process and also act as a template to form nanoporous structures (rather than a flat surface) [83].

1.5.5.1 Effect of the sintering temperature

The sintering temperature can also affect the surface morphology of the resulting titania, with a low sintering temperature causing surfactants/polymers to remain in the titania, forming 'flat' surfaces (rather than nanoporous features). More importantly, the sintering temperature can also change the phase of the titania with higher sintering temperatures promoting the formation of the rutile phase. The phase transition temperature from anatase to the rutile phase however also depends on the synthetic route taken (the precursor and pH). Sintering also increases the crystal size due to coalescence, which yields a highly porous titania film (fig 1-13). Titania substrates with large crystal sizes can cause optical scattering and form cloudy or opaque films.

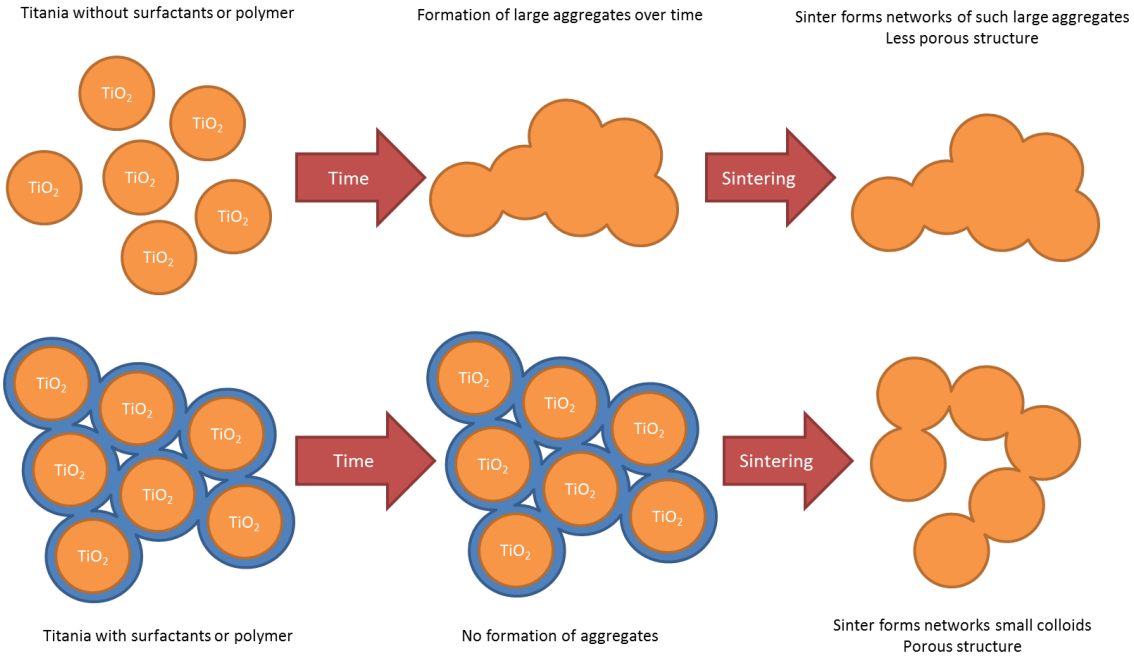


Fig. 1-14 Schematic showing the function of surfactant/polymer additives in 1) preventing aggregation of the titania colloids in sol-gel and 2) providing a template to form nanoporous structures upon sintering.

1.6 Summary

The development of portable low-cost POC devices with comparable sensitivities to conventional lab based instrumentation would revolutionise healthcare industries in both developing and developed worlds. Microfluidic technology has been identified by researchers around the globe as a core technology for delivering portable POC devices, and much research has been undertaken with respect to both assay implementation and analyte detection in microfluidic devices Optical methods, most notably fluorescence, have shown themselves to be the most appropriate detection method for the trace levels of analyte present in a typical diagnostic test.

A face-on arrangement of the excitation source and the detector is the most favoured geometry for a portable POC device construction. However, use of such geometry requires an effective optical filtration strategy to prevent the excitation light from flooding the detector. Current filters however have drawbacks that make their incorporation into highly sensitive, low-cost portable POC devices very difficult: Colour filters typically show strong autofluorescence, which renders accurate measurements of weak analyte fluorescence difficult; while Interference filters are costly and as such are unlikely to form part of an ultra-low cost disposable diagnostic device.

The key message of this chapter is the requirement to provide inexpensive optical filters, with minimal autofluorescence. To meet this need we report in Chapters 2 and 3 a new class of low cost optical filter (based on the use of dye sensitised nanoporous TiO_2) that exhibit excellent light filtration properties and low autofluorescence. In chapter four, an alternative 'filter-free' route to highly sensitive analyte detection is described using a combination of phosphorescent label and time-gated detection system.

CHAPTER 2

2

Nanoporous TiO_2 Optical Filters



2 Nanoporous TiO_2 Optical Filters

2.1 Optical filters based on TiO_2

In a typical low cost colour filter, a polymer of glass film is doped with organic dyes or pigments, which absorb the incoming light and are excited to a higher energy electronic state. This excited electronic state undergoes a combination of non-radiative and radiative decay to reach its ground state. In many cases filter autofluorescence can be significantly higher than the optical signal one wishes to detect preventing a reliable measurement. In this chapter we report a purely dye-based approach to fabricating high performance optical filters that avoids the expense and angular variability of interference filters, while overcoming the undesirable auto-fluorescence characteristics of conventional colour filters. Our approach exploits ultrafast electron-transfer between a photo-excited dye molecule and a transparent metal oxide onto which the molecule is absorbed - the same process that forms the basis for the charge-generation step in DSSCs [84, 85]. In essence, a monolayer of the dye molecule is adsorbed onto the surface of a highly porous metal-oxide such as titania (TiO_2), generating a diffuse interface between the two materials. The interface acts as an extremely efficient quenching site for the photo-excited excitons [86], reducing the photoluminescence quantum yield of the dye to a negligible level without significantly perturbing its absorption characteristics. The oxide itself has a wide optical gap (E_v > 3.2 eV for anatase titania), so does not absorb over the visible wavelength range typically used for diagnostic tests. Hence, providing the crystallite size is significantly smaller than the wavelength of light so as to minimise optical scattering, the oxide serves as an invisible scaffold for the dye molecule. The mechanism of the quenching process is well established, see Fig.2-3 [86]. Upon absorption by the dye, an electron is promoted to an unoccupied molecular orbital. From there, it undergoes an ultrafast charge injection into the continuum of conduction band states in the titania. The basic photophysical equation between the dye and the TiO_2 substrate can be written as the following [86]:

$$S^0 + hv \rightarrow S^* \rightarrow S^+ + e_{CB}^- (TiO_2).$$

Where S^0 is the ground state of the dye and S^* is the excited state to which the molecule is promoted by the electromagnetic energy, hv. When the energy of the photo-excited electrons in the dye lies higher in energy than the conduction band (CB) of the TiO_2, electron injection occurs, forming the dye cation (S^+). The electron relaxes by internal conversion to the conduction band-edge and then hops between titania sites until it reaches an interface with a dye-cation, whereupon it recombines non-radiatively to regenerate the dye. With the dye sensitized TiO_2 system, we do not observe fluorescence

in the final regeneration step since the TiO_2 CB edge and the trap state are well below the energy of the first excited state of the dye. Importantly, the initial charge-transfer step from the dye to the oxide typically occurs on a very short timescale (« 100 fs), [86-89] which means that the photo-excited electron is removed from the dye molecule long before it has any chance to relax radiatively to the ground-state. In this way, it is possible to reduce the fluorescence quantum yield of the dye molecule to a negligible level and so quench the autofluorescence by many orders of magnitude. ZrO_2 substrates undergo similar dye-coupling (as titania – section 1.5), but unlike the TiO_2 substrates; there is no electron injection into its CB due to its high energy barrier (Fig. 2-1). The relaxation of the excited electron via a trap state of ZrO_2 allows back transfer to the excited state energy level of the dye (v'=0) and hence emission remains possible. ZrO_2 substrates were used here as non-quenching metal oxide electrodes for comparison with TiO_2.

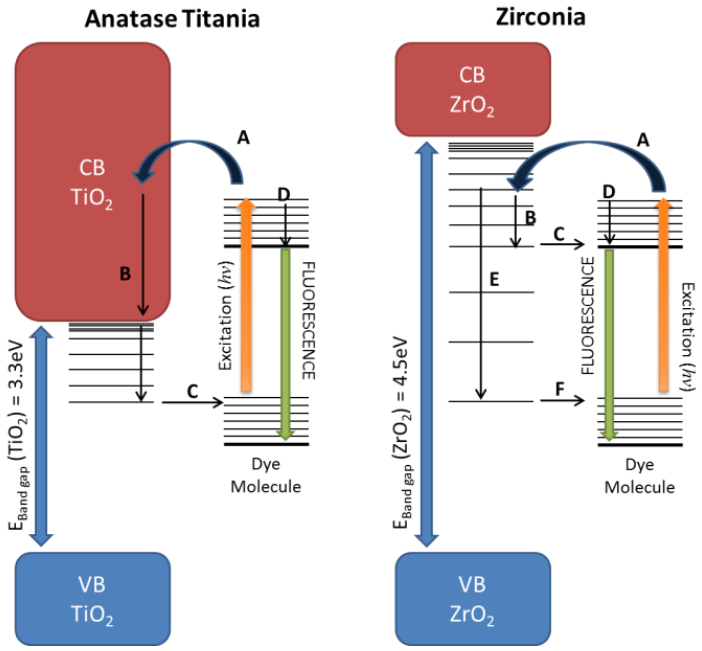


Fig 2-1 **Energy diagram for a dye coupled to anatase titania (Left) A)** Ultrafast electron injection (<100 fs, depending on the dye) into the conduction band of TiO_2. **B)** Relaxation of the excited electron in the conduction band and the trap states (Internal conversion). **C)** Non radiative charge recombination with the dye cation. **D)** Internal conversion with in the S_1 state followed by subsequent fluorescence emission.

Energy diagram for a dye coupled to ZrO_2 A) Ultrafast electron injection into the ZrO_2 trap state (<100 fs) **B)** Electron relaxes down the 'trap' energy levels, and **C)** back transfer into the lower vibrational level of the dye excited state energy level (450 fs) before relaxing down to the ground state via fluorescence (160 ps) **E&F)** Alternatively the electron relaxes down via trap states and recombine at the ground state Alizarin, with no emission (recombination time frame of 2.4 ps) (Adapted from [86]).

2.2 Experimental

2.2.1 Preparation of the Filter

2.2.1.1 Titanium Oxide Thin Films

Titania films of approximate thickness 4.4 µm were prepared by screen-printing 100 µL of as-received commercial titania gel (WA-15DPT 8% v/v, Nanopac, South Korea) onto glass substrates (Fig. 2-3). A glass substrate was taped onto a flat surface with a standard 3M scotch tape and 100 ml of the oxide paste was deposited on the substrate. A glass rod was used to spread the oxide paste on to the exposed region of the glass substrate and left to dry (turns transparent) for 10 min. The coated glass slides were then sintered in an oven at various temperatures for one hour, ramping the temperature gradually over a 30 min period (approximately 14 °C/min for 450 °C) to avoid cracking. To sensitize the resulting titania film, each titania-coated substrate was immersed overnight in a dye solution. The dyes were chosen according to the following criteria: firstly, the dyes should absorb in the desired optical range (i.e. 400-450 nm for long-pass filters); secondly, for the dyes to be effectively quenched, the lowest unoccupied molecular orbital (LUMO) of the dye should coincide with the conduction band of the titania (3.3 eV) [90] (E_{CB} titania = -0.5 V vs standard hydrogen electrode) [91]. Finally, the dyes must contain carboxyl groups to form a strong ester link with the titania surface hydroxyl groups. Other interactions such as electrostatic interaction and hydrogen bonding can also be employed with carbonyl and hydroxyl group containing dyes. The stained films were then washed repeatedly with a solvent (used to disperse the dye) to remove unattached dye molecules and finally dried in a stream of nitrogen.

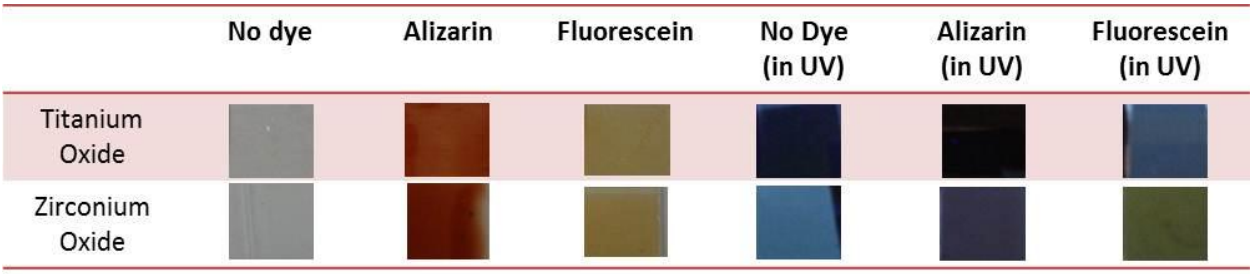


Figure 2-2 Titanium Oxide / Zirconium Oxide thin films, doped with corresponding dyes (Alizarin and Fluorescein) exposed under UV lamp (365 nm). Films prepared with Zirconium Oxide shows significant emission in comparison to the films prepared with titania. The zirconia films were highly scattering and so appear white and opaque in both visible and UV light.

Fig. 2-2 shows nanoporous titania/zirconia thin films prepared with the method outlined in section 2.2.1.1. The zirconia thin films sensitised with fluorescein and alizarin showed significant

fluorescence upon UV excitation. This effect was not observed with titania thin films sensitised with the same dye, demonstrating the fluorescence quenching nature of titania substrate.

2.2.1.2 Zirconium Oxide Thin Films

The Zirconium Oxide gel was prepared by adding 12g of ZrO_2 nano powder (Aeroxide ZrO_2, Evonik, Germany) into 4 ml of distilled water. This solution was then diluted with 16 ml of distilled water and 0.4 ml of Triton X100 (Aldrich) under continuous mixing, yielding a thick white paste of ZrO_2 [92]. The same procedure described for TiO_2 was used to produce zirconium oxide thin films, of approximate thickness of 5-6 µm and the same staining and washing procedures were followed.

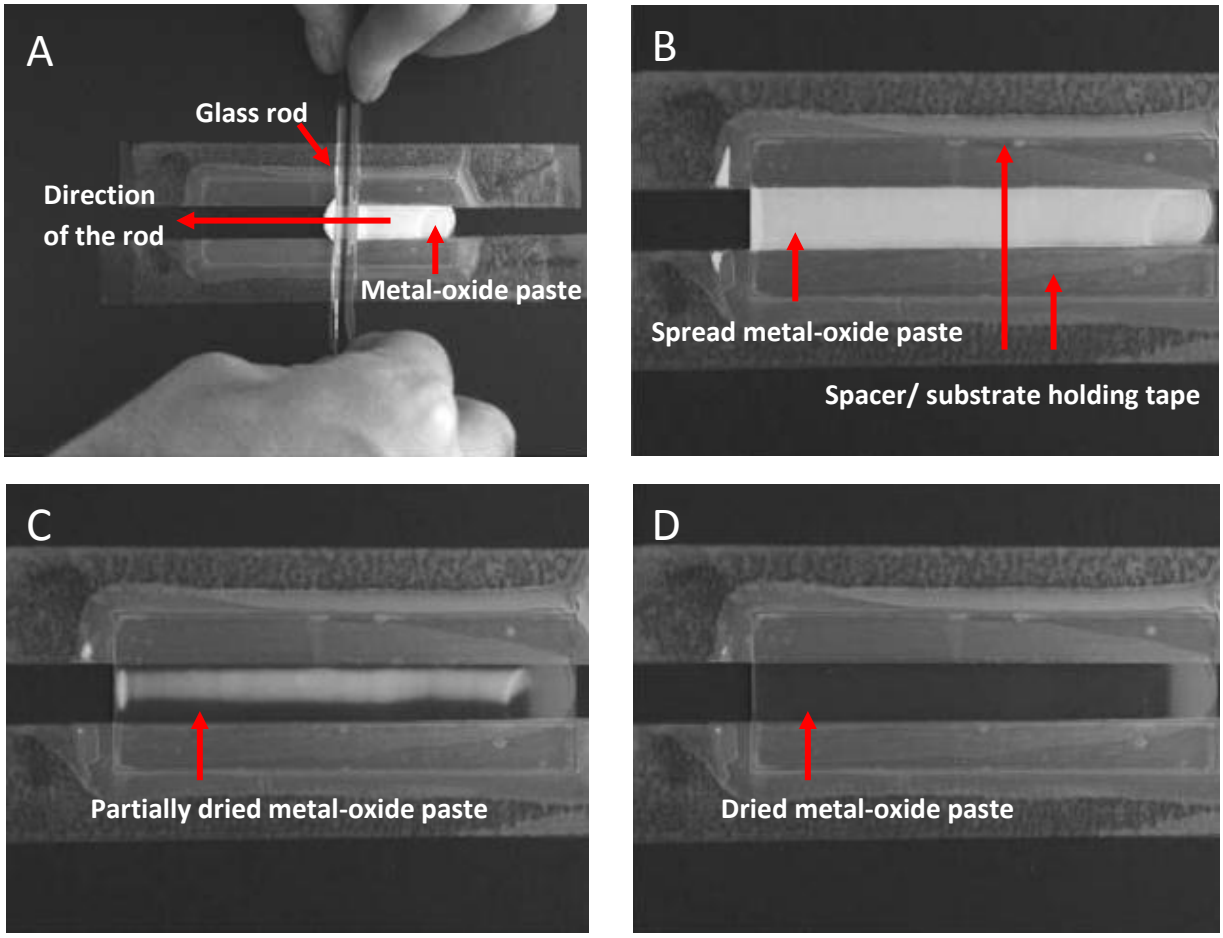


Fig. 2-3 Screen Printing Ti/Zr oxide paste onto a glass substrate. **A)** A Glass substrate is taped onto a flat surface with a standard 3M scotch tape and 100 ml of the oxide paste is deposited on the substrate. A glass rod is used to spread the oxide paste on to the exposed region of the glass substrate **B & C)** The oxide paste is left to dry for approximately 10 minutes causing the film to become clear. **D)** Dried oxide layer is now ready to be sintered in air.

2.3 Oxide Film - Characterization Methods

2.3.1 Scanning Electron Microscopy

Scanning Electron Microscopy (SEM) is a type of electron microscopy method that utilises high-energy electron beams to obtain very high resolution surface images (upwards of 300,000 x magnification compared to just 200-1000 x magnification with standard optical microscope). Scanning electron Microscopes also have a large depth of field due to their narrow electron beam, which allows '3D' images of the sample to be obtained, providing the samples are conductive (compared to the flat images optical microscopes produce). To provide necessary conductivity, all the titania samples described in section 2.4.1 were sputter coated with chromium. The sputter coater settings were set to 80 mV (at 1 min) and yielding a coating of approximately 5 nm thick on the surface of the sample. Furthermore, SEM samples were prepared on conductive Indium Tin Oxide (ITO coated glass, Sigma Aldrich, UK) coated glass for added conductivity.

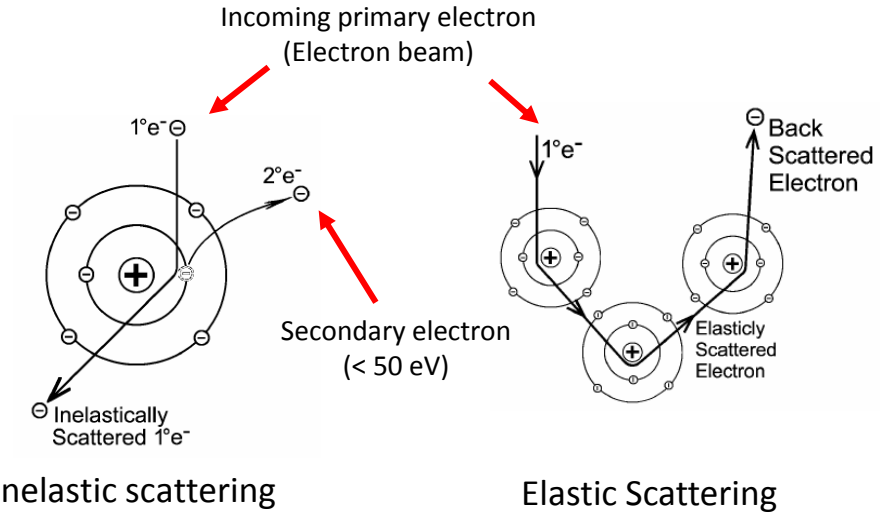


Fig. 2-4 Diagram illustrating inelastic and elastic scattering of electron.

In the SEM, electrons generated by a thermal emission source (e.g. heated tungsten filament) are focused into a beam by series of electromagnetic lenses. Scanning coils deflect and position the beam onto the sample. The sample can interact with the incoming electron beam ***inelastically*** or ***elastically***. Inelastic scattering occurs when the electron beam interacts with the electric field of the sample resulting in a transfer of energy to the electron of the sample. This is followed by emission of a low energy electron (compared to the incident electron with typical energy of 5 keV), also known as the secondary electron which typically has less than 50 eV of energy. Detection of secondary electrons is

useful for topological studies of a sample. Furthermore, if an electron from a higher orbital fills the electron vacancy that has been created, characteristic X-Rays are emitted which can help identify the chemical composition of the sample. Elastic events occur when the electron beam interacts with the electric field of the nucleus, which results in deflection of the electron without any significant loss in its energy. The loss in energy is typically less than 1 eV [93]. The electron is referred to as a 'back scattered electron' when it is deflected back out of the sample. Since heavy atoms and lighter atoms have different scattering properties, this technique, along with the X-ray detection technique provides useful compositional information.

2.3.2 Nitrogen Porosimetry

Nitrogen porosimetry allows data such as average pore volume, pore distribution, and the surface area of the material to be calculated by measuring the volume of nitrogen gas adsorbed by the sample. This technique can be used to investigate how the porosity/surface area is affected by the processing conditions and so help identify the optimal process parameters. The BET Surface analyser (Tristar BET Surface analyser, Micrometric, UK) allows precise measurement of the amount of nitrogen gas adsorbed by the porous TiO_2. This data in conjunction with BET (Brunauer Emmett Teller) theory (as discussed below) provides a simple means of determining the specific surface area of the titania i.e. the total microscopic surface area per unit geometrical area. Langmuir theorised that the adsorption of a molecule to the surface is related to the pressure. Based on this theory, an equation was derived which expressed the relationship between the pressure and the number of active sites undergoing adsorption assuming 1) a fixed number of adsorption sites is available on the surface, 2) all adsorption sites have equal shape and size to the adsorbent, 3) each site can only hold one adsorbent, 4) dynamic equilibrium exists between the adsorbed molecules and the free molecules. Langmuir theory assumes that the absorption is a monolayer but under high pressure situations, this assumption breaks down as multilayer adsorbent forms. BET theory is an extension of the Langmuir Theory. Where Langmuir theory is a theory defining the adsorption of monolayer [94], BET theory expands this to a multilayer adsorption based on three further assumptions: Firstly, gas molecules adsorb on solid substances. Secondly, there are no interactions between the adsorbed gas monolayer, and thirdly, Langmuir theory can be applied to each monolayer in the multilayer (meaning that a surface coverage of the surface is a function of pressure and Langmuir absorption coefficient).

To determine the adsorption isotherm of our nanoporous titania, known amounts of adsorptive gas are admitted stepwise into the sample cell, containing the sample that has been degassed and dried. The amount of gas adsorbed by the titania is the difference between the gas in the sample cell and the amount of gas admitted. The adsorption isotherm is then given by a plot of amount of gas adsorbed (in mol/g) as a function of relative pressure, P/P_0. (Equation 2A & fig 2-5)

The BET equation is expressed as:

$$\frac{P}{v(P_0-P)} = \frac{c-1}{v_m C}\left(\frac{P}{P_0}\right) + \frac{1}{v_m C} \tag{2A}$$

Where:

P = Equilibrium Pressure
P_0 = Saturation Pressure
v = Adsorbed Gas in unit volume
v_m = Monolayer Adsorbed volume
c = BET constant described in Equation 2F

and the BET constant can be described by where E_{Ads} is the heat of adsorption for the first layer and E_L is the heat of adsorption for the second and higher layer.

$$c = \exp\left(\frac{E_{Ads}-E_L}{RT}\right) \tag{2B}$$

E_{Ads} = Heat of adsorption for the first layer
E_L = Heat of condensation
R = Gas Constant (8.314$JK^{-1}mol^{-1}$)
T = Temperature in Kelvin (K)

Eqn. 2A denotes an adsorption isotherm and is plotted with $P/v(P_0-P)$ on the y-axis and P/P_0 as x-axis as shown on Fig. 2-5 This is called a BET plot where the slope (S) and its y-intercept (I) are used to calculate both the volume of monolayer adsorbed gas, V_m and the BET constant, c as follows.

$$v_m = \frac{1}{S+I} \tag{2C}$$

$$c = 1 + \frac{S}{I} \tag{2D}$$

The total surface area (S_{Tot}) and the specific surface area (S_{BET}) are defined as follows:

$$S_{BET,total} = \frac{v_m N s}{V} \tag{2E}$$

$$S_{BET} = \frac{S_{total}}{A} \quad (2F)$$

where in Equation 2E & 2F:

N = Avagadro's Number
S = adsorption cross section
V_m = molecular volume of the gas itself
A = molecular weight of the adsorbed gas.

The derivation of these equations is presented in reference [95]. In practice all data is analysed using the software supplied with the BET surface analyser. The TiO_2 samples were sintered at different temperatures to observe the effect on the surface area and the pore size distribution. This information was then used to optimize the sintering temperature of the titania substrate for maximum dye loading.

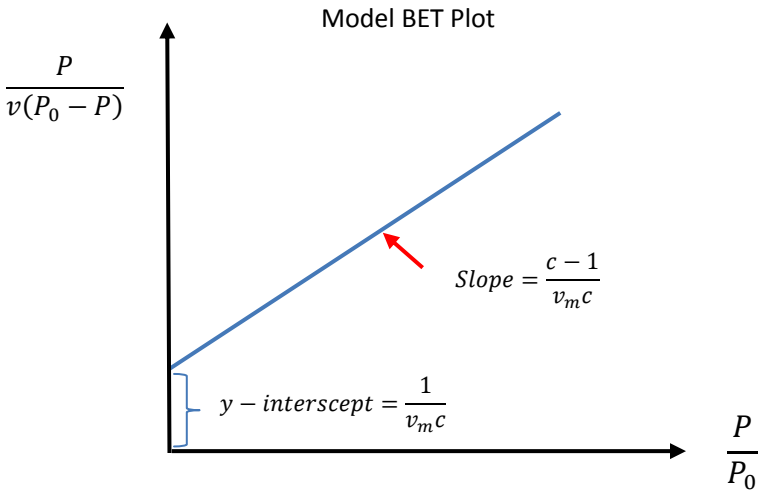


Fig 2-5 Diagram of a model BET plot showing the amount of gas adsorbed (in mol/g) vs relative pressure, P/P_0.

2.4 Oxide Film – Results

2.4.1 Scanning Electron Microscopy (SEM)

The titania samples shown here were fabricated using the method and materials outlined in section 2.2.1.1 without any dye sensitisation. All samples were sputter coated with approximately 5 nm of chromium using the setting described in section 2.3.2. (K500X Polaron, Quorum Technologies, UK). SEM images were taken with 2 x 10^5 x magnifications at 1.5 x10^{-9} T pressure (Fig. 2-6)

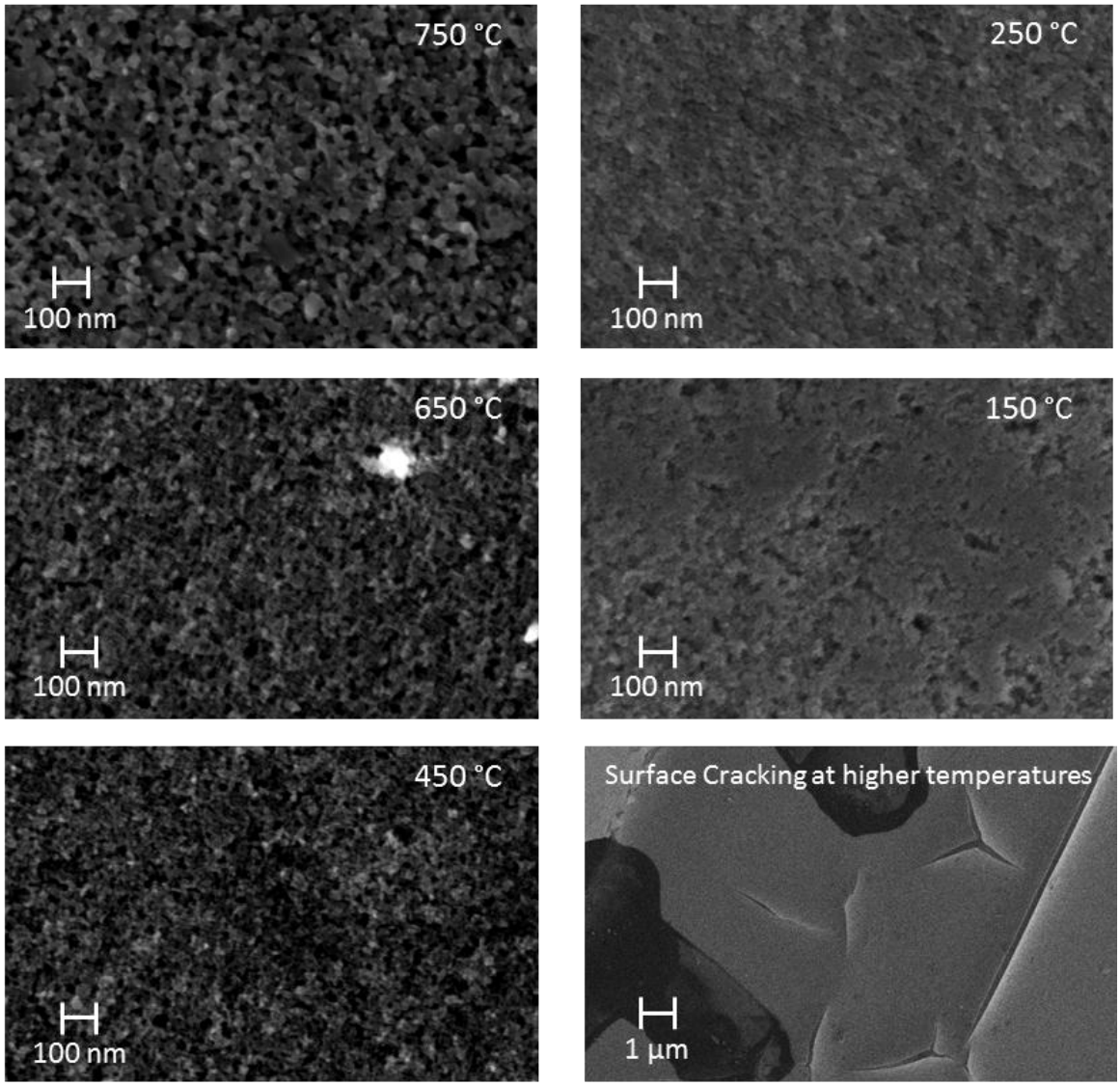


Fig 2-6 All images were taken at x200000 magnification and at 1.5 x10^{-9} T pressure. Images are in order of sintering temperature, starting from 750 °C down to 150 °C (750, 650, 450, 250, and 150). The last picture just shows the film cracking at high temperature sintering (in this case 750 °C.)

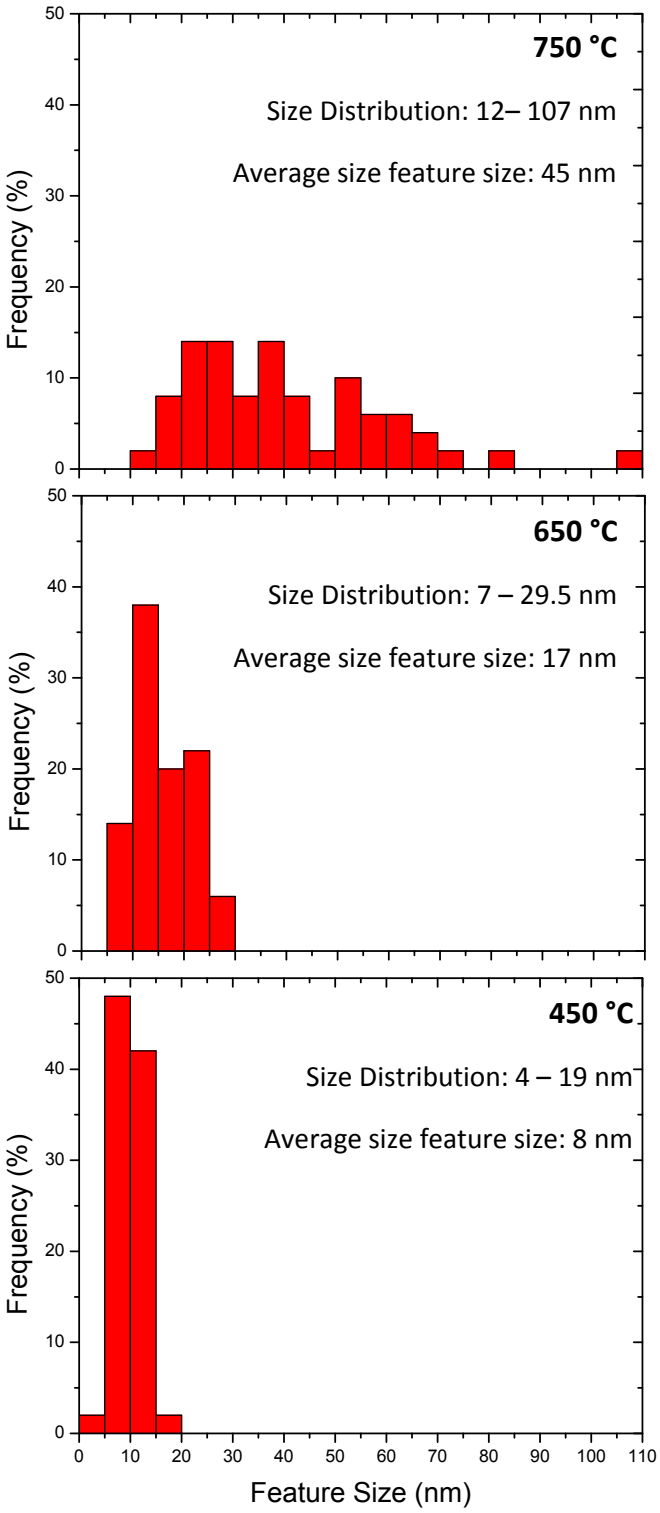


Fig 2-7 Size distributions of the surface features seen on the titania substrate sintered at 750 °C, 650 °C, and 450 °C. Size distributions of 100 random surface features were obtained through ImageJ analysis software.

The dark patches in the pictures signify deep areas, where secondary electrons were not detected. Titania sintered at higher temperature (450-750 ^oC) showed significantly more dark patches in the SEM pictures implying higher porosity. An increase in average feature size can be seen upon comparing the images of samples sintered at 450 ^oC and 750 ^oC. Using the ImageJ imaging software, it has been found that the average feature size in films sintered at 750 ^oC was 45 nm with approximately 10 % of the features exceeding 65 nm. The size distribution of the features ranged from 12 nm to 107 nm and this could be attributed to coalescence of the titania crystals at higher temperatures. The average feature size of films sintered at 650 ^oC was 17 nm and the size distribution ranged from 7 nm to 29.5 nm, which is attributed to reduced coalescence. It is evident from Fig. 2-7 that at 450 ^oC the features showed finer pore structures. The feature size averaged 8 nm with much tighter size distribution ranging from 4 nm to 19 nm. The two films sintered at lower temperatures (250 ^oC & 150^oC) showed formation of small pore features but also showed 'shallow' pores. This is because the temperature was not sufficient enough to burn off the surfactants (see next chapter) and hence the nanoporous features were not formed completely.

The data illustrates important points: Firstly controlling the porosity of the titania substrate is possible by simply altering the sintering temperature, with the most porous structure being achieved at 450 °C. Secondly, assuming that the dye can form a monolayer on the internal surface of the pores, dye loading on the film should be readily controllable by changing the porosity. Finally, films sintered at temperatures above 650 °C show larger titania features, which lead to optical scattering and are not suited for optical filter applications. Furthermore, using such high sintering temperatures caused surface cracking due to the expanding glass substrate [96].

For the purpose of using these nano-porous titania substrates in dye-sensitised optical filters, we required high porosity to maximise dye loading and hence filter attenuation. Furthermore, the anatase phase titania is preferred to maximise the transparency of the substrate - which would preclude any sintering temperatures above 650 °C as beyond this temperature, partial formation of rutile phase titania occurs.

2.4.2 Profilometer and Nitrogen Porosimetry

Thickness of the oxide film is a significant factor in the final properties of the optical filter since this determines the optical pathlength, and the amount of dye loading. The thickness and porosity were measured using a surface profilometer and nitrogen porosimetry. The films were prepared on standard microscope glass slides measuring 30 mm x 100 mm and the average thickness of the films were determined over a distance of 10 mm in the x-direction (across the short side of the glass slide).

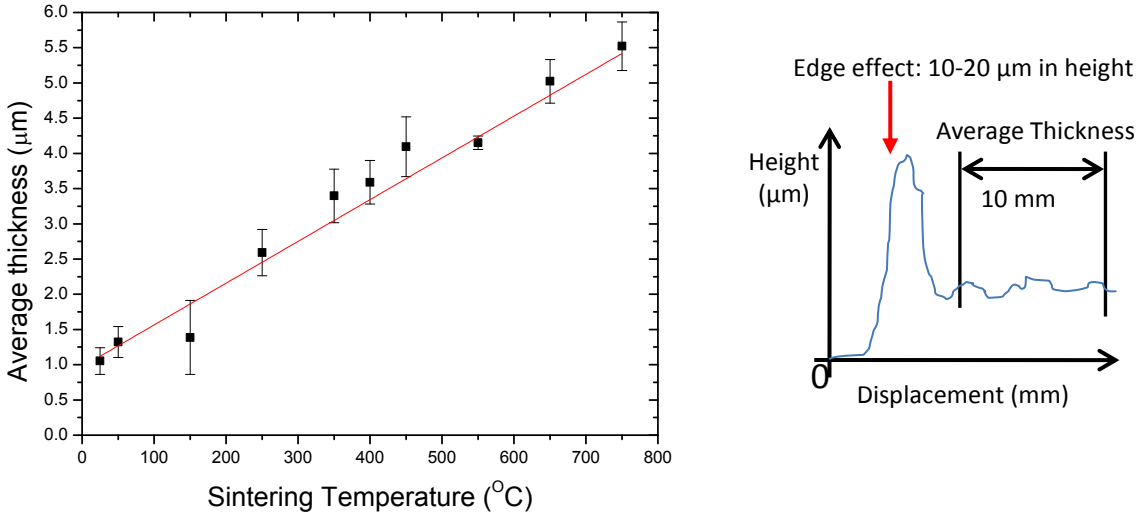


Fig. 2-8 Results from the profilometer, displaying average results of three films taken at three different points (9 measurements in total for each sintering temperature). The graph on the right shows a diagram of a typical result from a Profilometer

Nine measurements were taken in total for each temperature group and Fig. 2-8 shows the average thickness of the titania film. The thickest parts of the film are at the edges and these features are 10-20 µm in height. The height values were taken away from the edges to avoid this 'edge' effect (note, the edge effect is caused by tape used during the initial screen-printing procedure). The thickness profile of titania shows an approximately linear increase in thickness with sintering temperature (Fig. 2-8), varying from 1 µm to 5.5 µm as the sintering temperature is increased from room temperature to 750 °C. Titania becomes more porous as the sintering temperature increases. At higher temperatures the crystals coalesce forming larger pore volumes, which contributes to the overall thickness of the film. In fig 2-9 and table 2-1 we show the data obtained from the BET surface area measurement, which indicated an increase in pore volume with sintering temperature (Fig 2-9) and this is in agreement with the data from the Profilometer.

Sample	BET Surface Area m^2/g	Pore Volume (cm^3/g)	Effective TiO_2 Area (cm^2)
ITO Glass	30.0	N/A	N/A
25°C	37.2	N/A	1.28
50°C	39.8	N/A	1.37
150°C	43.7	0.0101	1.50
250°C	80.1	0.011	2.75
350°C	100.0	0.09	3.43
450°C	159.5	0.089	5.47
550°C	50.2	0.0154	1.72
750°C	42.4	0.0521	1.46

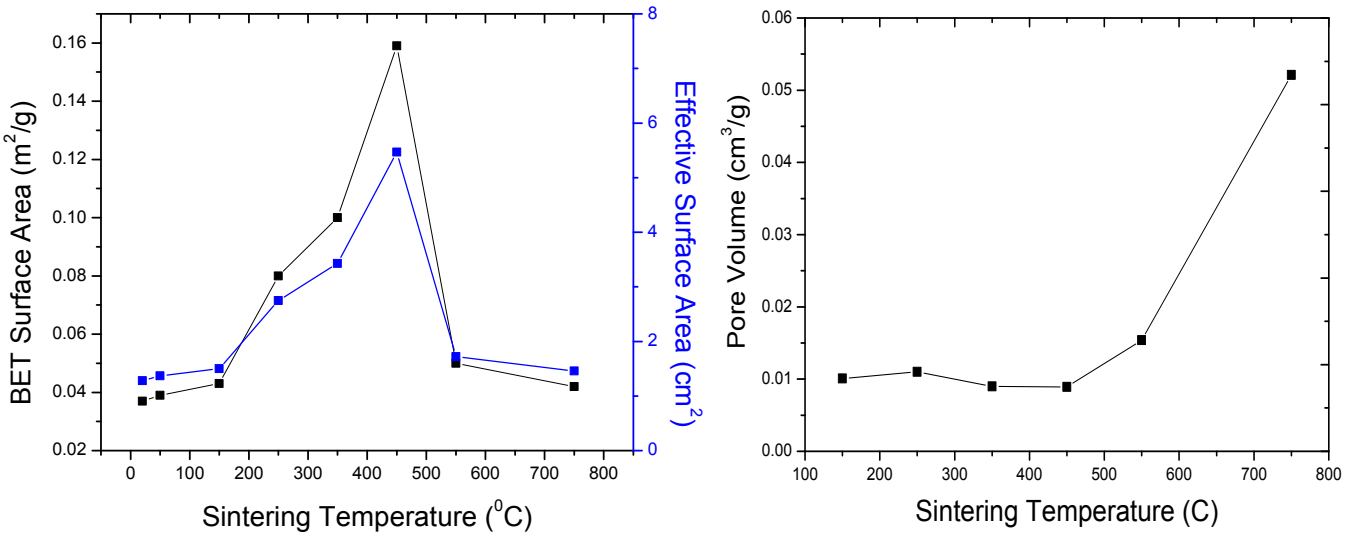


Fig. 2-9 & Table 2-1 Results from the BET surface analyser for non-dye doped titania films. All films were prepared as described in section 2.2.1. ITO glass of equal area is used as a reference to a lamellar type surface. Effective surface area of the TiO_2 film was calculated from the BET surface area and the amount of titania used to fabricate each film (34 mg for all samples).

The BET surface area ranged from 30 m^2/g to 160 m^2/g as the sintering temperature was increased from 25 °C (unsintered) to 450 °C above which it dropped significantly to less than 50 m^2/g. The 'peaked' appearance of the data comes as no surprise since we have already established from the SEM that films sintered at 450 °C showed the smallest surface features. This result is consistent with the literature, where Schneider et. al., observed similar results [97]. The effective surface area of the titania films is the product of specific BET surface area and the actual weight of the titania colloids used. This increases with sintering temperature, peaking at 450°C (24.77 cm^2) above which it declined again as titania coalesce to form larger features. The effective areas obtained using the lowest and highest sintering temperatures films were relatively low (1.28 – 1.72 cm^2). From the above data, we conclude that sintering the commercial paste at 450 °C adequately burned off the organic surfactant and allowed optimum coalescence to form highly nanoporous titania layers.

2.5 Dye Sensitization of TiO_2 – Results

In the following section, the dye solvents and the concentrations were altered to find the optimum sensitizing conditions to produce highly absorbing titania long pass filters. The transmission characteristics of the filters were measured with a dual-beam UV/Vis spectrometer (Perkin Elmer, Lambda 20, UK), keeping the reference path empty so as to determine the overall transmission properties of the filters (dye plus substrate as opposed to the dye alone).

Titania-coated substrates were sintered at 450 °C and immersed overnight in a 0.01 M solution of one of the following six dyes: Alizarin, Alizarin Red, Purpurin, Fluorescein , Fluorescein Disodium Salt (FDS) and Eosin Y (see table 2-2) —all of which were chosen for their ability to adsorb directly onto titania without surface functionalization [91, 98, 99] and to absorb visible light in the range 400 nm - 500 nm. Alizarin, Alizarin Red and Purpurin are anthraquinone-derived dyes with relatively low quantum efficiencies in solution in the range 0.2 to 3 % [87, 100] while the others are fluorescein derivatives with high efficiencies in the range 40 to 97 % [101]. Factors that determine how easily organic molecules will absorb onto an oxide surface include pH [102], temperature [102], the ionic strength of the dye [103], the structure and the concentration of the dye [102], and the surface chemistry of the substrate [102]. The stained films were then washed repeatedly with the same solvent that dissolved the dyes, to remove any unattached dye molecules and finally dried in a stream of nitrogen.

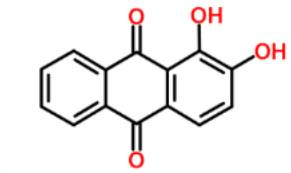
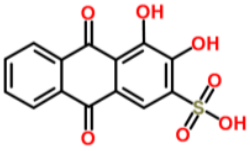
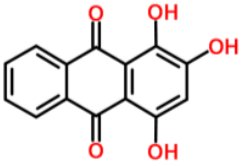
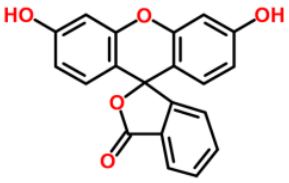
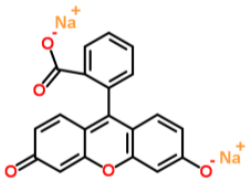
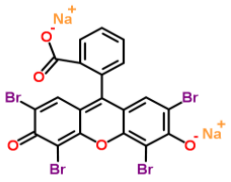
Chemical Name	Chemical Structures	Molecular Weight	Absorption in Solution
Alizarin		240.04	λ_{MAX}(Acetone) = 470nm λ_{MAX}(DMSO) = 458nm λ_{MAX}(Ethanol) = 465nm λ_{MAX}(Water pH7) = 460nm
Alizarin Red		319.99	λ_{MAX}(Acetone) = 470nm λ_{MAX}(DMSO) = 458nm λ_{MAX}(Ethanol) = 465nm λ_{MAX}(Water pH7) = 460nm
Purpurin		256.03	λ_{MAX}(Acetone) = 470nm λ_{MAX}(DMSO) = 458nm λ_{MAX}(Ethanol) = 465nm λ_{MAX}(Water pH7) = 460nm
Fluorescein		332.06	λ_{MAX}(Acetone) = 470nm λ_{MAX}(DMSO) = 458nm λ_{MAX}(Ethanol) = 465nm λ_{MAX}(Water pH7) = 460nm
Fluorescein disodium salt		376.03	λ_{MAX}(Acetone) = 470nm λ_{MAX}(DMSO) = 458nm λ_{MAX}(Ethanol) = 465nm λ_{MAX}(Water pH7) = 460nm
Eosin Y		687.67	λ_{MAX}(Acetone) = 470nm λ_{MAX}(DMSO) = 458nm λ_{MAX}(Ethanol) = 465nm λ_{MAX}(Water pH7) = 460nm

Table 2-2 Table to show the chemical structure and the optical properties of the dyes employed in fabricating long pass filters.

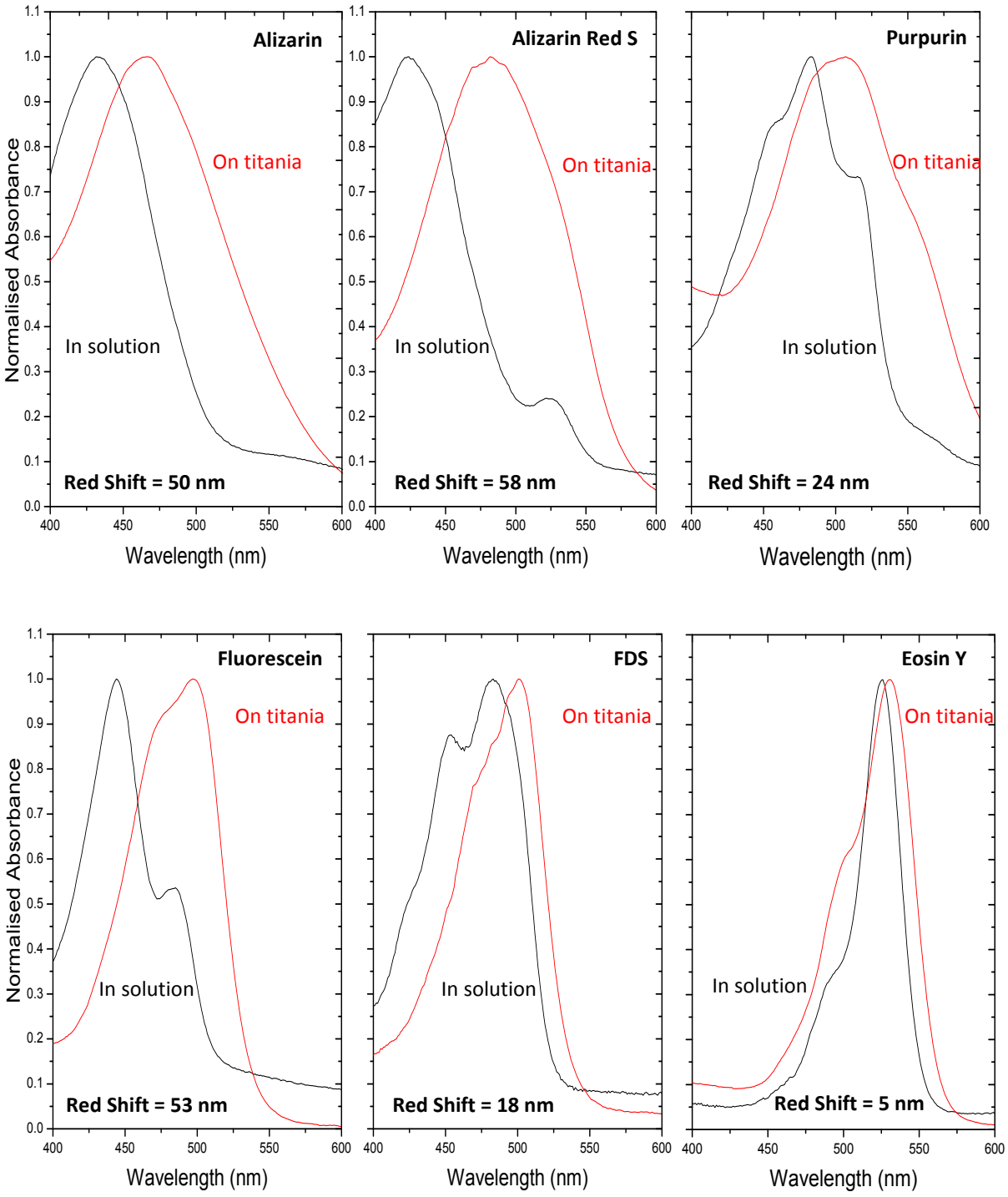


Fig. 2-10A Normalised absorption spectrum of the dye in solution and the titania long-pass filter.

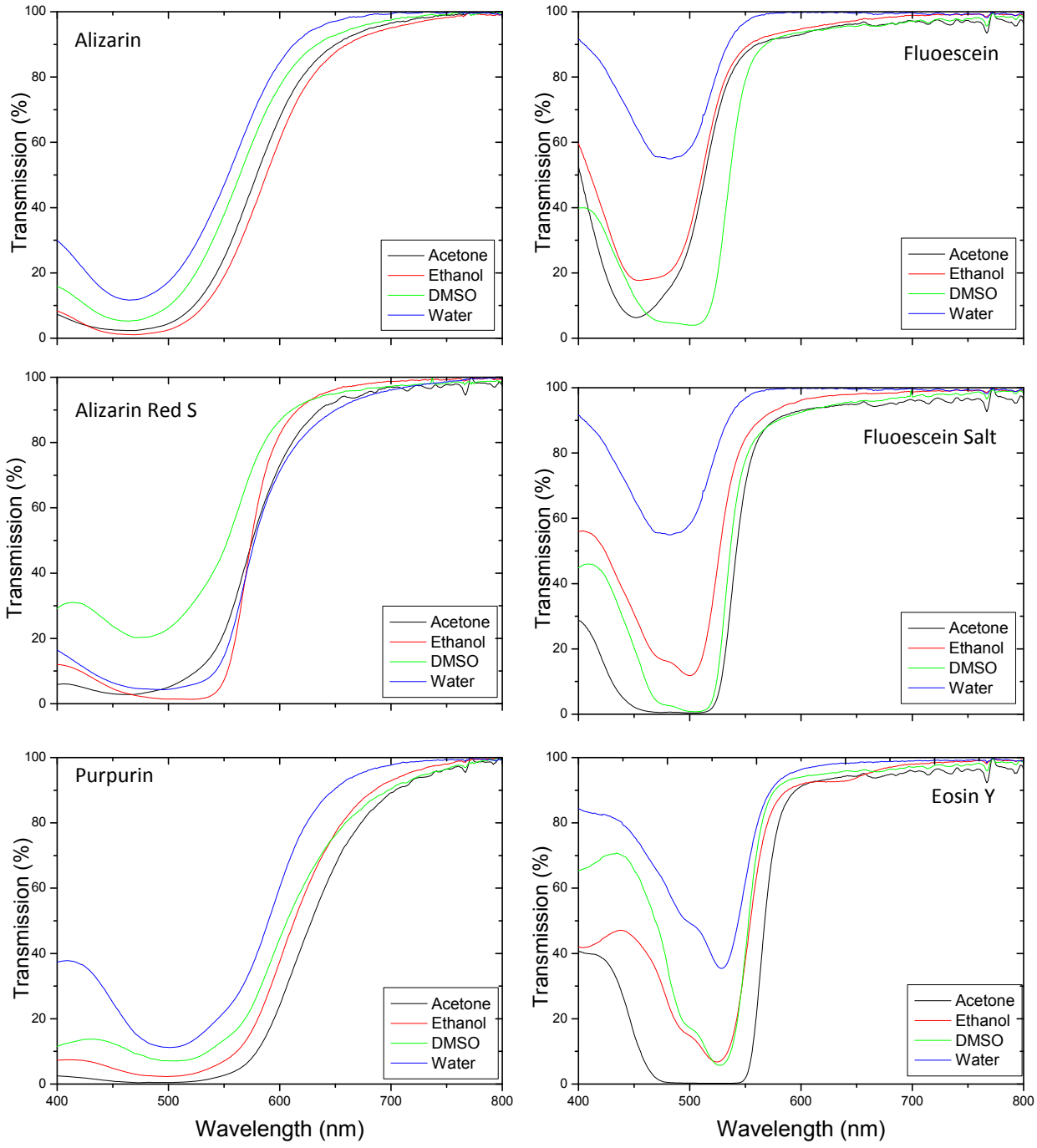


Fig. 2-10B Transmission spectrum of Titania long-pass filters prepared in different solvents.

The organic dyes listed in table 2-2, were dissolved in various solvents of different polarity and 0.01 M solutions of the respective dyes were prepared. The relative dielectric constants of the solvents employed are as follows: Acetone (21), Ethanol (24.3), DMSO (46.7), and water (78.4). As expected, the highest dye adsorption by the titania was observed for solvents with the highest solubility of the

corresponding dyes, leading to reduced optical transmission across the entire measurement range (400 – 800 nm), and particularly in the absorption band below 600 nm. Again, as the concentration of the dye solution increase, so did the amount of dye adsorbed by the titania leading again to increased optical density. Another important feature of the spectrum is a clear red shift relative to the dye in solution (Fig. 2-10A).

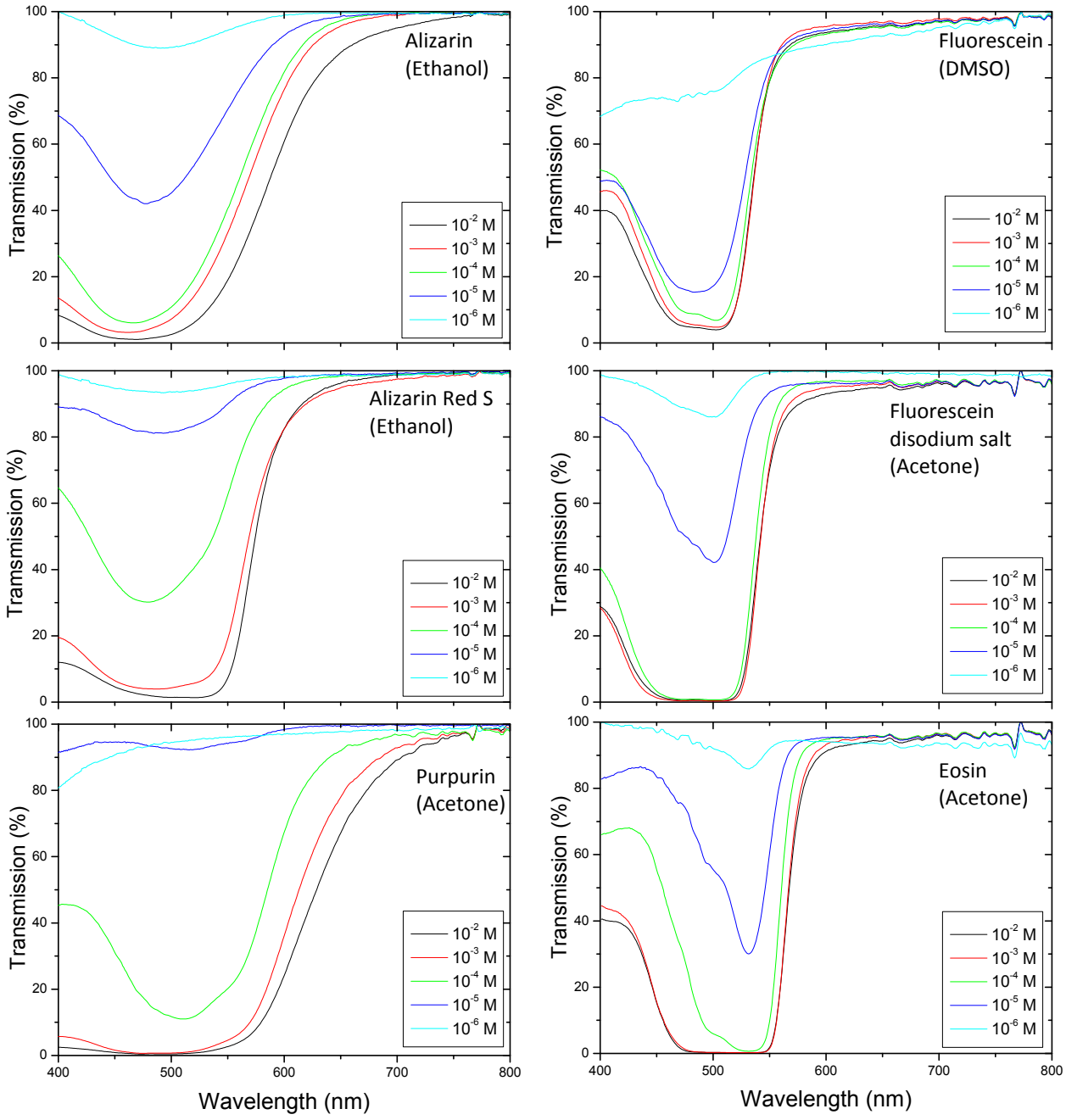


Fig. 2-11 Transmission spectrum of Titania long-pass filters prepared in solvents with the highest solubility of the corresponding dyes. Concentration ranged from 0.01 M to $1x10^{-6}$ M.

The absorption maximum for alizarin increased from 432 nm (in ethanol) to 482 nm (on titania), and similar results were observed with other anthraquinnone derived dyes (Alizarin red S: 424 nm (in ethanol) → 482 nm (on titania), Purpurin: 483 nm (in ethanol) → 507 nm (on titania), Fluorescein: 444 nm (in ethanol) → 497 nm (on titania) , Fluorescein Salt: 483 nm (in ethanol) → 501 nm (on titania), and Eosin Y: 526 nm (in ethanol) → 531 nm (on titania)). The observed red-shift in the absorption spectrum are in agreement with the literature where that attribitue this effect to the formation of new ligand to metal charge transfer band in between the usual π → π* absorption [104-106].

From the previous sections, the fabrication condition for producing highly absorbing titania based long pass filters were chosen as follows:

TiO Sintering Temp ^{O}C	Sensitisers	Solvent
450	Alizarin	Ethanol 0.01M
	Alizarin Red S	Ethanol 0.01M
	Purpurin	Acetone 0.01M
	Fluorescein	Dimethyl Sulphoxide 0.01M
	Fluorescein Salt (FDS)	Acetone 0.01M
	Eosin Y	Acetone 0.01M

Table 2-3 Table showing solvents for various filters.

2.6 Integrating sphere quantum yield measurements

2.6.1. Principles

In this section, the quantum yields of dye-sensitised titania and zirconia are compared to evaluate efficacy of the quenching process with titania. Photoluminescence quantum yield, η is defined by equation:

$$\eta = \text{Numbers of Photon emitted / Numbers of Photons absorbed} \quad (2G)$$

and is also given by the equation:

$$\eta = k_R/(k_R + k_{NR}) \quad (2H)$$

where k_R is the radiative and k_{NR} is the non-radiative rate constant. The quantum yield of a sample may be determined by comparison with a reference fluorophore with a well-defined quantum yield. The quantum yield of an unknown (η_X) is related to that of the reference (η_{ref}) by the equation:

$$\eta_X = (A_{ref}/A_X)(F_X/F_{ref})(n_X/n_{ref})^2 \eta_{ref} \quad (2I)$$

Where A is the absorbance at the excitation wavelength, F is the area under the corrected emission profile (expressed in number of photons per steradians per nanometer per second), and n is the refractive index of the solvent used. Parameters with subscripts *ref* and X refer to the reference and the unknown respectively. (Method described here and equations taken from ref. [107])

The equations described above are for solutions, and their measurements are relatively simple because one can assume an isotropic angular distribution of the emission. Measuring the photoluminescence quantum efficiency of thin films is problematic due to difficulties in determining the reflectivity, angular emission distribution and absorption of the sample under investigation [108]. To compare the quenching efficiencies of the films, it is essential to have an accurate and reproducible way of measuring their quantum yields. This is possible with an integrating sphere, which is a hollow sphere lined with a diffusely scattering material such as barium sulphate or polytetrafluoroethylene (PTFE). In an integrating sphere, the emission light is distributed isotropically within the sphere regardless of any angular dependence of the initial emission. Hence if N_Ω photons are received per second over a solid angle Ω, the total number of photons (N) emitted per second is equal to:

$$N = N_\Omega \left(\frac{4\pi}{\Omega}\right) \quad (2J)$$

The basic experimental setup is shown in Fig. 2-12. The setup consists of a CW He-Cd laser (Class 3B, Max Power 300mW), sample, integration sphere, optical cable, and a CCD spectrometer (Ocean Optics QE64000).

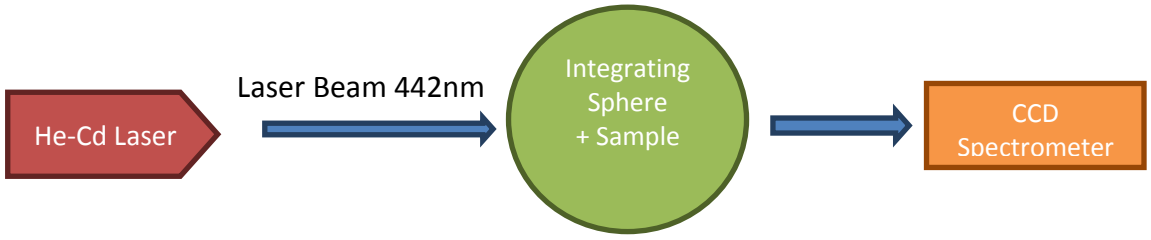


Fig. 2-12 Schematic of the integrating sphere setup.

The laser beam enters the integrating sphere through a small entrance hole. The integrating sphere is connected to the detector with an optical fibre, which sits flush with the interior wall of the sphere. A short distance in front of the optical fibre is a small "baffle" or obstacle coated with the scattering wall material to prevent direct illumination of the detector. Three different configurations are required to determine the quantum yield as shown in Fig.2-13. [108]

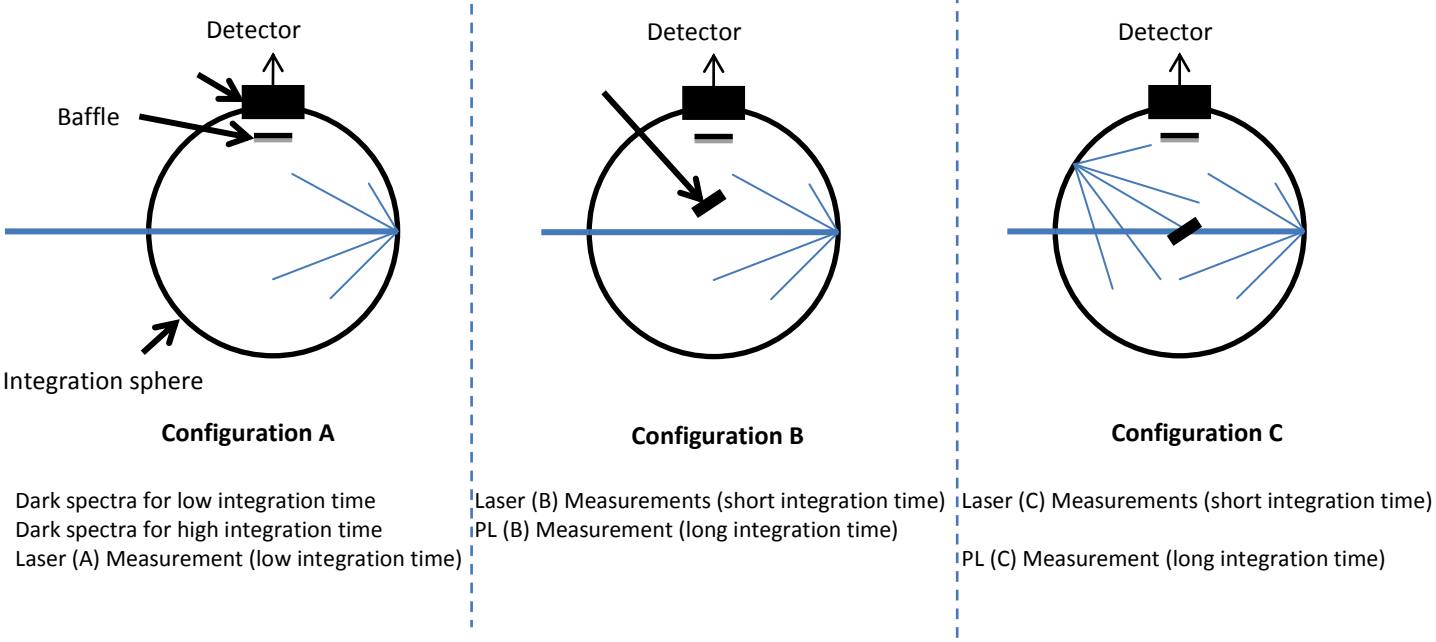


Fig. 2-13 – Diagram to show the three separate experiments for obtaining the photoluminescence quantum efficiency values for thin film samples

Configuration A – Only the laser light is detected (no sample) by the detector. One spectrum with the laser 'on' is recorded, and two further spectra when the laser is 'off' are recorded, each at two different integration times. The reason for the two different integration times is explained later.

Configuration B – The sample is placed within the integration sphere but the laser beam is directed towards the wall. Again, spectra are recorded at two different integration times.

Configuration C – The sample is under direct laser illumination. The sample is orientated so that any reflected light strikes the wall and is not lost via the entrance hole.

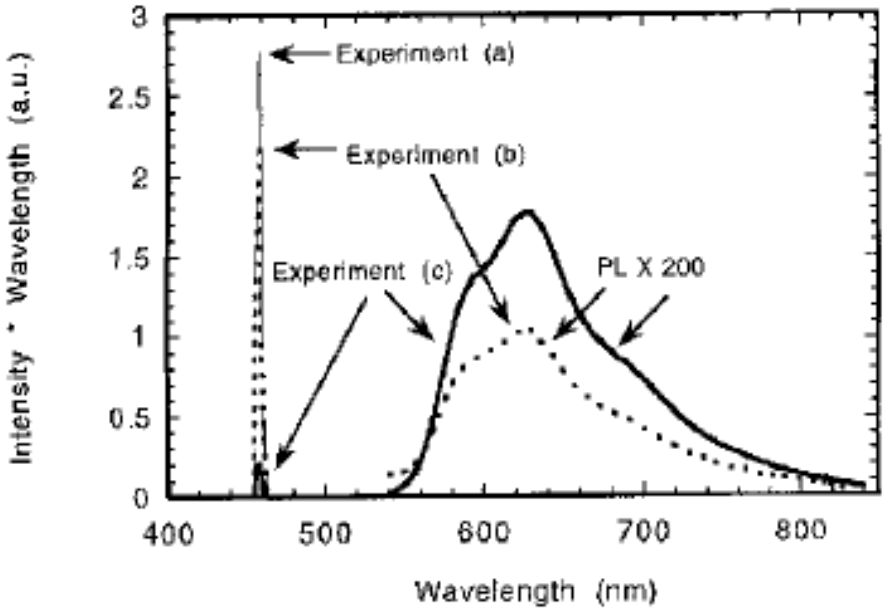


Fig. 2-14 – Example spectra for measurement of thin film MEH-PPV taken from ref. [108]

The area under the laser peak is proportional to the amount of unabsorbed laser light (expressed as a flux), and is denoted L. The area under the emission spectra is denoted P. The laser light incident on the sample has two contributions: a first contribution from the direct laser beam illumination and a second contribution from diffuse laser light reflected by the integrating sphere. In configuration B (Fig.2-13) we make the assumption that the laser light is scattered from the wall of the sphere and a fraction μ of the scattered light is absorbed by the sample. In configuration C the laser beam directly hits the sample and a fraction of this beam will be absorbed by the sample. The unabsorbed light hits the wall of the integrating sphere and scatters, and again a fraction μ of this light is absorbed by the sample. Therefore we can write equations 2G & 2H where the values, $L_{A,}\, L_B$, and L_C denote the values for L for the three configurations (fig 2-13):

$$L_B = L_A(1-\mu) \tag{2K}$$

$$L_C = L_A(1-A)(1-\mu) \tag{2L}$$

Hence we obtain the absorption coefficient A of the sample by:

$$A = \left(1 - \frac{L_C}{L_B}\right) \tag{2M}$$

In experiment B the detected light is composed of (i) absorbed laser light and (ii) the emission caused by scattered laser light that is subsequently absorbed by the sample. The number of photons detected is equal to L_B + P_B. In configuration C, a proportion of the laser beam is reflected, absorbed (A), and transmitted. The contribution of the scattered light to the data can be expressed by:

$$(1 - A)(L_B + P_B) \tag{2N}$$

The absorption of directly incident laser beam also contributes to the emission in experiment C ($\eta L_A A$), hence the total intensity in experiment C is given by:

$$L_C + P_C = (1 - A)(L_B + P_B) + \eta L_A A \tag{2O}$$

Eliminating L_B and L_C with equation 2M, this rearranges to give the quantum efficiency:

$$\eta = \frac{P_C - (1-A)P_B}{L_A A} \tag{2P}$$

The dark spectra obtained in configuration A were subtracted from the subsequent measurements. The short and long integration times were needed to record the strong signal laser light and the emission signal respectively. Neutral density filters and short integration times were used to prevent detector saturation. Verification of the integrating sphere method was performed using a dilute ethanolic solution of Rhodamine 6G (1 mM). The solution was placed in a small ampoule, and the laser beam was orientated to hit the curved surface of the ampoule, taking care to ensure that no reflected exited the integration sphere via the entrance hole. Measurements were taken for working out the absorption coefficient (area under the laser peak) and the photoluminescence (PL) spectrum of Rhodamine 6G. To obtain the PL efficiency it is necessary to obtain the area under the fluorescence spectrum from each experiment. These spectra were integrated over 550 to 800 nm. The equation for working out the photoluminescence quantum yield is in equation 2P.

2.6.1. Results

As mentioned previously, quantum yield measurements on solutions are relatively simple. Quantum yield measurement of dilute Rhodamine 6G solution has been reported by deMello et. al., using the comparative method described in the previous section. They obtained quantum yield of 60 ± 5 %, compared to our 55.4 ± 5 % obtained through the integrating sphere method described above. Hence there is reasonable agreement between the two. Five samples of dye-sensitized titania and zirconia films were prepared for each of the dyes and sintered at 450 ^{o}C. Here the quenching performance of the titania was assessed by the 'quenching factor', and this is deduced by dividing the photoluminescence quantum yield from the zirconia samples by the quantum yield of the titania samples. Significant quenching was observed with all three samples, where the quenching factors were: *Alizarin (502.437), Purpurin (442.129), and Alizarin Red S (292.820).* It is also interesting to note that dye-sensitised zirconia is only weakly fluorescent due to the system undergoing similar non-radiative relaxation mechanism as seen on titania substrates.

From these results it is evident for photoinduced charge transfer between the dye and the titania to occur, and the relaxation of the 'hot' electron undergoes relaxation via the non-radiative pathways as described in section 2.1. Dyes sensitised on zirconia could be dye-coupled in a similar manner to titania but showed weakly fluorescent characteristics (Non-radiative decay via 'trap' states – see Fig. 2-1). This confirms that the decrease in luminescence efficiency of the dye arises from its interaction with the titania substrate and not from any other effects.

	R6G	Zr-P	Zr-AL	Zr-ALRS	Ti-P	Ti-AL	Ti-ALRS
Expt. A (L_A)	1521686.67	1972100	2556883	1739533	1742680	1654363	2153697
Expt. B (L_B)	1280106.67	1251136.67	1440373	1392713	1492047	1419107	1379827
Expt. C (L_C)	694303.33	131076.67	124160	79446.67	666613.3	322423.3	33210
PL B (P_B)	151367.13	33219.78	23846.65	31816.48	4366.23	6349.9	6087.43
PL C (P_C)	467890.77	27678.2	20838.33	25831.13	1980.88	1463.15	2151.02
Abs Coeff. (A)	0.458	0.895	0.914	0.943	0.533	0.773	0.976
PLQY (%)	**55.4010 (±5)**	**1.3706 (±1)**	**0.8039 (±0.5)**	**1.4641 (±0.5)**	**0.0031 (±0.005)**	**0.0016 (±0.005)**	**0.0050 (±0.005)**
Quenching Factor					***442.129***	***502.437***	***292.820***

Table. 2-4 Overall results from the integration sphere measurements. PLQE of three titania samples and three zirconia samples (prepared at 450 ^{o}C) were measured. Results displayed here are the relative intensities in counts.

2.7 Autofluorescence Measurements

2.7.1 FDS doped Polydimethyl Siloxane (PDMS)

To mimic a conventional low cost colour filter, one of the dyes, fluorescein disodium salt (FDS), was dispersed in a polymer host. Adapting the method outlined in ref. [109], 1 ml of saturated FDS solution was prepared in ethanol and 1 ml of immiscible toluene was added to the FDS saturated ethanol solution. The two phased mixture was vigorously mixed until the toluene layer showed colouring. This toluene layer was separated from the ethanol layer and evaporated to increase the FDS concentration. This process was repeated until we achieved adequate amount of highly concentrated FDS toluene solution. In this way we were able to prepare a concentrated solution of FDS in toluene – a solvent in which it will not dissolve directly. The resulting FDS toluene solution was then mixed with 20 g of poly(dimethylsiloxane (PDMS) monomer and hardener pre-mixed at a ratio of 10:1 v/v (Sylgard 184 silicone elastomer kit, Dow Corning, Coventry, UK). This resulting slurry of dye doped PDMS was poured into a plastic petri dish and left to cure at room temperature for 48 hours, resulting in a coloured PDMS filter with approximate thickness of 5 mm.



Fig. 2-15 - Dye doped PDMS filter in petri dish after 48h of room temperature curing.

2.7.2 Absorption Measurements

The absorption characteristics of the titanium filters and those of commercial Schott glass colour filters (GG475, OG530, OG550) were measured with a dual-beam UV/Vis spectrometer (Philips Unicam, UK), using air as reference to determine the transmission properties of the filters (Fig. 2-15). Autofluorescence spectra were obtained by directing a 1.1 mW beam from a 442 nm HeCd laser (IK5552R-F, Kimmon Japan attenuated with Thor Labs 442 nm band-pass filter and a O.D. 2 Schott glass Neutral Density filter) onto the front side of each filter and placing a fibre-optic coupled to a CCD spectrometer (QE65000, Ocean Optics, US) at the rear of the filter. (See Fig. 2-17).

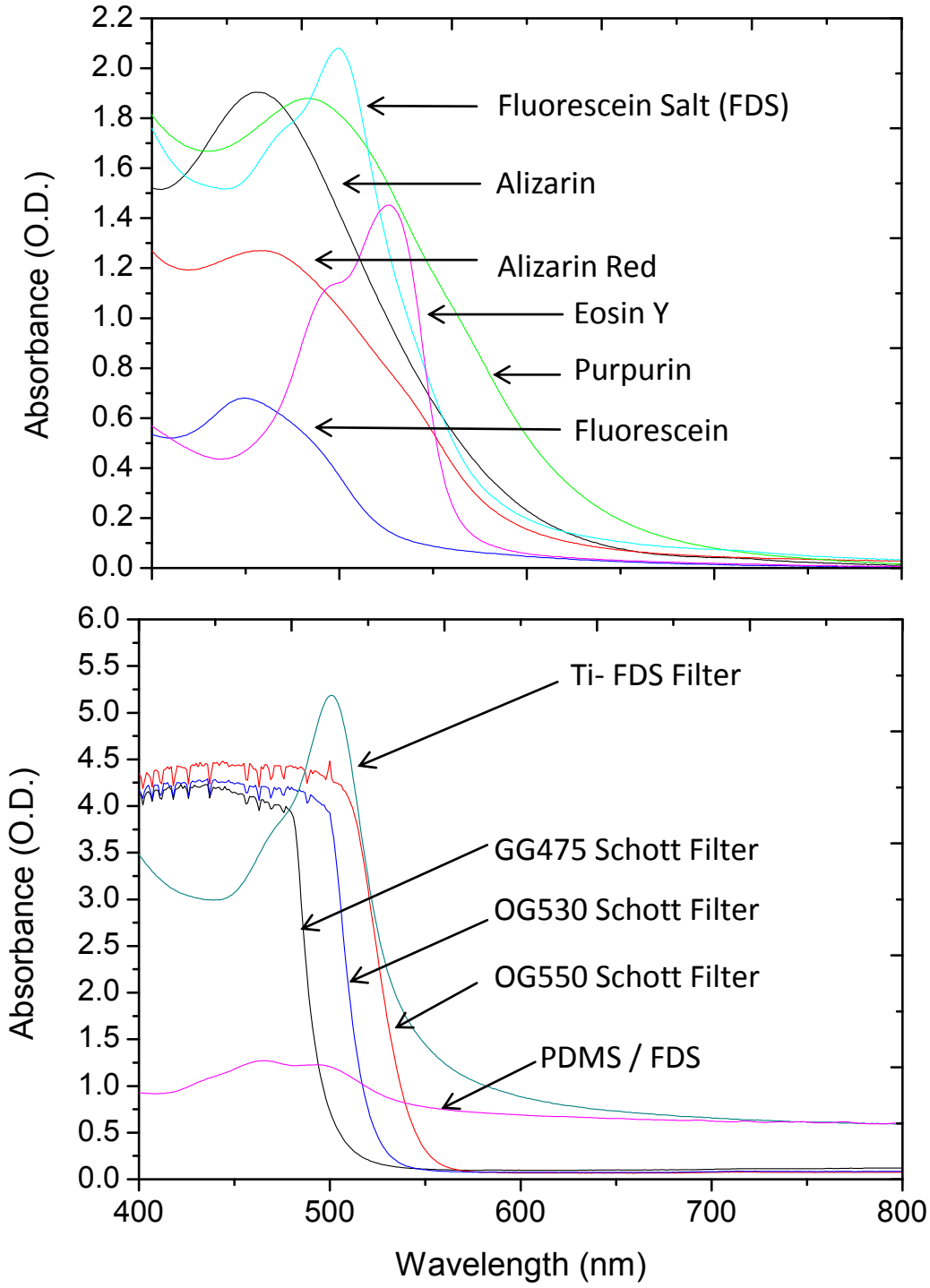


Fig. 2-16 **(Above)** Absorption spectra of single-layer titania films sensitised with various anthraquinone- and fluorescein-derived dyes. **(Below)** Absorption spectra of three commercially sourced Schott glass colour filters, and an FDS-doped PDMS filter; also shown for comparison are calculated absorption spectra for four-layer FDS- and Alizarin-sensitised titania stacks determined from the single-layer absorption spectra.

Fig. 2-16 shows the absorption spectra of the dye-sensitised titania films. Each long-pass filters shows a broad cut-on from the short-wavelength stop-band to the long-wavelength pass-band, with the absorbance approaching zero towards 800 nm. The absorbance in the stop-band was small in all filters, falling as low as 1.7 for Purpurin, 1.5 for Alizarin, 1.2 for Alizarin Red, 0.5 for Fluorescein, 1.5 for FDS, and 0.4 for Eosin Y. Whilst these OD values are certainly too low for most filter applications, improved OD can be achieved by stacking several dye-sensitised filters, albeit at the expense of transmission in the pass-band. From Fig. 2-16B it is evident that by stacking four layers of FDS-sensitised titania significantly improved blocking characteristics are attainable with a modest loss of transmission in the pass-band. Also shown for comparative purposes are absorption spectra for the FDS-sensitised PDMS film and the three Schott glass colour filters. The high baseline of the FDS-doped PDMS filter is due to the difficulty of uniformly dispersing FDS in PDMS, which results in a highly scattering film.

2.7.3 Autofluorescence measurements

The experimental configuration shown on Fig. 2-17 was chosen to mimic the typical situation in a microfluidic device where the light-source and the photodetector are directly opposite one another, and a long-pass filter is placed immediately in front of the photodetector to block the excitation light. Integration times of up to 15 minutes were used to collect the spectra due to the weak emission from the dye-sensitised titania films.

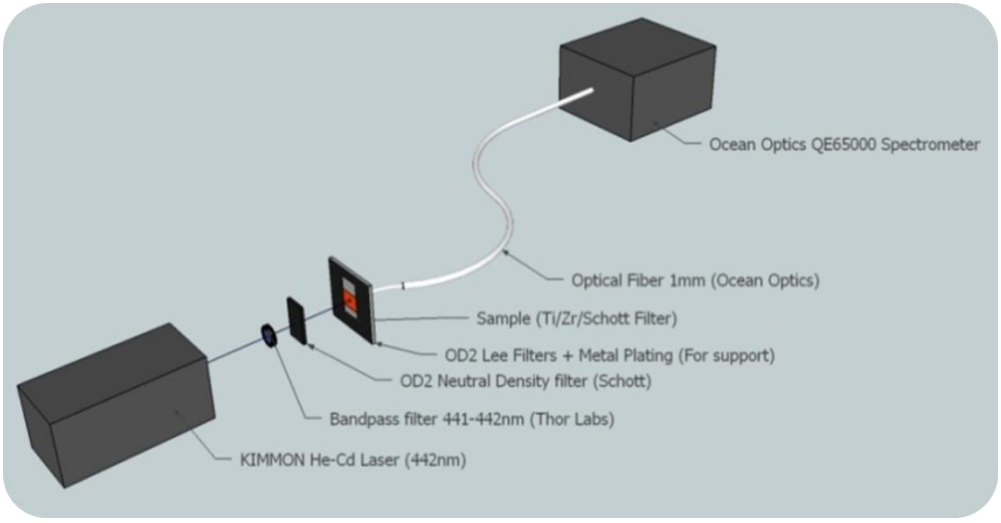


Fig. 2-17 - Schematic of configuration used for autofluorescence measurements. A 1.1 mW laser beam from a 442 nm HeCd laser is directed onto the front side of the filter and a fibre-optic coupled to a CCD spectrometer is placed against the rear-side of the filter immediately behind the laser spot, leading to collection of directly transmitted laser light and filter autofluorescence.

Fig. 2-18(A) shows the emission characteristics of the three Schott glass colour filters, the FDS-doped PDMS film and the four-layer FDS-sensitised titania stack, measured in the manner described on the previous page. It is evident that the three Schott glass filters and the dye-doped PDMS filter exhibit strong auto-fluorescence that would preclude their use in high sensitivity detection. On the other hand, the FDS-sensitised titania film exhibited extremely weak fluorescence that we were unable to detect even with a fifteen minute integration time on the CCD spectrometer. Fig. 2-18(B) shows on a magnified scale the emission characteristics of all six dye-sensitised titania films. In every case, the emission was strongly quenched and indeed only the fluorescein sensitised film had an emission spectrum that was (barely) detectable. It is evident that depositing a diffuse monolayer of dye molecules on a nanoporous titania scaffold is a highly effective method of quenching emission from the dye. Fig. 2-19 shows a picture taken during the autofluorescence measurements described above. It is evident that commercial glass filters and FDS-doped PDMS autofluoresce considerably compared to the FDS-sensitised titania film.

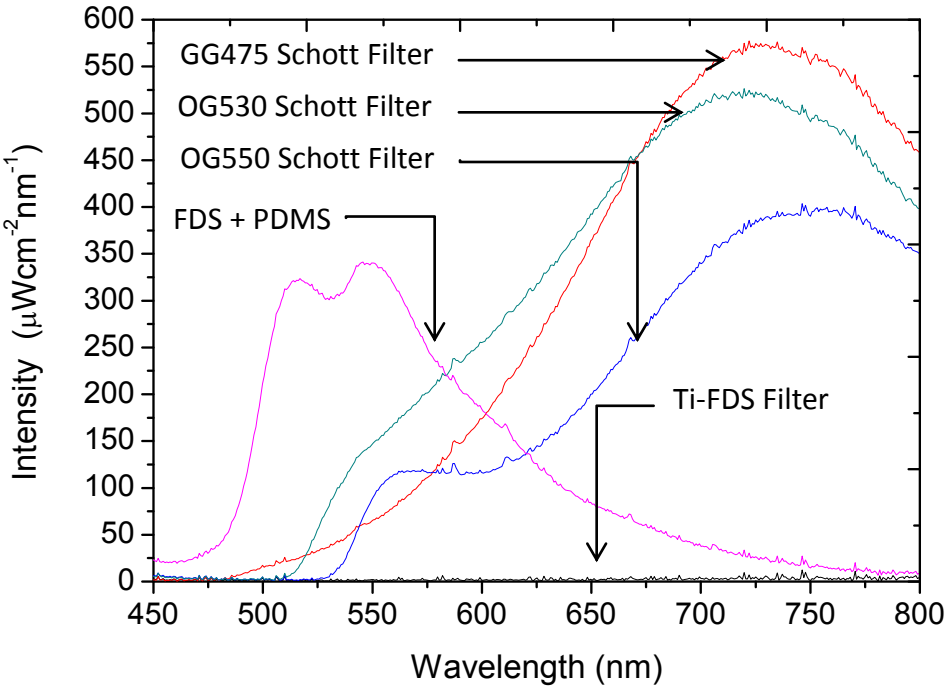


Fig.2-18A Autofluorescence spectra for the three Schott Glass colour filters, the FDS-doped PDMS and the FDS-sensitised titania filter. All samples were excited at 442 nm with an integration time of 15 min.

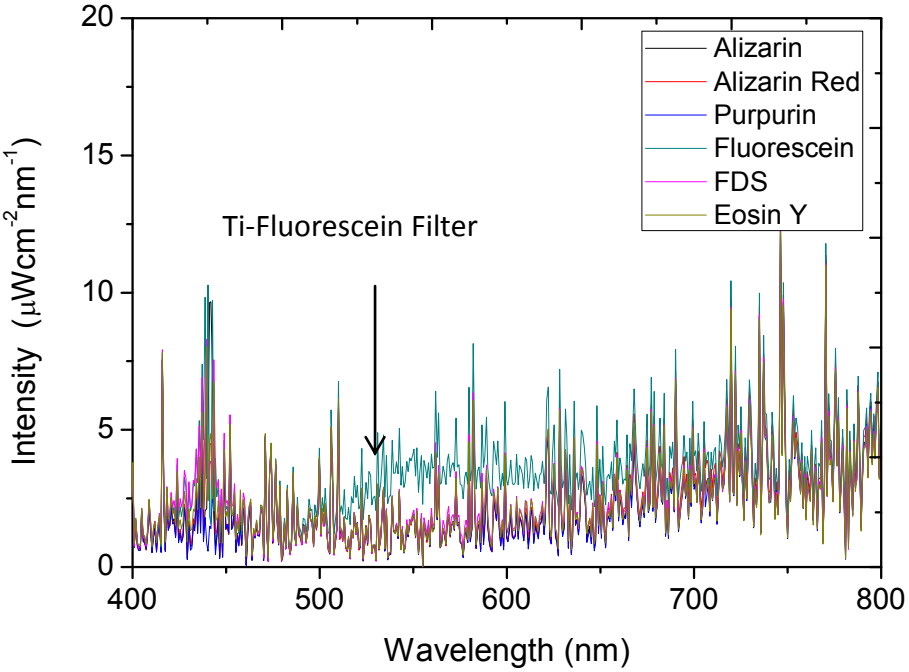


Fig.2-18B Autofluorescence spectra for the six dye-sensitised titania films under identical conditions. Note, the spectra are shown on a magnified scale relative to 2-18 (A).

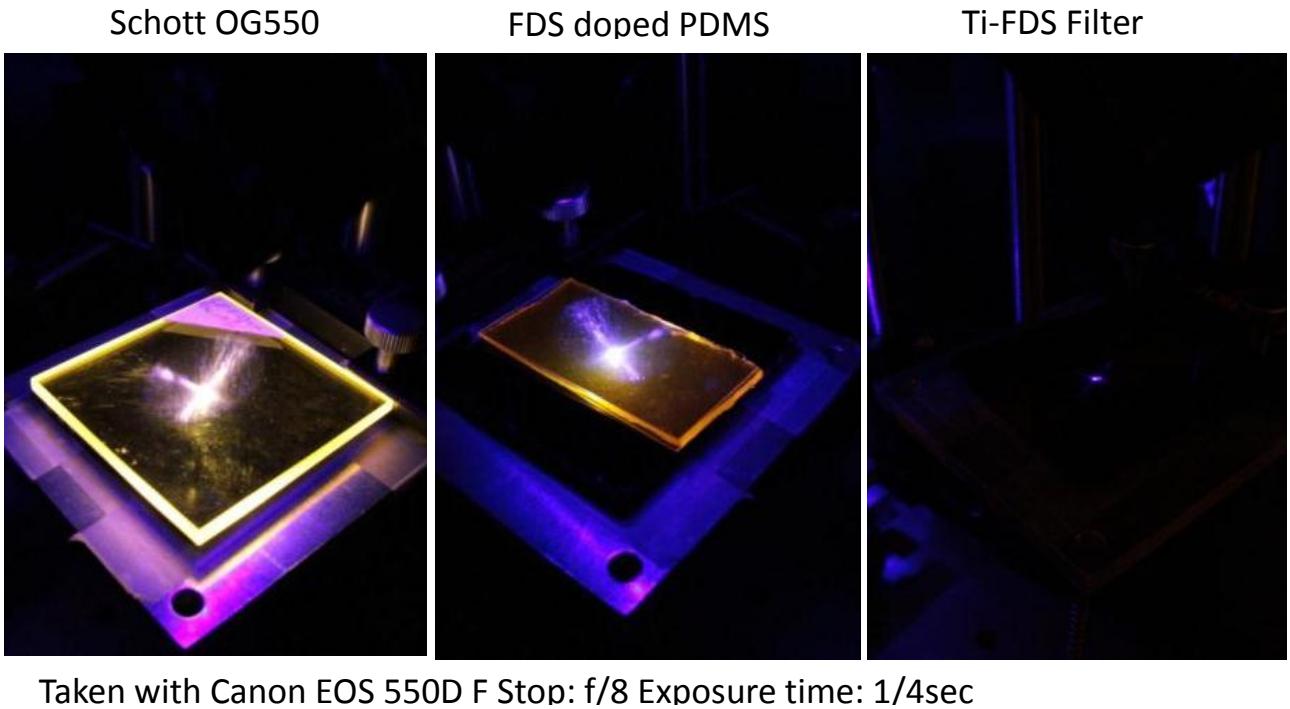


Fig.2-19 Photograph taken during the autofluorescence measurements using the conditions described in Fig. 2-17. Titania based filters sensitised (right) with FDS only shows a reflected laser spot, while commercial (left) and FDS-doped PDMS (center) shows significant autofluorescence.

2.8 Using the Filters

2.8.1 Detection of Rhodamine 6G

To evaluate the titania-based filters for fluorescence detection, we applied them to the fluorescence detection of Rhodamine 6G (R6G), using a 442 nm HeCd laser for optical excitation. Four-layer FDS- and Alizarin-sensitized titania stacks were selected as long-pass filters, both of which were chosen for their ability to provide good blocking of the laser and to transmit the R6G emission signal. Again, to mimic the conditions used in a typical microfluidic device, the detection configuration shown in Fig. 2-20 was used, in which the laser spot and photodiode were positioned in a face-to-face configuration. Ethanolic solution of R6G of various concentrations ($5x10^{-6}$ to 10^{-3} M) were placed in a 0.1 mm quartz cuvette, and positioned on top of the long-pass filter. For comparative purposes, the measurements were also repeated using the commercial Schott glass colour filter OG530.

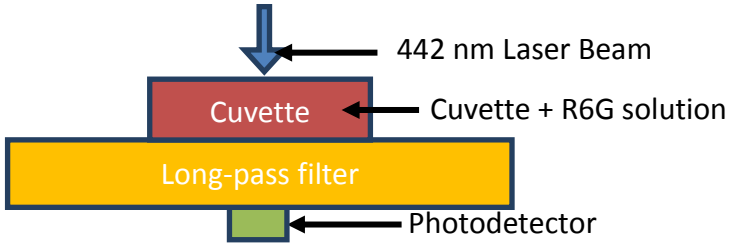


Fig.2-20 Schematic of configuration used for concentration measurements. The 1.1 mW laser spot from a 440 nm HeCd laser and a silicon photodiode were positioned opposite one another on the front and back surfaces of a cuvette, with the long-pass filter tightly inserted between the rear of the cuvette and the photodiode, leading to collection of transmitted laser light, analyte fluorescence and filter autofluorescence.

Fig. 2-21A shows the relationship between the signal intensity and the R6G concentration obtained using the three different long-pass filters. The filters employed were the Alizarin- and FDS-sensitised titania filters (four-layer stacks in both cases), and the commercial schott glass filter OG530. The signals were dark current corrected (dark current of 0.1 nA) in all cases. Excellent linearity was observed with the two Ti- based filters, with fairly low y-intercepts of 57.4 nA and 11.2 nA for the FDS- and Alizarin-sensitised filters, respectively. In both cases where titania filters were used, the signal baseline was attributable to incomplete blockage of the laser light. Defining the limit of detection (LOD), Λ as the concentration of analyte that yields a signal equal to the *y*-intercept plus three times the standard deviation (σ) of the blank (see Fig. 2-21B), we obtained $\Lambda = 2.5 \times 10^{-6}$ M (1.2 µg/ml) for the FDS-sensitised filter, and $\Lambda = 1.9 \times 10^{-6}$ M (0.91 µg/ml) for the Alizarin-sensitised filter. Good linearity but a much higher *y*-axis intercept value of 1.14 µA was

observed with the OG530 Schott due to strong autofluorescence from the filter, resulting in a significantly worse limit of detection of $\Lambda = 9.3 \times 10^{-6}$ M (4.43 µg/ml). From these measurements, it is evident that autofluorescence from the filters can severly impair the limit of detection. Filters with low autofluorescence are essential for high sensitivity detection. It is important to note though that our LOD is one orders of magnitude worse than the recently reported microfluidic chip utilising OLED and an OPD [47]. Pais et.al., achieved LOD of 0.1 X 10^{-6} M (0.0479 µg/ml) for R6G indicating that there is still much room for improvement.

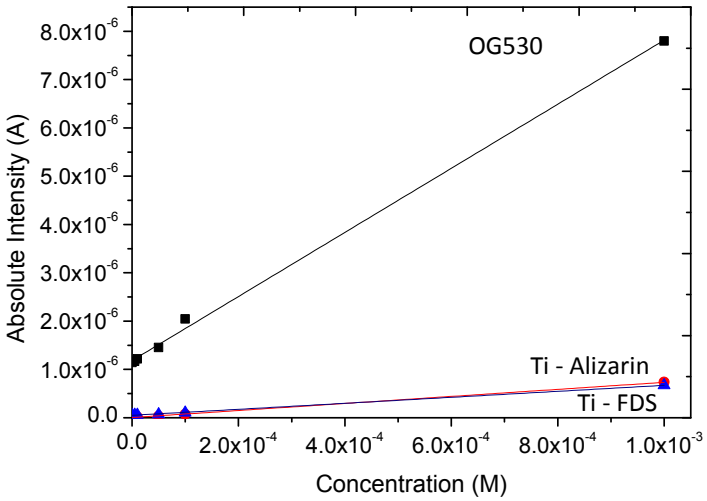


Fig. 2-21A Signal versus concentration of Rhodamine 6G in ethanol. Three types of filters were used: 1) a four-layer FDS-sensitised titania stack, 2) a four-layer Alizarin stack, and 3) a commercial Schott glass colour filter OG530. The experiment used 1.1mW HeCd Laser (KIMMON, Japan) as the light source, and the signal was detected using a Si photodiode (S1226-8BQ, Hamamatsu, Japan) coupled to a Keithley 6517 electrometer.

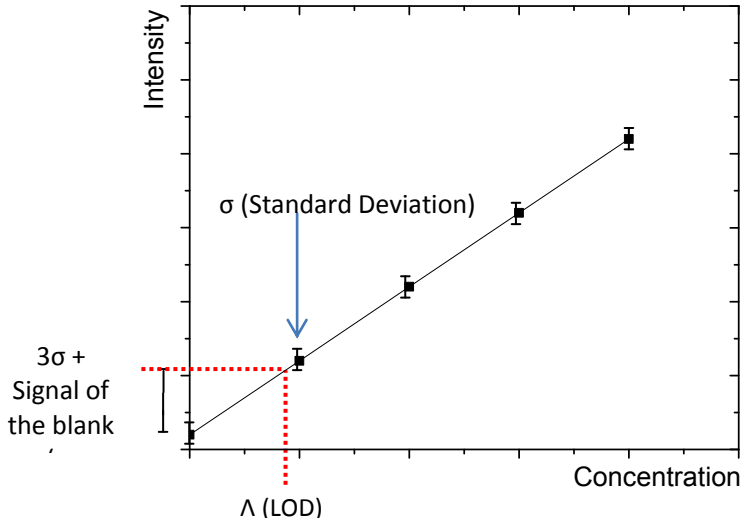


Fig. 2-21B Schematic to show the concept of LOD shown on a 'model' signal versus concentration plot (not to scale). Standard deviations (σ) obtained from repeated measurements are used to calculate the LOD.

2.9 Photo-degradation of Titania based filters

Sensitising nanoporous titania with appropriate dye molecules offers a viable means of creating low cost colour filters with competitive absorption characteristics and superior autofluorescence characteristics to conventional colour filters. However, since titania is widely used as a photocatalyst, it is pertinent to ask whether such filters can be stable under sustained illumination. Furthermore, the selected dye molecules are known to be susceptible to photo-degradation on Titania nano-colloids [110, 111]). With this in mind, the photostability of the TiO_2 filters was investigated by placing the filters in a Fluoromax-2 spectrometer (Fluoromax-2, Horiba Jobin Yvon, UK) and exposing the filter to 442 nm light of 0.04 mW/cm^2 for an extended period of time. (Intensity of this light was determined with a calibrated Silicon photodiode - S2281, Hammatsu, Japan)

In Fig. 2-22, we show the absorption spectra of the FDS based filter and the Alizarin based filter in open air, obtained under illumination at 0, 5, 15, 30, 60, 120 min and 24 h intervals, which shows rapid degradation in the blocking performance upon exposure to continuous illumination. The absorbance maxima of the Ti-FDS filters exposed with 442 nm light changed from O.D. 1 to O.D. 0.9 in the first 15 minutes, which equates to a approximate 10 % change. Over the period of 24 h, the absorbance decreased to O.D. 0.25 at 500 nm, implying an average degradation rate 0.052 $\%min^{-1}$. The observed photo-degradation after exposure to visible light can be attributed to a mechanism proposed by Liu *et al*., in which injected electrons react with the pre-absorbed oxygen to form oxidising species [112].

To protect the titania filters from moisture and oxygen-mediated photo-degradation, FDS- and Alizarin-sensitised filters were placed in a dry N_2 environment and briefly heated at 60 ^oC to drive off any moisture or solvents. The filters were then encapsulated using a UV-curable liquid epoxy (EE-1 Encapsulation Epoxy, Ossila), and a glass cover slide was placed on top to provide protection from the atmosphere. The dyed part of the filter was covered with aluminium foil before before placing the filters under a UV-lamp table to cure the epoxy.

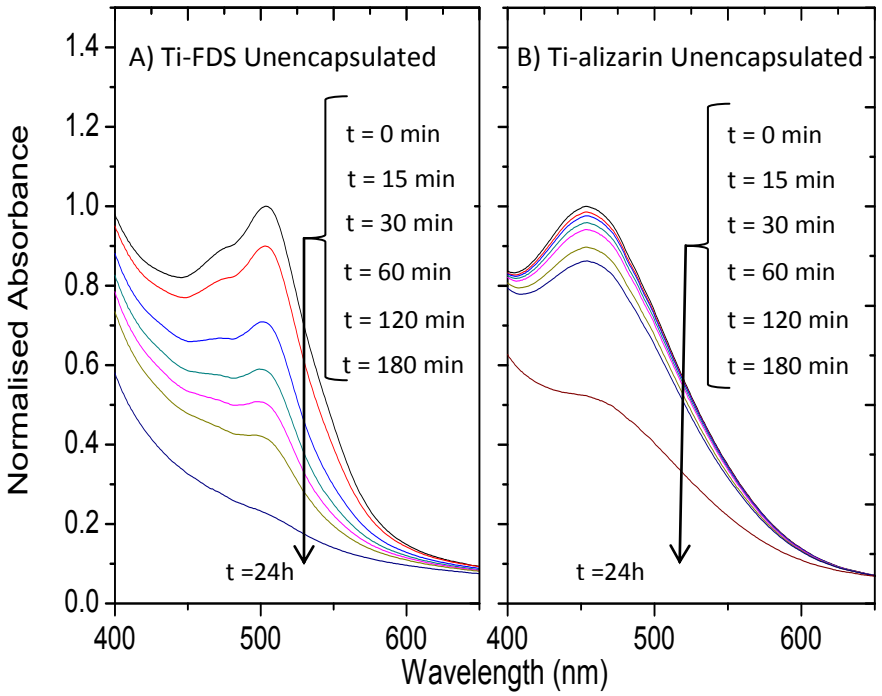


Fig. 2-22 Normalised absorbance of filters sensitised with A) Ti-FDS and B) Ti-Alizarin over period of 24h under continuous illumination by 442 nm of monochromatic light (0.04 mW/cm^2). A 50-80 % reduction in absorption is observed due to photodegradation.

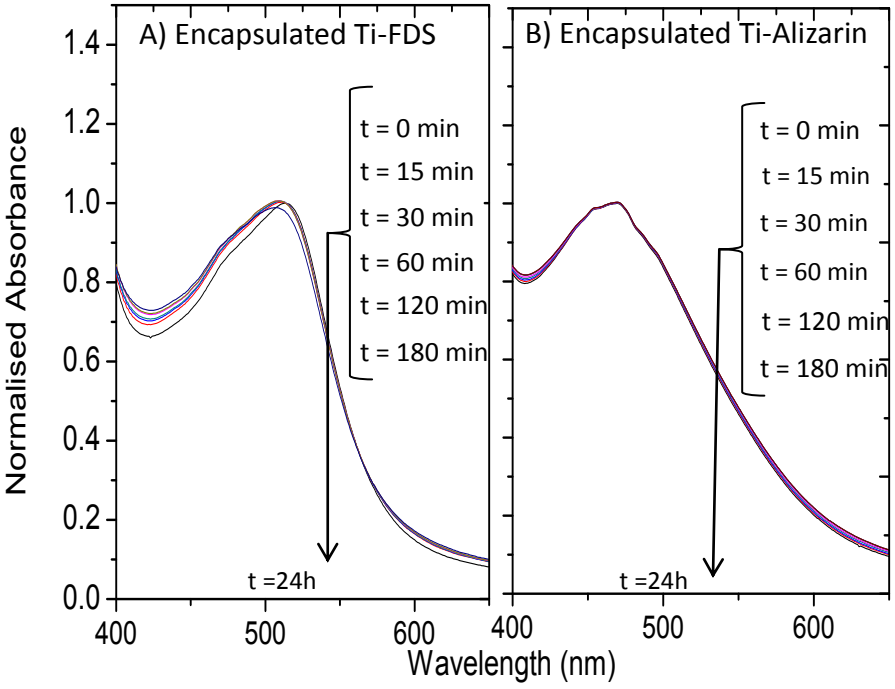


Fig. 2-23 Normalised absorbance of encapsulated filters based on A) Ti-FDS and B) Ti-Alizarin over period of 24 h under the same illumination conditions as Fig. 2-22

Fig. 2-23 shows the absorption spectra of encapsulated filters over the course of 24 hours, using the same experimental setup as before. The spectra show minimal changes and it is evident that encapsulating the filters in glass with epoxy resin and glass provides an effective protection against photo-degredation. The stability of the resulting filters is adequate for their use in low cost diagnostic applications, although slight photo-degradation was observed with Ti-FDS filters (O.D. 0.75 to 0.65 at 425 nm in 24 h). This could be addressed through the use of more photo-stable dyes and stringent fabrication/encapsulation procedures.

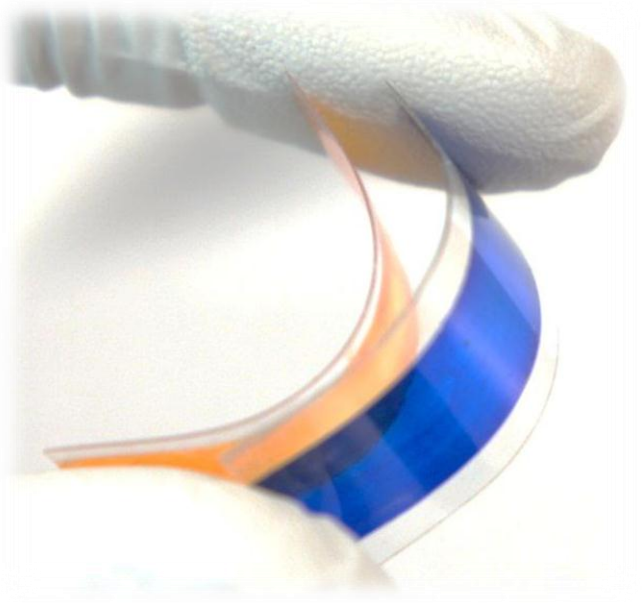
2.10 Summary

In summary we have developed a new type of colour filter with minimal autofluorescence that offers a viable low cost alternative to interference filters. The colour filters are prepared by overnight immersion of a substrate coated with highly porous nanoscale titania in an appropriate dye solution, followed by repeated washing to remove excess dye, resulting in monolayer coverage of the dye molecules on the diffuse titania surface. The interface between the titania and the dye molecule induces efficient quenching of photogenerated excitons in the dye molecule, reducing the photoluminescence quantum yield to a negligible value. The approach can be applied to a wide variety of dye molecules, providing they bind strongly to the titania surface and have compatible energy levels to ensure efficient electron transfer to the titania. (Note, in circumstances where the dye does not bind directly to the titania surface, a linker unit can be used to anchor the dye [113]). The resultant filters exhibit far lower autofluorescence than equivalent filters obtained by dispersing the same molecules in a host matrix, i.e. conventional colour filters. The dye sensitized titania filters were successfully applied in the detection of R6G. A commercial colour filter was also tested for comparison, but showed significantly worse limit. The photostability issue of the titania filters in air was relatively poor, but could be significantly improved by encapsulating them in glass with an UV-curing epoxy. In the next chapter we discuss the extension of this method to plastic substrates – a critical step for low cost applications.

CHAPTER 3

3

Short Pass Filters & Plastic TiO_2 Filter



3 Short Pass TiO_2 Filters

3.1 Introduction

Chapter two reported a new type of low cost colour filter based on titania which exhibit minimal autofluorescence and offer a promising alternative to expensive interference filters [15]. Upon comparing these filters to commercial Schott glass colour filters, significant improvements in the limit of detection were observed. As discussed in Chapter one, portable point-of-care diagnostic devices will incorporate low cost light sources such as inorganic LEDs which typically have a bandwidth profile which can range from 25 – 100 nm and a weak broad wavelength tail that can persist for several hundred nano-meters. Successful implementation of such devices is dependent upon their combined use with both short- and long pass filters. In previous experiments, laser light coupled to an interference band pass filter was used to ensure highly monochromatic excitation source hence long-pass filteration was sufficient for fluorescence detection. However in situations where the light source is not monochromatic, short pass filters are also required to sharpen the spectrum and suppress any "tail-light" from reaching the photodetector that may overlap with and obscure the analyte signal. In this chapter, titania short-pass filters sensitised with blue dye molecules were fabricated on glass and plastic substrates. Plastic long-pass filters were also developed. The plastic long- and short-ass filters were then used in conjunction with LED light source and a silicon photodiode for analyte detection.

3.2 Short Pass Filters

3.2.1 Sensitising Titania in the Red

Sensitising titania with red-absorbing dyes is a "hot" topic in the field of dye-sensitised solar cells (DSSC). Researchers in the DSSC field hope to maximise the light-harvesting efficiencies of DSSCs by using dyes that extend the absorption range, beyond 600 nm [114-119]. Hara et. al. fabricated a series of coumarin-based DSSCs where the chemical structures of the coumarin dyes are altered by introducing additional electron-withdrawing –CN groups to the π-conjugation bridge [117-119] with a view to extending the absorption range. Other groups have successfully sensitised titania with red-absorbing indoline [120], cyanine [121] and oligo-ene [122] based dyes. However all of these dyes require

complicated synthesis steps and have broad absorption range (400 – 700 nm). While appropriate for DSSCs, they are not suitable for our purposes since a short wavelength pass-band is required which the above dyes lack. For our short-pass filtering purposes, the dyes are required to adhere to the titania but absorb only above 550 nm to complement our long-pass filters. Very few dyes are available with the desired optical characteristics and in most cases, they do not readily adhere to titania surfaces due to an absence of suitable anchor groups. One approach to improve adhesion is to modify the surface charge of the titania to improve electrostatic cationic/anionic dye adhesion [123] (Fig. 3-2). An extensive search of the literature revealed only a handful of appropriate dyes and these were all of an ionic nature: Methyl Blue, Remazol Brilliant Blue, 1,1 diethyl -4,4 Carbocyannine iodide, and Xylene Cyanol (Fig 3-1 and Table 3-1).

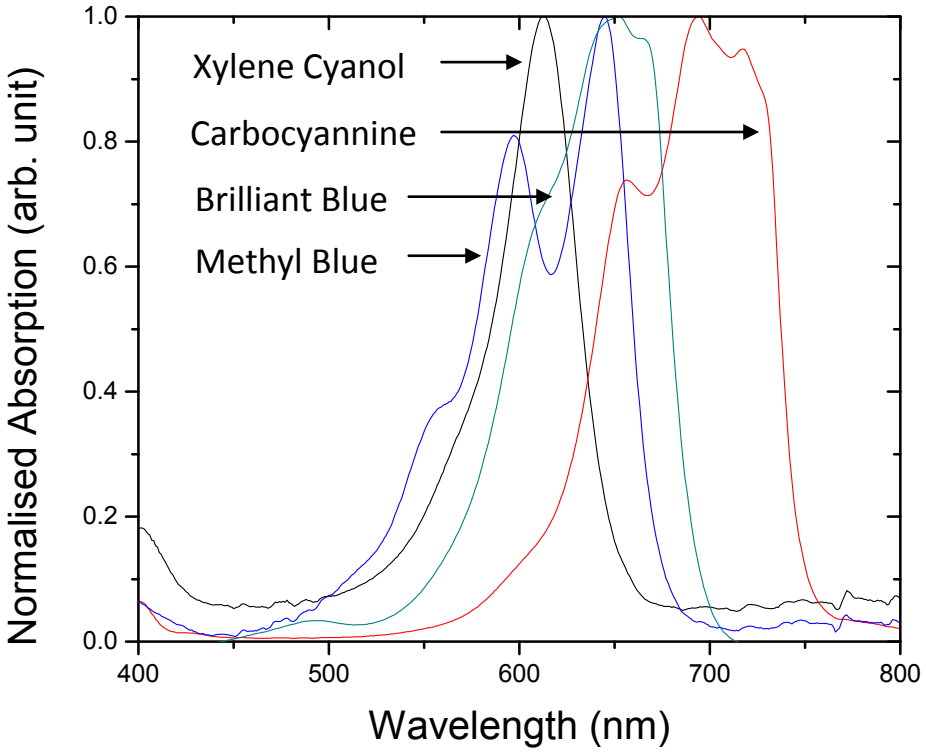


Fig. 3-1 Absorption Spectra of the blue dyes dispersed in ethanol.

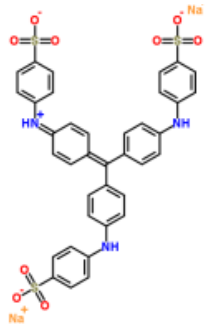
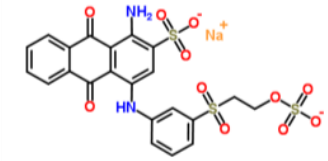
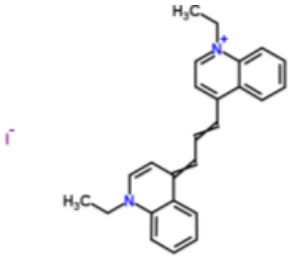
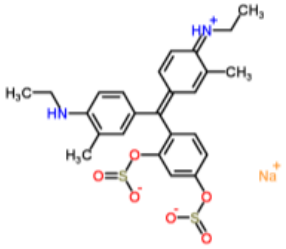
Chemical Name	Chemical Structures	Molecular Weight	Absorption in Solution
Methyl Blue (Anionic dye)		799.07	λ_{MAX}(Water pH7) = 660 nm λ_{MAX}(Ethanol) = 640,660 nm λ_{MAX}(Acetone) = 650 nm
Remazol Brilliant Blue R (Anionic dye)		625.97	λ_{MAX}(Water pH7) = 595 nm λ_{MAX}(Ethanol) = 580 nm λ_{MAX}(Acetone) = 570 nm
1,1'-diethyl-4,4' Carbocyannine Iodide (Cationic dye)		480.38	λ_{MAX}(Water pH7) = 625,700 nm λ_{MAX}(Ethanol) = 670 nm λ_{MAX}(Acetone) = 665 nm
Xylene Cyanol (Both anionic and cationic)		538.12	λ_{MAX}(Water pH7) = 620 nm λ_{MAX}(Ethanol) = 610 nm λ_{MAX}(Acetone) = 590 nm

Table 3-1 Properties of the dyes employed in fabricating short pass filters. Dyes with absorption characteristics well above the desired block band are selected since dyes adsorbed onto titania show blue shifts in their absorption bands.

3.2.2 Fabricating Short pass filters

Nanoporous titania coated glass was prepared using the method described in the previous chapter. The surface pH of the resulting titania films was altered by immersing them in a 0.1 M HNO_3 or 0.1 M NaOH solution depending on the anionic or cationic nature of the dyes used for sensitization (Table 3-1 & Fig. 3-2). Work by Herrmann and co-workers found that cationic/anionic dye absorption onto a titania surface is governed by electrostatic effects [124]. At high pH the surface of the immersed titania is negatively charged due to deprotonation of the surface hydroxyl groups (Fig. 3-2). Such titania films are able to electrostatically adsorb cationic dyes such as 1,1'-diethyl-4,4‘ carbocyannine iodide (Table 3-1). At low pH the hydroxyl group is protonated, leaving the titania with a positively charged surface, enabling electrostatic adsorption of anionic dyes such as xylene cyanol (Fig. 3-3).

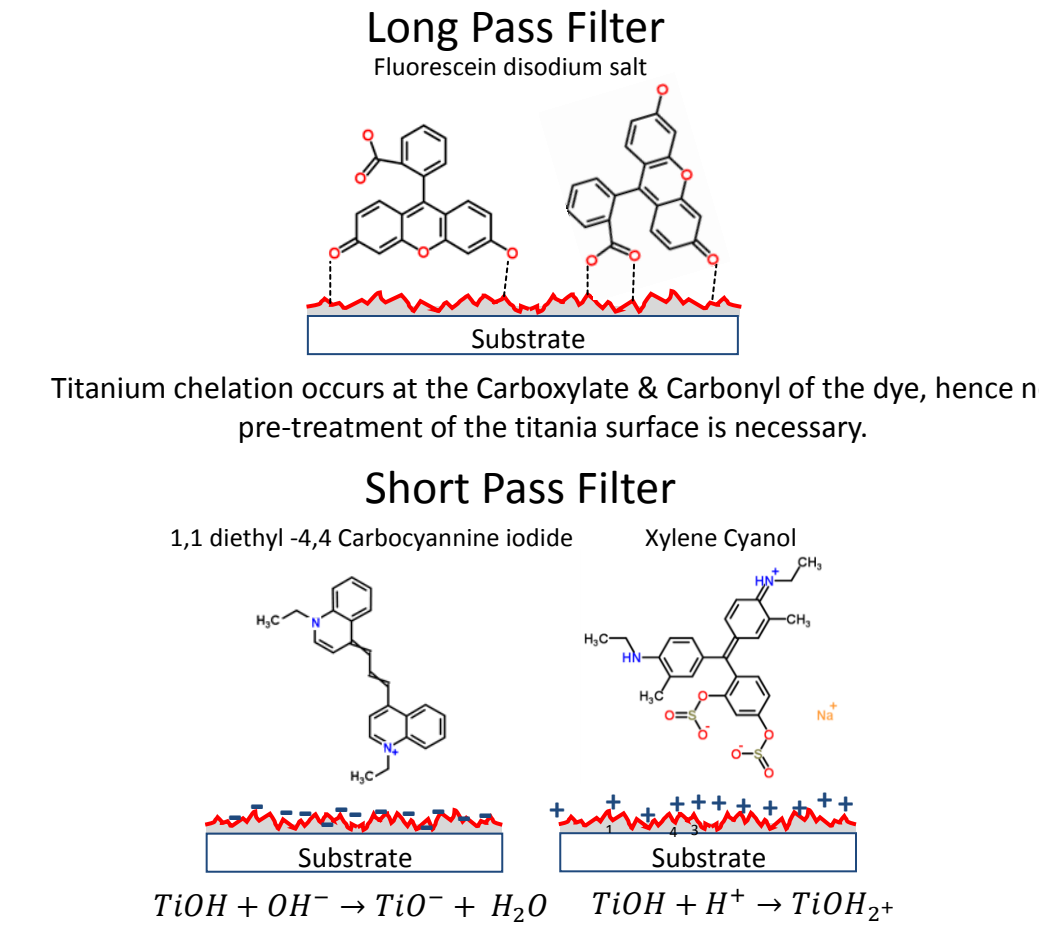


Fig. 3-2 Cationic and anionic dyes adhere to negatively and positively charged titania, respectively.

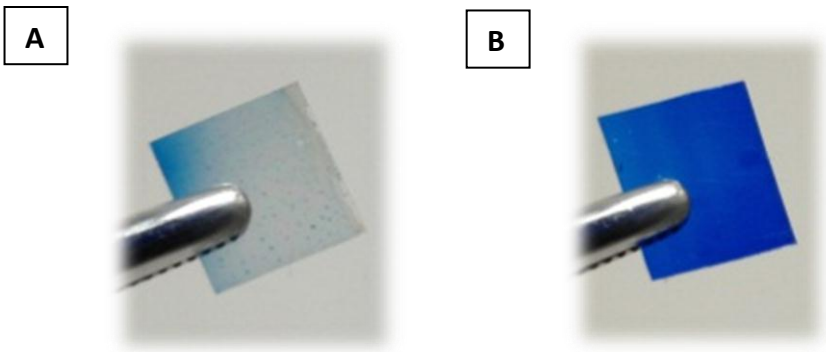


Fig. 3-3 (A) Titania film 'sensitised' with xylene cyanol dye without any surface charge altering treatment. The titania film shows of transparent patches where dye adhesion did not occur even after 24 h of immersion in the dye solution. (B) Titania film sensitised using surface charge treatment showed greatly improved dye adhesion.

After the surface pH alteration step, films were dried in open air, before being immersed in their respective ethanolic dye solution for 24 hours. The stained films were then washed repeatedly with ethanol, to remove any unattached dye molecules and finally dried in a stream of nitrogen. To prevent any photodegradation, the stained films were encapsulated with UV-curing epoxy and a glass cover slip. The absorption and the autofluorescence characteristics of the titania filters were measured in the manner described in chapter two.

Fig. 3-4 (A-D) shows the absorption spectra of the resulting dye-sensitised titania filters. As before, four-layer stacks were used to achieve high O.D. All filters show an absorbance of over one O.D. in the pass band. The absorbance values in the stop-band were high, as high as 6.25 for Methyl Blue, 3.90 for carbocyanine, and 3.80 - 4.00 for Xylene Cyanol. Several attempts were made to fabricate highly absorbing Remazol Brilliant Blue sesnitised filters, however optical densities higher than 3.0 were never obtained. Furthermore, the absorption maxima were too narrow for short pass filtering. Filters sensitised with methyl blue showed the highest absorbance (O.D. > 6) in the blocking band but also showed the highest absorbance in the pass-band. 1,1'-Diethyl-4,4' carbocyanine iodide shows a broad stop-band which ranges from 550 to 750 nm. However these filters have a very narrow pass-band and the use of these filters are limited to assays with excitation at around 500 nm. Xylene cyanol sensitised filters also have a broad stop-band which ranges from 550 nm to 680 nm and importantly display a broader pass band (450 -510 nm) than other filters, making them attractive for LED filtering applications.

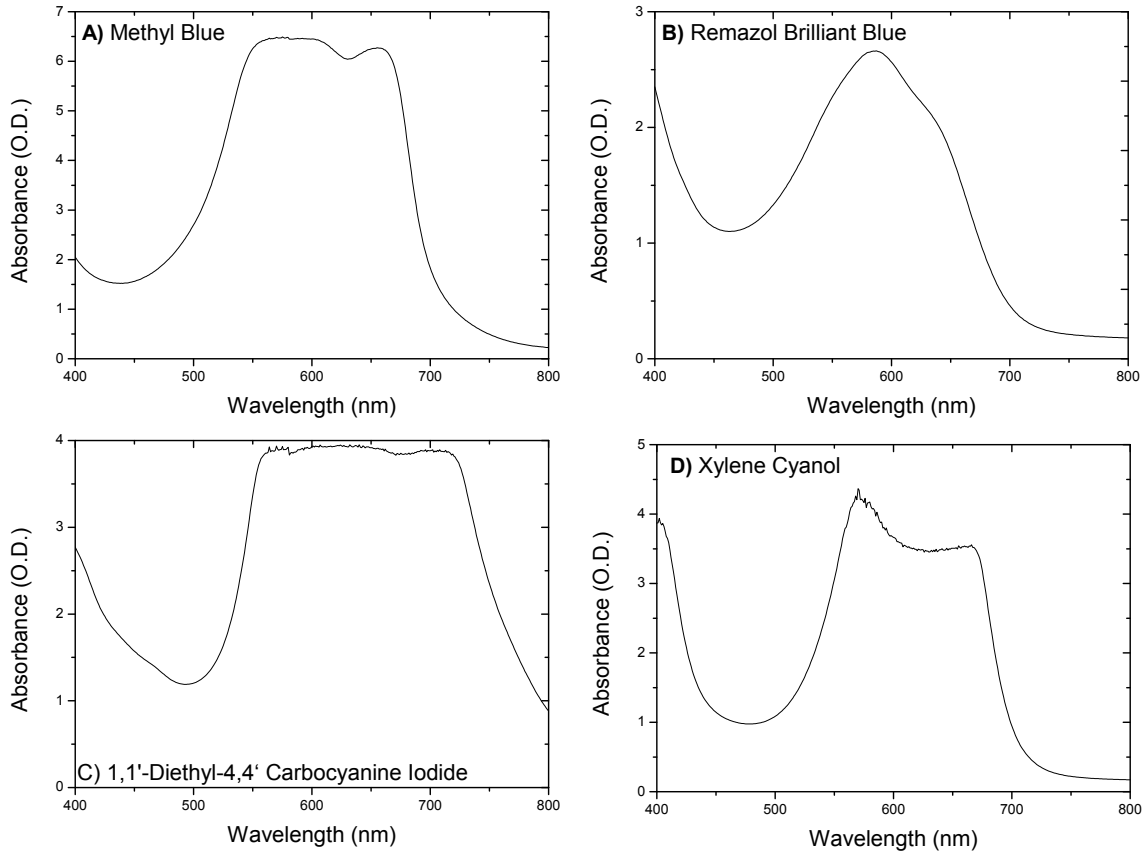


Fig. 3-4 (A) Absorption spectra of four-layer stacked titania films sensitised with Methyl Blue (B) Remazol Brilliant Blue. (C) 1,1'-Diethyl -4,4' Carbocyanine Iodide and (D) Xylene Cyanol.

3.3 Plastic Filters

3.3.1 Introduction

So far, all Ti- filters were prepared on glass by sintering a commercial TiO_2 colloidal paste at 450 °C. Such high sintering temperatures are required to remove the organic surfactant that these commercial pastes contain to achieve the highly nanoporous titania morphology needed for maximising the interfacial area between the titania and the dye, and hence maximising the optical density. However, such high sintering conditions limit the substrate to thermally resilient materials such as glass or quartz and increase cost. Ideally, the titania based filters should be fabricated on plastic substrates, which are more durable, flexible, thinner (hence easier to incorporate into portable diagnostic devices), lighter, cheaper, and offer optical transparency comparable to glass. However plastic substrates melt and decompose at high temperature, and often deform when the glass transition temperature, $T_{g,}$ is approached. Hence an alternative procedure is required for preparing the titania which avoids the high

temperature sintering step. Since titania is extensively used in fabricating dye-sensitised solar cells, which would also benefit greatly from using plastic substrates, there have been many attempts to produce nanoporous titania layers on plastic substrates. Previous methods include the use of a static press to apply 1500 $kgcm^{-2}$ of pressure onto a TiO_2 colloid dispersed in ethanol. However plastic dye-sensitised solar cells fabricated using this method obtained low conversion efficiency due to the thin nature of the resultant films [125] and hence fabricating our filters this way would almost certainly result in filters with low optical density. Another method utilised 28 GHz microwave to rapidly sinter commercially available titanium nano-powders [126]. Although utilising microwave radiation allows thin films to be fabricated extremely quickly (2 min), it is difficult to achieve uniform thickness due to the non-uniform nature of the microwave [126].

More recently, Jeong et. al., demonstrated the use of Plasma Enhanced Atomic Layer Deposition (PEALD) to deposit thin layers of titania onto a polyethersulfone (PES) substrate at low temperature (80 °C) [127] using titanium iso-propoxide as the substrate precursor. This method is effective where an extremely thin layer of the material is required (< 100 nm) however, only lamellar surfaces are produced which limits any surface area enhancement. For the purpose of fabricating filters with high optical density, we require cost effective and simple methods for producing thick titania layers (> 3 µm).

Other low temperature methods include the electrophoretic deposition as reported for instance by Miyasaka et. al., who applied a 200 Vcm^{-1} electric field to a mixture of P25 commercial TiO_2 nano-powder and acetonitrile sandwiched between two ITO coated PET substrates. The process resulted in formation of a formed weak inter-connected titania network and hence showed extremely low conversion efficiency when applied to DSSCs. The films fabricated using this method underwent series of chemical vapour deposition and UV radiation treatment to improve the conversion efficiency [128]. Titania based filters made using this method would require conductive substrates, which would obviously add to the cost.

The simplest method is to use existing titania pastes with a reduced sintering temperature conditions. Longo et. al., were able to produce mechanically stable titania film by sintering the surfactant containing titania gel at 130 °C in dry conditions (low enough for compatibility with PET-ITO substrates) [129, 130]. Dye absorption with films produced at higher temperature was better as demonstrated in the previous chapter. Pichot et. al., demonstrated that stable nanoporous titania on conductive glass can be achieved at low sintering temperature (100 °C) by removing the organic surfactant in the titania colloidal paste and by using a long sintering time (24 h) [131]. However with this

method, only thin films were mechanically stable (< 1 μm). Fabrication on plastic substrates (where flexing of the substrate can cause further instability) was not demonstrated. In the following section, different methods for producing thick titania films on plastic are discussed.

3.3.2 Fabricating filters on Plastic Substrates

3.3.2.1 Types of Plastics available

Regardless of its fabrication process, the plastic employed should be transparent in the visible region of the electromagnetic spectrum. Also, the choices of plastic used for the base substrate depends on the conditions needed to deposit nanoporous titania. The plastic should be cheap and readily available in thin film. The following plastics satisfy our core criteria: Poly vinyl chloride (PVC) film, Polyethylene terephthalate (PET), Polycarbonate (PC), and Acetate film. The PVC and PET films are readily available; they have good optical transparency, and have good chemical resistance. However, both plastics start deform at 70 °C which limits their use to room temperature fabrication processes. The only plastic that was investigated with high deformation temperature was PC. However PC films available commercially were thick (0.75 mm) and had limited flexibility. Acetate films are available in the form of adhesive tapes and were used as a sealant for our flexible plastic filters.

3.3.2.2 Using Conventional Paste

The pastes used in the previous chapter supplied by Nanopac (WA-15DPT) contains organic surfactant materials such as ethylene glycol to enhance the porosity of the sintered film. The organic additives act as a scaffold for the nanoporous structure [131] and are designed to be 'burned-off' at high temperatures. High sintering temperatures also help titania to form inter-particulate networks which enhances the mechanical stability and the electrical conductivity of the films (although latter is not a requirement for our purpose). However, previous studies have shown a degree of mechanical stability in films fabricated without any organic surfactants which raises the question whether surfactants are really needed for the purpose of producing filters [131]. Before completely ruling out the use of conventional pastes in fabricating plastic filters, other low temperature methods (other than sintering) for removing organic additives were evaluated.

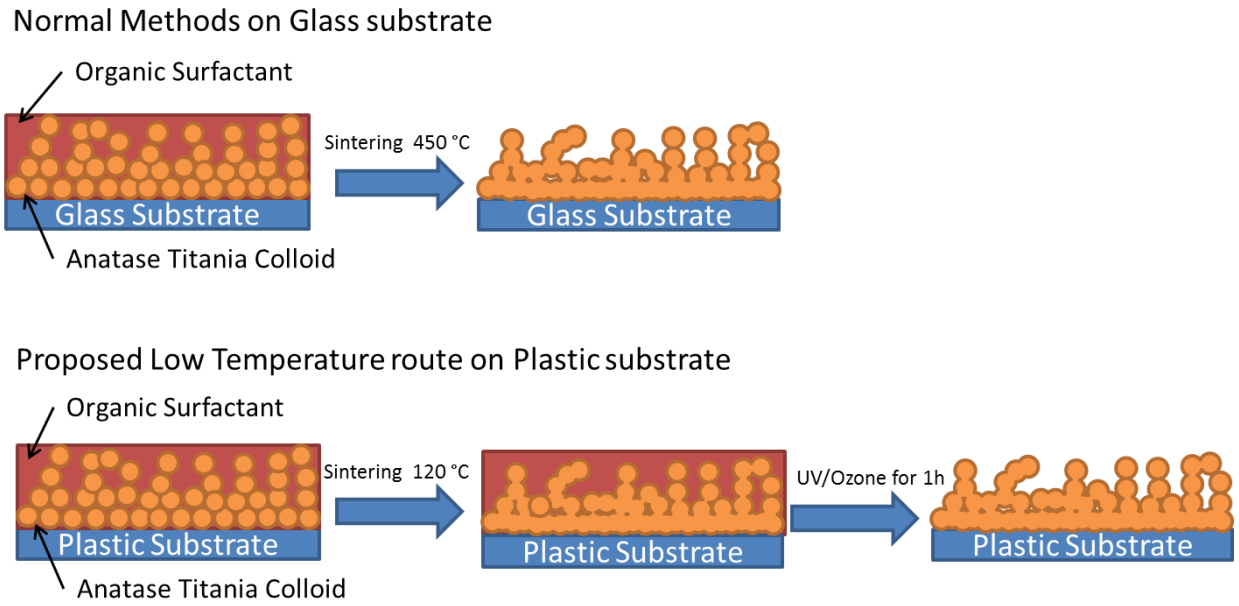


Fig. 3-5 Proposed low temperature fabrication steps for using conventional paste.

First we method we utilised examined a combination of low temperature (120 °C) sintering to form the inter-particulate titania network, followed by UV/ozone treatment to remove the organic content (Fig.3-5). Work by Clark et. al., had shown this to be an effective way to remove organic content from silica pastes to form mesoporous films at low temperature [132]. Other studies have shown that UV treatment of nanoparticulate titania films in air induces interconnection of the nanoparticles and removes the organic additives [133]. The removal of the organic additives can be attributed to the photocatalytic activity of titania under UV irradiation. Interparticulate connections formed under UV irradiation can be explained by the formation of hydrogen peroxide from the reaction of ozone (produced photocatyltically with water or supplied through O_3 treatment) with water absorbed on the surface of titania. Decomposition of hydrogen peroxide yields OH or –OOH radicals, which can react with the surface Ti^{3+} ion to form surface hydroxyl groups, that form interconnected titania via a series of oxolation reactions [133, 134].

Three separate methods were tried and compared against films that were prepared on glass substrate and sintered at 450°C:

1: Titania film prepared on plastic substrate with 120 °C sintering.

2: Titania film prepared on plastic substrate sintered at 120 °C, followed by UV/O_3 treatment.

3: Titania film was treated with UV/O_3 first, then followed by sintering at 120 °C.

In experiments 2&3, films were exposed to UV/O_3 treatment for 1h. With all experiments conducted, the resulting films were immersed in a 0.01 M ethanolic solution of FDS for 24 h and then washed repeatedly with ethanol to remove any unattached dye molecules before being dried in a stream of nitrogen. Absorbances of the filters were measured as described in chapter two.

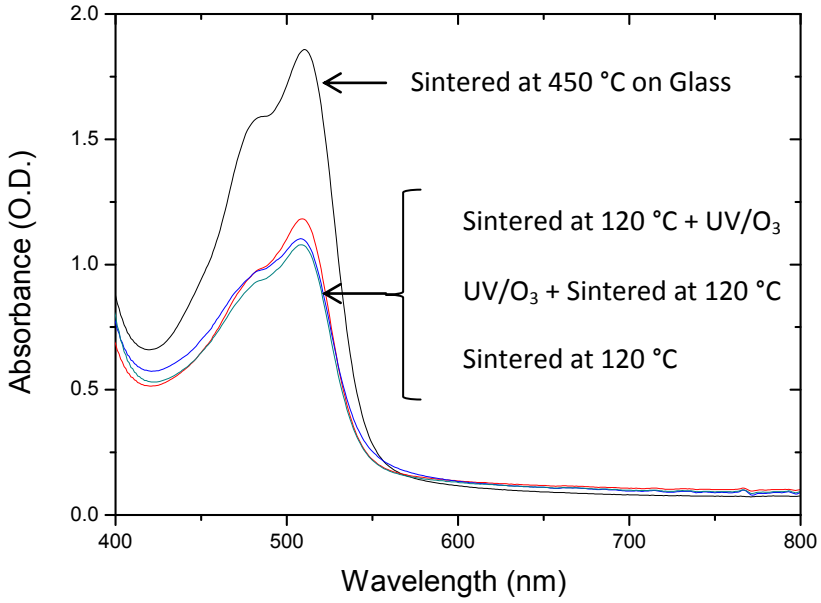


Fig. 3-6 Filters fabricated using conventional paste on **A**) glass with 450 °C annealing, **B**) plastic substrate (PC) with 120 °C followed by UV/O_3 treatment, (**C**) PC with UV/O_3 treatment first followed by 120 °C sintering, and D) PC with 120 °C sintering only. In all cases precursor from Nanopac, which contained surfactants was used.

Fig. 3-6 shows the absorbance spectra of the filters fabricated using the various methods. As expected, filters prepared on glass at 450 °C had the highest O.D. and showed the best dye loading. Plastic filters without the UV/O_3 treatment had the weakest dye loading and recorded a mere O.D.1 at 500 nm. It is evident that the sintering temperature was not sufficiently high to remove the organic content, presumably forming flat surfaces of the kind shown in Chapter two section 2.3.1. We did not observe any significant improvement (1% increase in O.D. at 500 nm) in dye loading for films treated with UV/O_3 before the sintering procedure, which implies that the UV/O_3 treatment is not effective in forming a porous titania layer. It is also possible that treating the film with UV/O_3 removes the organic surfactants and so upon sintering allows the titania colloids to coalesce into a flat surface.

Slightly better performance of 10 % increase in O.D. at 500 nm was observed when the precursor was sintered first and UV/O_3 treatment applied afterwards. This can be attributed to the formation of a slightly more porous surface. However, plastic filters fabricated using this method displayed poor mechanical stability and formed cracks when the substrate was flexed (Fig. 3-7). In all cases, the

absorbances of the filters were in the region of O.D. 1 – 1.2 at 510 nm, which is rather low for filtering applications.



Fig. 3-7 Ti-Short pass filter fabricated by 120 °C sintering followed by UV/O_3 treatment. The filter showed poor mechanical stability with the titania layer cracking and flaking off upon flexing the filter

3.3.2.3 Using Surfactant Free (SF) Paste

A study by Barbe et. al., showed that increasing the concentration of the organic surfactant in the paste increases the final porosity of the sintered film [135]. This effect is attributed to the dilution of the titania content of the paste, meaning that upon sintering fewer colloids form an inter-particulate network. This causes the titania layer to form more voids, and hence increases its porosity. However, we have shown that filters fabricated via the low temperature route have lower dye adsorption compared to filters fabricated at normal conditions. To avoid this, filters were fabricated from surfactant-free titania paste (Solaronix SA, Switzerland) using the standard doctor-blading technique (see chapter two). Titania filters made from SF pastes were also fabricated without sintering for purposes of comparison.

In general, the filters prepared with SF pastes had improved blocking (O.D. 1.4 at 500 nm) properties compared to films prepared with conventional paste using low temperature conditions. It is evident from Fig. 3-8 that the sintering temperature did not have any significant effect on the final absorbance of the filters. This is not surprising, since in the case of using SF pastes, the sintering process is only used to form inter-particulate network between the titania colloids. Interestingly, filters subjected to sintering were fragile and delaminated from the substrate when bent. Titania films prepared without sintering were more mechanically stable – a possible consequence of positively charged TiOH groups in the titania binding electrostatically to carbonyl groups on the PC substrate,

increasing adhesion. (The hydroxide groups are lost after prolonged heating) [136]. This was also the case in non-sintered titania films prepared on PET substrate. As is clear from Fig. 3-8, there were no differences in absorbance between the sintered and non-sintered FDS sensitized titania. Although filters fabricated on plastic have inferior blocking properties compared to those prepared by high temperature sintering of a surfactant-containing paste, they are significantly easier to handle i.e. they are much thinner, more robust, and can be 'cut' to desired dimension. Furthermore, for the purposes of fabricating optical filters, interconnectivity of the titania substrate is not a concern since the quenching occurs at the dye-titania interface. All filters described hereafter were fabricated from SF pastes without sintering, using PET as the base substrate (since it is cheaper and easier to handle than PC). The key fabrication steps for the plastic titania filters are summarised in Fig. 3-9.

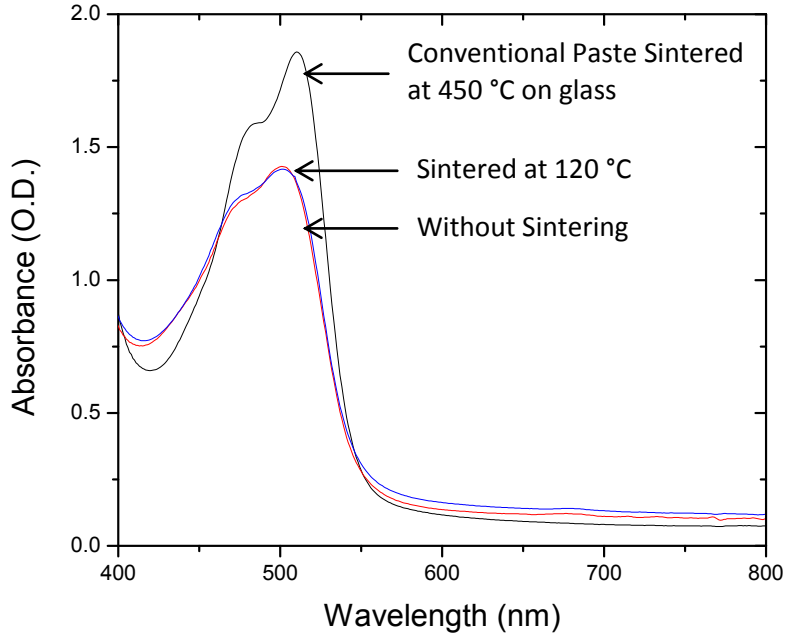


Fig. 3-8 Filters fabricated using conventional surfactant-containing pastes + 450 °C annealing on glass substrate, surfactant free paste with 120 °C annealing on plastic (PC), and surfactant free paste with no annealing on PC.

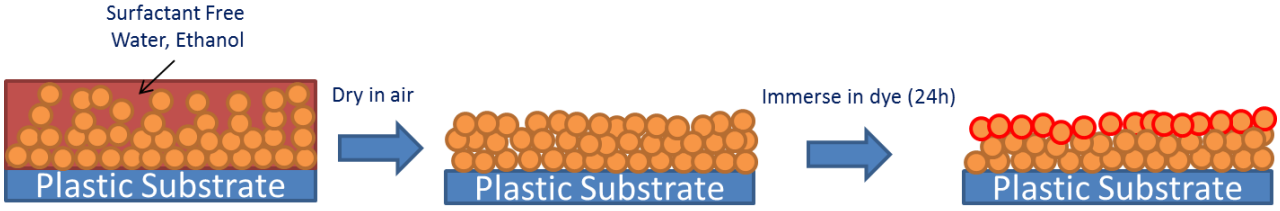


Fig. 3-9 Schematic to show the new filter fabrication steps on plastic substrates [137]. Additional titania surface charge moderation step may be necessary depending on the sensitizer.

3.3.2.4 Using Acetate tape as a Sealant

Once made, the plastic filters were encapsulated with adhesive acetate tape (3M) under N_2 atmosphere. Encapsulating the filter with such tape provided adequate protection from the atmosphere and improves film stability. This method also avoids the use of UV-curing and provids a cheap/ facile route to encapsulating the sensitised titania.

Fig. 3-10 shows the absorption spectra of tape-encapsulated titania short- and long-pass filters exposed to 0.04 $mWcm^{-2}$, 500 nm monochromatic light over the course of three hours. The experimental setup is the same is described in chapter two. The spectra show minimal changes and it is evident that encapsulating the filters with acetate tape provides effective (short-term) protection against photo-degradation. However a slight photo-degradation of the Ti-FDS filters was observed at a rate of approximately O.D. 0.015 h^{-1} which equates to approximately 50 h half-life at the test conditions. However the stability of the filters is certainly adequate for their use in low-cost diagnostic applications.

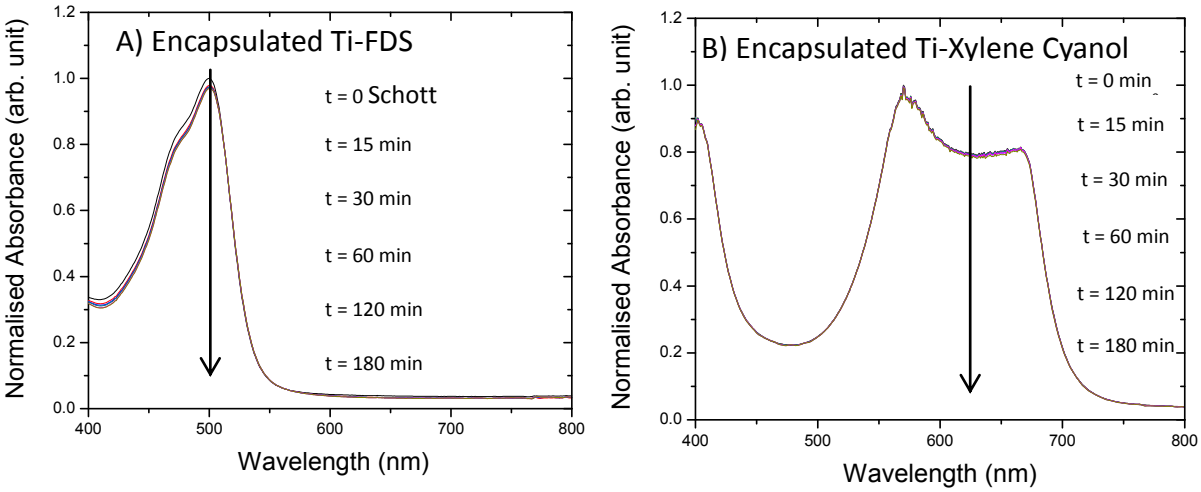


Fig. 3-10 Normalised Absorbance of A) acetate tape encapsulated Ti-FDS filters and B) Ti-Xylene Cyanol filters over a period of 3h under continuous illumination by 500 nm monochromatic light.

3.3.2.5 New Screen Printing Format

Use of our original screen printing procedure with the SF paste, yielded titania films of non-uniform thickness, ranging from approximately 1 µm to 3 µm on the same substrate, with thicker titania at the edge. This was attributed to the high water content of the SF paste, which forms a denser layer at the taped edge due to surface tension. A commercial coater was used in an attempt to produce more uniform films, but the supplied wire-wound coater bar were not smooth and prevented titania pastes from being spread evenly. To produce uniform titania film, a new screen printing format adapted from a commercial K-hand coater was applied (RK Printcoat Instruments, UK) and utilised (Fig. 3-11).

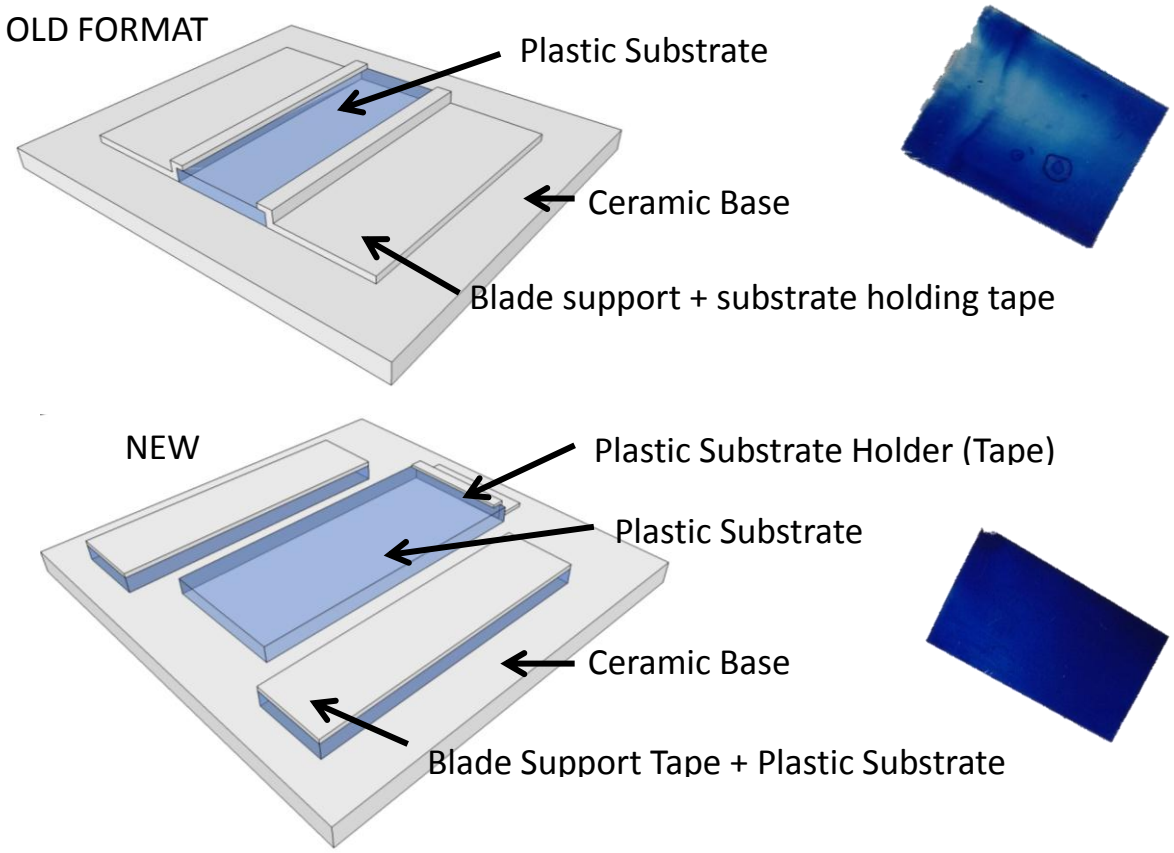


Fig. 3-11 Schematic to show the new doctor blading format used to fabricate uniformly sensitised titania plastic filters. The new format allows the titania to dry with uniform thickness. Inset shows a plastic Xylene Cyanol sensitized short pass filter fabricated using both the old and the new doctor blading formats

3.3.2.6 Summary

The method established to produce titania filters on plastic is summarised below:

1. SF titania paste (Solaronix SA, Switzerland) was screen printed onto a PET substrate using the new doctor blading format (Fig.3-11) and dried gently in a stream of N_2.
2. Dried substrates were then immersed in a 0.01 M ethanoic solution of FDS (for long-pass) or Xylene Cyanol (for short-pass) for 24 h.
3. The resulting sensitised films were washed repeatedly with ethanol, and dried again with N_2.
4. This dried film was placed in a N_2 atmosphere and encapsulated using adhesive 3M acetate film.

3.3.3 Autofluorescence measurement of the Plastic Filters

3.3.3.1 Autofluorescence measurement

In this section, the autofluorescence of short- and long-pass filters prepared on plastic were measured using the same experimental set up described in chapter two, section 2.6. As with the glass filters, four layers of plastic filters were stacked to achieve sufficient blocking of the excitation light. A 15 min integration time was again used to record the weak emission from the titania-based filters. FDS titania filters were illuminated with 442 nm, 1 mW HeCd. Xylene Cyanol titania based filters were illuminated with 0.5 mW HeNe Laser (633nm).

The absolute fluorescence signals for the plastic filters are shown in Fig. 3-12 and compared against a commercial Schott glass filter OG530. The absolute fluorescence intensity for the Schott OG530 filter was approximately 30,000 times more intense, than the Ti-FDS and Ti-Xylene Cyanol sensitised filters. It is evident that the autofluorescence quenching mechanism remains effective for the filters fabricated on plastic.

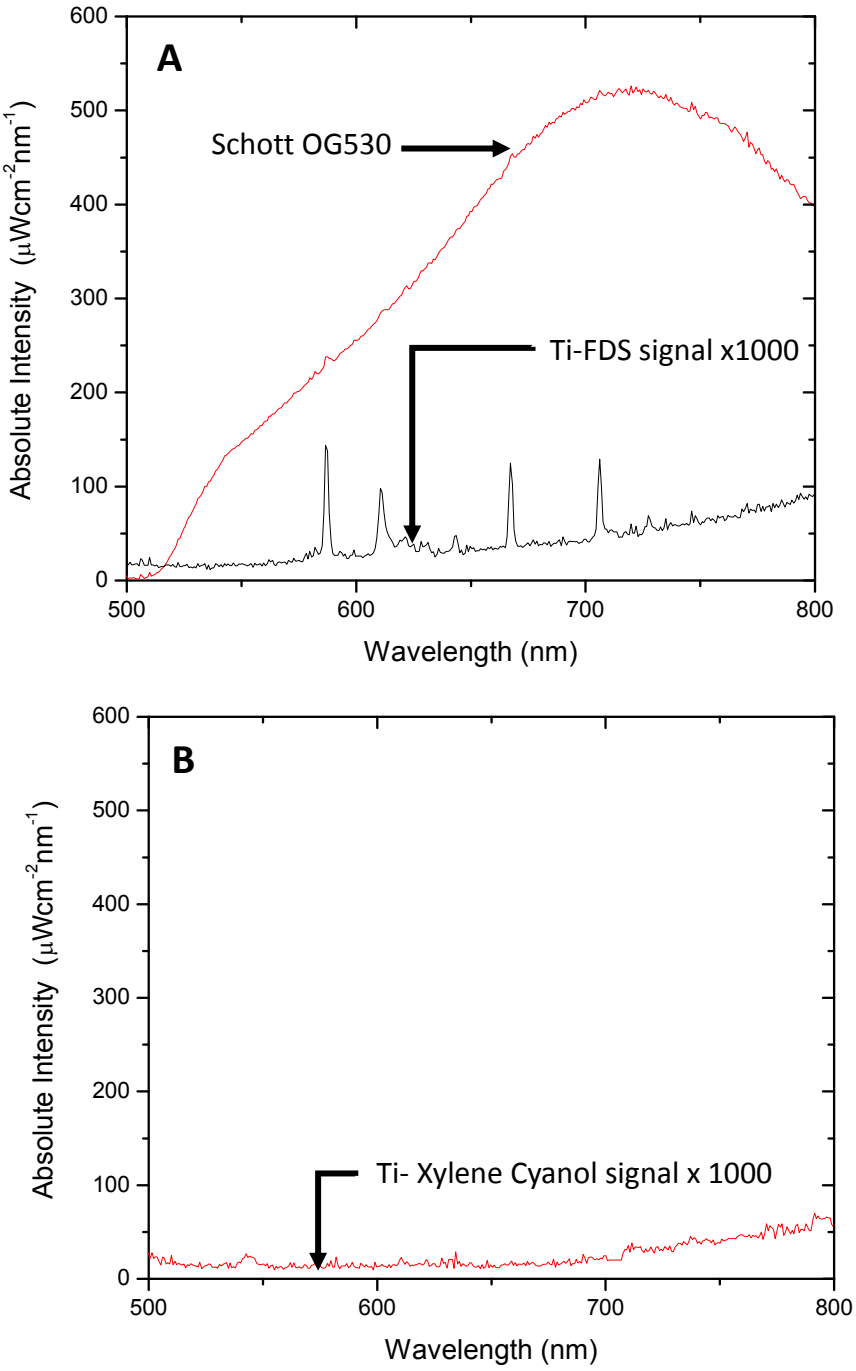


Fig. 3-12 (**A**) Autofluorescence spectra for an unsintered Ti-FDS long-pass filter on PET under 1 mW 442 nm HeCd excitation. Also shown for reference is a commercial Schott glass filter obtained under identical conditions. (**B**) Autofluorescence spectra for an unsintered Ti-XC short-pass filter on PET under 0.5 mW 633 nm HeNe excitation. All other acquisition conditions were the same. Spectra for the titania-based filters have been enlarged by a factor of 1000 for clarity.

3.4 Transfluosphere Detection

3.4.1 Testing the Plastic Short Pass filter with Transfluosphere

To evaluate the effectiveness of the long and short pass (LP & SP) plastic filters for fluorescence detection, a spectrally compatible transfluosphere bio-label T-8861 (Invitrogen ex:488nm em:605nm) was used. Emission and excitation characteristics for the beads are shown in Fig. 3-13. The peak of the absorption spectrum is at 500 nm, and the peak of the emission spectrum is at 600 nm.

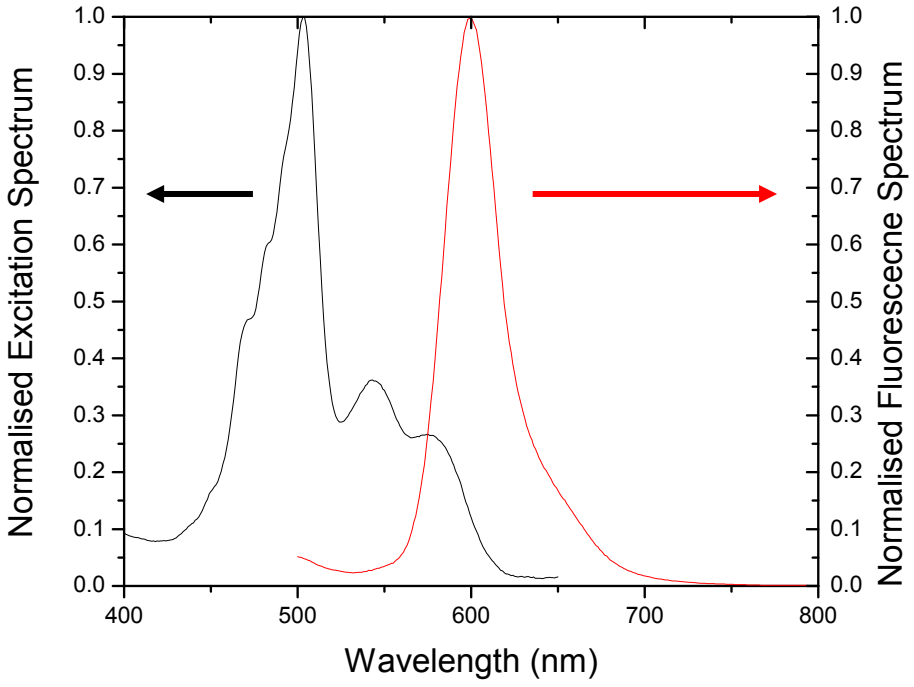


Fig. 3-13 Excitation and Emission spectra of the T-8861 Transfluospheres

The absorption characteristics of the short- and long-pass filters are shown in Fig. 3-14. The short-pass filters absorb strongly in the wavelength range 525 to 650 nm, which corresponds closely to the emission range of the beads. The long-pass filters block wavelengths up to about 525 nm and hence the transfluosphere can be excited at its maximum absorption wavelength. T-FDS and Ti-Xylene Cyanol filters have good spectral compatibility with the transfluospheres.

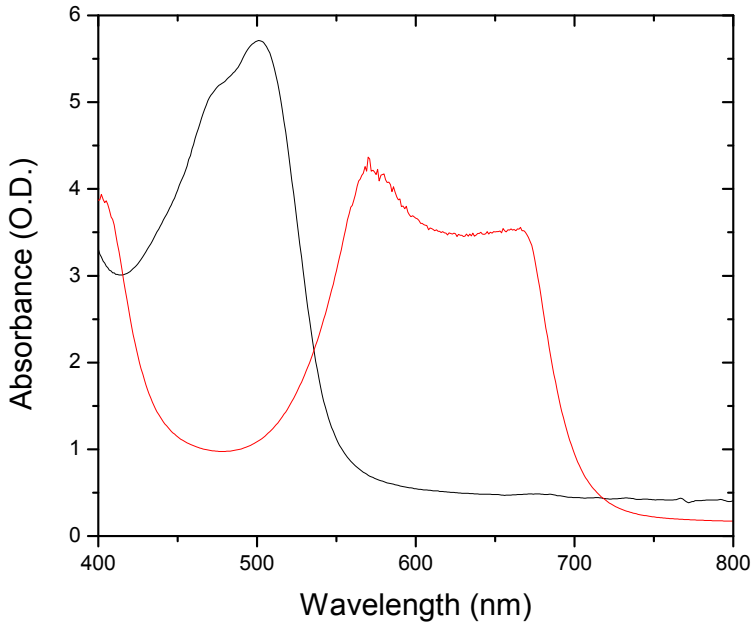


Fig. 3-14 Absorption spectra of FDS-sensitised titania long-pass filter and Xylene Cyanol- sensitised titania short-pass filter.

To fully mimic portable point-of-care devices of the kind described in chapter one, a simple test device, (see Fig 3-15A and photo's in Fig. 3-15B) was constructed from sheet plastic. It houses a standard 9V Battery (Duracell rechargeable 9V Battery, Duracell, UK), a 505 nm cyan LED (Luxeon REBEL LED Cyan, Philips Lumileds Lighting, N.V.) driven at 20 mA, and a silicon photodiode (S1226-8BQ, Hamamatsu, Japan). The photodiode is coupled to a (LabVIEW, controlled) Keithley 6485 electrometer to monitor and record the photocurrent. All measurements were carried out in the dark unless otherwise specified. The device also housed a stack of four Ti-XC films for short-pass filtering, a holder for 1 mm path-length cuvette, a stack of four Ti-FDS films for long-pass filtering.

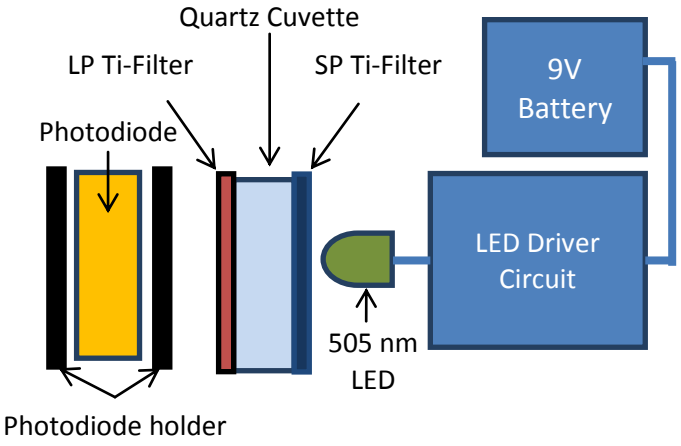


Fig. 3-15A Simple schematic diagram of the sheet plastic constructed test device

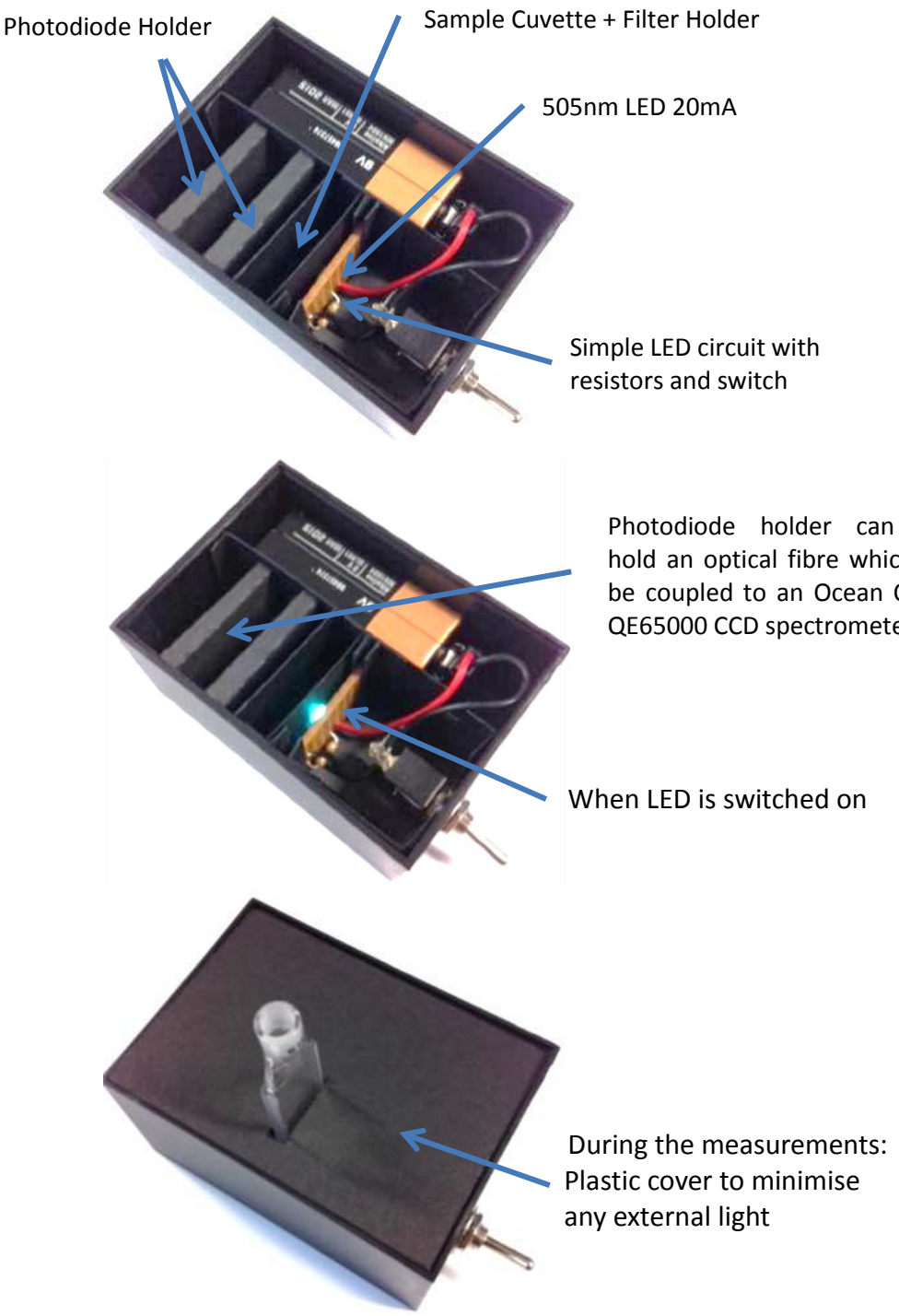


Fig. 3-15B Pictures of the test device used to measure the transfluosphere signal

Fig. 3-16 shows the emission characteristics of the LED, with and without a single short-pass filter in place. This measurement was taken by replacing the photodiode in the test device with a fibre optic coupled CCD spectrometer (QE65000, OceanOptics). Whilst causing a moderate (50 %) reduction in the peak intensity, the short-pass filter results in a distinct sharpening of the emission characteristics,

removing the problematic long tail beyond 525 nm that would otherwise overlap the emission from the transfluospheres beads. There is weak leakage of LED light beyond 700 nm due to the finite width of the short-pass filter's stop band. The inset photograph shows the appearance of the LED light after passing through the short-pass filter.

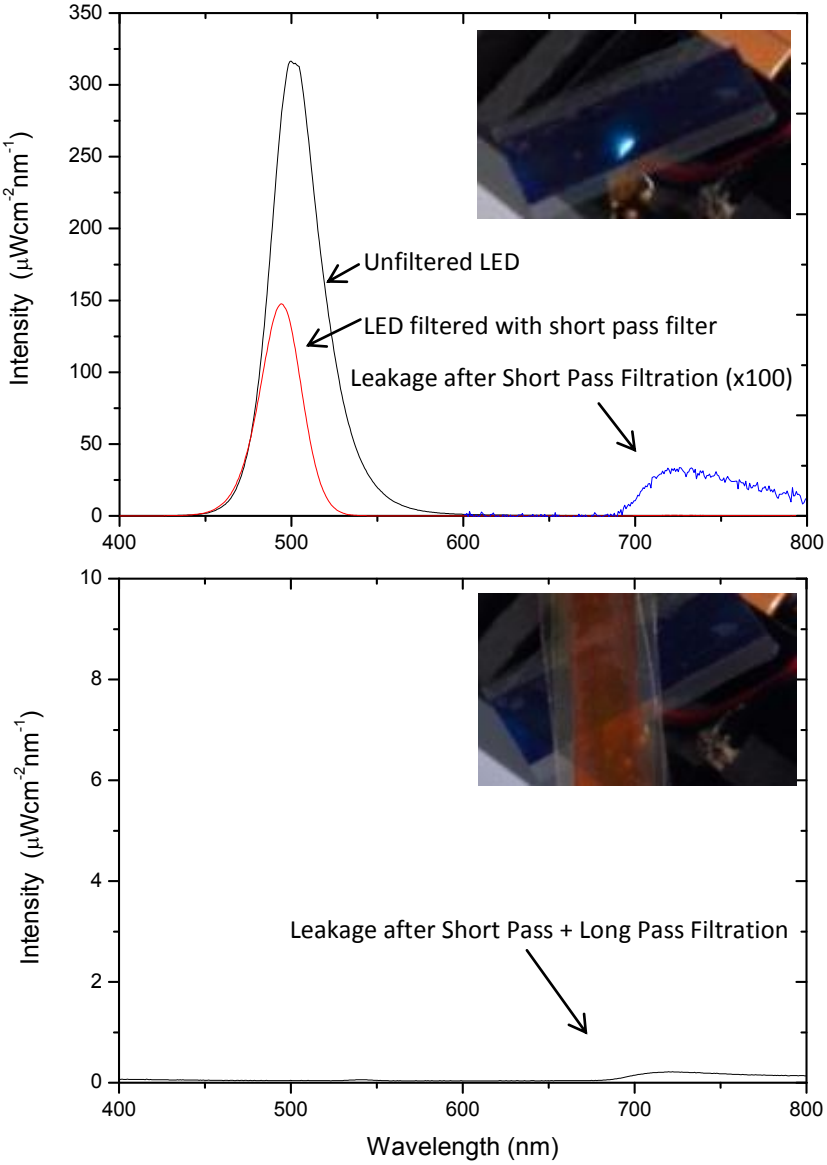


Fig. 3-16 (**Top**) Optical characteristic of the cyan LED (505nm) measured with a fibre-optic coupled CCD spectrometer. Inset picture and the spectra also show the LED with a single Xylene Cyanol sensitized glass Ti-short pass filter (**Bottom**) – Spectrum shows effective blocking of the cyan LED light up to 670 nm by using both the short and long pass filters. Inset picture shows no apparent light leakage.

Transfluosphere beads were diluted with water from the original aqueous beads suspension of $1x10^{10}$ beads μl^{-1} in distilled water and identical 1 mm cuvettes containing different concentrations of Transfluosphere beads were prepared. The concentration of the solutions ranged from $1.0x10^{5}$ to $1.0x10^{9}$ beads μl^{-1}. Signals were averaged over 100 readings and corrected for the signal obtained with a blank cuvette containing water only. Fig. 3-17 shows the corrected signal versus bead concentration.

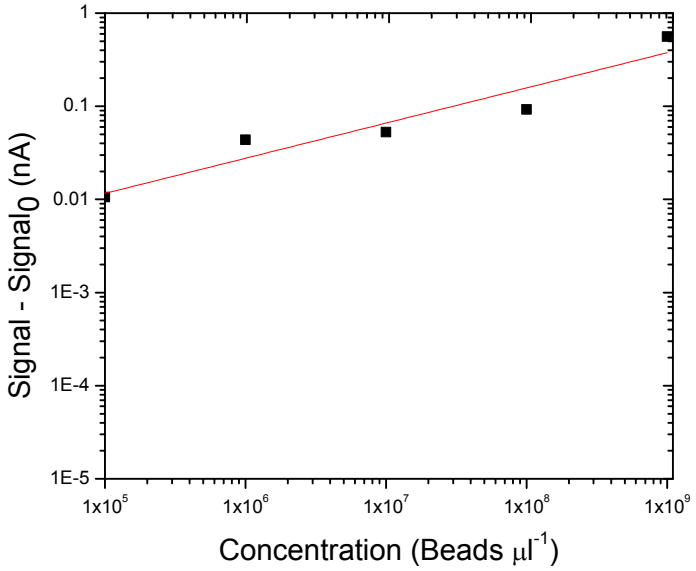


Fig. 3-17 Signal versus transfluosphere bead concentration using titania short and long pass filters. The measurement set up is shown in Fig. 15A.

As defined in chapter two, section 2.7, taking the limit of detection Λ as the concentration of analyte that yields a signal equal to the *y*-intercept plus three times the standard deviation of the blank, we obtained $\Lambda = 2.06 \times 10^{7}$ beads μl^{-1}. Considering that the stock bead concentration was $1.0x10^{10}$ beads μl^{-1}, the obtained limit of detection was comparatively poor; only accurately detecting hundred-fold dilution relative to stock solution and a typical assay would be expected to detect up to 100,000 fold dilution of the analyte. Initially, it was thought that this result could be attributed to the 'flimsy' nature of the sample/filter holder, which causes shifts in the alignment of the optical parts when changing the sample cuvettes. A more secure sample/filter holder was therefore constructed.

3.4.2 Machined Testing Rig

To address the need for a robust, rigid testing rig, sample holders were machined from a block of aluminium where the detector – light source configuration have been kept the same (Fig. 3-18). Additionally, the photodetector was housed in a plastic block, which was machined to be in direct line of

sight of the LED light source. Removable filter holders were also machined from aluminium for both the short- and long pass filters. The new rig was placed in a vice for added stability and the LED light source was driven at 20 mA with a 9V Battery.

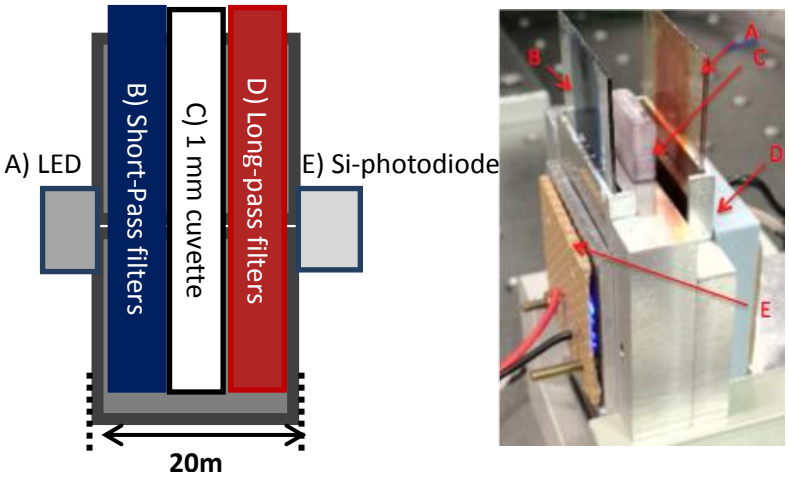


Fig. 3-18 Left (**A**) -505 nm LED (20 mA) connected to a 9 V battery supply. (**B**) - Plastic Short pass filter inserted in a filter holder. The short pass filter is placed directly in front of the LED light source. (**C**) - Quartz cuvettes containing the transfluosphere solutions are placed in the cuvette holder. The holder is machined so that cuvettes are held tightly. (**D**) - Plastic Long pass filter inserted in a filter holder. The Long pass filter is placed directly in front of the detector. (**E**) – silicon photodiode connected to Keithley electrometer. Right – photograph of the machined rig.

Fresh Transfluosphere solutions were prepared and all experimental details, except for the rig setup remained unchanged. Despite the improved mechanical stability, scatter in the obtained data was still high and the linearity remained poor, and only a slight improvement in the limit of detection was observed with $\Lambda = 1.49 \times 10^7$ beads μl^{-1} (Fig. 3-19).

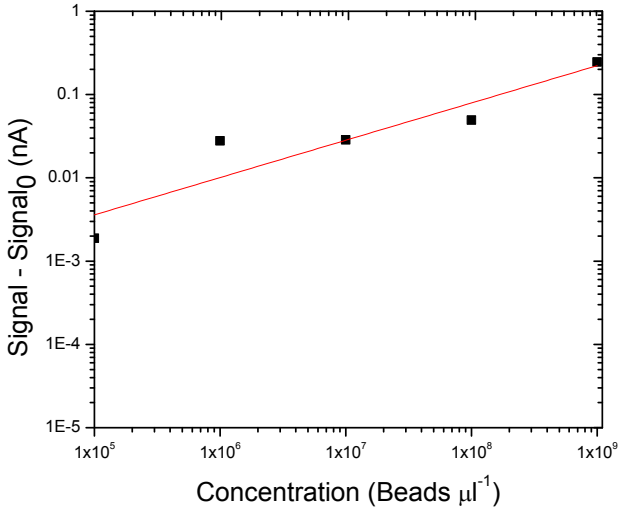


Fig. 3-19 Signal versus transfluosphere bead concentration in distilled water using the machined rig and titania short- and long-pass filters.

Upon comparing the data obtained using the original plastic rig and the newly machined rig, we found a striking similarity in the observed behaviour. This trend can be seen more clearly on Fig. 3-20, which highlights the sudden signal drop at low concentration of transfluosphere beads.

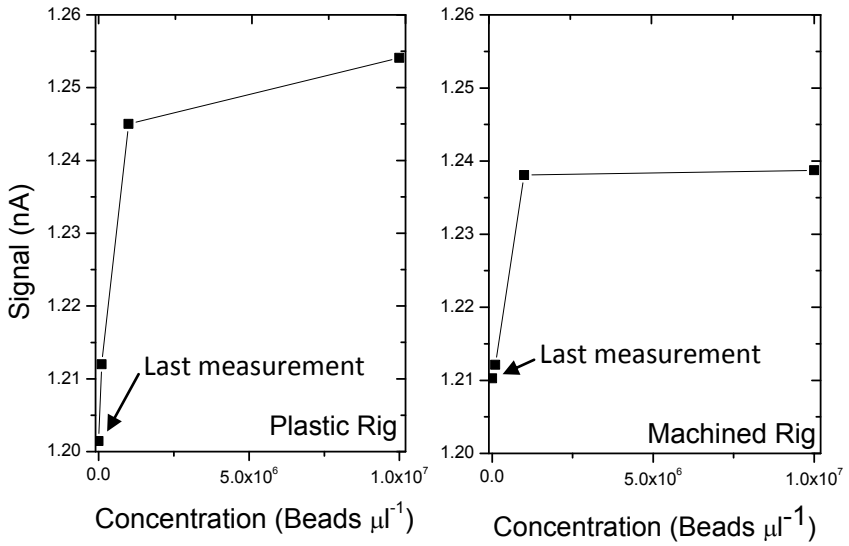


Fig. 3-20 Signal versus concentration of transfluosphere in distilled water. (Left) using the original plastic rig and (Right) Using the machined rid. The graph is plotted on a linear scale and focuses on the low concentration region.

Furthermore, a steady decrease in signal was observed at all concentrations during the acquisition. The cause for this phenomenon was found to be a drift in LED light intensity over time (Fig. 3-21). With LEDs or any other diodes, current is an exponential function of voltage and hence any change in voltage results in a large current change. During the discharge cycle, the battery voltage decreases, causing a significant change in LED light intensity overtime. To circumvent this drift, a simple constant current circuit was designed and incorporated into the LED driver (see appendix, section 7-1). Also the power source was switched from a 9V battery to a DC power supply. Using the same rig with the constant current LED driver, the intensity of the LED light was measured over time. Fig. 3-21 shows the comparison of the LED intensity with and without the constant current LED driver, normalised to their maximum light intensity. Under constant current drive the signal is stable with only slight fluctuations (±0.0018%) while under battery driven "constant voltage" operation it shows a gradual signal drain (note, that the scale on Fig 2-21A is small, specifically - 0.35% over 600 s with substantial instantaneous fluctuations. This shift due to the shifting background can drastically affect the measurements at lower concentration. Fluctuations in signal were also observed with D.C. power supply in constant voltage mode, which again highlights the importance of incorporating a constant current LED driver (fig 3-21).

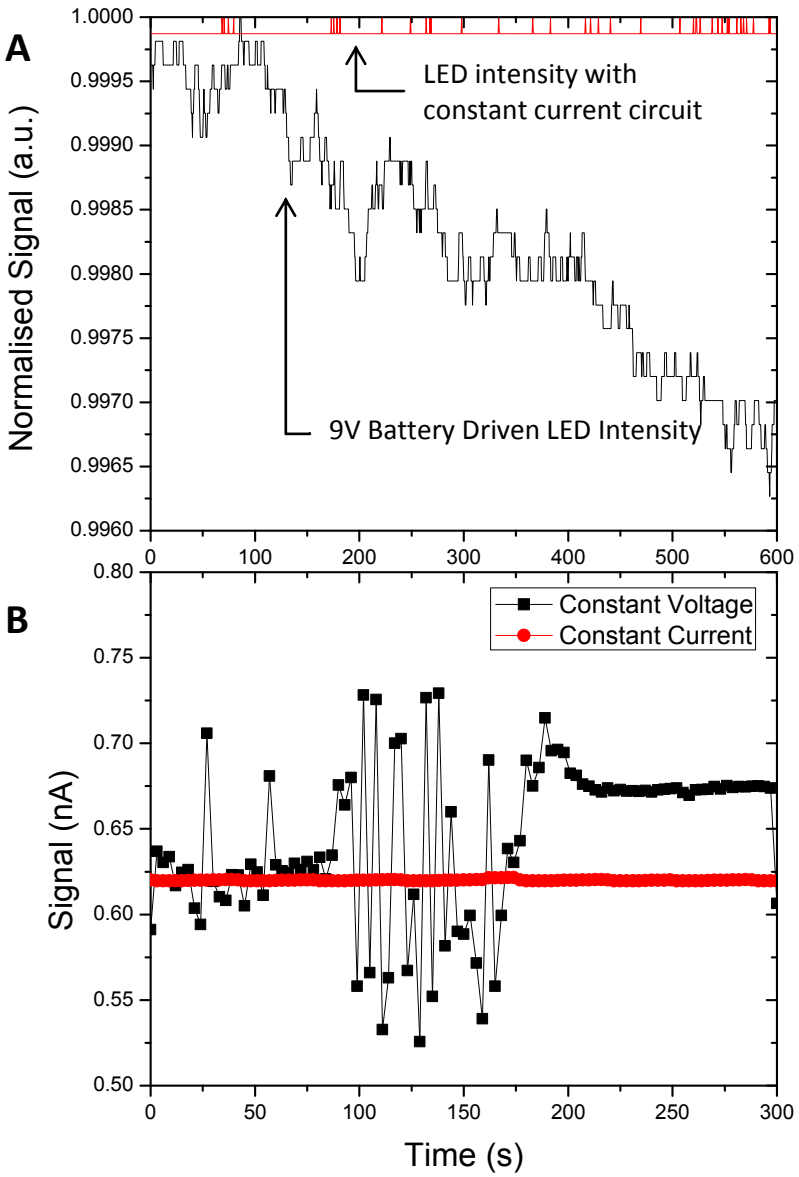


Fig. 3-21 (**A**) Variation in LED intensity with time under battery operation and constant current operation (**B**) Signal intensity for $1x10^9$ beads μl^{-1} using LED driven with a power supply at constant voltage and current over 300 s time period.

3.4.3 Machined Testing Rig with Constant Current LED Driver

Using the constant current LED driver yielded a dramatic improvement in linearity, the problematic signal drop at low concentrations was no longer observed, and the limit of detection, Λ, improved to $= 1.56 \times 10^6$ Beads μl^{-1} or ten thousand fold dilution relative to the original bead concentration (Fig. 2-22) However despite the evident improvement, due to the exposed nature of the setup, it was still vulnerable to sudden changes in background signal, due to changes in the ambient lighting which could adversely affect the limit of detection. This effect is shown on Fig. 3-23 where the

reading was repeated in a fully lit room. A background signal of 20.5 nA was recorded and this was approximately 45 times larger than the background signal recorded in the dark. In accordance with expectation, measurements performed in the light resulted in a significantly worsened LOD of 4.53 x 10^8 beads μl^{-1}. This therefore indicates a clear need for a signal acquisition method that is not affected by any changes in the background signal.

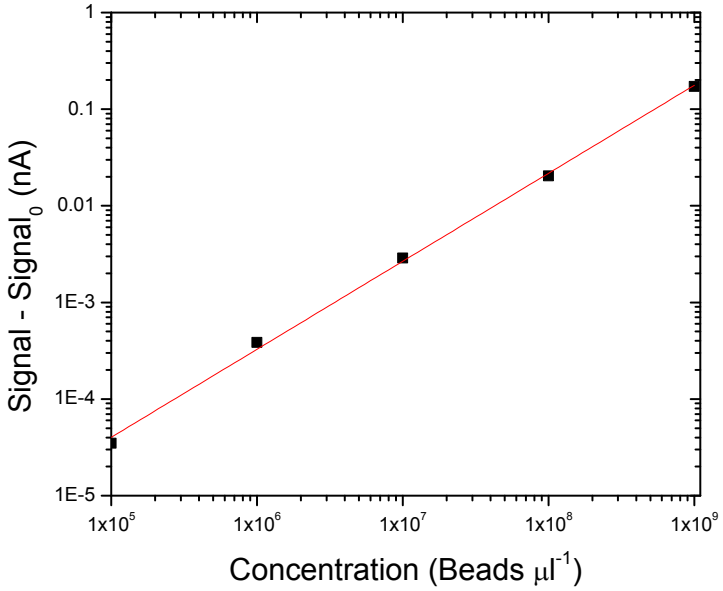


Fig. 3-22 Signal versus transfluosphere bead concentration in distilled water using the machined rig and titania short and long pass filters. The LED is driven with a homemade 20mA constant current driver. The graph is plotted on a log-log scale.

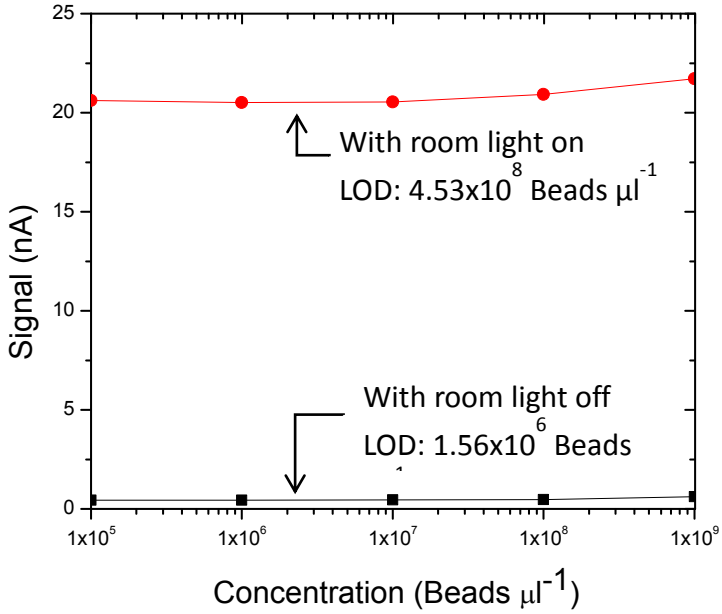


Fig. 3-23 Signal versus concentration of transfluosphere in distilled water using the machined rig and titania short- long pass filter. The LED is driven with an in-house 20 mA constant current driver.

3.4.3.1 Pulsed Constant Current LED Driver and Lock-in Amplifier

A lock-in Amplifier (LIA) is commonly used to detect and measure very small AC signals. Highly accurate measurements can be made even when the signal is obscured by an overwhelming background noise that may be many orders of magnitude larger. Lock-in amplification uses Phase-Sensitive Detection (PSD) to single out the signal at a specific frequency and phase. Hence, any background noises that have different frequency or phase to the input signal are rejected. Measurements using LIAs require a reference frequency that typically matches the frequency of the excitation source. In Fig. 3-24 the reference signal is a cosine wave at frequency ω_R.

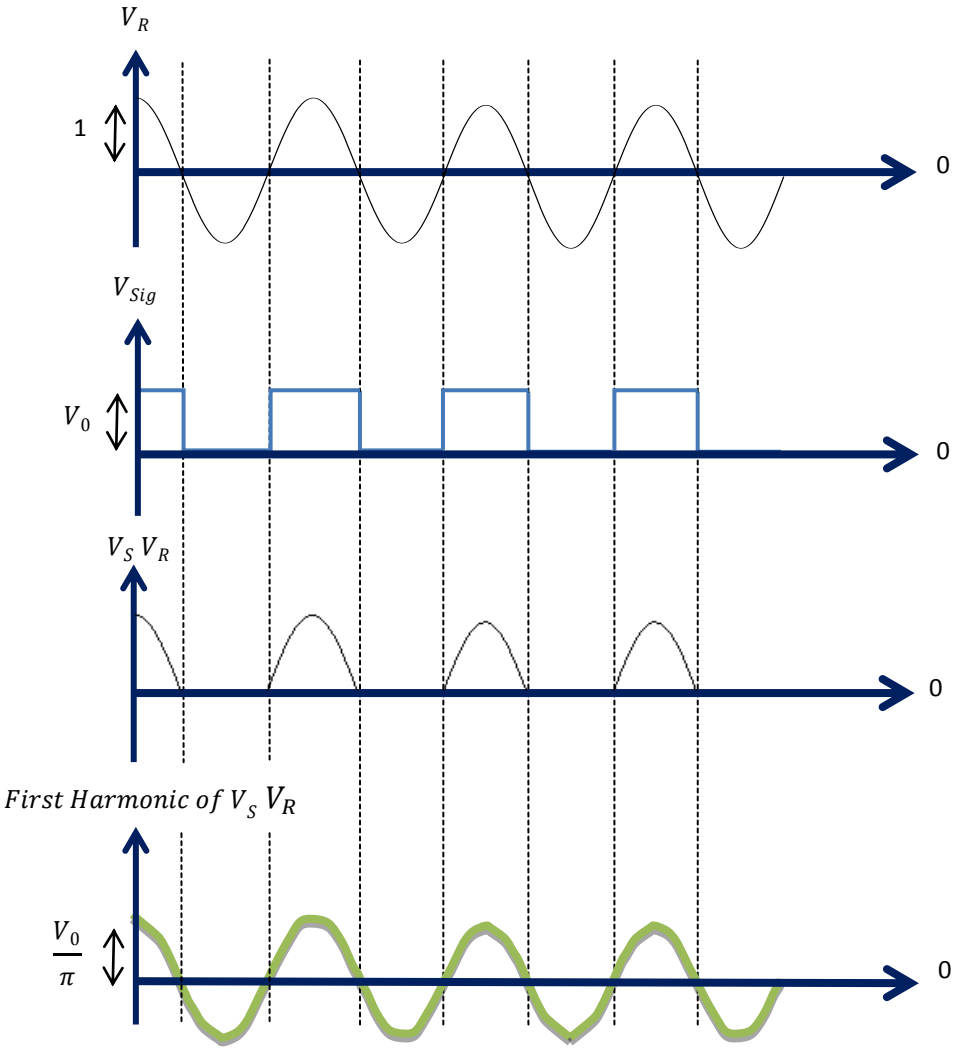


Fig. 3-24 Diagram to show the output response of a phase sensitive detection with cosine reference waveform and a square-wave signal waveform. More details in equation 3A-3F.

PSD in the LIA multiplies the measured signal by a reference cosine wave at the modulation frequency and then passes the product through a low-pass filter. To briefly demonstrate how a PSD work, consider that we have a square wave input signal, $V_{sig}(t)$ with frequency, ω. Using fourier series, decomposition of the waveform can be written as:

$$V_{Sig}(t) = V_0\left[\frac{1}{2} + \frac{2}{\pi}(\cos\omega t - \frac{1}{3}\cos 3\omega t + \frac{1}{5}\cos 5\omega t \ldots)\right] \quad (3A)$$

which can be written:

$$V_{Sig}(t) = \left(\frac{V_0}{2}\right) + \left(\frac{2V_O}{\pi}\cos\omega t\right) - \left(\frac{2V_0}{3\pi}\cos 3\omega t\right) + \left(\frac{2V_0}{5\pi}\cos 5\omega t\right) - \cdots \quad (3B)$$

We also have a reference signal at frequency, ω_R :

$$V_R(t) = \cos\omega_R t \quad (3C)$$

Product of the two when both frequencies are the same ($\omega = \omega_R$) gives:

$$V_{Sig}(t)V_R(t) = \left[\frac{V_0}{\pi}(cos\omega t)\right] + \left[\frac{2V_0}{\pi}(cos^2\omega t)\right] - \left[\frac{2V_0}{3\pi}(\cos 3\omega t\ cos\omega t)\right] + \left[\frac{2V_0}{5\pi}(\cos 5\omega t\ cos\omega t)\right] - \cdots \quad (3D)$$

Using the trigonometric identities,$(cosut\ cosvt) = \frac{1}{2}[\cos(u-v) + \cos(u+v)]$, 3D may be rewritten :

$$V_{Sig}(t)V_R(t) = \left[\frac{V_0}{2}\cos\omega_R t\right] + \left[\frac{V_0}{\pi}\right] + \left[\frac{V_0}{\pi}\cos 2\omega t\right] - \left[\frac{V_0}{3\pi}\cos 2\omega t\right] - \left[\frac{V_0}{3\pi}\cos 4\omega t\right] + \left[\frac{V_0}{5\pi}\cos 4\omega t\right] + \left[\frac{V_0}{5\pi}\cos 6\omega t\right] - \ldots \quad (3E)$$

The only term remaining after low-pass filtering is the DC term (Fig. 3-25):

$$V_{OUT} = \frac{V_0}{\pi} \quad (3F)$$

i.e. the lock-in voltage is proportional to the amplitude of the signal. “White-noise” contains uniform contributions at all frequencies, and therefore all noise is filtered out except that close to the modulation frequency. A home-made constant current pulsed LED driver (see appendix, section 7-2) was used to drive the LED at constant light intensity, using a square wave of 170 Hz. The detector response was recorded using a Stanford Research Systems SR830 lock-in amplifier with a 3s time constant. Fig. 3-25 shows the signal versus bead concentration for measurements obtained using the Lock-in amplifier setup in both dark and ambient conditions. In both cases the signal showed good linearity with bead concentration, yielding 3σ limits of detection, of 6.5 x 10^5 and 4.91 x 10^5 beads μl^{-1}

for dark and light conditions respectively i.e. the same to within experimental error. While an expensive commercial Lock-in amplifier was used for this purpose, cheap analogue systems can be built for a few pounds, meaning this approach is very applicable for low cost POC applications.

The intensity of fluorescence emission of the analyte is usually very weak compared to the intensity of excitation light; hence it is crucial to suppress the LED tail light which overlaps the emission from the analyte in order to improve the signal to noise ratio and the limit of detection. (A typical Si-photodetector has a wide spectral range, ranging from the visible to the NIR) There are several ways in which this tail light could be suppressed to improve the limit of detection for our system and this is discussed in the next section.

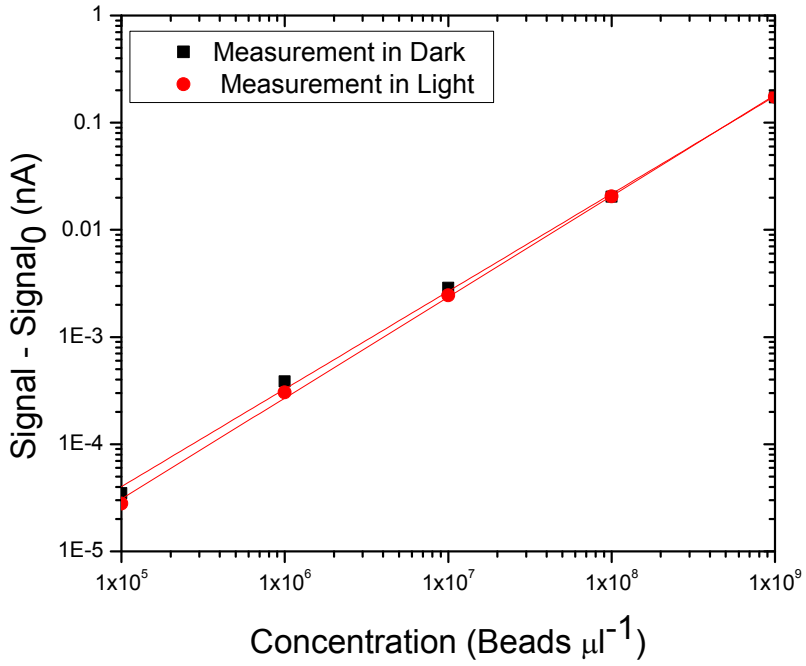


Fig. 3-25 Signal versus transfluosphere bead concentration in distilled water using the machined rig and titania short and long pass filter. The LED was driven with an in-house 20 mA pulsed constant current driver. The signal was measured with a Si-photodetector coupled to a lock-in amplifier.

3.4.4 Suppression of LED tail light in the NIR to improve Detection Limits

The easiest way to suppress the NIR transmission is to add an NIR-blocking optical filter between the Ti-long pass filter and the photodiode. There are various interference filters available commercially that block NIR (>700 nm) and have suitable optical characteristics for our detection system. However, the use of such filters is incompatible with our objective of developing a low-cost detection system. NIR-blocking (or sensitising) dyes have recently attracted much attention in the field of dye-sensitised solar

cells to harness the energy in the IR region of sunlight. In particular, asymmetrical squaranine dyes [138-141] and various cyanine based dyes [142, 143] have been reported to absorb in the NIR region and beyond. Most dyes of this kind have complicated synthesis procedures, and the few that are commercially available are extremely expensive. However there are efforts by commercial firms such as Kentek, USA to develop lower cost dye-based plastic filters to block the NIR region. An alternative method reported in the patent literature uses inorganic cobalt & nickel complexes doped in polymer substrates to provide the requisite absorption characteristics [144, 145].

3.4.4.1 NIR Absorbing Dye Based Plastic Filter

A prototype NIR absorbing dye-based plastic filter was kindly provided by Kentek USA, and used with the Ti – Filters in an attempt to further improve the LOD. The transmission spectrum of the NIR filter showed good blocking beyond 800 nm, but still transmitted approximately 10-30 % of NIR light in the desired blocking region (Fig. 3-26). The NIR filter was placed after the long pass filter to minimise autofluorescence from the filter. Initial measurements showed very promising results with the background signal dropping from 440 pA to 58.1 pA with the NIR filter in place (Table 3-2). Increasing the number of NIR filters had no further effect on the background signal and hence further measurements used a single NIR filter. The signal with the LED off was 1.24 pA, suggesting the remaining 56.8 pA of the background signal is a leakage light from other parts of the spectrum. At first, LED tail light at the transmission window of the Ti-short and long pass filter set was thought to be the cause (where the absorption of light is the lowest at around 600 nm). This was tested by addition of extra Ti-short and long pass filters which only resulted in a small decrease in the background signal to 56.9 pA. Blocking the photodetector with an opaque shim while the LED was on, resulted in a significant drop in signal, indicating that the background signal arises from stray light rather than noise from the electronics. This may be due to unabsorbed light from the short wavelength (<450 nm) region of the spectrum – a possibility that I unfortunately did not have an opportunity to investigate. To test the NIR filter, the same experimental setup, Ti-filters, and transfluosphere solutions as described section 3.4.2 were used. With the addition of the NIR filter between the long pass filters and the photodiode, the LOD was calculated to be 4.83×10^4 beads μL^{-1} which is approximately a 200,000 fold dilution from the original stock solution (Fig. 3-27). As noted with the NIR filter in place the background signal was 58 pA compared to 1.2 pA with the LED switched off and it is therefore clear that the LOD could be further improved by blocking the NIR region completely and this possibility is explored in the next section.

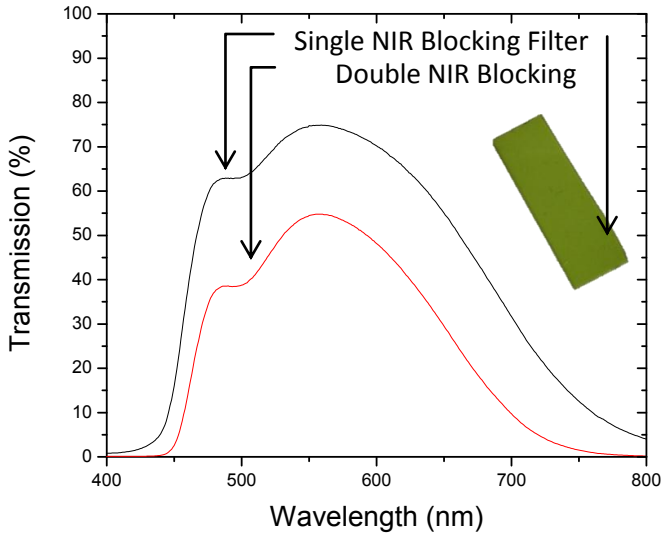


Fig. 3-26 The transmission spectra of the Kentek prototype NIR blocking filter shows between 5-30% transmission in the desired stop band (700 – 800 nm) and relatively good transmission at the transfluosphere emission (70 %). Inset shows the actual NIR blocking filter. Inset shows a picture of the prototype plastic IR filter.

Configuration	Signal (pA)
LED + Ti Filters (4x SP & LP)	440.0
LED + Ti Filters (4x SP & LP) + NIR Filter	58.1
LED + Ti Filters (4x SP & LP) + 2x NIR Filter	58.0
LED + Ti Filters (5x SP & LP) + 2x NIR Filter	56.9
Dark + Ti Filters (4x SP & LP)	1.2

Table 3-2 A table to show the summary of the background signal under different conditions.

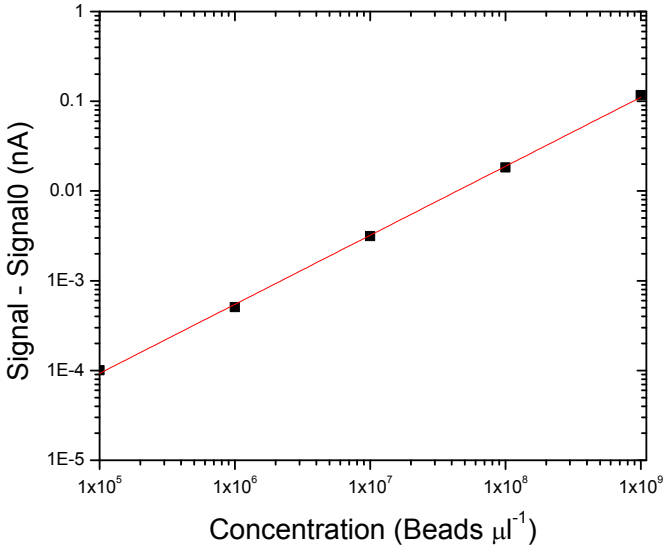


Fig. 3-27 Signal versus transfluosphere bead concentration using the machined rig and titania short- long pass filter. The LED is driven with an in-house 20 mA pulsed constant current driver. The signal was measured with a Si-photodetector was coupled lock-in amplifier. An additional NIR blocking filter was added at the front of the photodetector to cut the LED tail light leakage in the NIR region

3.4.4.2 NIR Blocking filter based on Cobalt Complex

Metal halide complexes such as cobalt bromide and nickel chloride (MX_4^{2-}) have broad absorption spectra with steep cut offs in the spectral range 600 nm to 750 nm. However these complexes tend to crystallise readily and have low solubility in common solvents such as water. Jones et. al. identified a quaternary ammonium counterion which has improved solubility and also shows the desired IR absorption [144]. Methyltrioctyl-ammonium (TOMA) is available from Sigma-Aldrich in the form of bromide or chloride salts. Solutions of TOMA salts (either cobalt (Co^{2+}) or nickel (Ni^{2+})) have sharp blocking characteristics in the NIR region, and following Jones et. al., in this section their potential as NIR blocking filters was explored. The NIR-absorbing complexes used here was the (TOMA) salt of cobalt since nickel complexes was reported by Jones et. al. to dissociate. Furthermore, the cobalt complexes are more transparent in the visible range of the spectrum [144]. In a very recent publication from 2012, $(TOMA)_2CoBr_4$ (Fig. 3-28) was applied in a microfluidic device for fluorescence detection of water pollutant by Lefevre et. al., and he showed that these cobalt complexes are easily incorporated into a polymer host to fabricate an optical filter [146].

3.4.4.3 $(TOMA)_2CoBr_4$ doped Polyvinylpyrrolidone (PVP) filter.

$(TOMA)_2CoBr_4$ was synthesised by adding 0.575 g of anhydrous $CoBr_2$ and 2.43 g of methyltrioctylammonium bromide ((TOMA)Br) – both salts supplied from Sigma Aldrich) to 50 ml of ethyl acetate. This solution was stirred and refluxed for 1 h until complete dissolution of the solids. The resulting cyan solution was cooled to room temperature and treated with activated charcoal to remove any uncoordinated TOMA . This black solution was stirred vigorously for 1 h and the activated charcoal was removed by filtration. The resulting clear cyan solution was heated at 60 °C to evaporate off all the ethyl acetate to form viscous $(TOMA)_2CoBr_4$ [144]. 10 ml of 33 % w/w PVP solution in ethyl acetate was prepared. To this, 1 ml of saturated solution of $(TOMA)_2CoBr_4$ in ethyl acetate was added. This thick mixture was drop cast (on a heated glass substrate) or spin coated (at 1000 rpm for 1 min) on a glass substrate to produce a thin $(TOMA)_2CoBr_4$ -doped PVP layer on glass (Fig . 3-29). (Fabrication on plastic would also be straight forward.)



Fig. 3-28 Structure of $(TOMA)_2CoBr_4$. $(TOMA)^+$ and Br^- ions have weak electric fields and cause low energy gap in d-orbital splitting which corresponds to their absorption in the Red region of the spectrum.

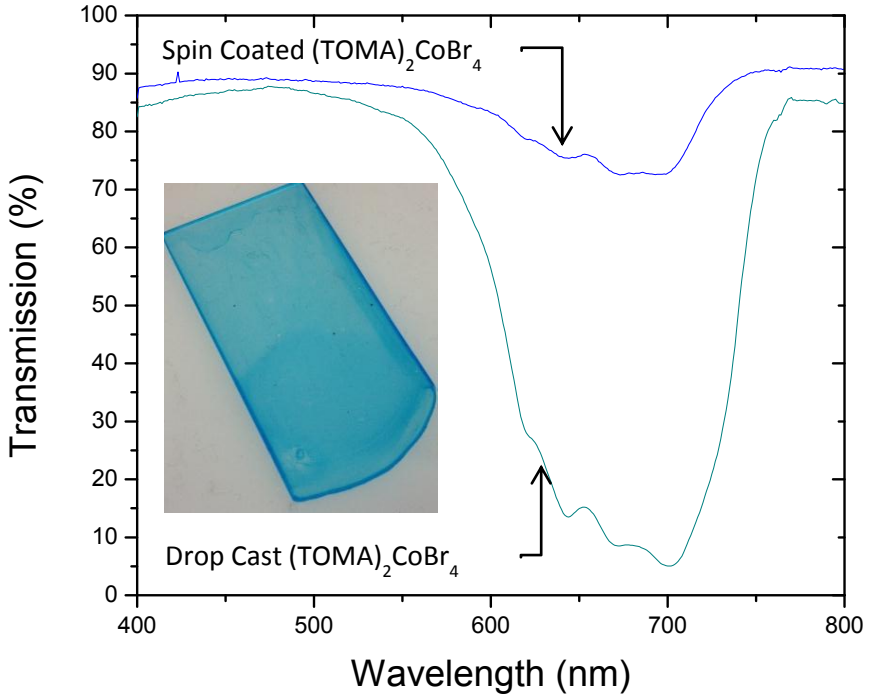


Fig. 3-29 (Above) Transmission spectrum of single spin coated and drop casted $(TOMA)_2CoBr_4$ doped PVP on glass. Inset picture shows the drop casted $(TOMA)_2CoBr_4$ doped PVP on glass.

The transmission spectrum of the $(TOMA)_2CoBr_4$ shows sharp drop beyond ~575 nm and shows promising results for NIR filtering. However it was not fit for our purposes due to its high transmission (80 %) beyond 750 nm., meaning it could not effectively block the problematic LED tail light in the NIR region (750 800 nm). Furthermore, it has a relatively low transmission in the transfluosphere emission band (45 %) which would further reduce the sensitivity.

Electronic transitions that correspond to NIR transitions are rare, and they are typically observed in F block elements which are known to exhibit weak 'low energy' electronic transitions [147]. Also a small HOMO-LUMO gap arises from metal-to-ligand charge transfer (MLCT) or Ligand-to-metal charge transfer (LMCT) where the barrier for intramolecular redox activity is sufficiently high [148]. Large extended π-conjugated systems can also exhibit low energy absorption due to the low energy π-π* transitions.[149].

The absorption band of cobalt complexes can be shifted by using radical-containing ligands which are known to show low energy MLCT, LMCT and inter–ligand π-π* transitions. One of the characteristic properties of stable organic molecules is their wide HOMO-LUMO gaps which only allow absorption in the UV and the visible region. One electron reduction or oxidation creates the radical form of such molecules, forming singly occupied molecular orbitals which allows low energy transitions that corresponds to NIR absorption [150]. This transition is illustrated in Fig. 3-30 for both radical cations and anions. Several examples of radial anions that can be used as a potential ligand for metal coordination, such as 2'2-bipyridine [151] have been identified. Further optimization of the cobalt complexes by using such radical ligands may provide improved blocking characteristics in the NIR region and better satisfy the requirements of our application.

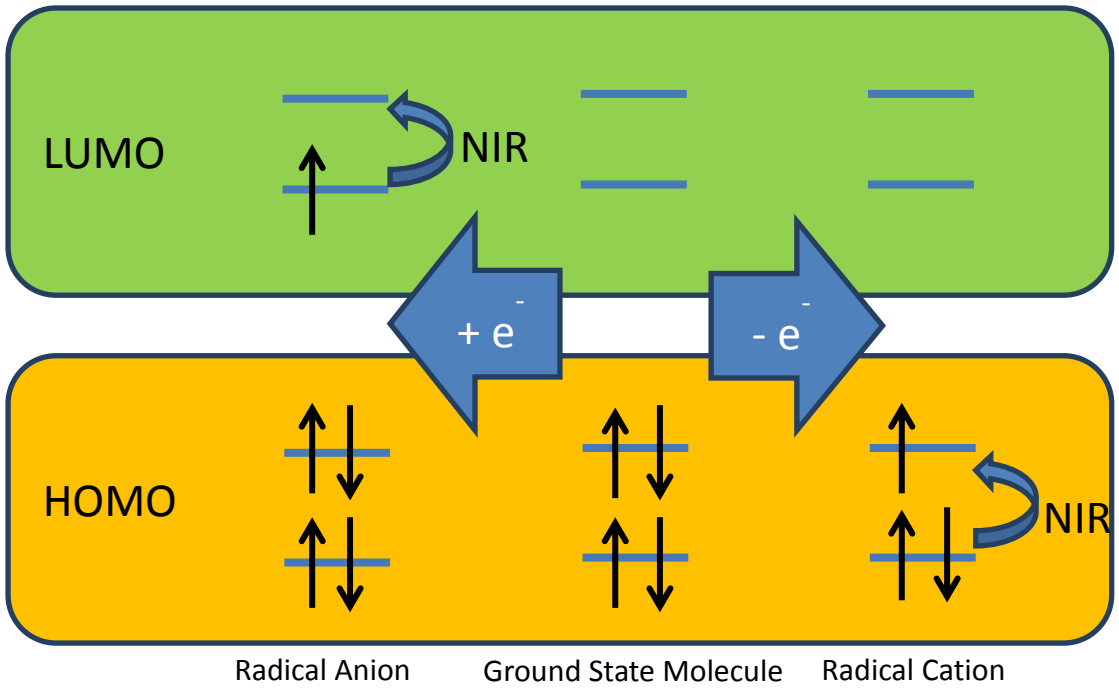


Fig. 3-30 A schematic to show the NIR absorption in radicals. This schematic has been adapted from [150].

3.4.4.4 Photodetector with a narrower Spectral Response

Another way to minimise the effect of the LED tail light in the non-blocking region of the Ti-long and short pass filters is the use of a photodiode with narrower spectral response. Si-photodiodes have a wide spectral range, typically ranging from 190 – 1100 nm, but cheap Si-photodiodes (using proprietary filters) that are designed to mimic the spectral response characteristics of a human eye are commercially available. The Hamamatsu S7686 Si-photodiode is one example, and it offers spectral response range of 480 – 650 nm. The S7686 photodetector was used in conjunction with the lock-in amplifier to investigate its effectiveness in further improving the LOD of the transfluospheres. The same experimental methods, detector-light source configuration, and transfluosphere concentrations were used as before.

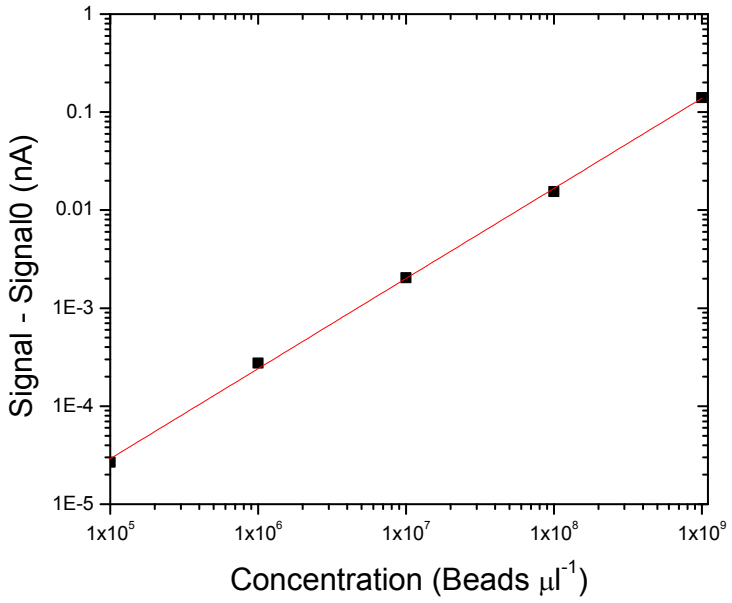


Fig. 3-31 Signal versus transfluosphere bead concentration in distilled water using the machined rig and titania short- long pass filter. The LED was driven with an in-house 20mA pulsed constant current driver. The signal was measured with a Hamamatsu S7686 narrow spectral response Si-photodetector coupled to a lock-in amplifier (Stanford Research Systems, SR830).

Fig 3-31 shows a linear dose response characteristics of the transfluorsphere beads The use of the S7686 photodiode lead to a significant reduction in the background from the previously obtained values of 440.0 pA (Lock-in setup with no IR filter) and 58.1 pA (with IR blocking filter) to 22 pA was observed. The LOD was also improved to 2.86 x 10^4 beads μL^{-1}, which is approximately 350,000 fold dilutions relative to the stock solution (Fig. 3-31). This compares favourably with a previous value of

6×10^4 beads μL^{-1} (~170,000 fold dilutions relative to the stock) obtained using a combination of colour filters and polarisers [152]. The LED/Ti-XC/T8661/Ti-FDS/Si-photodiode combination reported here offers a highly attractive solution for sensitive, low cost, integrated fluorescence detection in a microfluidic chip that is readily applicable to a wide range of bead-based immunodiagnostic assays.

3.5 Summary

Titania based short-pass filters were fabricated using a variety of long wavelength absorbing dyes. Surface acid/base treatment of the titania surface was used to electrostatically attract anionic/cationic dyes that would otherwise not coordinate to titania. A facile method for fabricating mechanically stable titania filters on plastic (PET) substrates at room temperature was also devised, allowing the filters to be applied to portable detection devices requiring thin plastic high performance filters. Plastic short- and long-pass filters were made with xylene cyanol and FDS and applied to transfluorsphere detection. Subsequent experimental details and their results are summarized in the table 3-3 below:

Experimental conditions	Filters Used	Background	LOD (beads μL^{-1})
Plastic LED/Detector Holder Keithley Electrometer	4x Xylene Cyanol Ti-SP filter 4x FDS Ti-LP filter	1200 pA	2.06×10^7
Machined LED/Detector Holder Keithley Electrometer	4x Xylene Cyanol Ti-SP filter 4x FDS Ti-LP filter	1210 pA	1.49×10^7
Machined LED/Detector Holder Constant Current LED Driver Keithley Electrometer	4x Xylene Cyanol Ti-SP filter 4x FDS Ti-LP filter	1090 pA	1.59×10^6
Machined LED/Detector Holder Constant Current Pulsed LED Driver Lock-in Amplifier	4x Xylene Cyanol Ti-SP filter 4x FDS Ti-LP filter	440 pA	4.91×10^5
Machined LED/Detector Holder Constant Current Pulsed LED Driver Lock-in Amplifier	4x Xylene Cyanol Ti-SP filter 4x FDS Ti-LP filter Kentek NIR Blocking filter	58 pA	4.83×10^4
Machined LED/Detector Holder Constant Current Pulsed LED Driver Lock-in Amplifier Hamamatsu S7678 Photodiode	4x Xylene Cyanol Ti-SP filter 4x FDS Ti-LP filter	22 pA	2.86×10^4
In complete Dark using Standard Si-Photodiode	4x Xylene Cyanol Ti-SP filter 4x FDS Ti-LP filter	1.0 pA	N/A
In complete Dark using S7686 Si-Photodiode	4x Xylene Cyanol Ti-SP filter 4x FDS Ti-LP filter	0.6 pA	N/A

Table 3-3 A table to show the summary of the transfluosphere detection experiments.

Initially the transfluosphere detection was performed in a plastic rig. The LED was powered by a 9V battery and the signal was recorded with a Keithley electrometer. A poor limit of detection of 2.06 x 10^7 beads μL^{-1} and a high background signal of 1200 pA was observed. At first, this result was thought to be caused by the 'flimsy' nature of the plastic LED/detector holder. To make sure that all the components (LED/cuvettes/detector) remained in the same position for each measurement, a new rig was machined out of an aluminium block. This ensured that all the components were rigidly fixed in place. Using the same transfluosphere concentrations the dose-response measurements were repeated again. To our disappointment, the background signal was still high compared to the signal with the LED off and showed significant scatter.

It was subsequently discovered that the LED intensity was drifting due to battery discharge. To correct this effect, a constant current LED driver circuit was added to the rig. Improvement in the signal profile was immediately apparent and a ten-fold improvement in the LOD was observed to 1.59 x 10^6 beads μL^{-1}. However this was still only a 6000 fold dilution relative to stock solution and a typical assay would be expected to detect up to 100,000 fold dilution of the analyte. The background signal at 1090 pA was still very high compared to the signal when the LED was off (or the photodiode blocked with an opaque shim) at 1.0 pA. By reducing the background, one would expect the sensitivity to improve and this was achieved by using a lock-in amplifier coupled to a pulsed LED (to eliminate constant + slowly varying background interference). An approximate 60 % reduction in the background signal was achieved this way, under dark ambient conditions, improving the LOD to 4.91 x 10^5 beads μL^{-1}. Moreover, virtually the same LOD could now be achieved with the room fully lit. Since the lock-in amplifier filters any external background, the 440 pA of background observed were attributed to leakage from the LED, in particular the LED tail light leakage observed in the NIR region of the spectrum.

A plastic dye-based NIR absorbing filter was used to block the leakage from reaching the detector and this was successful in greatly reducing the background signal to 58 pA. The LOD was also improved to 4.86 x 10^4 beads μL^{-1} which is equivalent to an approximately 200,000 fold dilutions. In an attempt to further lower the background signal and improve the transmission in the pass band of the NIR-Filters, a NIR blocking plastic filter based on $(TOMA)_2CoBr_4$ complex was investigated. The synthesized $(TOMA)_2CoBr_4$ was doped in a PVP polymer host, yielding a filter with a sharp cut-on and desirable optical properties for a short pass NIR filter. Unfortunately the complex had high transmission beyond 750 nm and did not provide adequate blocking in the desired blocking band (750-800 nm). The

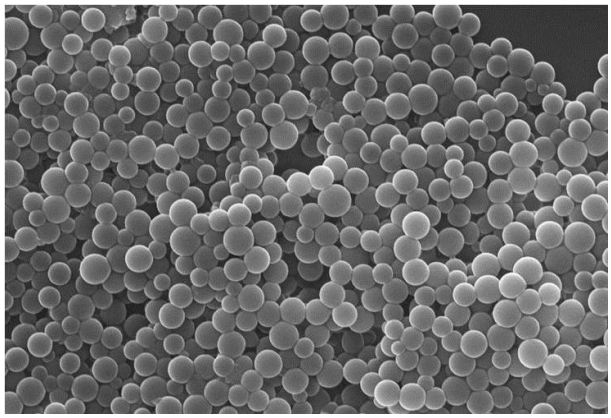
NIR absorption for complexes of this kind can be altered and further investigation might well identify suitable candidate.

Finally, a narrow spectral response Si-photodiode was also tested in conjunction with the approaches described above. The background signal was further suppressed to 22 pA (compared to 0.6 pA in the dark). An improved LOD of 2.86×10^4 was achieved, making it possible for this setup to detect transfluosphere concentrations that are 350,000 times more dilute than the stock solution.

CHAPTER 4

4

Phosphorescence Detection



4 Phosphorescence Detection

4.1 Introduction

In the past few decades, advancements in the field of biochemistry have affected many aspects of life, with new detection and imaging techniques allowing for better understanding of human biology. One such advancement is in the detection of specific antigens using immunoassays. Such immunoassays rely on the binding of antibodies to their specific antigens to form an sparingly insoluble complex [153]. Antibodies are proteins produced by the immune system in response to infection or foreign matter. Antigens are any substance (from the environment or made within the body) that induce the production of antibodies by the immune system. The most commonly used antibody for bio-analysis is Immunoglobulin G (IgG) which has a y-shaped protein structure comprising two separate parts: a fragment crystallisable (FC) part which is common to most antibodies and they can be used to immobilise them on a solid support [154] and a fragment antibody binding (FAB) region which allows the antibody to selectively bind to antigens (Fig. 4-1).

Immunoassays can be designed so that either an antigen or the antibody is the analyte. At high concentration, bound antibodies and antigens precipitate out of their solution, providing a visual indication of successful binding. However for low concentration analytes, alternative methods for detecting binding are necessary [155]. Luminophore-doped polymer beads provide an effective means of detecting such interactions. Polymer based micro and nanoparticles with different surface functionalization can be prepared by simple co-polymerisation using a variety of monomers, allowing them to be conjugated to a broad range of biomolecules. Furthermore, many different types of luminophores can be incorporated into the beads such as dyes [9, 156], metal nanoparticles [157-159], and quantum dots [160-162] which can then be detected optically. Importantly, since the luminophores are encapsulated in a polymer matrix, they are protected from the external environment. Many studies have showed improved chemical stability and luminescence in dye-doped polymer beads compared to free dye, with the emission characteristics of the incorporated dye remaining unchanged even when the external conditions of the assays are altered (an important consideration if the assay is to be performed in *in-vivo*).

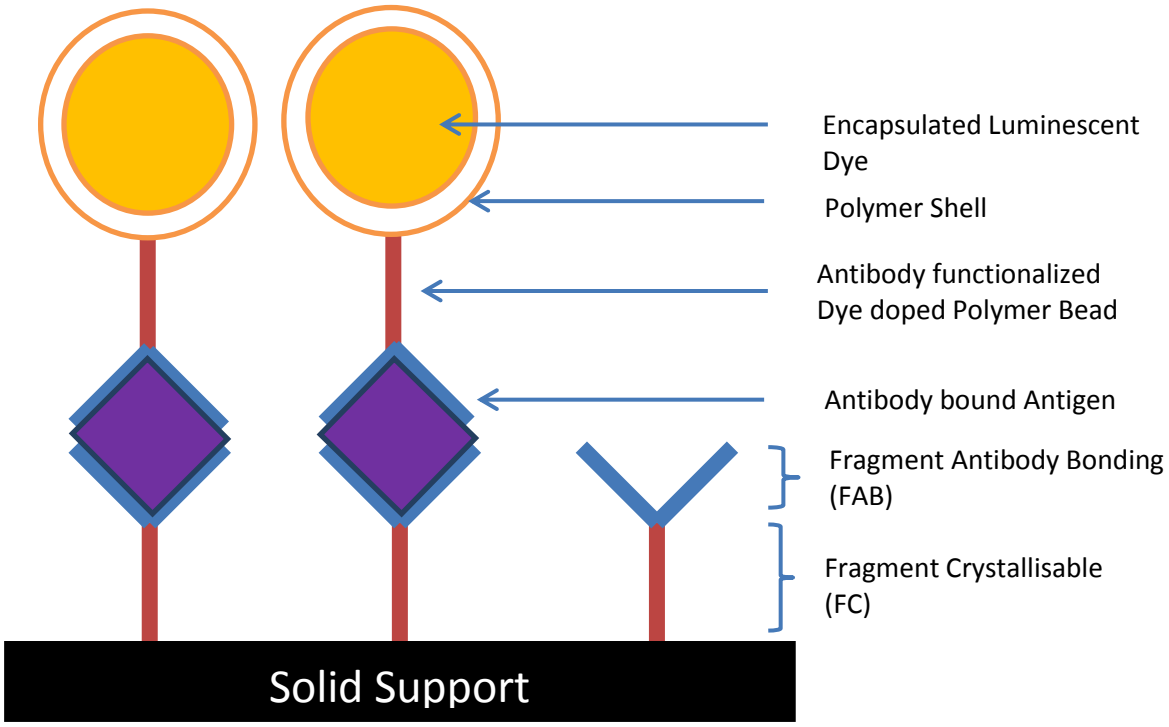


Fig. 4-1 Schematic to show mechanism of a commonly found immunoassay using an antibody functionalised luminescent polymer beads

Polymer beads are typically prepared by precipitation polymerisation. An ideal dye-doped polymer bead for biomolecule detection would be a non-coagulating spherical bead with high dye loading. To achieve this, one must optimize several factors, such as choice of the constituent polymers, dyes, solvents, and their concentrations. There are many luminescent polymer beads that are available commercially, but they tend to be costly and frequently require UV excitation which precludes their use with low cost visible-LEDs (that are often found in low-cost detection platforms [163].) This chapter extends earlier work by Dr. Angharad Edwards of Imperial College London [163], who developed a protocol for preparing stable phosphorescent dye-doped nano- beads discussed in the next section.

The objective of this work was to optimize the phosphorescent polymer bead synthesis proposed by Edwards and to test the optimised beads in conjunction with time-gated phosphorescence detection set-up (see next section) to measure their limit of detection. Furthermore, the beads will be bio-functionalised and a simple biotin assay implemented to demonstrate their biomedical applicability.

4.1.1 Time-gated detection

Time-gated detection is a highly sensitive detection technique that is widely used in bio-analysis as an elegant means of eliminating backgrounds due to the light source and autofluorescence from biomolecules. It works by setting a time delay between the excitation pulse and signal detection, hence allowing the emission from the light source and autofluorescence of biomolecules to decay to a negligible level before measuring the phosphorescence signal from the label [164, 165]. This detection method is well suited for our beads, since phosphorescent beads have significantly longer lifetime than any fluorescence or the switching time of the light source. Schematics to show how the time-gated detection operates are shown in Fig. 4-2.

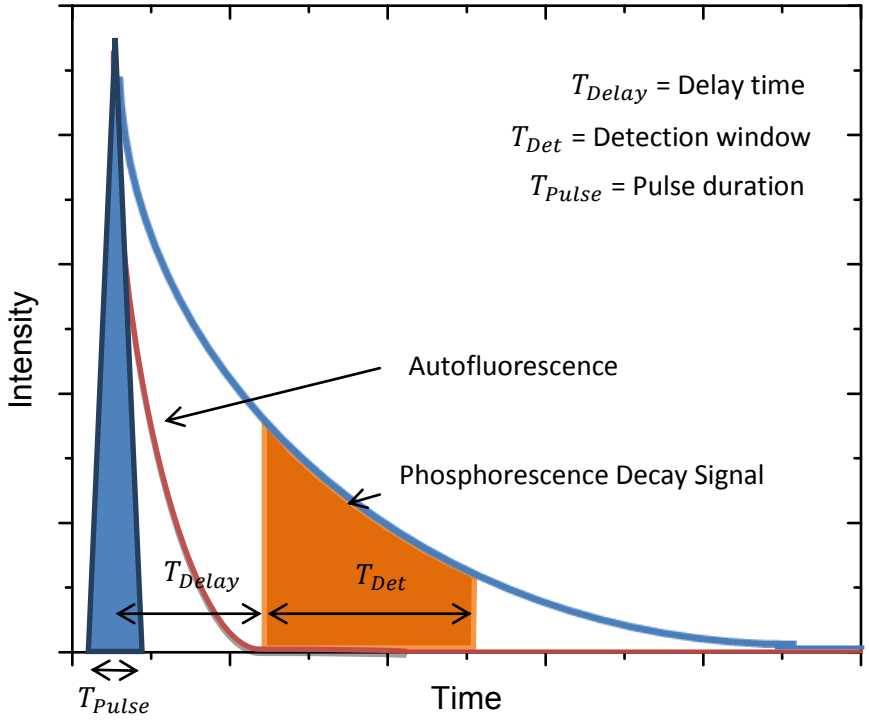


Fig. 4-2 Schematic to show how time-gated detection works. Adapted from [165].

As shown in Fig. 4-2, the analyte sample is excited by a short burst of light (typically a pulsed LED, lamp, or laser [166]). This is followed by a time delay (T_{Delay}) which lasts longer than the pulse duration (T_{Pulse}) or any autofluorescence signal that may arise from such photo excitation. After this time delay, the detector is switched 'on' for the duration of the detection window, T_{Det} to measure the phosphorescence delay of the label. The detector is switched off and the measured signal is integrated, after which this cycle is repeated. The duration of this cycle depends on the properties of the

components used in the detection system – such as the excitation source/detector response time and the label life-time.

Despite its considerable advantages over steady state fluorescence detection, phosphorescence detection format is not widely used in portable detection systems [163]. One of the main reasons is the expensive and bulky nature of the equipment required to carry out sensitive time-gated detection. However a very recent report in 2011 by Wang *et. al.,* reported an ultra-portable time-resolved fluorescence analysis device for detecting explosives which utilises CMOS sensors and pulsed LED light sources [167]. The detection system was limited to low vapour pressure nitro-aromatic compounds and only achieved moderate detection limits. Another report in 2012 by Chen *et. al.,* described a portable time-gated luminescence detector for the detection of environmental pollutants. The system used multiple excitation sources such as UV-LEDs and Xenon flash lamps. The final device was housed in a small briefcase, which weighed 5 kg, and achieved ng/ml-level detection limits [168]. However, the examples outlined above were constructed to analyse short lived fluorophores (τ < 0.5 µs) and at such time scales, the requirement for fast electronics coupled with potential interference from autofluorescent molecules adds significantly to detection complexity. Although there is much scope for improvement, the idea of applying time-gated detection to portable platforms is gaining momentum.

4.2 Phosphorescent dye doped polymer beads

4.2.1 Dye selection and their optical properties

Tris(4,7-diphenyl-1,10-phenanthroline)-ruthenium ($Ru(dpp)_3$) which is chemically and structurally very similar to the widely-studied Ruthenium based dye, Tris(bipyridine)ruthenium(II) ($[Ru(bpy)_3]^{2+}$). Unlike $Ru(bpy)_3$ (which has bipyridine ligands), in $Ru(dpp)_3$ the Ru metal centre is surrounded by three bidentate diphenyl phenanthroline ligands arranged in an octahedral geometry as seen in Fig. 4-3A. Unlike other commonly used Ruthenium-based dyes, $Ru(dpp)_3$ is not water soluble which makes it suitable for use in dye-doped polymer beads prepared by precipitation method. (See section 4.2.3.)

$Ru(dpp)_3$ in dimethyl formaldehyde (DMF) absorbs strongly in the blue region of the spectrum (absorption maximum at 465 nm, see Fig. 4-3B) and so can be excited by with low cost blue inorganic

LEDs as supposed to UV-LEDs which are typically needed for exciting phosphorescent dyes. According to the crystal field theory, six electrons in the d-orbitals of the Ruthenium metal centre split into two higher degenerate orbitals (e_g) and three lower degenerate orbitals (t_{2g}) upon the formation of the octahedral complex. The absorption of 465 nm blue light arises from the promotion of an electron from the singlet ground state (t_{2g}) to the π* orbitals of the dpp (singlet metal-to-ligand charge transfer state, Fig. 4-3B). This absorption is followed by ultrafast intersystem crossing into the triplet metal-to-ligand charge transfer state (^{3}MLCT) as seen in Fig. 4-4 [169, 170]. Other competing decay paths such as fluorescence or internal conversion are not observed since intersystem crossing to the ^{3}MLCT occurs much faster ($k_{isc} >> k_F$).

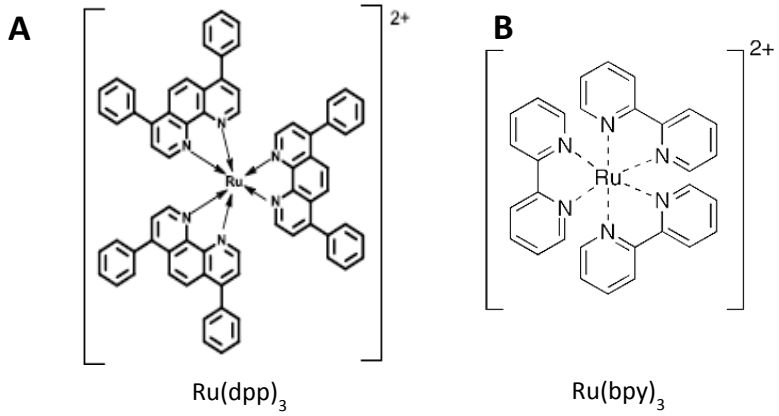


Fig. 4-3A Chemical structures of **A**) $Ru(dpp)_3$ and **B**) $Ru(bpy)_3$.

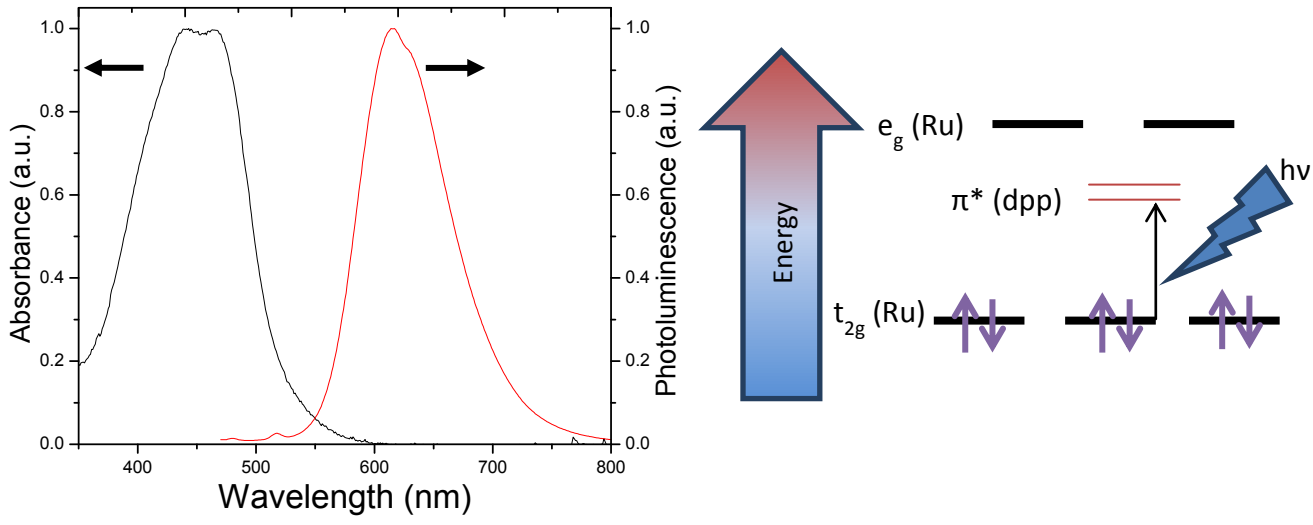


Fig. 4-3B (**Left**) Normalised absorption and emission spectra of $Ru(dpp)_3$ in DMF. (λ_{ex} = 470 nm) (**Right**) Metal-to-Ligand Charge Transfer (MLCT) that occurs in $Ru(dpp)_3$ upon absorption.

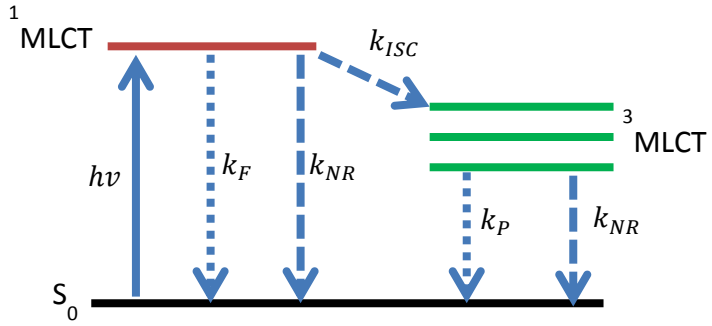


Fig. 4-4 A Jablonski diagram to illustrate the decay paths of $Ru(dpp)_3^{2+}$. k_F is the rate of fluorescence, k_{NR} rate of non-radiative decay, k_{ISC} rate of inter system crossing, and k_P rate of phosphorescence.

According to literature inter system crossing occurs ≈100 % for $Ru(dpp)_3$ [171] due to their strong spin-orbit coupling with the heavier ruthenium metal centre. Non-radiative relaxation is suppressed due to the large energy gap between the ^{1}MLCT and the ground state. Due to this strong spin-orbit coupling, the formally spin forbidden transition from the long-lived ^{3}MLCT state to the ground state becomes available via phosphorescence with a luminescence life time of $\tau \approx 5\mu s$. However it is strongly quenched by oxygen via energy transfer or charge transfer mechanism [172], making this dye also useful for oxygen sensing applications. For the purpose of making luminescent polymer beads, the dye must be encapsulated in oxygen-impermeable polymer to prevent quenching. The photoluminescence quantum efficiency, Φ_P (PLQE) is defined by:

$$\Phi_P = \eta_{ISC} k_P \tau_{T1} \tag{4A}$$

where η_{ISC} is given by:

$$\eta_{ISC} = \frac{k_{ISC}}{k_{ISC}+k_F} \tag{4B}$$

where k_{ISC} = rate constant for intersystem crossing and k_F = radiative rate constant

τ_{T1} is the lifetime of the ^{3}MLCT state and is given by:

$$\tau_{T1} = \frac{1}{k_P k_{NR}} \tag{4C}$$

where k_P = rate constant of phosphorescence and k_{NR} = rate constant of non-radiative decay.

Since $\eta_{ISC} \approx 1$, combining equation 4A and 4C gives:

$$\Phi_P = \frac{k_P}{k_P+k_{NR}} \tag{4D}$$

Edwards previously obtained a value of $\Phi_P \approx 30 \pm 5$ % for encapsulated $Ru(dpp)_3$, which is relatively high compared to other phosphorescent iridium and ruthenium complexes reported in other literatures ($\Phi_P \approx 20$ % and 6.1% respectively) [173-175]. Please see section 2.6 and section 7.4 on photoluminescence quantum yield acquisition of the phosphorescent beads.

The $Ru(dpp)_3$ emission maximum in DMF is 610 nm (Fig. 4-3) which is easily detectable using commonly available Si-photodetectors. Furthermore the large Stokes' shift of 160 nm is beneficial for detection platforms that use optical filters (with or without time-gated detection) since it lessens the need for sharp filter transitions as explained in chapter one. $Ru(dpp)_3^{2+}$ is an attractive dye for polymer bead incorporation since it has a long luminescence lifetime of 5 µs, which can be readily detected using sub-MHz bandwidth low-cost time-gated detection instrumentation (more details in section 4.2.4). It can also be excited and detected within the visible range of the spectrum, and so is compatible with low-cost inorganic LEDs and detectors.

4.2.2 Polymer Selection

Many varieties of polymers and have been used for bead preparation. The most common polymers include: polystyrene (PS) [176-178], poly(acetonitrile) (PAN) [179-181], and poly (methyl methacrylate) (PMMA) [182]. There are two key characteristics that one must look for when selecting polymer for bead synthesis. Firstly, parts of the polymer must be hydrophobic to maximize $Ru(dpp)_3$ incorporation, since the dye is hydrophobic in nature. Higher dye-loading would leads to higher emission intensities which are advantageous for detection. Secondly, parts of the polymer must have hydrophobic polar groups to ensure the beads can be dispersed in aqueous media. Furthermore, the polymers should also contain polar groups such as carboxylic acids that can be readily bio-functionalised for assay applications.

Work by Edwards *et. al.,* has demonstrated that an amphiphilic polymer, polystyrene-co-maleic acid (PS-co-MA) (see Fig. 4-5) can yield non-coalescing spherical beads using precipitation polymerization. Beads synthesized with this polymer were found to be highly impermeable to oxygen and were effective at preventing oxygen quenching of the encapsulated $Ru(bpp)_3$. Furthermore, the carboxyl group present in PS-co-MA can covalently bond to biomolecules allowing for easy surface functionalization. Cross-linking is another important factor that must be considered when synthesizing polymer beads. Liu et. al., investigated the effect of cross-linking polystyrene-co-divinylbenzene with

polypropane and discovered that cross-linked polymer beads had improved dye loading and showed less tendency to coalesce [183]. Bisphenol A glycidyl ether (BPA) was chosen by Edwards as the cross-linker since its epoxy group readily reacts with the carboxylic acid groups on the PS-co-MA polymer [163, 184]. Edwards showed that BPA cross-linked beads had improved dye loading and luminescence quantum efficiencies than to uncross-linked beads. Importantly the cross-linked beads displayed less tendency to coalesce and so all the beads in this chapter were cross-linked [163].

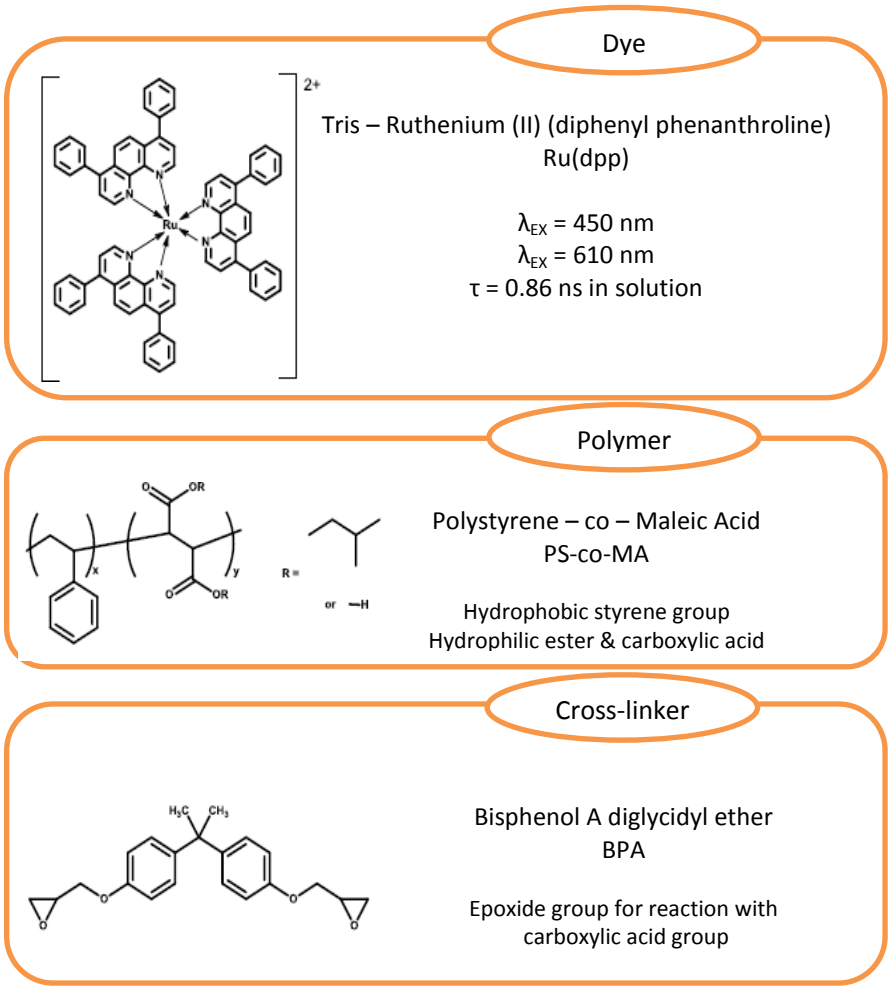


Fig. 4-5 Selection of Ruthenium dye, polymer, and cross-linking agents for producing phosphorescent polymer micro-beads described in this chapter.

4.2.3 $Ru(dpp)_3$ PS-co-MA/BPA nano-beads

4.2.3.1 Precipitation Polymerization

There are two main methods for producing polymer nano-beads. Emulsion polymerisation typically starts with a water-insoluble monomer and water. Surfactants or other water soluble polymers

are added to this mix, 'emulsifying' the monomer. The polymerisation reaction takes place within the formed monomer particles forming the polymer beads. The beads are stopped from coagulating with each other because they are surrounded by surfactants which electrostatically repel each other. This polymerization technique is compatible with a wide selection of monomers, but it is difficult to remove the surfactant and hence polymer beads made via this route are not ideal for bio-assay applications.

As an alternative to the above approach, precipitation polymerization developed by Kürner [185] and Song *et. al* [184] involves a simple preparation route that produces high quality bio-compatible beads. Edwards successfully demonstrated the use of precipitation polymerization to produce $Ru(dpp)_3$ doped PS-co-MA/BPA nano-beads [163, 186]. Precipitation polymerization is a surfactant-free approach that requires the use of dyes and polymers that dissolve in water-miscible solvents such as dimethylformamide (DMF), but not in the corresponding water/solvent mixture. The process of bead formation via precipitation is illustrated in Fig. 4-6. A solution of PS-co-MA polymer and dye is stirred vigorously in DMF and excess water is added slowly which causes the nano-beads to form spontaneously (due to the solubility differences of the different groups on the polymer) [163]. Edwards also found that crosslinking the polymers yielded crosslinked beads had better dye loading, size and less coalescence than their non-crosslinked equivalents. The resultant polymer beads are crosslinked by heating them to 85 °C.

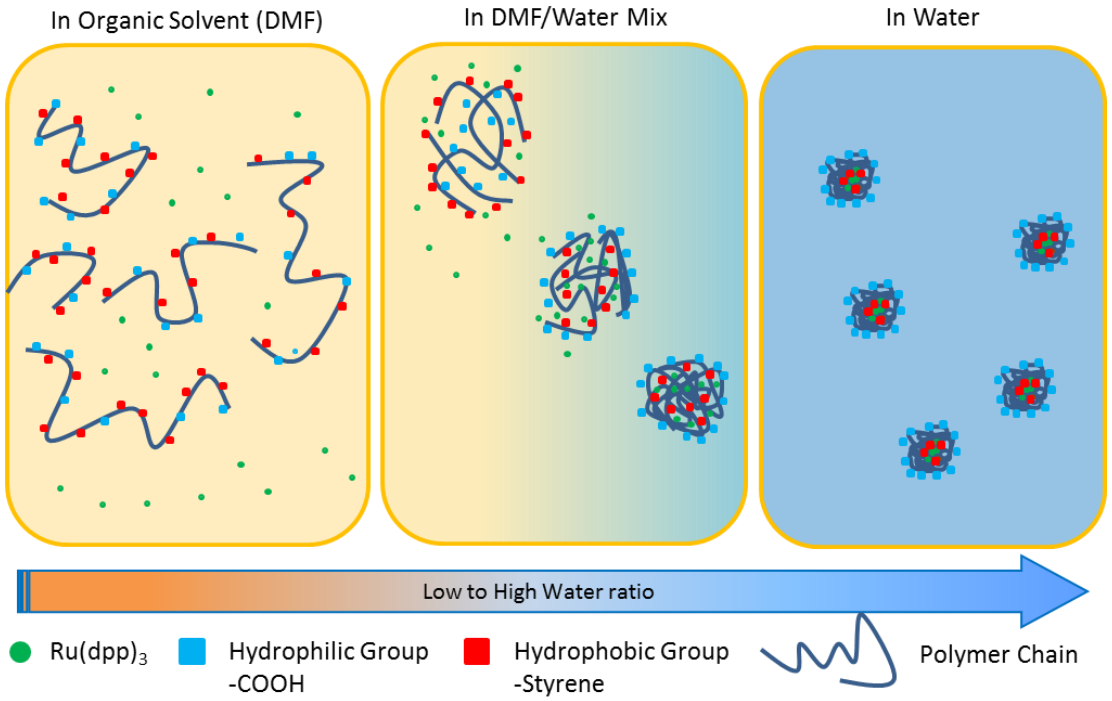


Fig. 4-6 A schematic to show the formation of $Ru(dpp)_3$-doped polymer nano-beads by precipitation .

4.2.3.2 Experimental

100 mg of PS-co-MA (polymer) and 25 mg of BPA (cross-linker) were dissolved in 20 ml DMF using a glass-coated magnetic stirring bar. To this colourless solution, 1 mg of $Ru(dpp)_3$ dissolved in 5 ml DMF was added, giving the solution an orange tint. 120 ml of distilled water was added at a rate of 2 ml/min. After 5 min the solution turned from clear orange to a cloudy orange solution as nano-beads started to form. The resulting solution was left to stir for 10 min after which it was centrifuged and washed with distilled water three times to eliminate any DMF. All DMF was removed to prevent bead coalescence. The solution was then heated overnight at 85 °C to induce cross-linking with BPA [163]. The stabilized beads were kept in the dark and stored at -20 °C. (Fig. 4-7)

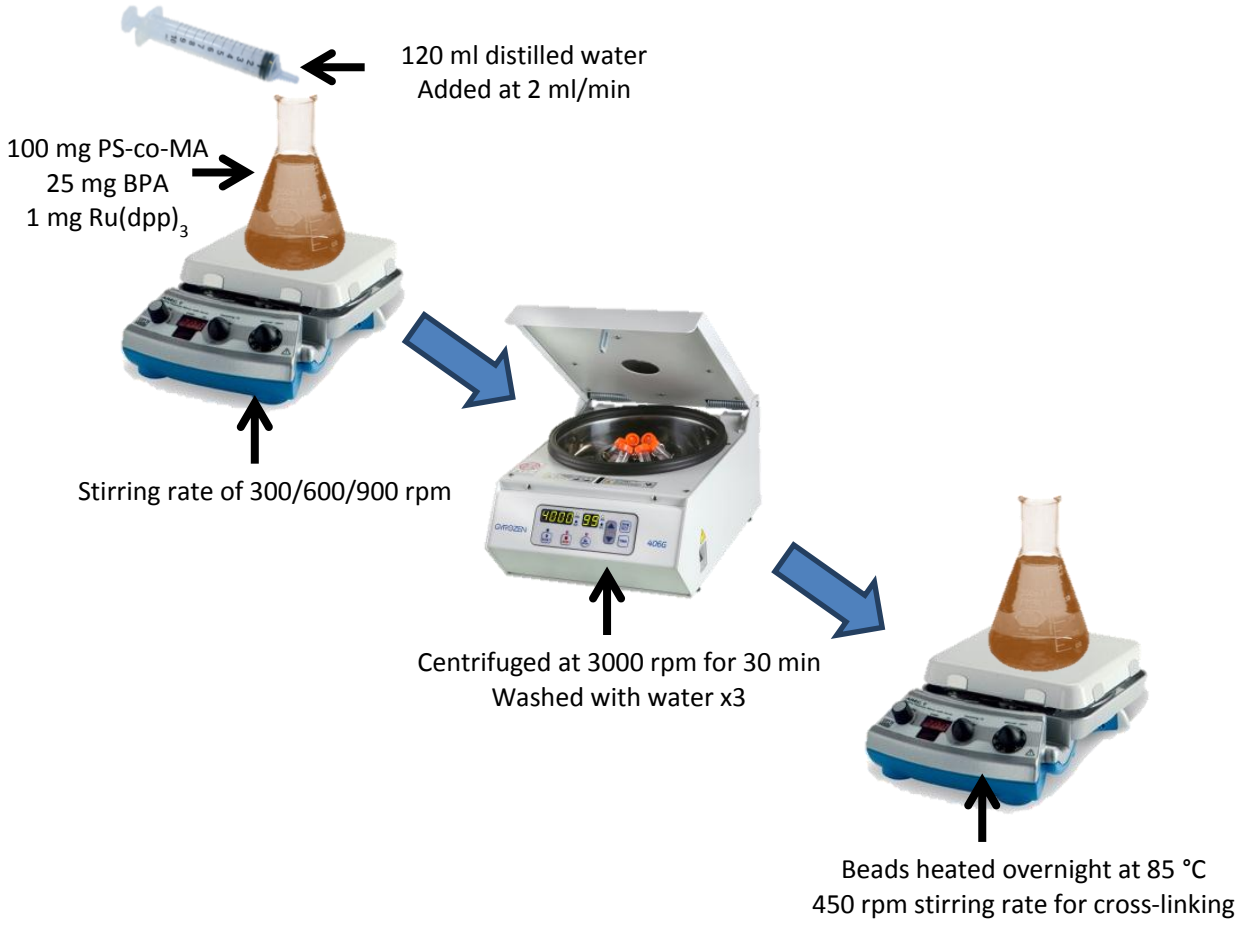


Fig. 4-7 Schematic of synthesis procedure for $Ru(dpp)_3$ doped PS-co-MA/BPA polymer nano-beads

4.2.3.3 Determining the ideal Synthesis Conditions

For the purpose of bioassay optimisation, all beads should be spherical in nature and have a narrower size distribution to ensure they all have similar binding affinity to the target analyte. Furthermore, the beads should show structural stability and not coalesce. They should also have as high dye loading as possible to maximize their quantum yields without compromising all the attributes mentioned above.

The synthesis procedure, suggested by Edwards was selected for its optimum dye loading (determined by their quantum yield experiment [163]) and its ability to form spherical beads. However the synthesized beads still had tendency to coalesce after prolonged storage, which suggested there was still room for improvement. Previous studies have shown that synthesis steps such as stirring rate greatly influence the properties of the resulting polymer beads. Therefore, in this section, the stirring rate of the polymer solution during the water addition step was optimized to further improve the characteristics of the phosphorescent polymer beads [187-189].

4.2.3.4 Stirring rate influence

Dye-loaded polymer beads were synthesized using three different stirring rates: 300, 600, and 900 rpm. (600 rpm is the speed previously used by Edwards) The water addition rate was kept constant at 2 ml/min for all experiments. The resulting beads were analysed by SEM to measure the bead diameter and their size distribution. This work was carried out in collaboration with Ms. Roxanne Jourdain of Imperial College London.

Fig. 4-8 shows the SEM micrograph of the beads prepared at different stirring rates. It is evident that beads prepared with 300 rpm stirring rates had the best characteristics in terms of the size, shape, and resistance to coalescence. The as-made 300 rpm beads had a size (diameter) of 301 ± 120 nm (Fig. 4-9), and narrower distributions down to 180 ± 20 nm can be achieved by further filtration. Beads prepared at the higher stirring rates formed non-spherical or aggregated structures. Altering the stirring rate had a fairly weak effect on the mean size or the size distribution. There was a significant difference however in the ratio of the spherical- to non-spherical beads at: 95 %, 50 %, and 10 % for 300, 600, and 900 rpm respectively. All polymer beads used in this work were synthesised using 300 rpm stirring rate.

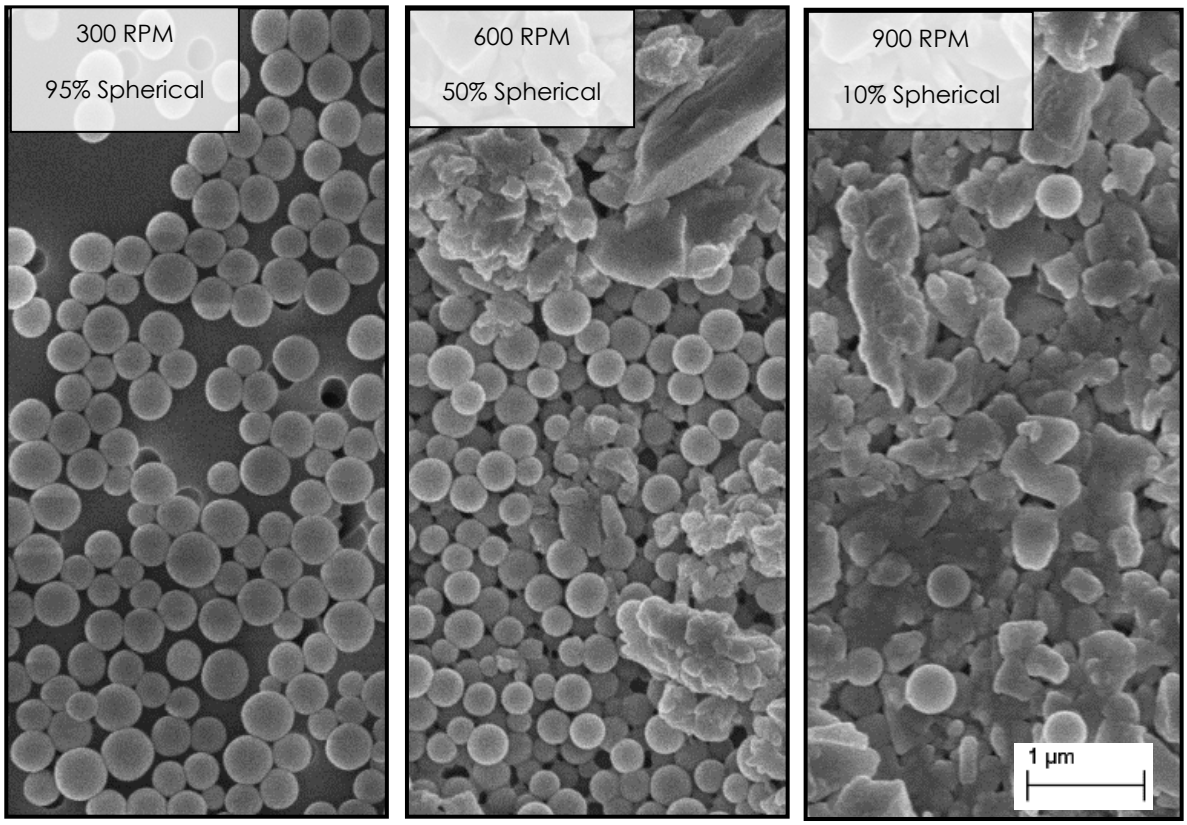


Fig. 4-8 SEM images of the $Ru(dpp)_3$ doped PS-co-MA/BPA beads synthesised at different stirring rates. Beads synthesised at 600 rpm was the conditions used by Edwards.

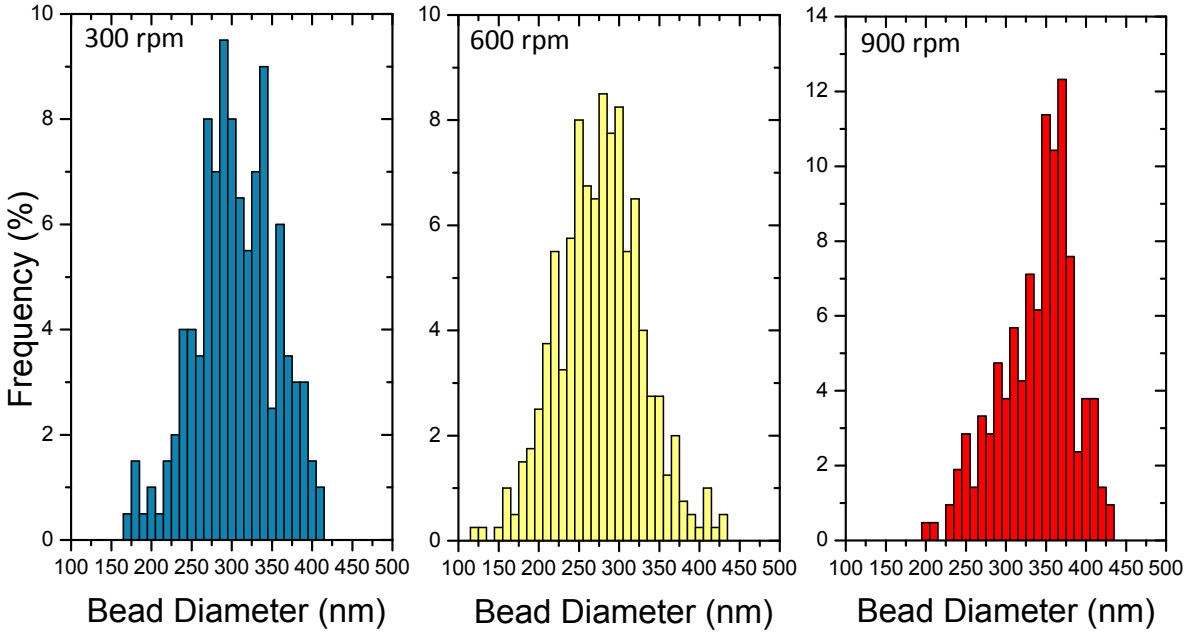


Fig. 4-9 Size distribution of the spherical $Ru(dpp)_3$ doped polymer beads. Non-spherical beads were omitted from the count.

4.2.3.5 Surface carboxyl group quantification

Surface carboxyl groups present on the surface of the dye-doped PS-co-MA/BPA nano-beads can be used to functionalize the surface with bio-molecules such as proteins and antibodies. Functionalised nano-beads are useful for analyte quantification and imaging. The density of surface carboxyl groups determines the number of bio-molecules that can conjugate to an individual bead. Past studies have determined the surface density of carboxyl groups of polymeric nano-beads using conductometric titration [190, 191], zeta-potential measurements [192], fluorescence dye absorption [193] and FTIR spectroscopy [194].

Among these, conductometric titration requires the least sample pre-treatment and can be carried out in the same manner as a conventional titration, but using conductivity to determine the neutral point. When a base such as NaOH is added to an acidic solution (Phase 1, Fig. 4-10), the fast moving H^+ ions are essentially replaced by 'slower' Na^+ ions (Phase 2, Fig 4-10 & Equation 4E), which reduces the conductivity of the titrate.

$$H^+ + OH^- + H_2O + NaOH \rightarrow Na^+ + OH^- + 2H_2O \quad (4E)$$

This trend continues until an equivalence point is reached. Beyond this point, addition of base simply increases the number of ions in the solution and the conductivity increases again (Phase 3, Fig. 4-10). This equivalence point is essentially the minimum on the titration curve, which can be interpreted as the neutral point of the titration. The amount of base added to reach this equivalence point can be used to calculate the density of surface carboxyl groups on the beads. Before carrying out the titration, a conductivity meter (EC-con 6, RMS, UK) was first calibrated using a hydrochloric acid reference solution. 114.5 mg of the dye-doped beads were dispersed in 49 ml of distilled water and to this, 1 ml of 0.05 M sodium chloride solution was added. Titrations of the beads were carried out by adding 10 µl of 0.05 M sodium hydroxide solution at 1 min intervals with continuous stirring. The conductivity of the resulting solution was monitored and recorded carefully to determine the intersection point (Phase 2) (Fig. 4-10). This procedure was repeated three times with independent batches of polymer beads prepared using the optimised conditions determined in the previous section. (This experimental procedure was adapted from ref. [195])

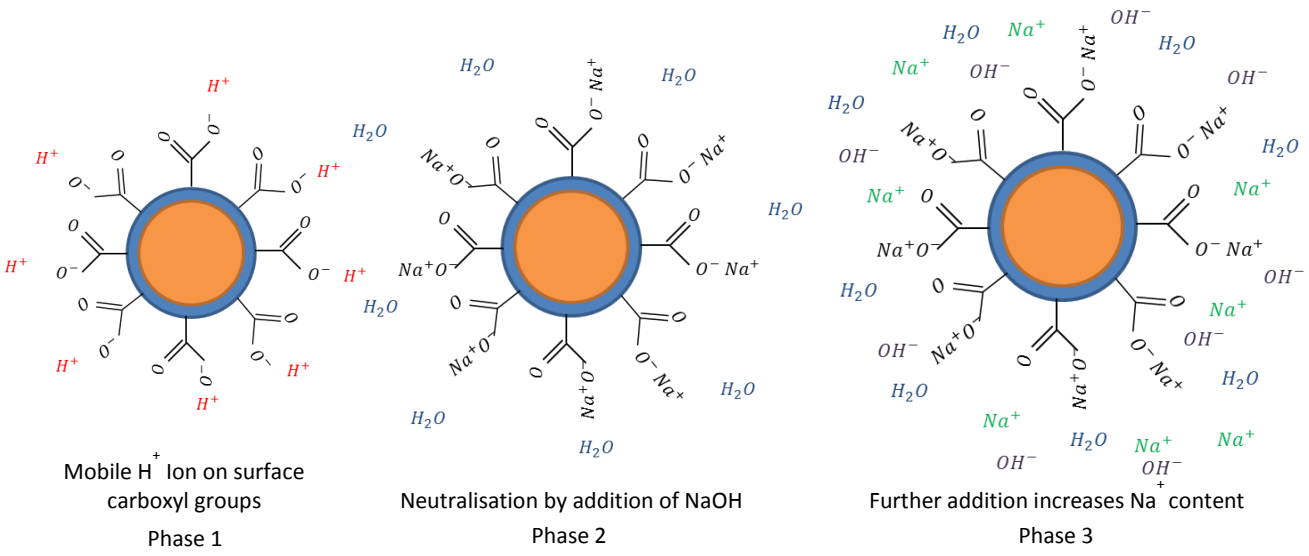


Fig. 4-10 – Schematic to show the titration procedure of $Ru(dpp)_3$ doped PS-co-MA/BPA bead. Phase 1) Beads are suspended in 1 mM NaCl solution to promote ion exchange and to further liberate protons. Phase 2) slow addition of 0.05 M NaOH solution neutralises the liberated protons, decreasing the solution conductivity due to decreased ion mobility. Phase 3) further addition of NaOH increases the overall ion content of the titrates, increasing the conductivity.

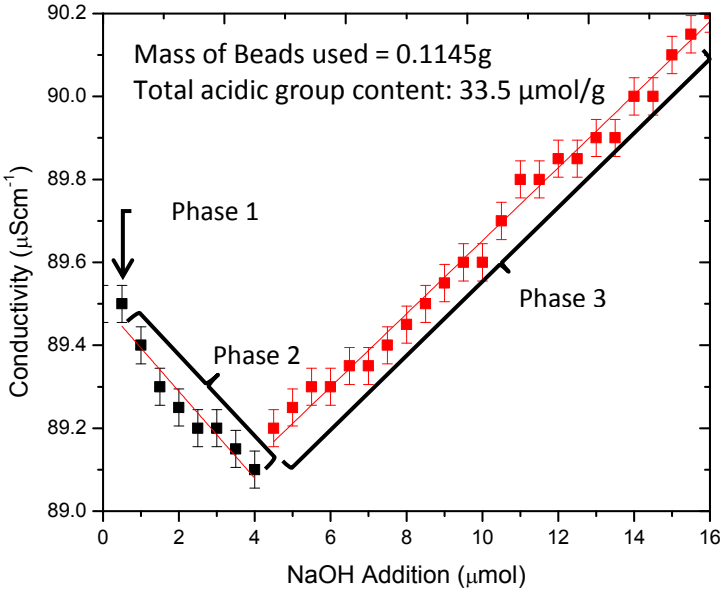


Fig. 4-11 Titration curve of $Ru(dpp)_3$ doped PS-co-MA/BPA bead. Equivalence point was reached with 76.8 µl of 0.05 M NaOH solution, which equates to 35.5 µmole/g of surface acidic group content.

From Fig. 4-11, it is evident that the equivalence point was reached upon addition of 76.8 µl of 0.05 M NaOH solution (3.84 µmol) to 114.5 mg of beads, which equates to 35.5 µmol g^{-1} of acidic group content. This value is far lower than the literature reported value for poly(methyl methacrylate)/ poly(acrylic acid) polymer beads (diameter = 6 µm, 240 µmolg^{-1} of surface acidic group content), but this can be controlled by altering the size of the polymer beads

4.2.3.6 Reality Check

Since there is no literature or data available for surface acidic group content of PS-co-MA/BPA nano-beads, the experimental value obtained in section 4.2.3.5 was checked for reasonability. Taking the density of the polymer beads to be approximately 1 gcm^{-3} and the distribution of bead diameter from Fig. 4-9, the numbers of polymer beads (table 4-1) was estimated to be 7.73 x 10^{13} g^{-1}.

	Diameter (nm)	Distribution (g)	Volume (cm^{-3})	Mass a single bead (g)	Number of beads (g^{-1})
	175	5.00E-03	2.81E-15	2.81E-15	1.78E+12
	185	1.50E-02	3.32E-15	3.32E-15	4.52E+12
	195	5.00E-03	3.88E-15	3.88E-15	1.29E+12
	205	1.00E-02	4.51E-15	4.51E-15	2.22E+12
	215	5.00E-03	5.20E-15	5.20E-15	9.61E+11
	225	1.50E-02	5.96E-15	5.96E-15	2.51E+12
	235	2.00E-02	6.80E-15	6.80E-15	2.94E+12
	245	4.00E-02	7.70E-15	7.70E-15	5.19E+12
	255	4.00E-02	8.68E-15	8.68E-15	4.61E+12
	265	3.50E-02	9.75E-15	9.75E-15	3.59E+12
	275	8.00E-02	1.09E-14	1.09E-14	7.35E+12
	285	7.00E-02	1.21E-14	1.21E-14	5.77E+12
	295	9.50E-02	1.34E-14	1.34E-14	7.07E+12
	305	8.00E-02	1.49E-14	1.49E-14	5.38E+12
	315	6.50E-02	1.64E-14	1.64E-14	3.97E+12
	325	5.50E-02	1.80E-14	1.80E-14	3.06E+12
	335	7.00E-02	1.97E-14	1.97E-14	3.56E+12
	345	9.00E-02	2.15E-14	2.15E-14	4.19E+12
	355	2.50E-02	2.34E-14	2.34E-14	1.07E+12
	365	6.00E-02	2.55E-14	2.55E-14	2.36E+12
	375	3.50E-02	2.76E-14	2.76E-14	1.27E+12
	385	3.00E-02	2.99E-14	2.99E-14	1.00E+12
	395	3.00E-02	3.23E-14	3.23E-14	9.30E+11
	405	1.50E-02	3.48E-14	3.48E-14	4.31E+11
	415	1.00E-02	3.74E-14	3.74E-14	2.67E+11
Total	N/A	1.00E+00	3.96E-13	3.96E-13	**7.73E+13**

Table 4-1 Total number of beads per gram taking into accounts the beads size distribution of the beads.

76.8 µL of 0.05 M NaOH solution was added to the bead suspension to reach the neutralisation point which equates to 35.5 µmol or 2.02 x 10^{19} NaOH molecules. From table 4-1 we calculated the theoretical number of beads in each size distribution. Multiplying by the surface area for each size calculated (table 4-2) we calculated the total surface area of the beads per gram. Assuming

that all carboxyl groups at the surface of the beads, dividing the number of NaOH molecules added by the total surface area per gram (1.99x 10^{21} $Å^2$ per gram), we obtain the surface area occupied by a single carboxyl groups, which is 98.65 $Å^2$. The surface area occupied by a single carboxyl group can be square-rooted to give the approximate spacing which equates to 9.93 Å (3.s.f). Assuming that all neutralised protons derive from carboxyl group are tightly packed (which in reality is an overestimate), this is within the reasonable range of the estimates.

	Diameter (nm)	Surface area of beads ($Å^2$)	Number of beads	Total Surface Area (Å^2)
	175	9.62E+06	1.78E+12	1.71E+19
	185	1.08E+07	4.52E+12	4.86E+19
	195	1.19E+07	1.29E+12	1.54E+19
	205	1.32E+07	2.22E+12	2.93E+19
	215	1.45E+07	9.61E+11	1.40E+19
	225	1.59E+07	2.51E+12	4.00E+19
	235	1.74E+07	2.94E+12	5.11E+19
	245	1.89E+07	5.19E+12	9.80E+19
	255	2.04E+07	4.61E+12	9.41E+19
	265	2.21E+07	3.59E+12	7.92E+19
	275	2.38E+07	7.35E+12	1.75E+20
	285	2.55E+07	5.77E+12	1.47E+20
	295	2.73E+07	7.07E+12	1.93E+20
	305	2.92E+07	5.38E+12	1.57E+20
	315	3.12E+07	3.97E+12	1.24E+20
	325	3.32E+07	3.06E+12	1.02E+20
	335	3.53E+07	3.56E+12	1.25E+20
	345	3.74E+07	4.19E+12	1.57E+20
	355	3.96E+07	1.07E+12	4.23E+19
	365	4.19E+07	2.36E+12	9.86E+19
	375	4.42E+07	1.27E+12	5.60E+19
	385	4.66E+07	1.00E+12	4.68E+19
	395	4.90E+07	9.30E+11	4.56E+19
	405	5.15E+07	4.31E+11	2.22E+19
	415	5.41E+07	2.67E+11	1.45E+19
Total	N/A	(Total: 7.24E+08)	7.73E+13	1.99E+21

Table 4-2 Surface areas of beads per gram taking into account the beads size distribution.

No. of NaOH molcule	Total surface area of beads (g)	Area occupied per group ($Å^2$)	Approximate spacing (Å)
2.02E+19	1.99E+21	98.65	9.93

Table 4-3 approximate spacing per surface carboxyl group taking into account the bead size distribution.

4.2.4 Time-Gated Photoluminescence Detection of the beads

The time-gated detection described in this section is a miniaturised detection system in development by *de Mello et. al.,* which focuses on detection of long-lived phosphorescence (τ > 1.0 µs): in particular, phosphorescence from the aforementioned $Ru(bpp)_3$ doped PS-co-MA/BPA nano beads. A photo of the device construction is shown in Fig. 4-14 and further technical details are provided in the appendix section 7-3. The time-gated device used an inorganic blue (480 nm) LED (E1L31-3B0A2, Toyoda Gosei, Japan) as the excitation source. This was driven with 20 mA, and pulsed at 20 kHz with a pulse duration of 6.154 µs. After the LED pulse, a long delay time of 3.249 µs was used to allow the LED light and any autofluorescence to decay to zero. The detection window follows shortly after this delay, and lasts for 40 µs which is sufficiently long to detect much of decay profile of $Ru(dpp)_3$. This cycle is repeated multiple times, where the total time taken per cycle was approximately 50 µs. A schematic to show the sequence of events in the time-gated detection is seen in Fig. 4-12.

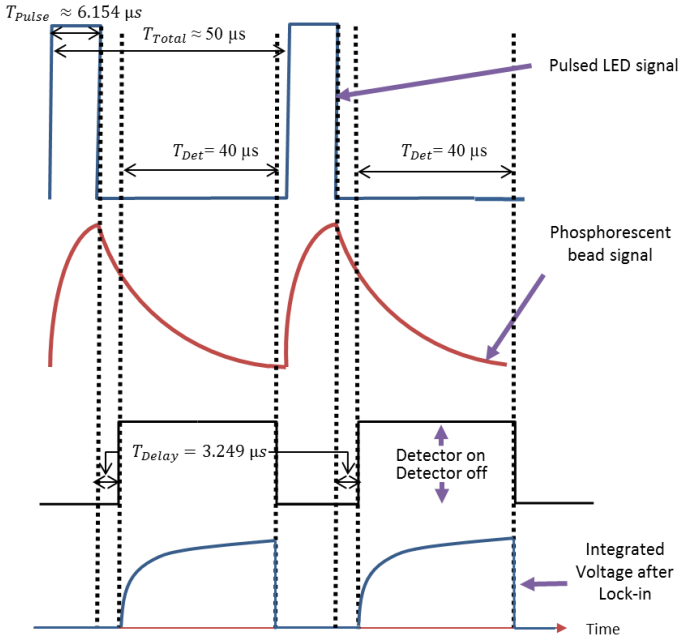


Fig. 4-12 Schematic to show the sequence of events in time-gated detection. One cycle is approximately 50 µs.

$Ru(dpp)_3$ doped PS-co-MA/BPA beads were fabricated under the optimised conditions described above and dispersed in water at various concentrations in the range 6.5 x 10^{-6} to 1.3 x 10^{-1} g/ml. experimental setup described in appendix section 7.3 was used in conjunction with a commercial digital lock-in amplifier (Stanford Research Systems SR830 lock-in amplifier instead of the 'miniaturised lock-in amplifier described in appendix – more details later in this section) to obtain the dose response curve

shown in Fig. 4-13A which shows a good linear response. The LOD of the beads was calculated to be 3.78 x 10^{-6} g/ml which is equivalent to 3.8 nmol (or 5 x 10^{-6} g) of $Ru(dpp)_3$ dye. This result is in agreement with earlier work by Edwards and demonstrates the highly sensitive nature of using a combination of phosphorescent labels and time-gated detection [163].

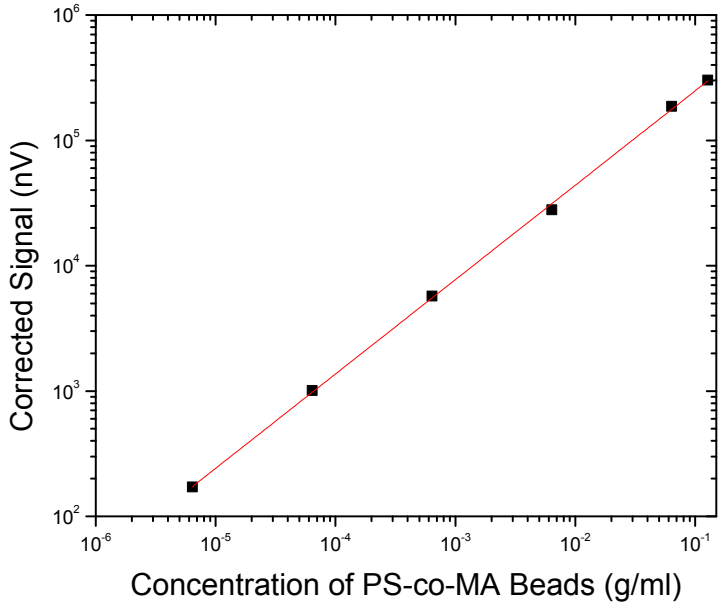


Fig. 4-13A Dose response curve for $Ru(dpp)_3$ doped PS-co-MA/BPA in aqueous solution, obtained using the time-gated detection system. Inorganic LED (E1L31-3B0A2, Toyoda Gosei, Japan) was used as an excitation source and silicon photodetector (S5972, Hamamatsu, Japan) as the detector.

Typical bio-assays require samples to undergo complex pre-treatment and analyte purification steps to preclude autofluorescence biomolecules – for example vast numbers of species in human urine autofluorescence under UV/blue light excitation [196]. To verify that phosphorescence detection does indeed solve this problem, 100 µL of highly fluorescent 0.01 M aqueous FDS solution (1 µmol) was added to our 200 µL phosphorescent bead suspension to create a strong fluorescence background. At the highest bead concentration (6.5 x 10^{-2} g/ml), $Ru(dpp)_3$ content was 93.6 nmol which makes the ratio between the $Ru(dpp)_3$ dye (phosphorescent) and FDS dye (fluorescent) approximately 1:1000, falling to 1:10,000,000 at the lowest bead concentration of 6.5 x 10^{-6} g/ml. All experimental details (concentration range and the time-gated setup) were kept exactly the same as before. For purpose of comparison dose response curves were also conducted without FDS (Fig. 4-13B). Measurements were taken so that signal intensity for FDS-free bead were recorded first, followed by an addition of FDS solution. The bead-FDS mixture was vigorously shaken before its luminescence intensity was recorded and this was repeated for all concentrations.

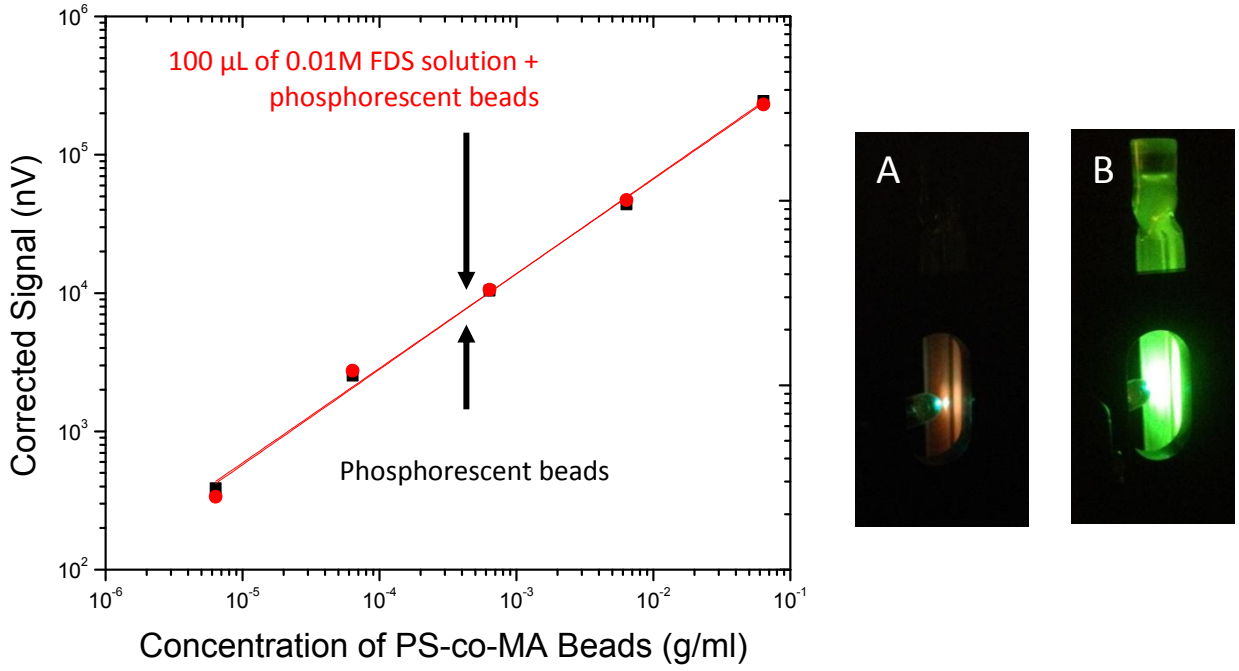


Fig. 4-13B (**Left**) Dose response curve for $Ru(dpp)_3$ doped PS-co-MA/BPA in aqueous solution, obtained using the time-gated detection system. Measurements shown on fig 4-13A were repeated with a fresh batch of beads. 100 µL of 0.01 M aqueous FDS solution were added to the FDS-less bead solution during the measurements. (**Right**) Picture taken during the experiment conducted in Fig. 4-13B. (**A**) $Ru(dpp)_3$ doped PS-co-MA/BPA in aqueous suspension and (**B**) the same $Ru(dpp)_3$ doped PS-co-MA/BPA aqueous suspension with 100 µL of 0.01 M aqueous FDS solution.

It is evident from fig. 4-13B that the addition of FDS did not affect the signal intensities of the phosphorescent beads. The LOD for both situations were found to be approximately 4.04 x 10^{-6} g/ml. This, along with pictures shown on Fig. 4-13B demonstrates the extremely high signal selectivity of the time-gated setup.

As a first step to low-cost phosphorescence detection miniaturised analogue lock-in amplifier (taken from ref [197] and built by Mr. Steve Atkins of Imperial College London) were built to replace the commercial SR830 lock-in amplifier and to demonstrate low-cost lock-in amplification (circuit diagram in appendix section 7.3). As a preliminary test of device operation, two sets of dye doped PVP polymer film on glass were fabricated using fluorescent FDS (fluorescein salt) and phosphorescent $Ru(dpp)_3$ respectively. Polymer films were fabricated by dissolving the dyes in an ethanoic solution of PVP and drop casted on glass slides. Fig 4-14A, 14B, and 14C shows a simple visual demonstration of the time-gated detection system using such dye doped polymer films and low cost lock-in amplification.

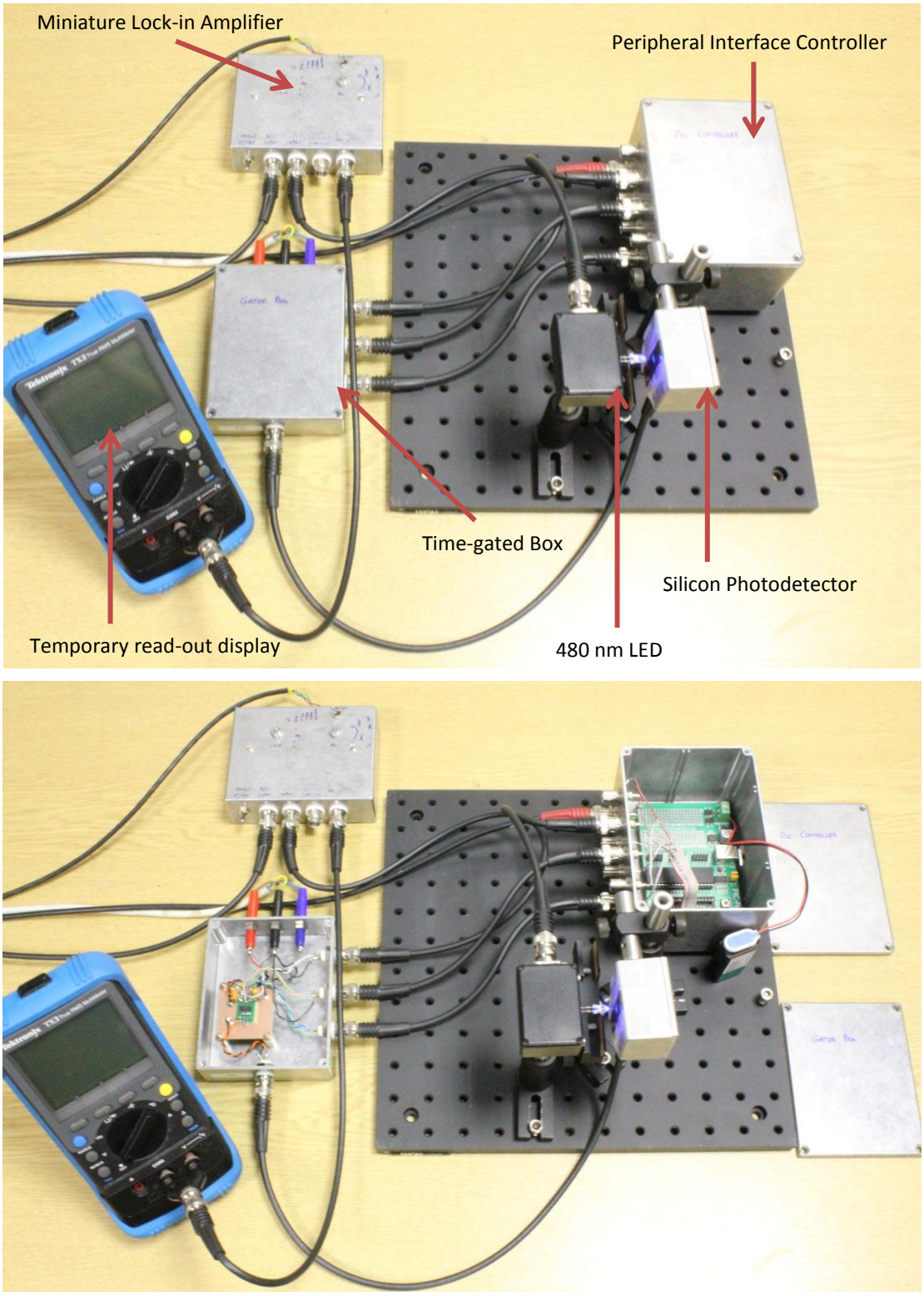


Fig. 4-14A Picture shows the prototype time-gated detection system under development by deMello et. al. The setup is connected to a voltmeter as a temporary read-out display for easier presentation. Picture below shows the internal electronics - needless to say that this device can be further miniaturised.

Both polymer films exhibited strong luminescence under 480 nm LED excitation. FDS in polymer films have a very short lifetime of 7ps, [198] and hence the no emission is detectable in the detection window of 9.403 to 49.403 µs.

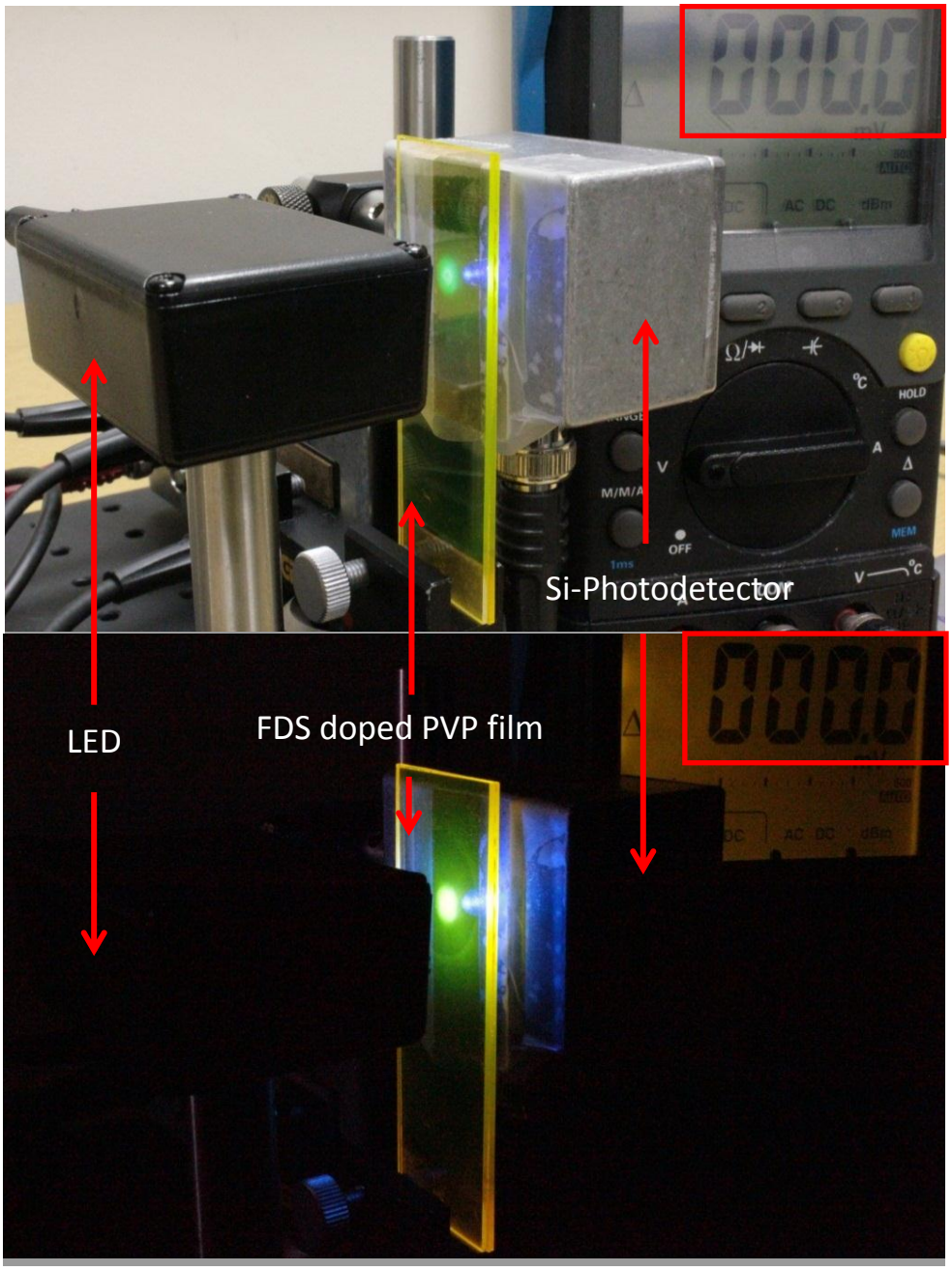


Fig. 4-14B Picture shows the time-gated setup under operation with FDS doped PVP film. Read out from the Lock-in amplifier indicates no-signal in both dark and ambient light conditions for FDS PVP films, since time-gated detection rejects signals that are not in its detection window.

On the other hand, the same measurement repeated with a $Ru(dpp)_3$-doped PVP film, gave a high signal (105.9 mV). This is because $Ru(dpp)_3$ has a long luminescence life-time ($\tau \approx 5\mu s$) which overlaps with the detection window of the time-gated system. This system is still under development by deMello et. al. and the time-gated measurements reported henceforth used the commercial lock-in amplifier

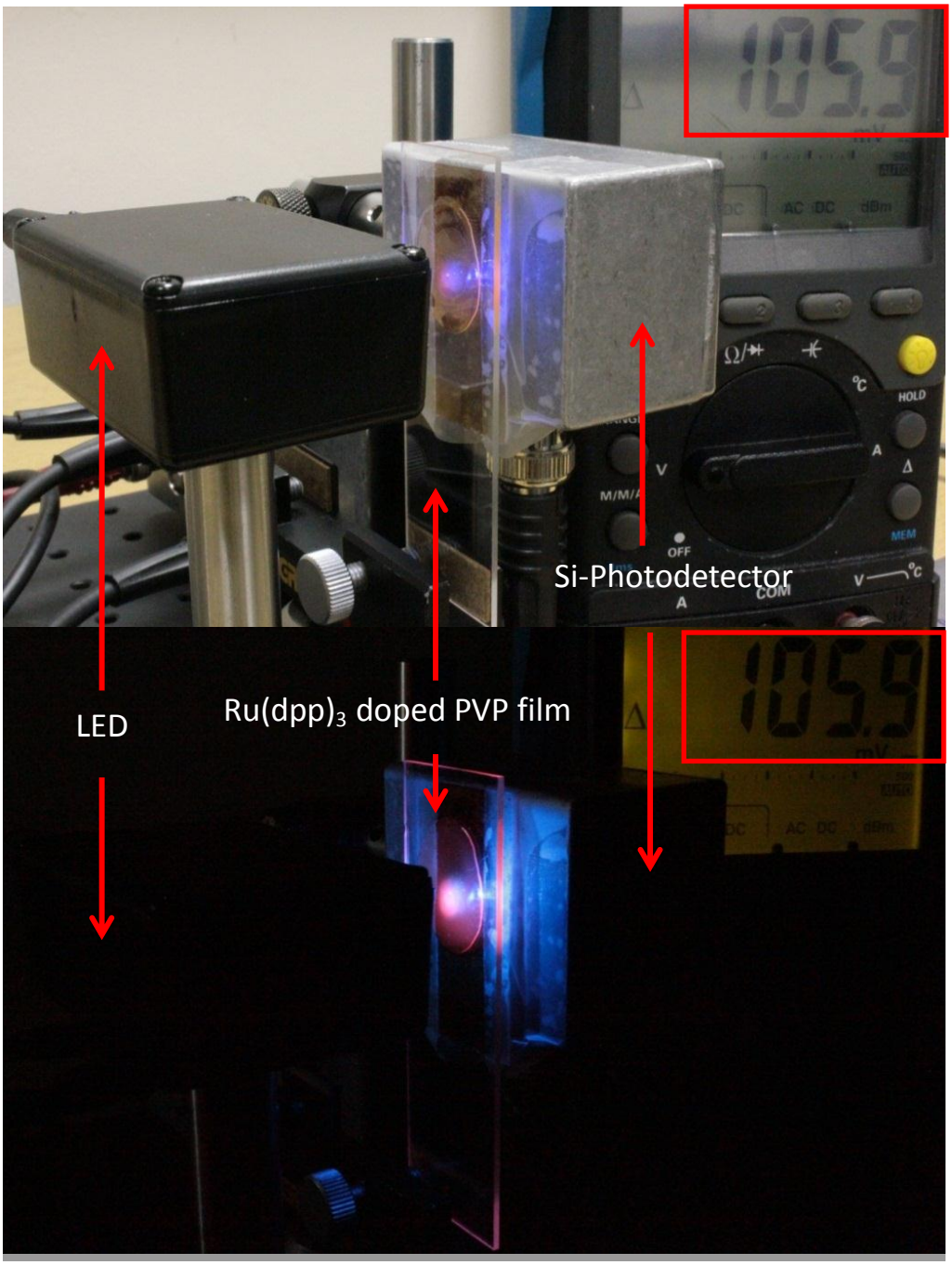


Fig. 4-14C Picture shows the time-gated setup under operation with $Ru(dpp)_3$ doped PVP film. Read out from the Lock-in amplifier indicates high luminescence signal in both dark and ambient light conditions, since time-gated detection can detect the long-lived phosphorescent decay signal that overlaps with its decay window.

4.3 Biotin Detection using $Ru(dpp)_3$-doped PS-co-MA/BPA beads

4.3.1 Bio-functionalized Polymer beads

4.3.1.1 Introduction to Biotinylation

Biotin is also known as Vitamin H or Vitamin B_7 and it is a water-soluble vitamin. It is essential for cell growth and metabolism of various biomolecules (such as fats and amino acids) [199]. While biotin is synthesised in various bacteria [200, 201] and plants [202], humans are incapable of synthesising biotin and our need for this vitamin is met by dietary intake. Biotin deficiency in humans can lead to serious pathological symptoms such as Sudden Infant Death Syndrome (SIDS), Leiner disease and Rett syndrome [203]. Hence it is crucial to diagnose and monitor patients with biotin deficiency. It is also important to accurately determine the levels of biotin in food and supplements. Hence it is not surprising that various analytical techniques, such as microbiological culturing and physicochemical methods [199] have been developed to quantify the biotin levels. The latter predominantly relies on the strong non-covalent interaction of biotin and a labelled streptavidin.

Streptavidin is a protein with an extremely high affinity for biotin, with a dissociation constant (K_d) of 4 x 10^{-14} M, is the strongest noncovelant biological interaction known [204]. Biotin-streptavidin conjugates are extensively used in biochemistry due to their stability over a wide range of pH values and temperatures [204]. Importantly, properties of biotin, such as its solubility and specific reactivity, can be customised very easily without compromising its streptavidin binding capabilities. Biotin is made from two components: a streptavidin binding component and a valeric acid component (Fig. 4-15). The valeric acid component can be altered to give various forms of biotin, such as amine-PEG_8-biotin, which has increased solubility in aqueous medium due to its polyethylene glycol spacer arm, and can be readily biotinylated with carboxyl groups present on other molecules. A wide range of customised biotins are commercially available, which simplifies the process of designing assays based on biotin-streptavidin conjugates.

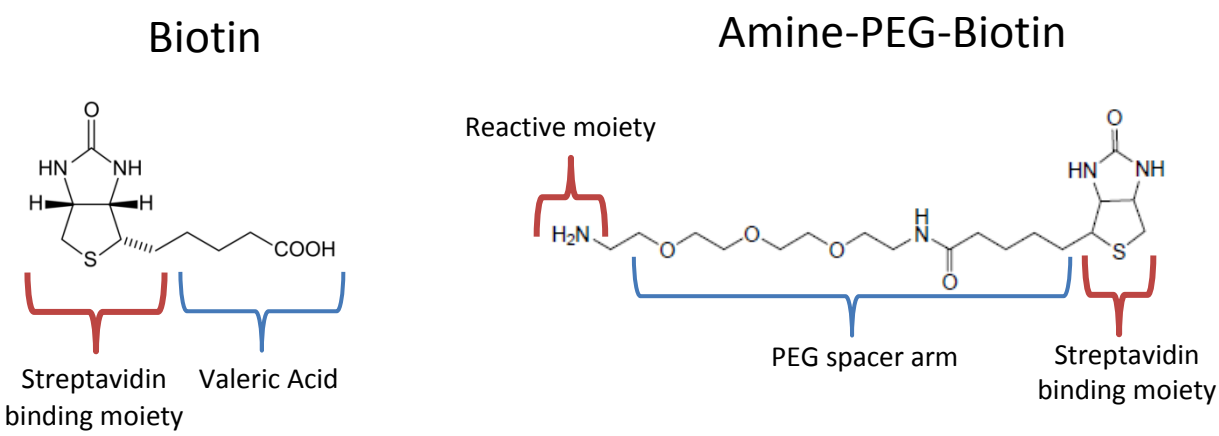


Fig 4-15 Chemical structure of Biotin and its variant, amine-PEG-Biotin. Valeric acid component of Biotin can be modified to accommodate side groups such as amine-polyethylene glycol (PEG) spacer arms. Solubility of the biotin can be modified through use of such side groups, and spacer arm lengths are typically modified to reduce steric hindrance (to improve detection sensitivity).

To use our synthesised phosphorescent beads for bio-sensing applications, the surface carboxyl groups must be bio- functionalised [205]. Biotinylation of surface carboxylic acid containing polymer beads has been reported before by Gole et. al., and can be effected by simple 1-ethyl-3-(3-dimethylaminopropyl) carbodiimide hydrochloride (EDC) mediated cross-linking chemistry [206]. Biotinylation of the $Ru(dpp)_3$ doped PS-co-MA beads was carried out using the methods outlined in ref. [207, 208] as described in the next section.

4.3.1.2 Biotinylating the Phosphorescent Nano Beads

The materials used for biotinylating the beads were: 1) Amine-PEG_8-Biotin (Sigma Aldrich, UK) which is a water solubility-enhanced biotin with a long PEG spacer arm to reduce any steric hindrance between the beads and streptavidin. 2) EDC (Thermo Scientific, UK) as a carboxyl and amine reactive cross-linker and 3) Sulpho-NHS (Thermo Scientific, UK) to stabilise the formed ester bond between the carboxyl groups on the bead and the EDC (Fig. 4-16) which prevents carboxyl regeneration (i.e. formation of non-biotinylated beads). EDC-mediated biotinylation is activated at pH 6.0 [208] and hence all biotinylation reactions were carried out with a 0.1 M MES buffer (2-(*N*-morpholino)ethanesulfonic acid buffer, Sigma Aldrich, UK). $Ru(bpp)_3$ doped PS-co-MA/BPA nano-beads were prepared according to the procedures outlined in section 4.2.3.2. The resultant beads were weighed and centrifuged three times with a 0.1 M MES buffer. The bead concentration was kept constant at 10 mg/ml. To this washed bead solution, 100 µl of 10 mM EDC solution (in MES buffer) and 1.1 mg of Sulpho-NHS was added and shaken vigorously for 15 minute at room temperature. 0.5 to 0.05 nmol of amine-PEG_8-biotin MES solution was added to the resultant solution. The resulting mixture was vigorously shaken for 2 h to

allow the biotinylation to complete. The biotinylated beads were centrifuged again for three times with 0.1 M PBS (Phosphate buffered saline at pH 7.2, Sigma Aldrich, UK) to stop the reaction and to remove any free biotin/cross-linkers.

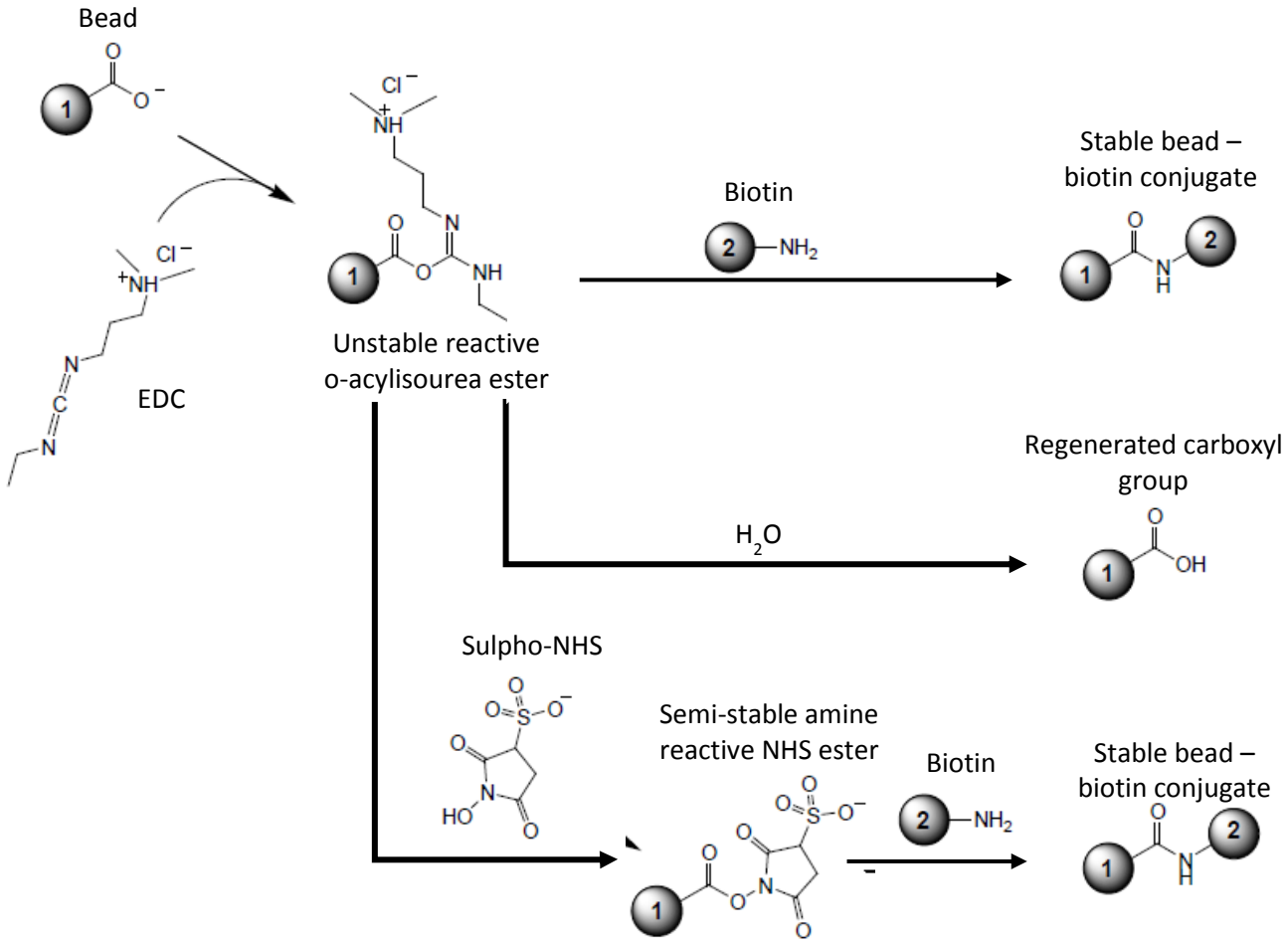


Fig 4-16 Scheme showing how the biotinylation of the synthesised beads was carried out. Addition of EDC and Sulpho-NHS to the beads forms semi-stable amine reactive NHS ester. This prevents any carboxyl groups from being regenerated and ensures that all available carboxyl have reacted. Addition of amine-PEG_8-biotin forms a stable amide bond between the carboxyl groups on the beads and the amine moiety of biotin. The reaction is carried out in a 0.1 M MES solution at pH 6.0. Finally the reaction is 'quenched' by washing the biotinylated beads with 0.1 M pH 7.2 PBS. Beads were purified multiple times using a centrifuge to remove any free biotin and reactants.

Attenuated Total Reflectance – Fourier Transform Infra-Red (ATR-FTIR) analysis is a technique that enables the measurement the IR absorbance spectra without any pre-sample treatment [209]. Study of biotin with ATR-FTIR has been reported by Barbucci et. al., [209] and in the current context offers a simple means to confirm successful biotinylation.

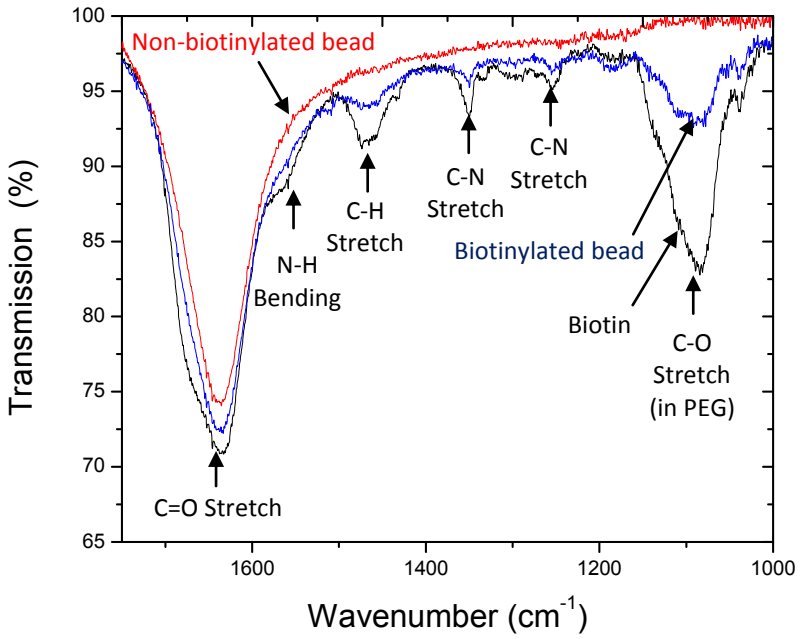


Fig 4-17 ATR-FTIR spectrum of biotinylated $Ru(dpp)_3$-doped PS-co-MA/BPA beads. Also shown are the control spectrum of non-biotinylated $Ru(dpp)_3$-doped PS-co-MA/BPA beads and biotin for comparison. Biotinylated beads were extensively washed with 0.1 M PBS to eliminate any un-bound biotin.

Fig. 4-17 shows the IR absorption spectra of the biotinylated beads, obtained using an ATR-FTIR spectrometer (Universal diamond ATR-3, Perkin-Elmer, U.S.). For comparison, spectra of biotin and non-biotinylated beads were also recorded. Characteristic C=O peaks (ν = 1650 cm^{-1}) [209] were observed for all samples corresponding to the carbonyl group on both the biotin and the beads. All other amine (C-N /N-H bond stretch at 1550, 1350, and 1260 cm^{-1} respectively) and ether (C-O bond stretch at 1081 cm^{-1} in PEG) related peaks were observed in the IR spectrum of the biotin and the biotinylated beads. These peaks were not observed with the non-biotinylated beads. It is evident from Fig. 4-17 that biotinylation of the beads were successful. However, functionalization of nanoparticles can have an adverse effect on their optical properties. Examples of such negative interactions have been reported by Aslan *et.al,* where reduction in emission was observed upon biotinylating a fluorphore-labelled anti-biotin, [210] reducing the sensitivity of the bead. To evaluate the effect of biotinylation on the optical performance of the beads, emission and excitation spectra, emission lifetime, and quantum efficiencies were measured before and after biotinylation. Emission and excitation spectra were obtained using the same experimental procedure outlined in section 2.7.2 (Fig. 4-18). (Note: Clean absorption spectra could not be obtained due to scattering from the beads)

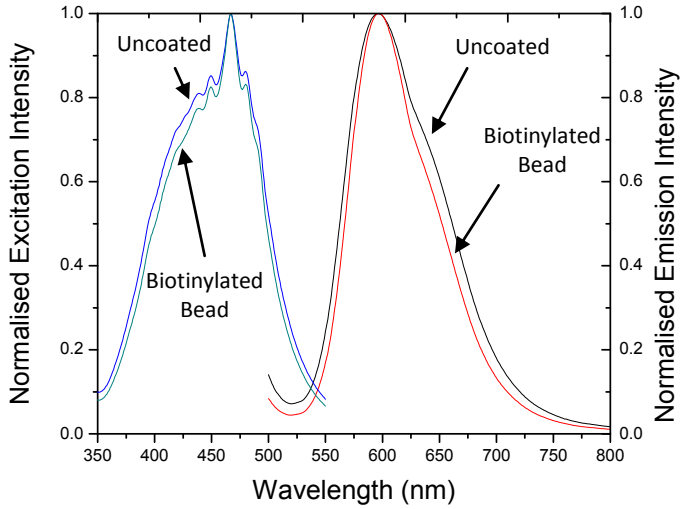


Fig 4-18 Emission and excitation spectra of the biotinylated beads. Also for comparison are the spectra for non-biotinylated beads.

An approximate 8 % reduction in both excitation and emission intensities was observed upon biotinylation, attributable to the weak biotin absorption in the visible range [211, 212] and a potential loss of surface-bound $Ru(dpp)_3$ dye during the biotinylation procedure. Phosphorescence lifetimes of the beads were measured using the Time Correlated Single Photon Counting technique (TC-SPC)- see appendix section 7.5. Photoluminescence quantum efficiencies (PLQEs) of the beads were also measured to evaluate any changes in the photo-physical properties upon biotinylation although no significant differences were expected given the similarity in emission lifetimes. The time resolved data reveals that biotinylation has a minimal effect on the lifetime of the beads (Fig. 4-19). This suggests that PS-co-MA/BPA is a stable encapsulant, and implies that majority of the dye is out of reach from any dissolved oxygen quencher.

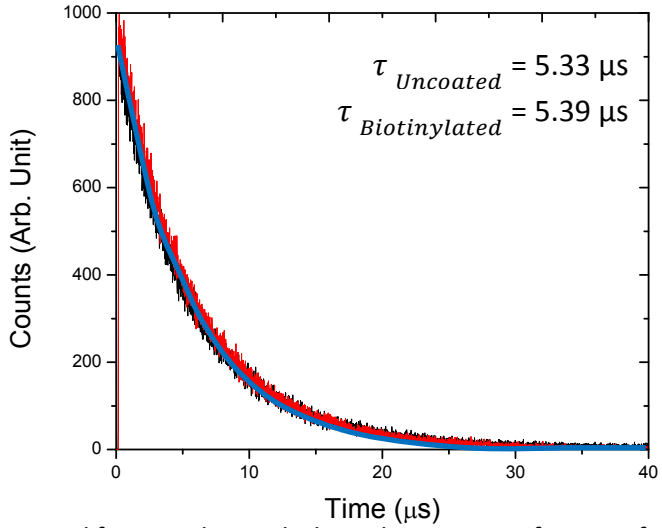


Fig 4-19 Phosphorescence lifetime obtained through TC-SPC. Lifetime of both beads show negligible differences.

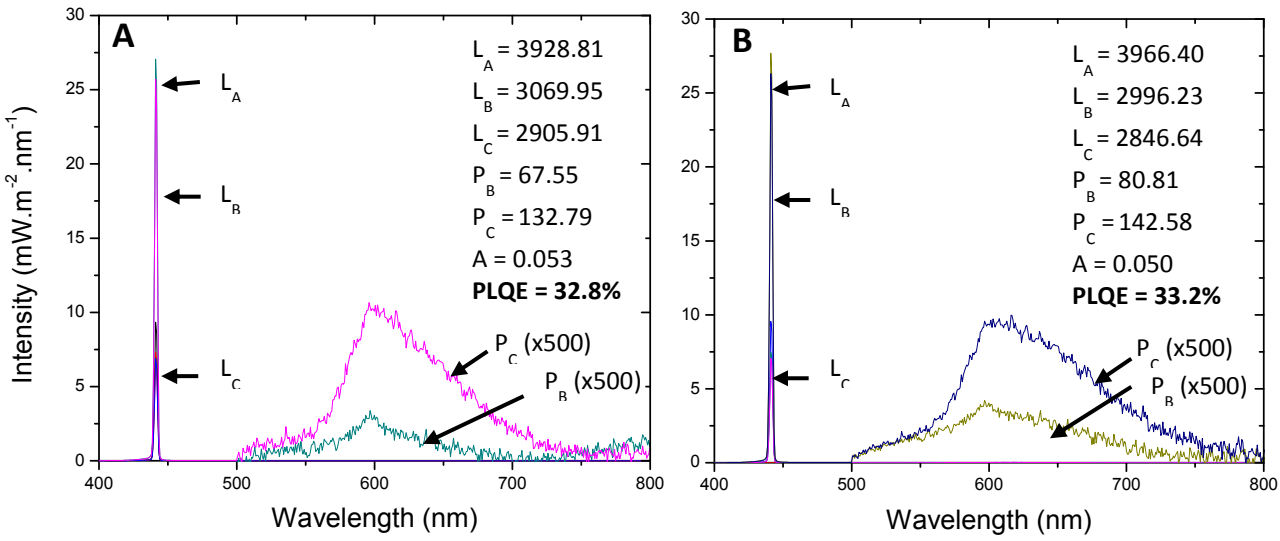


Fig 4-20 PLQE data obtained through integration sphere measurements of **A**) non-biotinylated beads and **B**) biotinylated beads due to the scattering nature of the beads. Equipment used for this experiment is identical to that of chapter two, section 2.6. Measurements were carried out with 8 ms and 30 ms integration times – see chapter 2 section 2.6. Units for all the experimental parameters are in mW.m^{-2}.

Measuring the photoluminescence quantum yield by comparison with a reference solution [107] proved to be very difficult since the bead solutions were very scattering and hence the same experimental setup and procedure as that from section 2.6 was used. Samples used were 1) 0.06 g/ml phosphorescent beads, 2) approximately 0.06 m/ml of biotinylated beads, and 3) magnetic-bead-biotinylated bead conjugate (with 0.5 nmol of biotin). 0.1 mm quartz cuvettes were used for all measurements. The photoluminescence quantum yield for the non-biotinylated beads was 32.8 ± 5% which is in agreement with the results that Edwards observed [163]. Biotinylation of the beads had no significant effect on the PLQE of the beads, which was recorded to be 33.2 ± 5 %. (Fig. 4-20)

4.3.2 Magnetic Beads

4.3.2.1 Using magnetic beads

Up until this point the biotinylated beads were purified by centrifugation in PBS buffer to remove any small molecular weight solute such as unbound biotin and EDC. However, this did not allow us to separate the biotinylated beads from the non-biotinylated beads. Typically, in other assays employing polymer labels, the conjugated beads are separated by a using lengthy dialysis/desalting column process [213, 214], which relies on filtering the molecules through a semi-permeable membrane. Using such techniques often results in high sample loss and makes accurate quantification of the analyte difficult. The use of magnetic nano-beads offers a simple and elegant way of separating the biotinylated

and non-biotinylated beads. The magnetic beads used here had an iron core and were magnetised when subjected to an external magnetic field [215] i.e. they were superparamagnetic. The outer shell polymers can be purchased with specific molecular tags, which in our case was streptavidin. As previously mentioned, streptavidin has a high binding affinity with biotin and the streptavidin/biotin linkage can be used to join the magnetic beads and the biotinylated beads. The magnetic beads can then be extracted by using a magnet, taking with them any biotinylated beads to which they are attached. (Fig. 4-21A & 21B)

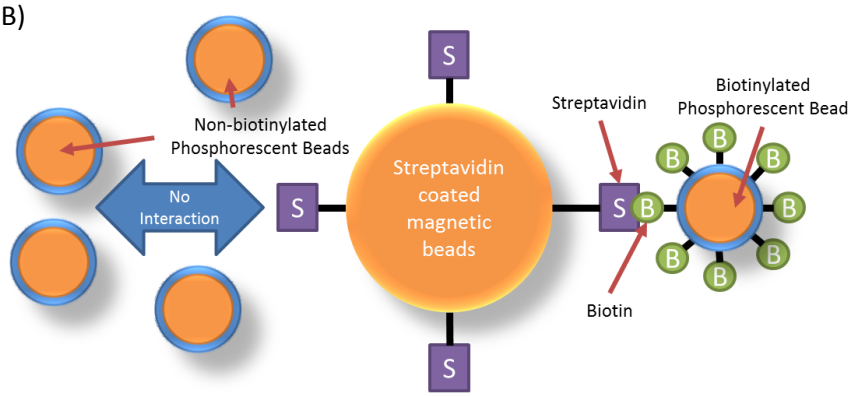


Fig 4-21 Schematic to show the biotinylated bead filtration using the streptavidin coated magnetic beads (Dynabeads®MyOne™ Streptavidin C1, Life Technology, UK). The magnetic beads are large in size (1 µm) compared to the phosphorescent beads (approximately 300nm). The long spacer arm of the amine-PEG_8-biotin (Sigma Aldrich, UK) allows multiple beads to be anchored to the magnetic beads via the streptavidin-biotin link.

4.3.2.2 Experimental

Five bead (in PBS) solutions with concentration of 0.1 g/ml were biotinylated with various biotin concentrations outlined in table 4-4. These concentrations were chosen according to the biotin binding capability of the streptavidin coated magnetic beads (2.5 nmol/mg) (Dynabeads®MyOne™ Streptavidin C1, 10mg/ml Bead suspended in PBS, Life Technology, UK) The biotinylated beads were thoroughly washed in pH 7, 0.1 M PBS solutions. The beads were also washed three times in PBS solution immediately before use and re-suspended in 1 ml of PBS solution. 100 µL of Dynabeads were added to our washed biotinylated beads and shaken for 2 hours. The magnetic beads and any bound biotinylated beads were extracted by using a neodymium magnet as shown on Fig. 4-22. The neodymium magnet was placed in close proximity to the sample container for 5 min and the conjugated magnetic beads were collected on the inner container surface. Using a pipette, the supernatant PBS solution containing the non-biotinylated beads was carefully removed and the magnetic beads were re-suspended in 1 ml of fresh PBS solution. This process was repeated three times before re-dispersing the solid in a 1.0 mm quartz cuvette with 0.01 M PBS solution for analysis using the time-gated detection system. The

removed supernatant solution from the first wash was also washed by centrifugation, re-suspended, and stored for further analysis.

Sample No.	Bead (g/ml)	Biotin added (nmol)	Magnetic Bead Added (µL)	Binding Capability of Magnetic Beads (nmol/µL)
1	0.1	0	100	2.5
2	0.1	0.005	100	2.5
3	0.1	0.05	100	2.5
4	0.1	0.25	100	2.5
5	0.1	0.5	100	2.5

Table 4-4 Amount of biotin used in the biotinylation step. Amounts of Magnetic beads added were determined by their binding capacity.

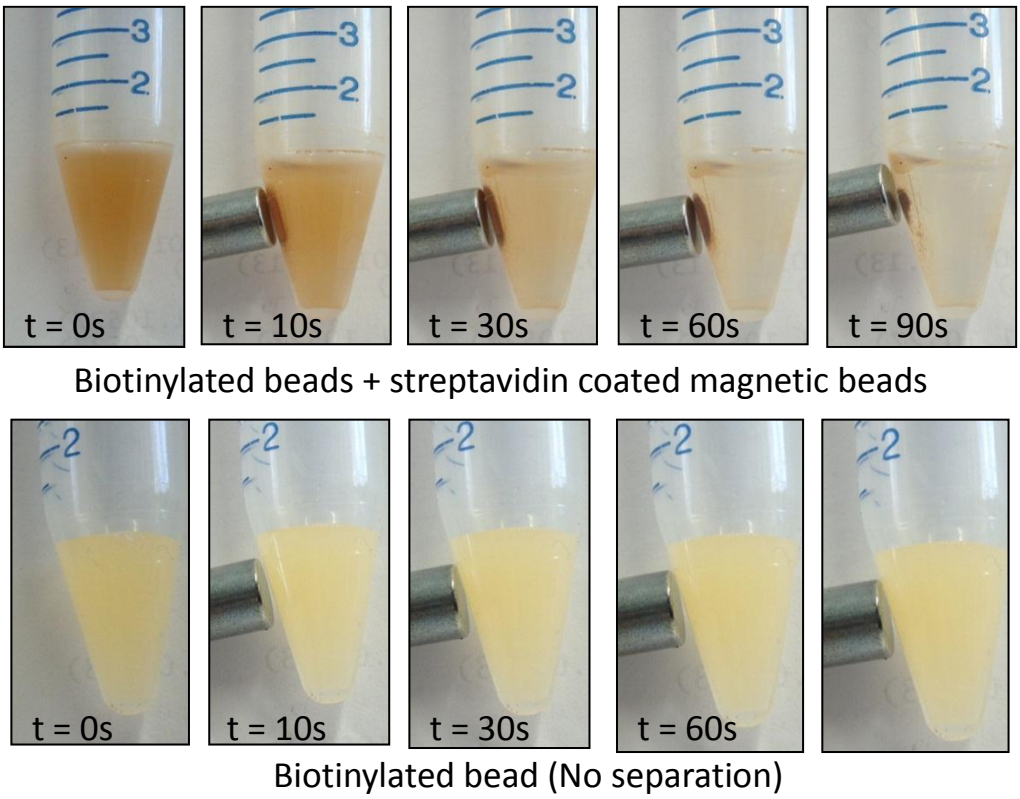


Fig. 4-22 Pictures taken at various time intervals during the magnetic beads removal process. Also shown for comparison are the biotinylated beads without the magnetic beads. The magnet was used to attract the magnetic beads (magnetic beads-streptavidin-biotin bead conjugate) to the side, and the supernatant solution containing the non-biotinylated beads was pipetted out. This purification procedure was repeated at least four times and the final solid was then dispersed in 1 ml 0.1 M PBS.

Time-gated detection described here used the same experimental set-up outlined in section 4.2.4. 100 readings at one second interval were recorded and the dose response curves obtained through these measurements are shown in Fig. 4-23. Also shown for comparison are the signals measured for the supernatant solution for each of the biotin concentrations.

4.3.2.3 Effect of conjugation

Conjugation to the magnetic beads did not cause any change to the bead's optical characteristics. Fig. 4-23 shows the excitation/emission spectra, lifetime, and the PLQE measurements for phosphorescence beads in isolation and coupled to the magnetic beads.

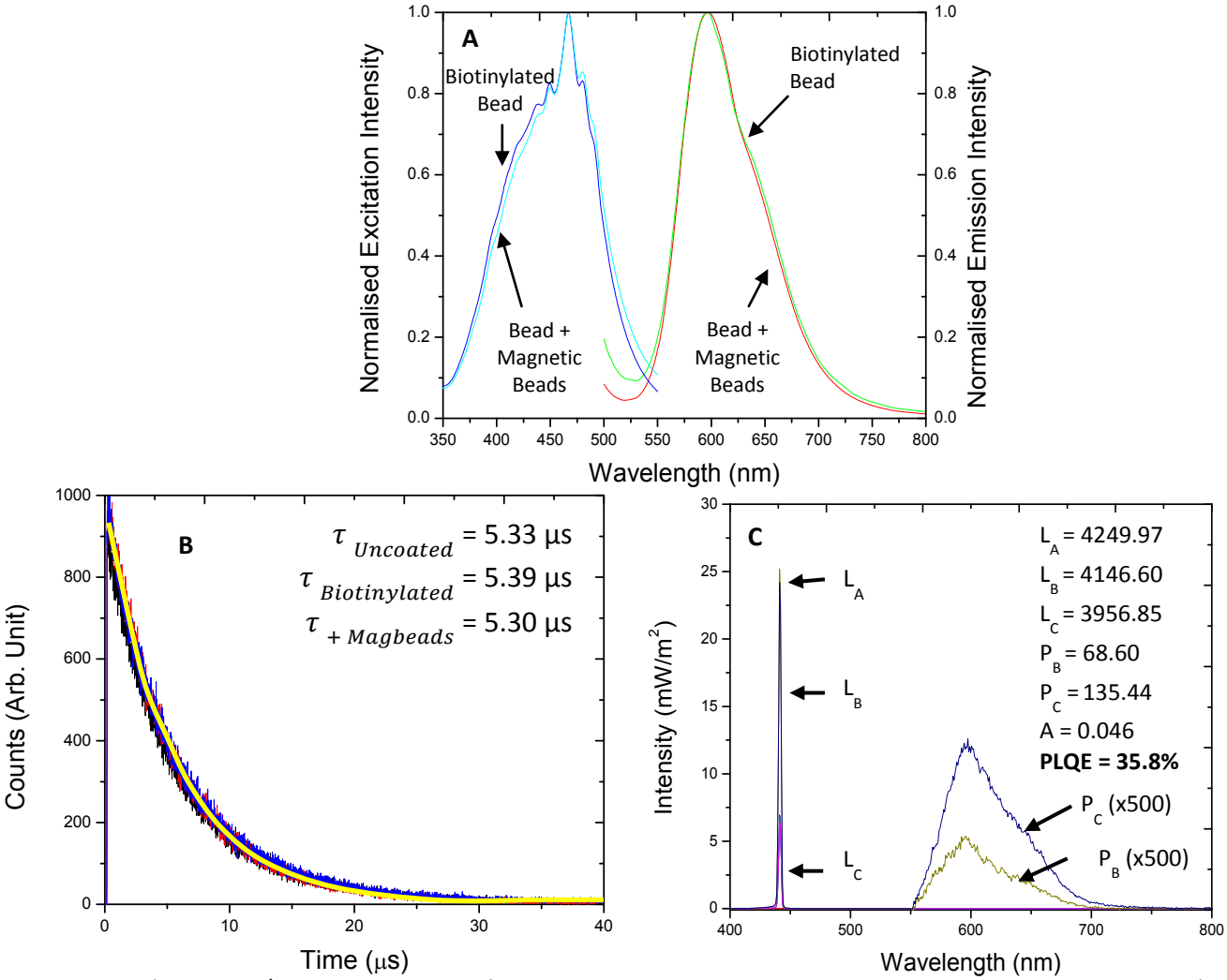


Fig. 4-23 A) Emission/excitation spectra of the magnetic bead conjugate compared to biotinylated beads. B) Phosphorescence lifetime of the magnetic bead conjugate. Also shown are results for the bead in their biotinylated and biotinylated forms. C) PLQE spectra of the magnetic bead conjugate. All measurements were acquired with the same procedure and equipment as section 4.3.1.2.

An approximate 1-2 % reduction in both excitation and emission intensities can be attributable to potential bead loss during the centrifugation procedure. It is evident from Fig. 4-23 that there was negligible change in both lifetime and photoluminescence quantum yield values which suggests that $Ru(dpp)_3$-doped PS-co-MA/BPA polymer beads can be bio-functionalised without any consequence to its optical characteristics.

4.3.2.4 Biotin detection

Looking at Fig. 4-24, it is evident that magnetic beads were able to interact with the biotinylated beads and the extraction of the conjugated beads was successful. As shown in Fig. 4-24, correlation between the biotin concentration and the signal intensity was not linear and showed a power fit response ($y = 28369x^{0.452}$). Defining the limit of detection Λ as the concentration of analyte that yields a signal equal to the blank plus three times the standard deviation of the blank, we obtained LOD of , $\Lambda = 3.78 \times 10^{-6}$ g/ml for the non-biotinylated beads (obtained in section 4.2.4). This is equivalent to 0.6 nmol of biotin detection limit - assuming 100 % biotin coverage of the beads, but the actual LOD of biotin was found to be better than expected, with a 0.011 nmol/ml detection limit. This indicates that there was lower surface biotin coverage of individual beads due to the low availability of biotin at lower concentration, which meant that the biotin: phosphorescent bead ratio is higher at lower concentration, giving rise to relatively high phosphorescence intensity. This may explain the power relationship between the biotin concentration and the phosphorescence signal intensity, where at higher concentrations each beads has a higher biotin coverage, which decreases the sensitivity of the beads. (Fig. 4-24)

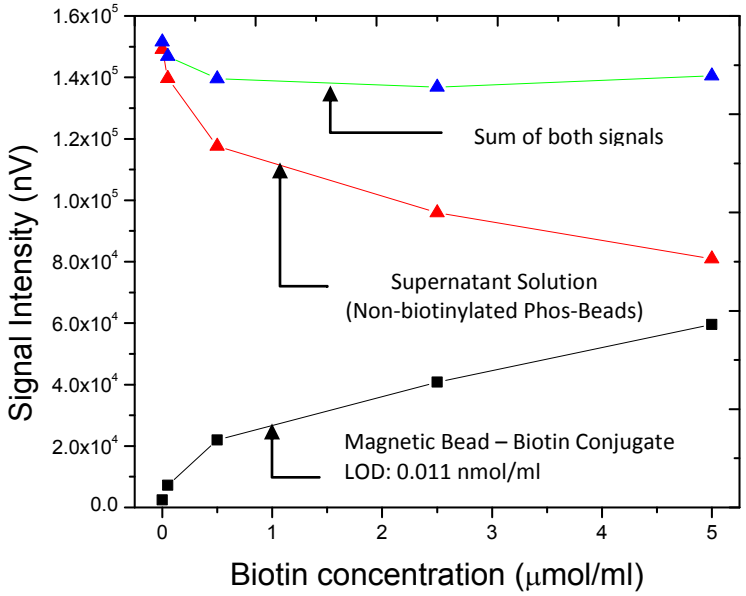


Fig. 4-24 Phosphorescence signal intensity response to biotin concentration. Also plotted are the signal intensity of the supernatant and the sum of both phosphorescence signals.

As expected, the phosphorescence intensity of the supernatant (non-biotinylated beads) was the approximate mirror image of the signal obtained from the biotinylated beads. Adding the two intensities together should give the phosphorescence intensity of the total beads used (0.1 g/ml) which,

according to the results acquired in section 4.2.4, is expected to be approximately $1.6x10^5$ nV. However the signal intensity returned was $1.46x10^5 \pm 4x10^3$ nV. The most probable reason for this 8.7% decrease is due to the loss of non-biotinylated beads during the washing stage of the supernatant. These measurements were repeated with a fresh batch of beads which yielded similar results.

To see the effect of the magnetic bead concentration on the phosphorescence signal, the experiment was repeated with half the number of Dynabeads (from 100 µL → 50 µl). The concentrations of all other parameters were kept the same. As expected, the signal intensity maximum is reached faster (see Fig. 4-24) and a similar LOD of 0.009 nmol/ml was observed. Furthermore, the phosphorescence intensity of the supernatant non-biotinylated beads was measured without any washing procedure. Adding the signals from the magnetic beads and the non-biotinylated beads from the supernatant, gave us full signal recovery, and the decrease in total signal noted above was not observed.

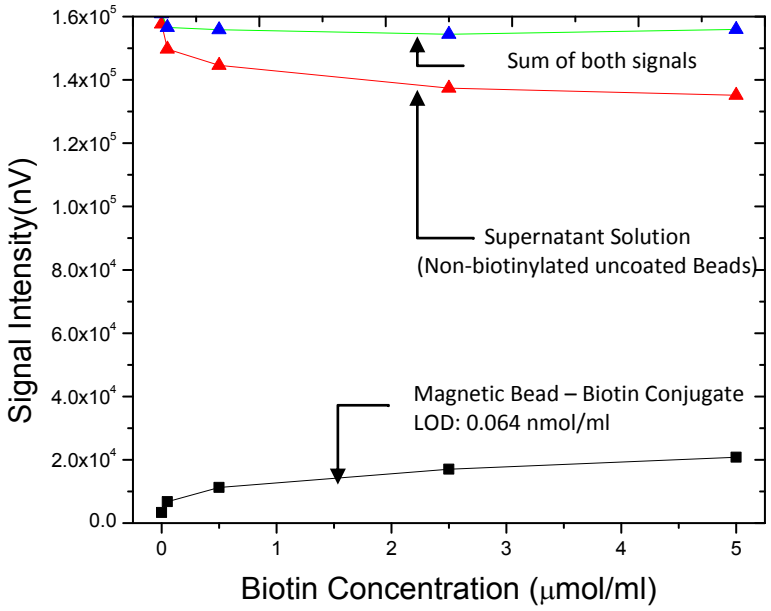


Fig 4-24 Plot shows the phosphorescence signal intensity response to biotin concentration. Also plotted are the signal intensity of the supernatant and the sum of both phosphorescence signals. Concentration of the magnetic beads used here was halved and the supernatant solutions were not 'washed'.

Commercial fluorescent label based biotin assays that use microplate reader, have typically has a LOD of approximately 0.005 nmol/ml [216] which shows the highly competitive nature of our low-cost time-gated detection system. With further optimisation of the phosphorescent bead's sensitivity there is no doubt that we can achieve far better LOD.

4.3.2.5 Photostability of the Beads

One of the most important properties that these luminescent polymer beads must have for their application in bio-assays is stable luminescence over time. In some cases, the photostability of such beads can be low due to insufficient encapsulation, allowing dissolved oxygen in the environment to permeate through the bead. The photostability of the phosphorescent beads and their conjugates was determined by recording their luminescence intensity over time using the time-gated detection system from section 4.2.4. The light source used an inorganic blue LED (E1L31-3B0A2, Toyoda Gosei, Japan) driven at 20mA to give a light intensity of 1300 mcd.

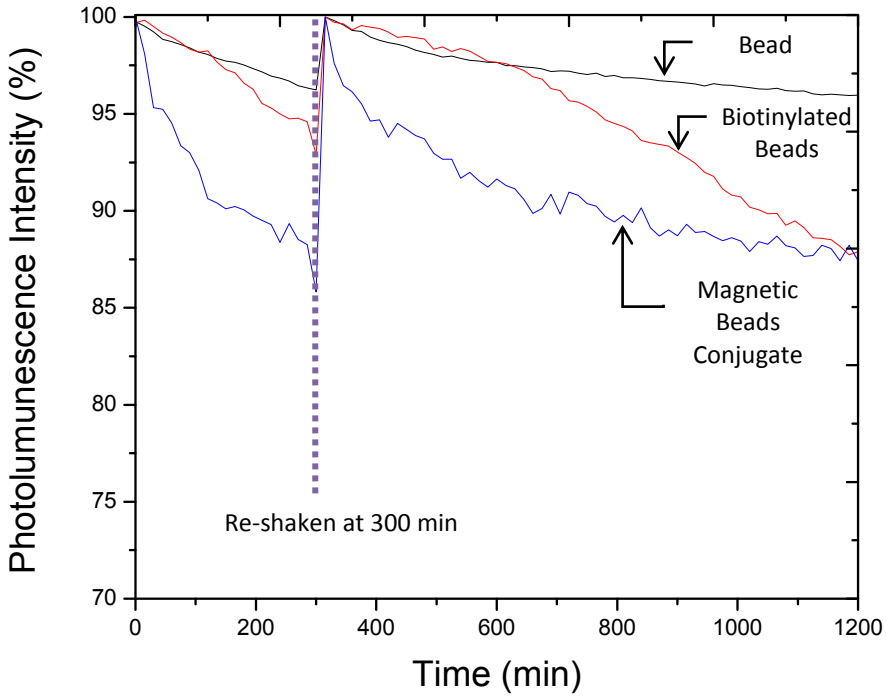


Fig 4-25 Plot shows the phosphorescence signal intensity of the beads over a span of 1200 min

In the first 300 min of testing, a rather worrying reduction in photoluminescence stability was observed for all three beads of order 5 %-15 %. However this is attributable to the 'dense' nature of the beads where the beads 'settle' to the bottom over time. Signal intensity was recovered by shaking the samples to re-disperse the bead sedimentation. It is evident from fig 4-25 that the signal falls away fastest for the heaviest magnetically coupled bead samples, undergoing a 15 % reduction in the first 300 min. The signal of the lightest uncoated phosphorescence beads showed much slower decrease rate of just 3 %. Fig. 4-26 shows a photo of a plastic 10 x 10 mm cuvette containing phosphorescent beads

suspended in water, left to settle for 48 h at standard room temperature. It is evident from Fig. 4-26 that the beads 'sank' to the bottom of the cuvette. Beads could be re-dispersed upon vigorously shaking the cuvette. The fact that the luminescence intensity returned to its original level when reshaken at 300 min shows that negligible photobleaching had occurred within that time.

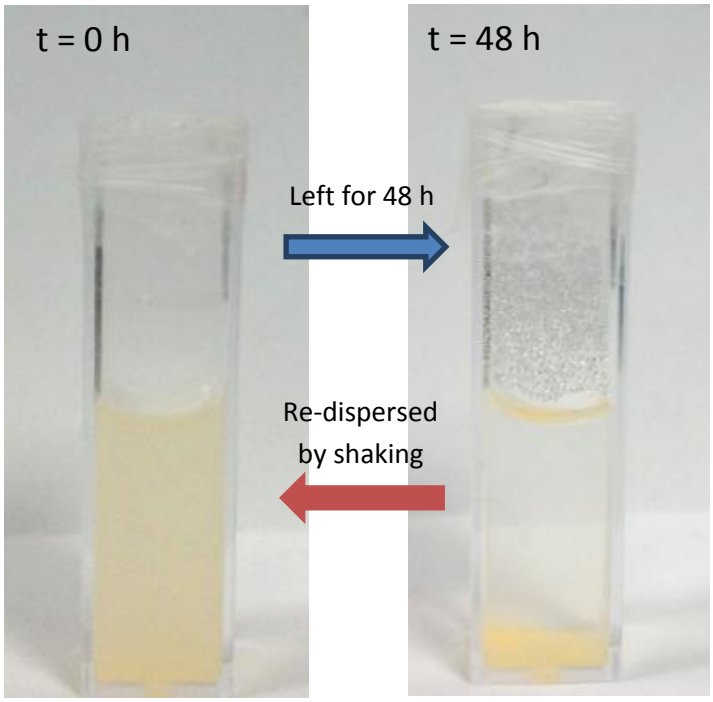


Fig 4-26 Picture to show the sedimentation of phosphorescent beads after 48 h.

4.4 Summary

The $Ru(dpp)_3$-doped PS-co-MA/BPA phosphorescent beads developed by Edwards, are highly luminescent polymer bead with a long luminescence life-time, of 5 µs. Luminophores with such long lifetimes can be used in conjunction with time-gated detection, as an alternative to filter-based detection. The synthesis procedure for the beads was improved from the original report by optimising the stirring rate of the polymer solution to 300 rpm. This new synthesis condition gave a high proportion of spherical beads (approximately 90%) and a tighter bead size distribution. Dilution series of the synthesised beads were made, and their photoluminescence intensities were measured with the time-gated detection system. Beads and the detection system worked in harmony, giving us a very good LOD of 3.78×10^{-6} g/ml which is equivalent to 3.78×10^{8} beads/ml.

In order to demonstrate the applicability of the beads in bio-assays, the bead surface requires bio-functionalization. Since the surface carboxyl groups have the potential to be used in bio-analytical applications, they were quantified by conductometric titration. Beads synthesised under the optimised route were found to have approximately 35.5 µmol/g surface carboxyl groups, which is in good agreement with an estimate that was derived from the bead size distribution. Beads were biotinylated with various concentrations of Amine-PEG_8-Biotin. (Sigma-Aldrich, UK) using an EDC (Life Technology, UK) mediated carboiimide cross-liking reaction. ATR-FTIR confirmed that the beads were successfully biotinylated. The photo-physical properties of the beads remained unchanged upon biotinylation, and this was confirmed through examining their excitation/emission, lifetime, and PLQE characteristics.

To filter the biotinylated beads from the non-biotinylated beads, commercial streptavidin magnetic polymer microspheres, Dynabeads®MyOne™ Streptavidin C1 (Life Technology, UK) were used. The beads were separated by using the strong biotin-streptavidin interaction to bind the biotinylated beads to the magnetic beads. The magnetic bead conjugates were readily extracted from the supernatant (containing the non-biotinylated beads) using a rare-earth magnet. Again, by using the time-gated detection system, luminescence from the biotinylated beads was successfully measured, giving a LOD of 0.011 nmol/ml for Biotin. Furthermore, reducing the magnetic bead concentration had no effect on their LOD, but signal levelled as higher biotin concentration was reached. Finally the photostability of the beads and their conjugates was measured over a span of 1200 min using the same time-gated detection system setup. Initially, the photoluminescence intensity of the beads was found to decrease over time, but full signal intensity was recovered after re-suspension of the bead sediment indicating that no photobleaching had occurred.

To summarise, highly luminescent and stable $Ru(dpp)_3$ doped PS-co-MA/BPA phosphorescent beads were used in conjunction with a commercial streptavidin coated magnetic beads as an assay to detect biotin. This demonstrated the use of such beads with the time-gated detection system to be a promising approach for analyte detection.

CHAPTER 5

5

Conclusion & Future Work



5 Conclusion & Future work

5.1 Conclusion

Microfluidic devices are attracting interest for point of care diagnostics on account of their low unit cost, low reagent and sample usage, fast analysis times and portability. A typical microfluidic test comprises several assay steps (sampling, filtering, labeling, separation etc.), followed by some means of analyte detection. Fluorescence is the most widely used detection method in microfluidics due to its high sensitivity, excellent dynamic range, ease of implementation and non-invasive nature. However, reported microfluidic devices often utilise conventional optical detection apparatus, which tends to be bulky and expensive. In this thesis, work was undertaken to develop a low-cost LED/photodiode based detection system that offers a viable low cost solution for sensitive, integrated luminescence detection on a microfluidic chip. Two different detection methods were explored, both of which enable the use of low cost LEDs and Si-photodetectors, namely fluorescence detection using optical filters and filter-less time-gated phosphorescence detection.

5.1.1 Dye-sensitised titania based filters

Work initially focused on fabricating dye-sensitised titania-based optical filters that exhibit extremely low autofluorescence. Upon optimising various fabrication conditions, two separate routes were devised for fabricating titania filters on glass and plastic substrates. Titania filters on glass were fabricated by sintering titania colloidal paste at 450 °C and by immersing the resultant nanoporous titania films in 0.01 M dye solutions. Filters fabricated on plastic substrates used modified titania colloid pastes (without surfactants) and required no such sintering procedures. Further to this, surface acid/base treatment of titania was used to electrostatically adhere anionic/cationic dyes to the surface, which greatly increased the range of dyes available for producing titania filters. Both short and long pass titania filters were fabricated using a range of dyes and shown to exhibit much lower autofluorescence than equivalent filters obtained by dispersing the same dyes in a host polymer matrix. Upon comparison to commercial schott glass colour filters, it was found that the autofluorescence from the titania-based filters was approximately 10,000 times lower.

Initial experiments that were designed to demonstrate the effect of autofluorescence on the LOD used titania long-pass filters on glass in the detection of R6G. (The excitation source was a 1.1 mW HeCd laser and hence did not require short-pass filtration.) Experiments that used the titania filters achieved far better limits of detection (Λ = 1.2 µg/ml for the FDS-sensitised filter, and Λ = 0.91 µg/ml for the Alizarin-sensitised filter) than a control experiment that used a commercial schott glass colour filters (Λ = 4.43 µg/ml for Schott OG530 colour glass filter)

To enable cheap LEDs to be used as the excitation source and to facilitate integration with microfluidic devices, a complementary set of short- and long-pass filters (Ti-Xylene Cyanol and Ti-FDS respectively) were fabricated on plastic. The filter properties were well matched to the spectral characteristics of T8661 Transfluosphere beads. The titania short-pass filter was able to sharpen the broad LED emission that would otherwise overlap with the transfluosphere signal. Using the filters in conjunction with a 505 nm Cyan LED and a Si-photodiode, dose-response plots were obtained for T8661 fluorescent beads in the concentration range 1×10^{9} to $\times10^{5}$ beads ml^{-1}. After several optimisations, which resulted in the use of an in-house pulsed constant current LED driver, lock-in amplifier, and a photopic Si-photodiode, the best LOD was found to be 2.86×10^{4} beads ml^{-1} which is equivalent to an approximate 350,000 fold dilutions of the original stock solution (1×10^{10} beads ml^{-1}). This LOD exceeded the best reported result in the literature using a similar LED / optical filter / polarisers / silicon photodetector configuration.

5.1.2 Time-gated phosphorescence detection

As a filter-less alternative to the above approach, highly phosphorescent $Ru(dpp)_3$ doped PS-co-MA/BPA polymer beads developed by Edwards were used in conjunction with a time-gated detection system. Polymer beads were synthesised via the precipitation method outlined in chapter four, where the stirring rate was optimised from the original (as proposed by Edwards) 600 to 300 rpm. Beads synthesised via the optimised route showed narrow size distribution and gave the highest proportion of spherical beads (95%). Furthermore, the number of surface carboxyl groups was quantified by a conductometric titration method. It was found that beads produced under the optimised synthetic route had approximately 35.5 µmol g^{-1} of surface acidic group content, knowledge of which can be useful in designing a bioassay. This value is lower than the literature reported value for poly(methyl methacrylate)/ poly(acrylic acid) polymer beads (diameter = 6 µm, 240 $\mu molg^{-1}$ of surface acidic group content), but can be controlled by altering the size of the polymer beads [217].

To test the applicability of these beads in a bioassay, they were used in conjunction with commercial bio-functionalised magnetic beads (Dynabeads®MyOne™ Streptavidin C1) to form a simple biotin assay. Phosphorescent beads were biotinylated using standard carbodiimide (EDC) mediated cross-linking chemistry with various concentrations of biotin (Amine-PEG_8-Biotin). To this mixture, streptavidin-coated magnetic beads were added to separate the biotinylated beads from the supernatant using a bar magnet. Magnetic beads provided an elegant way of removing the biotinylated beads by the virtue of strong biotin-streptavidin interaction. The separated magnetic-phosphorescent bead conjugates were re-dispersed in a 0.1 M phosphate buffer saline solution, and their phosphorescent signals were measured using the time-gated detection technique described in chapter four. The limit of detection for biotin was found to be 0.011 nmol/ml, which offers comparable sensitivity to fluorescent label based biotin assays (using microplates, LOD – 0.005 nmol/ml see chapter four section 4.3.2.4 for reference). Importantly, no change was observed in the emission/excitation characteristics of the beads upon conjugation, indicating successful encapsulation of $Ru(dpp)_3$ from the environment.

5.2 Future work

Fabrication of non-emissive, titania based colour filters developed during the course of this project can be further optimised to provide filters with higher optical densities and a wider range of absorption characteristics. During the course of this thesis, high O.D. was achieved by stacking individual filters on top of one another. This method was adopted due to difficulties in fabricating thick titania layers with sufficient mechanical stability. Multi-layered titania filters with polymer multilayers that act as a solid support can potentially yield thinner titania filters (compared to a stacked approach) with high O.D. (Fig. 5-1).

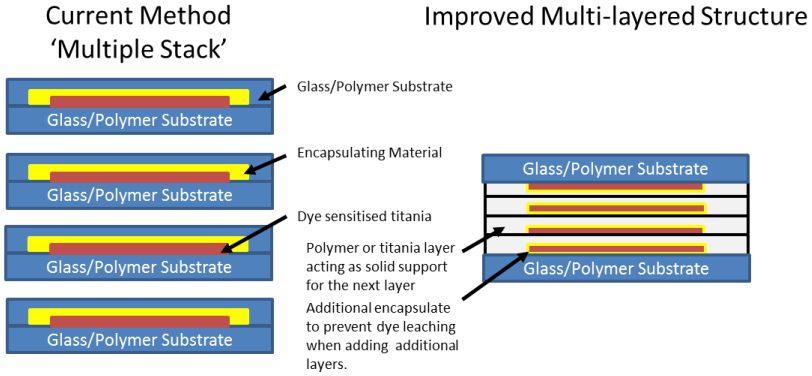


Fig. 5-1 diagram showing the structure of the proposed multi-layered titania filter.

However, there is a potential problem of dye leaching into the multilayer structure and the filter's non-emissive property thus being compromised. This would require further preventative measures to be investigated – such as altering the hydrophilic/hydrophobic nature of the polymers and dyes. An additional encapsulating polymer could perhaps be added between the sensitised titania layer and the solid support layer. (Fig. 5-1)

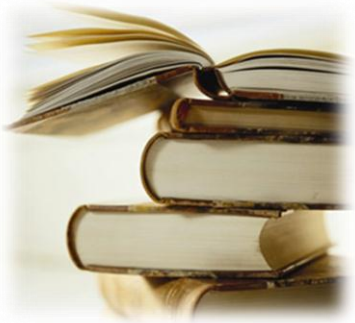
Other sensitising species such as quantum dots could also be investigated as an alternative to organic dyes. Use of quantum dots would allow more control of the absorption characteristics of the filters. Filters with sharper transitions between the blocking-band and pass-band would be highly advantageous to the sensitivity of the assay. Furthermore, species that can sensitise in the near infrared and UV could be employed to reduce the tail-light leakage in this region, further improving the background signal. Ultimately it would be useful to test these titania based filters in a microfluidic device to fully demonstrate their potential as a key component in future POC diagnostic devices.

Regarding the phosphorescent beads, synthesis procedures such as the rate of water addition and dye loading can be further optimised. Altering such synthesis parameters should allow more control over the bead size, size distribution, and sensitivity (Note, that smaller beads could prevent the sedimentation effect seen in section 4.3.2.5.). In chapter four, section 4.3.2.3 PS-co-MA/BPA was shown to be an excellent encapsulant. Other hydrophobic luminescent species should be tested to demonstrate the use of polymer beads in other assays and imaging applications. Again, it would be useful to test these beads in a microfluidic device, which would require further miniaturisation of the time-gated detection system.

CHAPTER 6

6

References



6 References

1. Berger, D., *A brief history of medical diagnosis and the birth of the clinical laboratory.* Medical Laboratory Obsever, 1999. **31**(12): p. 5.
2. Verghese, A., *A History of Physical Examination Texts and the Conception of Bedside Diagnosis.* Transactions of the American Clinical and Climatological Association, 2010. **122**: p. 290.
3. Kononenko, I., *Machine learning for medical diagnosis: history, state of the art and perspective.* Artificial Intelligence in Medicine, 2001. **23**(1): p. 89-109.
4. Doi, K., *Computer-aided diagnosis in medical imaging: historical review, current status and future potential.* Computerized medical imaging and graphics, 2007. **31**(4-5): p. 198.
5. Simerville, J.A., *Urinalysis: a comprehensive review.* American family physician, 2005. **71**(6): p. 1153.
6. Lorincz, A.E., et al., *Urinalysis: current status and prospects for the future.* Annals of clinical & laboratory science, 1999. **29**(3): p. 169-175.
7. *Monoclonal Antibody Based Products: A Global Stratigic Business Report*, 2008, Global Industry Analysis.
8. *Invest in Finland: Global IVD Market Trend*, 2011, Invest in Finland.
9. *Next generation handheld diagnostic solutions for point-of-care*. 2010; Available from: http://www.newscenter.philips.com/main/standard/news/backgrounders/2010/20100107_handheld_diagnostics.wpd.
10. Whitesides, G.M., *The origins and the future of microfluidics.* Nature, 2006. **442**(7101): p. 368-373.
11. deMello, A.J. and R.C.R. Wootton, *Miniaturization: Chemistry at the crossroads.* Nat Chem, 2009. **1**(1): p. 28-29.
12. Franke, T.A., *Microfluidics for miniaturized laboratories on a chip.* ChemPhysChem, 2008. **9**(15): p. 2140.
13. Balagaddé, F.K., *Long-term monitoring of bacteria undergoing programmed population control in a microchemostat.* Science, 2005. **309**(5731): p. 137.
14. Riffle, M., *The Yeast Resource Center Public Data Repository.* Nucleic acids research, 2005. **33**(Database Issue): p. D378.
15. Yamazaki, M., *Non-emissive colour filters for fluorescence detection.* Lab on a chip, 2011. **11**(7): p. 1228.
16. Hofmann, O., et al., *Thin-film organic photodiodes as integrated detectors for microscale chemiluminescence assays.* Sensors and actuators. B, Chemical, 2005. **B106**(2): p. 878.
17. Yao, B., et al., *A microfluidic device using a green organic light emitting diode as an integrated excitation source.* Lab on a chip, 2005(5): p. 1041-1047.
18. Hofmann, O., et al., *Towards microalbuminuria determination on a disposable diagnostic microchip with integrated fluorescence detection based on thin-film organic light emitting diodes.* Lab on a chip, 2005. **5**(8): p. 863.
19. Wang, X., et al., *Integrated thin-film polymer/fullerene photodetectors for on-chip microfluidic chemiluminescence detection.* Lab on a chip, 2007. **7**(1): p. 58.
20. Edel, J.B., et al., *Thin-film polymer light emitting diodes as integrated excitation sources for microscale capillary electrophoresis.* Lab on a chip, 2004. **4**(2): p. 136.
21. Brennan, D., et al., *Emerging optofluidic technologies for point-of-care genetic analysis systems: a review.* Analytical and bioanalytical chemistry, 2009. **395**(3): p. 621.

22. Kamei, T., *Microfluidic genetic and amino acid analysis using an integrated a-Si:H detector IEEE Sensors Conference*. 2003.
23. Moon, S., et al., *Integrating microfluidics and lensless imaging for point-of-care testing* Biosensors and Bioelectronics, 2009. **24**(11): p. 3208-3214.
24. Thrush, E., et al., *Monolithically integrated semiconductor fluorescence sensor for microfluidic applications.* Sensors and actuators. B, Chemical, 2005. **B105**(2): p. 393.
25. Seo, J. and L.P. Lee, *Disposable integrated microfluidics with self-aligned planar microlenses.* Sensors and actuators. B, Chemical, 2004. **B99**(2): p. 615.
26. Hofmann, O., et al., *Monolithically integrated dye-doped PDMS long-pass filters for disposable on-chip fluorescence detection.* Lab on a chip, 2006. **6**(8): p. 981.
27. Chang, C.-P., et al., *Compact optical microfluidic uric acid analysis system.* Biosensors and Bioelectronics, 2011. **26**(10): p. 4155-4161.
28. Zhiliang, W., H. Zeng, and A. Feinerman, *Area-tunable micromirror based on electrowetting actuation of liquid-metal droplets.* Appl. Phys. Lett, 2006. **89**(201107).
29. Hosokawa, K., K. Hanada, and R. Maeda, *A polydimethylsiloxane (PDMS) deformable diffraction grating for monitoring of local pressure in microfluidic devices.* Journal of micromechanics and microengineering, 2002. **12**(1): p. 1.
30. Balslev, S., et al., *Lab-on-a-chip with integrated optical transducers.* Lab on a chip, 2006. **6**(2): p. 213.
31. Irawan, R., et al., *Integration of optical fiber light guide, fluorescence detection system, and multichannel disposable microfludic chip.* Biomedical Microdevices, 2007. **9**(3): p. 413.
32. Andreu, L., et al., *Monolithic PDMS passband filters for fluorescence detection.* Lab on a chip, 2010. **10**(15): p. 1987.
33. Bliss, C., J.N. McMullin, and C.J. Backhouse, *Integrated wavelength-selective optical waveguides for microfluidic-based laser-induced fluorescence detection.* Lab on a chip, 2008. **8**(1): p. 143.
34. Manz, A., et al., *Planar chips technology for miniaturization and integration of separation techniques into monitoring systems: Capillary electrophoresis on a chip.* Journal of Chromatography A, 1992. **593**(1–2): p. 253-258.
35. Harrison, D.J., et al., *Micromachining a Miniaturized Capillary Electrophoresis-Based Chemical Analysis System on a Chip.* Science, 1993. **261**(5123): p. 895-897.
36. Colyer, C.L., *Microchip-based capillary electrophoresis of human serum proteins.* Journal of chromatography. A, 1997. **781**(1): p. 271.
37. Colyer, C.L., *Clinical potential of microchip capillary electrophoresis systems.* Electrophoresis, 1997. **18**(10): p. 1733.
38. Jiang, G., et al., *Red diode laser induced fluorescence detection with a confocal microscope on a microchip for capillary electrophoresis.* Biosensors and Bioelectronics, 2000. **14**(10–11): p. 861-869.
39. Bliss, C.L., J.N. McMullin, and C.J. Backhouse, *Rapid fabrication of a microfluidic device with integrated optical waveguides for DNA fragment analysis.* Lab on a chip, 2007. **7**(10): p. 1280-1287.
40. Sia, S.K., et al., *An Integrated Approach to a Portable and Low-Cost Immunoassay for Resource-Poor Settings.* Angewandte Chemie International Edition, 2004. **43**(4): p. 498-502.
41. Shrinivasan, S., et al., *A Low-Cost, Low-Power, Consumption Miniature Laser-Induced Fluorescence System for DNA Detection on a Microfluidic Device.* Journal of the Association for Laboratory Automation, 2006. **11**(4): p. 254-259.
42. Hu, Z., et al., *Integrated microspectrometer for fluorescence based analysis in a microfluidic format.* Lab on a chip, 2012.

43. Yang, F., et al., *A facile light-emitting-diode induced fluorescence detector coupled to an integrated microfluidic device for microchip electrophoresis.* Talanta, 2011. **84**(4): p. 1099-1106.
44. Kuswandi, B., et al., *Optical sensing systems for microfluidic devices: A review.* Analytica Chimica Acta, 2007. **601**(2): p. 141-155.
45. Otoole, M., *Absorbance based light emitting diode optical sensors and sensing devices.* Sensors, 2008. **8**(4): p. 2453.
46. Peumans, P., *Small molecular weight organic thin-film photodetectors and solar cells.* Journal of applied physics, 2003. **93**: p. 3693.
47. Pais, A., *High-sensitivity, disposable lab-on-a-chip with thin-film organic electronics for fluorescence detection.* Lab on a chip, 2008. **8**(5): p. 794.
48. Tanaka, D., *Ultra high efficiency green organic light-emitting devices.* Japanese journal of applied physics, 2007. **46**: p. L10.
49. Schmidt, M.C., *High power and high external efficiency m-plane InGaN light emitting diodes.* Japanese journal of applied physics, 2007. **46**: p. L126.
50. Lee, J., *High efficiency organic multilayer photodetectors based on singlet exciton fission.* Applied physics letters, 2009. **95**: p. 033301.
51. Christopher Hardee, R.K., Travis Wakefield, and Robert Johnson. *Interference Filters for Fluorescence Microscopy*. 2004; Available from: http://www.olympusfluoview.com/theory/interferencefilters.html.
52. Murphy, D.B. *Introduction to Light Interference*. Available from: http://www.microscopyu.com/articles/polarized/interferenceintro.html.
53. AG, S., *Interference filters and special filters*, 2012.
54. Richard, C., *An integrated hybrid interference and absorption filter for fluorescence detection in lab-on-a-chip devices.* Lab on a chip, 2009. **9**(10): p. 1371.
55. Chen, K.M., *SiO/TiO omnidirectional reflector and microcavity resonator via the sol-gel method.* Applied physics letters, 1999. **75**: p. 3805.
56. Fujishima, A., *Hydrogen production under sunlight with an electrochemical photocell.* Journal of the Electrochemical Society, 1975. **122**: p. 1487.
57. Ulrike, D., *The surface science of titanium dioxide.* Surface Science Reports, 2003. **48**(5–8): p. 53-229.
58. Mo, S.D., *Electronic and optical properties of three phases of titanium dioxide: Rutile, anatase, and brookite.* Physical review. B, Condensed matter, 1995. **51**(19): p. 13023.
59. Chen, X., *Titanium dioxide nanomaterials: synthesis, properties, modifications, and applications.* Chemical reviews, 2007. **107**(7): p. 2891.
60. Watson, S., et al., *Preparation of nanosized crystalline TiO₂ particles at low temperature for photocatalysis.* Journal of Nanoparticle Research, 2004. **6**(2): p. 193-207.
61. Linsebigler, *Photocatalysis on TiO2 Surfaces: Principles, Mechanisms, and Selected Results.* Chemical reviews, 1995. **95**(3): p. 735-758.
62. Barthelmy, D. *Mineralogy Database*. Available from: http://webmineral.com/.
63. Tang, H., *Electrical and optical properties of TiO2 anatase thin films.* Journal of applied physics, 1994. **75**(4): p. 2042.
64. Hagfeldt, A., *Molecular photovoltaics.* Accounts of chemical research, 2000. **33**(5): p. 269.
65. Magne, C., *Brookite TiO2 Nanoparticle Films for Dye‐Sensitized Solar Cells.* ChemPhysChem, 2011. **12**(13): p. 2461.
66. Kalyanasundaram, K., *Applications of functionalized transition metal complexes in photonic and optoelectronic devices.* Coordination chemistry reviews, 1998. **177**(1): p. 347.
67. Topsøe, N.-Y., *Characterization of the nature of surface sites on vanadia-titania catalysts by FTIR.* Journal of Catalysis, 1991. **128**(2): p. 499-511.

68. Kumar, C.S.S.R., *Nanostructured Thin Films and Surfaces*. 2010: Wiley. 451.
69. Wang, C.C., *Sol-gel synthesis and hydrothermal processing of anatase and rutile titania nanocrystals.* Chemistry of materials, 1999. **11**(11): p. 3113.
70. Reyes Coronado, D., *Phase-pure TiO2 nanoparticles: anatase, brookite and rutile.* Nanotechnology, 2008. **19**: p. 145605.
71. Russo, M., *Titanium Oxide Hydrates: Optical properties and applications*, in *Engineering and Material Sciences*2010, University of London.
72. Klein, S.M., *Synthesis of rutile titania powders: Agglomeration, dissolution, and reprecipitation phenomena.* Journal of materials research, 2003. **18**(6): p. 1457.
73. Nagase, T., *Hydrothermal synthesis of brookite.* Chemistry Letters, 1999(9): p. 911.
74. Jiao, Y., *Insight into the crystal lattice formation of brookite in aqueous ammonia media: the electrolyte effect.* CrystEngComm, 2011. **13**(12): p. 4167.
75. Bahnemann, D., A. Henglein, and L. Spanhel, *Detection of the intermediates of colloidal TiO2-catalysed photoreactions.* Faraday Discussions of the Chemical Society, 1984. **78**: p. 151-163.
76. Alivisatos, A.P., *Semiconductor Clusters, Nanocrystals, and Quantum Dots.* Science, 1996. **271**(5251): p. 933-937.
77. Kochuveedu, S.T., D.-P. Kim, and D.H. Kim, *Surface-Plasmon-Induced Visible Light Photocatalytic Activity of TiO2 Nanospheres Decorated by Au Nanoparticles with Controlled Configuration.* The Journal of Physical Chemistry C, 2011.
78. Alivisatos, A.P., *Perspectives on the physical chemistry of semiconductor nanocrystals.* The journal of physical chemistry. A, 1996. **100**(31): p. 13226.
79. Burda, C., *Chemistry and Properties of Nanocrystals of Different Shapes.* Chemical reviews, 2005. **105**(4): p. 1025-1102.
80. Murray, C.B., C.R. Kagan, and M.G. Bawendi, *SYNTHESIS AND CHARACTERIZATION OF MONODISPERSE NANOCRYSTALS AND CLOSE-PACKED NANOCRYSTAL ASSEMBLIES.* Annual Review of Materials Science, 2000. **30**(1): p. 545-610.
81. Wang, Y., *Nanometer-sized semiconductor clusters: materials synthesis, quantum size effects, and photophysical properties.* The journal of physical chemistry. A, 1991. **95**(2): p. 525.
82. Anpo, M., *Photocatalytic hydrogenation of propyne with water on small-particle titania: size quantization effects and reaction intermediates.* The journal of physical chemistry. A, 1987. **91**(16): p. 4305.
83. Negishi, N., K. Takeuchi, and T. Ibusuki, *The surface structure of titanium dioxide thin film photocatalyst.* Applied Surface Science, 1997. **121–122**(0): p. 417-420.
84. Gratzel, M., *Photoelectrochemical cells.* Nature, 2001. **414**(6861): p. 338-344.
85. Gratzel, M., *Dye-sensitized solar cells.* Journal of photochemistry and photobiology. B, Biology, 2003. **4**(2): p. 145.
86. Huber, R., *The role of surface states in the ultrafast photoinduced electron transfer from sensitizing dye molecules to semiconductor colloids.* The journal of physical chemistry. A, 2000. **104**(38): p. 8995.
87. Hannappel, T., B. Burfeindt, and W. Storck, *Measurement of ultrafast photoinduced electron transfer from chemically anchored Ru-dye molecules into empty electronic states in a colloidal anatase TiO2 film.* The journal of physical chemistry. B, 1997. **101**(35): p. 6799.
88. Kamat, P.V., *Interfacial charge transfer processes in colloidal semiconductor systems.* Progress in reaction kinetics, 1994. **19**(3): p. 277.
89. Moser, J.E., *Observation of temperature independent heterogeneous electron transfer reactions in the inverted Marcus region.* Chemical physics, 1993. **176**(2-3): p. 493.

90. Meng, S., J. Ren, and E. Kaxiras, *Natural Dyes Adsorbed on TiO2 Nanowire for Photovoltaic Applications: Enhanced Light Absorption and Ultrafast Electron Injection.* Nano Letters, 2008. **8**(10): p. 3266-3272.
91. Wang, Z.-S., K. Sayama, and H. Sugihara, *Efficient Eosin Y Dye-Sensitized Solar Cell Containing Br-/Br3- Electrolyte.* The Journal of Physical Chemistry B, 2005. **109**(47): p. 22449-22455.
92. Kavan, L., et al., *Preparation of TiO2 (anatase) films on electrodes by anodic oxidative hydrolysis of TiCl3.* Journal of Electroanalytical Chemistry, 1993. **346**(1–2): p. 291-307.
93. Hafner, B. *scanning electron microscopy primer*. 2007.
94. Langmuir, I., *THE CONSTITUTION AND FUNDAMENTAL PROPERTIES OF SOLIDS AND LIQUIDS. PART I. SOLIDS.* Journal of the American Chemical Society, 1916. **38**(11): p. 2221-2295.
95. Brunauer, S., *Adsorption of gases in multimolecular layers.* Journal of the American Chemical Society, 1938. **60**(2): p. 309.
96. Mahé, M., et al., *Cracking of titania nanocrystalline coatings.* Journal of the European Ceramic Society, 2008. **28**(10): p. 2003-2010.
97. Schneider, M., *High-surface-area titania aerogels: preparation and structural properties.* Journal of materials chemistry, 1992. **2**(6): p. 587.
98. Wang, X.-F., et al., *Development of Solar Cells Based on Synthetic Near-Infrared Absorbing Purpurins: Observation of Multiple Electron Injection Pathways at Cyclic Tetrapyrrole–Semiconductor Interface.* The Journal of Physical Chemistry C, 2011. **115**(49): p. 24394-24402.
99. Dworak, L., V.V. Matylitsky, and J. Wachtveitl, *Ultrafast Photoinduced Processes in Alizarin-Sensitized Metal Oxide Mesoporous Films.* ChemPhysChem, 2009. **10**(2): p. 384-391.
100. Miliani, C., *A spectrophotometric and fluorimetric study of some anthraquinoid and indigoid colorants used in artistic paintings.* Spectrochimica acta. Part B, Atomic spectroscopy, 1998. **54**(4): p. 581.
101. Meallier, P., *Photochemistry of fluorescein and eosin derivatives.* Dyes and pigments, 1999. **40**(2-3): p. 95.
102. Harris, R.G., J.D. Wells, and B.B. Johnson, *Selective adsorption of dyes and other organic molecules to kaolinite and oxide surfaces.* Colloids and Surfaces A: Physicochemical and Engineering Aspects, 2001. **180**(1–2): p. 131-140.
103. Pefferkorn, E., L. Nabzar, and R. Varoqui, *Polyacrylamide Na-kaolinite interactions: Effect of electrolyte concentration on polymer adsorption.* Colloid & Polymer Science, 1987. **265**(10): p. 889-896.
104. Wu, W., *Efficient and stable dye-sensitized solar cells based on phenothiazine sensitizers with thiophene units.* Journal of materials chemistry, 2010. **20**(9): p. 1772.
105. Strataki, N., V. Bekiari, and P. Lianos, *Study of the conditions affecting dye adsorption on titania films and of their effect on dye photodegradation rates.* Journal of Hazardous Materials, 2007. **146**(3): p. 514-519.
106. Strataki, N., et al., *Effect of aggregation of dyes adsorbed on nanocrystalline titania films on the efficiency of photodegradation.* Journal of Photochemistry and Photobiology A: Chemistry, 2007. **191**(1): p. 13-18.
107. Fery Forgues, S., *Are fluorescence quantum yields so tricky to measure? A demonstration using familiar stationery products.* Journal of chemical education, 1999. **76**(9): p. 1260.
108. de Mello, J.C., H.F. Wittmann, and R.H. Friend, *An improved experimental determination of external photoluminescence quantum efficiency.* Advanced Materials, 1997. **9**(3): p. 230-232.
109. Hofmann, O., *Monolithically integrated dye-doped PDMS long-pass filters for disposable on-chip fluorescence detection.* Lab on a chip, 2006. **6**(8): p. 981.
110. Song, L., et al., *Photobleaching Kinetics of Fluorescein in Quantitative Fluorescence Microscopy.* Biophysical Journal, 1995. **68**: p. 2588.

111. Chen, C. and C. Chen, *Effect of transition metal ions on the TiO2-assisted photodegradation of dyes under visible irradiation: a probe for the interfacial electron transfer process and reaction mechanism.* The journal of physical chemistry. B, 2002. **106**(2): p. 318.
112. Liu, G., *Photoassisted degradation of dye pollutants. 8. Irreversible degradation of alizarin red under visible light radiation in air-equilibrated aqueous TiO2 dispersions.* Environmental science & technology, 1999. **33**(12): p. 2081.
113. Koumura, N., et al., *Alkyl-Functionalized Organic Dyes for Efficient Molecular Photovoltaics.* Journal of the American Chemical Society, 2006. **128**(44): p. 14256.
114. Tachibana, Y., et al., *Quantitative Analysis of Light-Harvesting Efficiency and Electron-Transfer Yield in Ruthenium-Dye-Sensitized Nanocrystalline TiO2 Solar Cells.* Chemistry of Materials, 2002. **14**(6): p. 2527-2535.
115. Nishimura, S., et al., *Standing Wave Enhancement of Red Absorbance and Photocurrent in Dye-Sensitized Titanium Dioxide Photoelectrodes Coupled to Photonic Crystals.* Journal of the American Chemical Society, 2003. **125**(20): p. 6306-6310.
116. Hara, K., et al., *A coumarin-derivative dye sensitized nanocrystalline TiO solar cell having a high solar-energy conversion efficiency up to 5.6%.* Chemical Communications, 2001(6): p. 569-570.
117. Hara, K., et al., *Molecular Design of Coumarin Dyes for Efficient Dye-Sensitized Solar Cells.* The Journal of Physical Chemistry B, 2002. **107**(2): p. 597-606.
118. Kurashige, Y., et al., *Theoretical Investigation of the Excited States of Coumarin Dyes for Dye-Sensitized Solar Cells.* The Journal of Physical Chemistry A, 2007. **111**(25): p. 5544-5548.
119. Wang, Z.-S., et al., *Molecular Design of Coumarin Dyes for Stable and Efficient Organic Dye-Sensitized Solar Cells.* The Journal of Physical Chemistry C, 2008. **112**(43): p. 17011-17017.
120. Horiuchi, T., *High Efficiency of Dye-Sensitized Solar Cells Based on Metal-Free Indoline Dyes.* Journal of the American Chemical Society, 2004. **126**(39): p. 12218-12219.
121. Ma, X., *A high-efficiency cyanine dye for dye-sensitized solar cells.* Tetrahedron, 2008. **64**(2): p. 345.
122. Hagberg, D.P., et al., *A novel organic chromophore for dye-sensitized nanostructured solar cells.* Chemical Communications, 2006(21): p. 2245-2247.
123. Mills, A., *Adsorption and photocatalysed destruction of cationic and anionic dyes on mesoporous titania films: Reactions at the air-solid interface.* Applied catalysis. B, Environmental, 2009. **89**(1-2): p. 189.
124. Lachheb, H., *Photocatalytic degradation of various types of dyes (Alizarin S, Crocein Orange G, Methyl Red, Congo Red, Methylene Blue) in water by UV-irradiated titania.* Applied catalysis. B, Environmental, 2002. **39**(1): p. 75.
125. Lindström, *A New Method for Manufacturing Nanostructured Electrodes on Plastic Substrates.* Nano letters, 2001. **1**(2): p. 97-100.
126. Uchida, S., et al., *Flexible dye-sensitized solar cells by 28 GHz microwave irradiation.* Journal of photochemistry and photobiology. A, Chemistry, 2004. **164**(1): p. 93.
127. Jeong, H.Y., *A low-temperature-grown TiO2-based device for the flexible stacked RRAM application.* Nanotechnology, 2010. **21**: p. 115203.
128. Miyasaka, T., *Efficient nonsintering type dye-sensitized photocells based on electrophoretically deposited TiO 2 layers.* Chemistry Letters, 2002. **31**(12): p. 1250.
129. Longo, C., *Solid-state and flexible dye-sensitized TiO2 solar cells: a study by electrochemical impedance spectroscopy.* The journal of physical chemistry. A, 2002. **106**(23): p. 5925.
130. Zardetto, V., *Substrates for flexible electronics: A practical investigation on the electrical, film flexibility, optical, temperature, and solvent resistance properties.* Journal of polymer science. Part A, Polymer chemistry, 2011. **49**(9): p. 638.

131. Pichot, F., J.R. Pitts, and B.A. Gregg, *Low-Temperature Sintering of TiO2 Colloids: Application to Flexible Dye-Sensitized Solar Cells.* Langmuir, 2000. **16**(13): p. 5626-5630.
132. Theotis Clark, J., *A New Application of UV–Ozone Treatment in the Preparation of Substrate-Supported, Mesoporous Thin Films.* Chemistry of Materials, 2000. **12**(12): p. 3879-3884.
133. Tebby, Z., *Low-temperature UV-processing of nanocrystalline nanoporous Thin TiO2 films: An original route toward plastic electrochromic systems.* Chemistry of Materials, 2008. **20**(23): p. 7260.
134. Sanchez, C., *Design, Synthesis, and Properties of Inorganic and Hybrid Thin Films Having Periodically Organized Nanoporosity†.* Chemistry of Materials, 2008. **20**(3): p. 682.
135. Barbé, C.J., et al., *Nanocrystalline Titanium Oxide Electrodes for Photovoltaic Applications.* Journal of the American Ceramic Society, 1997. **80**(12): p. 3157-3171.
136. Fowkes, F.M., *Acid-Base Interactions in Polymer Adhesion*, in *Tribology Series*, J.M. Georges, Editor. 1981, Elsevier. p. 119-137.
137. Miyasaka, T., M. Ikegami, and Y. Kijitori, *Photovoltaic Performance of Plastic Dye-Sensitized Electrodes Prepared by Low-Temperature Binder-Free Coating of Mesoscopic Titania.* Journal of the Electrochemical Society, 2007. **154**(5): p. A455-A461.
138. Funabiki, K., et al., *Design of NIR-Absorbing Simple Asymmetric Squaraine Dyes Carrying Indoline Moieties for Use in Dye-Sensitized Solar Cells with Pt-Free Electrodes.* Organic Letters, 2012. **14**(5): p. 1246-1249.
139. Beverina, L. and P. Salice, *Squaraine Compounds: Tailored Design and Synthesis towards a Variety of Material Science Applications.* European Journal of Organic Chemistry, 2010. **2010**(7): p. 1207-1225.
140. Pandey, S.S., et al., *Alkyl and fluoro-alkyl substituted squaraine dyes: A prospective approach towards development of novel NIR sensitizers.* Thin Solid Films, 2010. **519**(3): p. 1066-1071.
141. Maeda, T., et al., *Near-infrared Absorbing Squarylium Dyes with Linearly Extended π-Conjugated Structure for Dye-sensitized Solar Cell Applications.* Organic Letters, 2011. **13**(22): p. 5994-5997.
142. Funabiki, K., et al., *Synthesis of a novel heptamethine-cyanine dye for use in near-infrared active dye-sensitized solar cells with porous zinc oxide prepared at low temperature.* Energy & Environmental Science, 2011. **4**(6).
143. Geiger, T., et al., *Low-Band Gap Polymeric Cyanine Dyes Absorbing in the NIR Region.* Macromolecular Rapid Communications, 2008. **29**(8): p. 651-658.
144. Michael, J., *United States Patent 7081991 B2*, 2006.
145. Fabian, J., H. Nakazumi, and M. Matsuoka, *Near-infrared absorbing dyes.* Chemical Reviews, 1992. **92**(6): p. 1197-1226.
146. Lefevre, F., et al., *Algal fluorescence sensor integrated into a microfluidic chip for water pollutant detection.* Lab on a Chip, 2012. **12**(4): p. 787-793.
147. Bukietyńska, K., et al., *The role of molecular dynamics in the f-f transition intensities in lanthanide compounds.* Journal of Alloys and Compounds, 1995. **225**(1–2): p. 52-54.
148. Kohlmann, S., *Extremely Long‐Wavelength Charge‐Transfer Absorptions of Binuclear Complexes with Azo‐Modified 2, 2′‐Bipyridyl Ligands.* Angewandte Chemie (International ed.), 1985. **24**(8): p. 684.
149. Zhao, W. and E.M. Carreira, *Conformationally Restricted Aza-Bodipy: A Highly Fluorescent, Stable, Near-Infrared-Absorbing Dye.* Angewandte Chemie International Edition, 2005. **44**(11): p. 1677-1679.
150. Wolfgang, K., *Concepts for metal complex chromophores absorbing in the near infrared.* Coordination Chemistry Reviews, 2011. **255**(21–22): p. 2503-2513.

151. Braterman, P.S., et al., *EPR and absorption spectra of singly reduced mono- and dinuclear diorganoplatinum complexes of heterocyclic .alpha.-diimines.* Inorganic Chemistry, 1992. **31**(2): p. 222-224.
152. Ryu, G., et al., *Highly sensitive fluorescence detection system for microfluidic lab-on-a-chip.* Lab on a Chip, 2011. **11**(9).
153. Diamandis, E.P., *Analytical methodology for immunoassays and DNA hybridization assays — current status and selected systems — critical review.* Clinica Chimica Acta, 1990. **194**(1): p. 19-50.
154. Hamaguchi, Y., *Use of rabbit antibody IgG bound onto plain and aminoalkylsilyl glass surface for the enzyme-linked sandwich immunoassay.* Journal of Biochemistry, 1977. **82**(1): p. 261.
155. Gribnau, T.C.J., J.H.W. Leuvering, and H. van Hell, *Particle-labelled immunoassays: A review.* Journal of Chromatography B: Biomedical Sciences and Applications, 1986. **376**(0): p. 175-189.
156. Burns, A., *Fluorescent core–shell silica nanoparticles: towards "Lab on a Particle" architectures for nanobiotechnology.* Chemical Society reviews, 2006. **35**(11): p. 1028.
157. Zhao, X., *Ultrasensitive DNA detection using highly fluorescent bioconjugated nanoparticles.* Journal of the American Chemical Society, 2003. **125**(38): p. 11474.
158. Clark, H.A., *Second harmonic generation properties of fluorescent polymer-encapsulated gold nanoparticles.* Journal of the American Chemical Society, 2000. **122**(41): p. 10234.
159. Quaroni, L., *Preparation of polymer-coated functionalized silver nanoparticles.* Journal of the American Chemical Society, 1999. **121**: p. 10642.
160. Chan, W.C.W., *Luminescent quantum dots for multiplexed biological detection and imaging.* Current opinion in biotechnology, 2002. **13**(1): p. 40.
161. Goldman, E.R., et al., *Avidin: A Natural Bridge for Quantum Dot-Antibody Conjugates.* Journal of the American Chemical Society, 2002. **124**(22): p. 6378-6382.
162. Han, M., et al., *Quantum-dot-tagged microbeads for multiplexed optical coding of biomolecules.* Nat Biotech, 2001. **19**(7): p. 631-635.
163. Edwards, A.N., *Development of Luminescent Labels for use in Miniaturised diagnostic Devices*, in *Chemistry*2011, Imperial College London.
164. Thibon, A. and V.r.C. Pierre, *A Highly Selective Luminescent Sensor for the Time-Gated Detection of Potassium.* Journal of the American Chemical Society, 2008. **131**(2): p. 434-435.
165. Inc., J.Y.H., *Time-Gated Separation of Lanthanide Luminescence*, 2003.
166. Li, Q., P.K. Dasgupta, and H. Temkin, *A time-gated fluorescence detector using a tuning fork chopper.* Analytica Chimica Acta, 2008. **616**(1): p. 63-68.
167. Wang, Y., et al., *Ultra-portable explosives sensor based on a CMOS fluorescence lifetime analysis micro-system.* AIP Advances, 2011. **1**(3): p. 032115.
168. Chen, G., *A 5-kg time-resolved luminescence photometer with multiple excitation sources.* Applied spectroscopy, 2012. **66**(3): p. 341.
169. Lakowicz, J.R., *Principles of Fluorescence spectroscopy*. 2006: Springer.
170. Juris, A., *Ru (II) polypyridine complexes: photophysics, photochemistry, electrochemistry, and chemiluminescence.* Coordination chemistry reviews, 1988. **84**: p. 85.
171. Roth, T., *Ruthenium (II) diimine complexes for luminescence-based oxugen sensors and impedance spectroscopy of nitrogen dioxide sensitive polymeric membranes*, 2000, ETH: Zurich.
172. Barry Halliwell, J.M., *Free Radical in Biology and Medicine.* 2 ed. 1982, Oxford: Clarwndon Press.
173. You, Y. and S.Y. Park, *Phosphorescent iridium(iii) complexes: toward high phosphorescence quantum efficiency through ligand control.* Dalton Transactions, 2009(8): p. 1267-1282.
174. Tavasli, M., et al., *Colour tuning from green to red by substituent effects in phosphorescent tris-cyclometalated iridium(iii) complexes of carbazole-based ligands: synthetic, photophysical,*

computational and high efficiency OLED studies. Journal of Materials Chemistry, 2012. **22**(13): p. 6419-6428.
175. Lee, K.W., *Photophysical properties of tris (bipyridyl) ruthenium (II) thin films and devices.* PCCP. Physical chemistry chemical physics, 2003. **5**(12): p. 2706.
176. Gómez Hens, A., *Nanostructures as analytical tools in bioassays.* TrAC. Trends in analytical chemistry, 2008. **27**(5): p. 394.
177. Behnke, T., *Encapsulation of Hydrophobic Dyes in Polystyrene Micro- and Nanoparticles via Swelling Procedures.* Journal of fluorescence, 2011. **21**(3): p. 937-944.
178. Borisov, S.M., et al., *New Plastic Microparticles and Nanoparticles for Fluorescent Sensing and Encoding Fluorescence of Supermolecules, Polymers, and Nanosystems*, M.N. Berberan-Santos, Editor. 2008, Springer Berlin Heidelberg. p. 431-463.
179. Borisov, S.M., et al., *Composite Luminescent Material for Dual Sensing of Oxygen and Temperature.* Advanced Functional Materials, 2006. **16**(12): p. 1536-1542.
180. Baleizão, C., et al., *Dual Fluorescence Sensor for Trace Oxygen and Temperature with Unmatched Range and Sensitivity.* Analytical Chemistry, 2008. **80**(16): p. 6449-6457.
181. Kocincova, A.S., et al., *Fiber-Optic Microsensors for Simultaneous Sensing of Oxygen and pH, and of Oxygen and Temperature.* Analytical Chemistry, 2007. **79**(22): p. 8486-8493.
182. Im, S.H., *Polymer hollow particles with controllable holes in their surfaces.* Nature Materials, 2005. **4**(9): p. 671.
183. Liu, Q., et al., *Preparation and characterization of crosslinked polymer beads with tunable pore morphology.* Journal of Applied Polymer Science, 2011. **121**(2): p. 654-659.
184. Song, X., L. Huang, and B. Wu, *Bright and Monodispersed Phosphorescent Particles and Their Applications for Biological Assays.* Analytical Chemistry, 2008. **80**(14): p. 5501-5507.
185. Kürner, J.M., *Inert phosphorescent nanospheres as markers for optical assays.* Bioconjugate chemistry, 2001. **12**(6): p. 883.
186. Wang, J., et al., *Monodisperse, Molecularly Imprinted Polymer Microspheres Prepared by Precipitation Polymerization for Affinity Separation Applications.* Angewandte Chemie International Edition, 2003. **42**(43): p. 5336-5338.
187. Darbandi, M., R. Thomann, and T. Nann, *Single Quantum Dots in Silica Spheres by Microemulsion Synthesis.* Chemistry of Materials, 2005. **17**(23): p. 5720-5725.
188. Bogush, G.H., M.A. Tracy, and C.F. Zukoski Iv, *Preparation of monodisperse silica particles: Control of size and mass fraction.* Journal of Non-Crystalline Solids, 1988. **104**(1): p. 95-106.
189. Shi, Y., et al., *Uniform molecularly imprinted poly(methacrylic acid) nanospheres prepared by precipitation polymerization: the control of particle features suitable for sustained release of gatifloxacin.* Journal of Materials Chemistry, 2012. **22**(9): p. 3889-3898.
190. Liu, Z.L., et al., *Preparation and characterization of polymer-coated core–shell structured magnetic microbeads.* Journal of Magnetism and Magnetic Materials, 2003. **265**(1): p. 98-105.
191. Hen, J., *Determination of surface car□yl groups in styrene/itaconic acid copolymer latexes.* Journal of Colloid and Interface Science, 1974. **49**(3): p. 425-432.
192. Goddard, J.M. and J.H. Hotchkiss, *Polymer surface modification for the attachment of bioactive compounds.* Progress in Polymer Science, 2007. **32**(7): p. 698-725.
193. Rödiger, S., et al., *Fluorescence Dye Adsorption Assay to Quantify Carboxyl Groups on the Surface of Poly(methyl methacrylate) Microbeads.* Analytical Chemistry, 2011. **83**(9): p. 3379-3385.
194. Yu, S. and G.M. Chow, *Carboxyl group (-CO2H) functionalized ferrimagnetic iron oxide nanoparticles for potential bio-applications.* Journal of Materials Chemistry, 2004. **14**(18): p. 2781-2786.
195. Pohl, H.A., *Determination of Carboxyl End Groups in Polyester, Polyethylene Terephthalate.* Analytical Chemistry, 1954. **26**(10): p. 1614-1616.

196. Leiner, M.J.P., M.R. Hubmann, and O.S. Wolfbeis, *The total fluorescence of human urine.* Analytica Chimica Acta, 1987. **198**(0): p. 13-23.
197. Sengupta, S.K., J.M. Farnham, and J.E. Whitten, *A Simple Low-Cost Lock-In Amplifier for the Laboratory.* Journal of Chemical Education, 2005. **82**(9): p. 1399.
198. Luchowski, R., *Self-quenching of uranin: Instrument response function for color sensitive photo-detectors.* Journal of luminescence, 2010. **130**(12): p. 2446.
199. Livaniou, E., et al., *Analytical techniques for determining biotin.* Journal of Chromatography A, 2000. **881**(1–2): p. 331-343.
200. Birnbaum, J., *Biosynthesis of Biotin in Microorganisms V. Control of Vitamer Production.* Journal of bacteriology, 1967. **94**(6): p. 1846.
201. Broquist, H.P., *Biotin and bacterial growth.* Journal of biological chemistry, 1951. **188**(1): p. 431.
202. Pinon, V., *Biotin synthesis in plants. The first committed step of the pathway is catalyzed by a cytosolic 7-keto-8-aminopelargonic acid synthase.* Plant physiology, 2005. **139**(4): p. 1666.
203. Bachmann, C., *Biotin and Rett syndrome.* American journal of medical genetics. Part B, Neuropsychiatric genetics, 1986. **25**(S1): p. 323.
204. Holmberg, A., *The biotin‐streptavidin interaction can be reversibly broken using water at elevated temperatures.* Electrophoresis, 2005. **26**(3): p. 501.
205. Drechsler, U., *Nanoparticles: Scaffolds for molecular recognition.* Chemistry - A European Journal, 2004. **10**(22): p. 5570.
206. Gole, A. and C.J. Murphy, *Biotin−Streptavidin-Induced Aggregation of Gold Nanorods: Tuning Rod−Rod Orientation.* Langmuir, 2005. **21**(23): p. 10756-10762.
207. Bronfman, F.C., *Ligand-induced internalization of the p75 neurotrophin receptor: a slow route to the signaling endosome.* The Journal of neuroscience, 2003. **23**(8): p. 3209.
208. *Instructions: EZ-Link® Amine-PEO2-Biotin*, 2006, Pierce Biotechnology Inc.
209. Barbucci, R., *Antigen–antibody recognition by Fourier transform IR spectroscopy/attenuated total reflection studies: Biotin–avidin complex as an example.* Biopolymers, 1991. **31**(7): p. 827.
210. Aslan, K., *Nonradiative Interactions between Biotin-Functionalized Gold Nanoparticles and Fluorophore-Labeled Antibiotin.* Plasmonics, 2006. **1**(2): p. 111-119.
211. Sastry, M., et al., *Optical Absorption Study of the Biotin−Avidin Interaction on Colloidal Silver and Gold Particles.* Langmuir, 1998. **14**(15): p. 4138-4142.
212. Walash, M., *Kinetic Spectrophotometric Determination of Biotin in Pharmaceutical Preparations.* International Journal of Biomedical Science, 2008. **4**.
213. Limoges, B., *Avidin–Biotin Assembling of Horseradish Peroxidase Multi-Monomolecular Layers on Electrodes.* Australian journal of chemistry, 2006. **59**(4): p. 257.
214. Chaiet, L. and F.J. Wolf, *The properties of streptavidin, a biotin-binding protein produced by Streptomycetes.* Archives of Biochemistry and Biophysics, 1964. **106**(0): p. 1-5.
215. Smith, C., *Striving for purity: advances in protein purification.* Nat Meth, 2005. **2**(1): p. 71-77.
216. Probes, I.M., *FluoReporter ® Biotin Quantitation Assay Kit *for biotinylated nucleic acids* (F30755)*, 2005.
217. Hennig, A., et al., *Simple Colorimetric Method for Quantification of Surface Carboxy Groups on Polymer Particles.* Analytical Chemistry, 2011. **83**(12): p. 4970-4974.
218. Johnson, D. *Constant current LED driver*. 2004; Available from: http://www.discovercircuits.com/PDF-FILES/CONSTANTCURRETLED1.pdf.

CHAPTER 7

7

Appendix

7 Appendix

7.1 Constant current LED driver

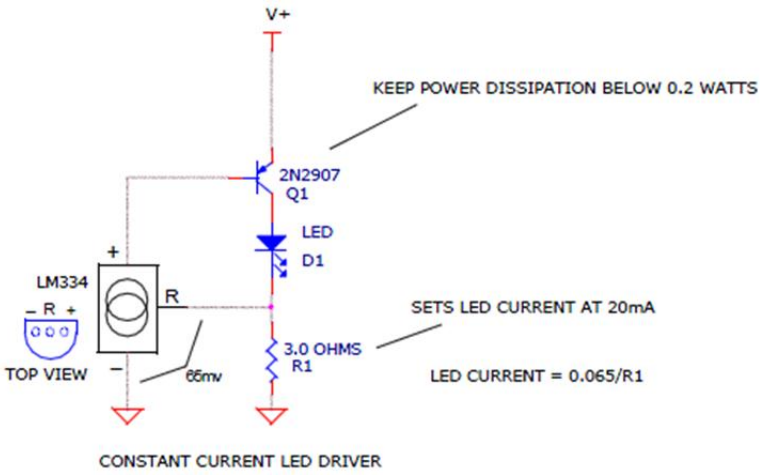


Fig. 7-1 Circuit diagram of the constant current LED driver used in section 3.4.3. Uses a LM344 current source and a single resistor to maintain the current at 20 mA. Taken from ref. [218].

7.2 Constant current pulsed LED driver

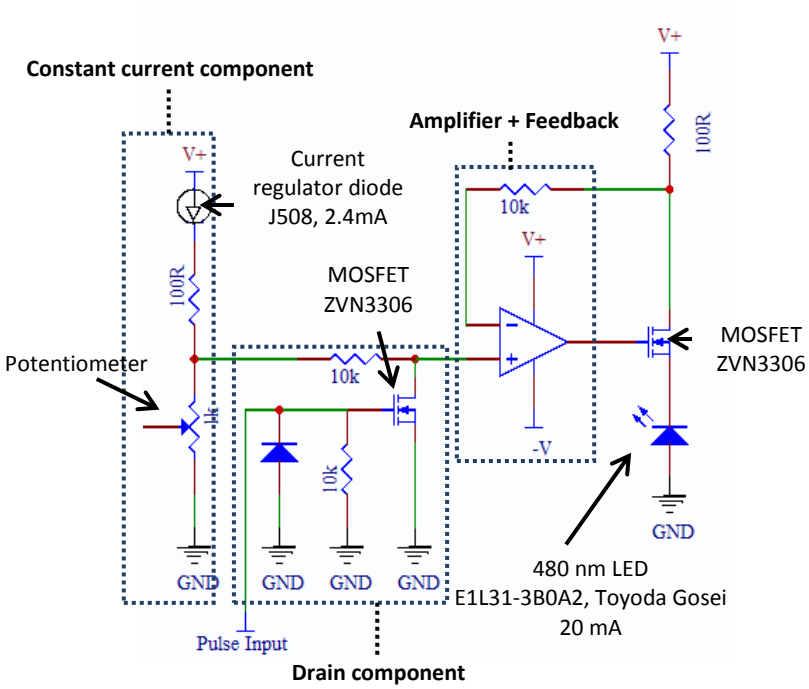


Fig. 7-2 Circuit diagram of the pulsed constant current LED driver used in section 3.4.3.1. Uses a HP 8011A pulse generator for the pulse input. Circuit was designed and built by Mr Steve Atkins of Imperial College London

7.3 Time-gated detection

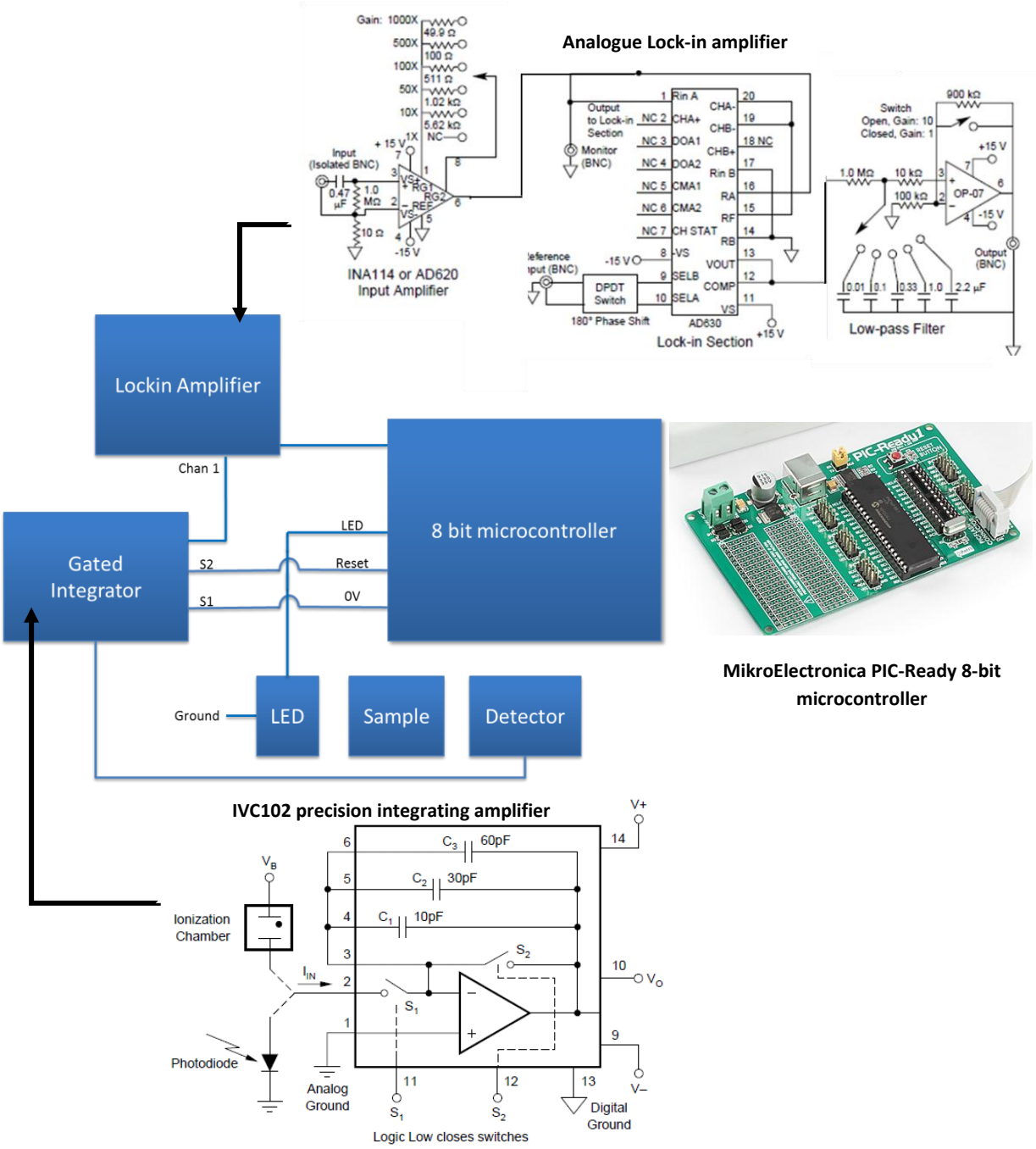


Fig. 7-3 Schematic of the equipment used in Chapter 4, section 4.2.4. Time-gated detection was performed using a PIC board (MikroElektronika, PIC-Ready) driven 480 nm LED at 8.8 kHz. Gated integrator used the IVC102 IC precision integrating amplifier which can integrate low-level input current for a user-defined period. Input current charges a small feedback capacitors and the voltage across the capacitors are measured before being reset. Analogue Lock-in circuit used were taken from ref [197] and constructed by Mr Steve Atkins of Imperial College London.

7.4 PLQE measurements of the beads

Same experimental setup and procedure as that from section 2.6 was used. Samples used were 1) 0.06 g/ml phosphorescent beads, 2) approximately 0.06 m/ml of biotinylated beads, and 3) magnetic-bead-biotinylated bead conjugate (with 0.5 nmol of biotin). 1 mm quartz cuvette were used for all measurements.

7.5 TC-SPC

Time-resolved photoluminescence spectroscopy was performed by using a time-correlated single photon counting system (Horiba Jobin Yvon, Fluorocube). LED laser diode at 467 nm was used as the excitation source and the emission was detected at 610 nm. The obtained histograms were fitted using a mono-exponential function: $y = A1exp(-{}^{x}/_{t}) + y_0$

7.6 List of Publications

Non-emissive colour filters for fluorescence detection

Mikihide Yamazaki , Oliver Hofmann , Gihan Ryu , Li Xiaoe , Tai Kyu Lee , Andrew J. deMello and John C. deMello, ***Lab Chip***, 2011,**11**, 1228-1233 **DOI:** 10.1039/C0LC00642D